Title
The Photometric Properties of Nearby Type Ia Supernovae

Author
Ganeshalingam, Mohan

Publication Date
2012

Peer reviewed|Thesis/dissertation

The Photometric Properties of Nearby Type Ia Supernovae

by

Mohan Ganeshalingam

A dissertation submitted in partial satisfaction of the
requirements for the degree of
Doctor of Philosophy

in

Astrophysics

in the

Graduate Division
of the
University of California, Berkeley

Committee in charge:
Professor Alexei V. Filippenko, Chair
Professor Joshua S. Bloom
Professor Steven E. Boggs

Fall 2012

The Photometric Properties of Nearby Type Ia Supernovae

Abstract

The Photometric Properties of Nearby Type Ia Supernovae

by

Mohan Ganeshalingam
Doctor of Philosophy in Astrophysics

University of California, Berkeley

Professor Alexei V. Filippenko, Chair

Type Ia supernovae (SNe Ia) are the final brilliant explosion of a carbon-oxygen white dwarf accreting mass from a companion star. At peak brightness, a SN Ia can outshine an entire galaxy of billions of stars. Most SNe Ia have a standardizable luminosity, ideal for use as an extragalactic distance indicator. Measurements of a large sample of SNe Ia over a range of distances enables the estimate of cosmological parameters to help determine the mass-energy content of the Universe (Riess et al. 1998; Perlmutter et al. 1999; Riess et al. 2004; Astier et al. 2006; Riess et al. 2007; Wood-Vasey et al. 2008; Kowalski et al. 2008; Hicken et al. 2009a; Amanullah et al. 2010; Sullivan et al. 2011a; Suzuki et al. 2012).

The cosmological application of SNe Ia is predicated upon relationships between the intrinsic luminosity and light-curve properties. Despite the successful measurement of cosmological parameters using SNe Ia, our understanding of SNe Ia themselves is surprisingly lacking. The SN Ia progenitor system has never been directly observed, making it unclear how many different channels exist to make a SN Ia. The physical nature of the relationship between light-curve parameters and luminosity is also not well understood, and it remains to be seen whether other correlations exist to improve SN Ia distance estimates.

The goal of this dissertation is to shed light on the physics of SNe Ia and search for new correlations to improve distance estimates to SNe Ia by analyzing a large sample of well-observed, high-quality SN Ia light curves. I have collected, reduced, and analyzed optical photometric data for 165 nearby SNe Ia as part of the Lick Observatory Supernova Search (LOSS). These data represent a significant contribution to the existing sample of nearby SN Ia light curves.

After giving a general overview of SNe Ia in Chapter 1, I present the methods used to obtain and reduce the LOSS data in Chapter 2. In Chapter 3, I use the LOSS data in an analysis of the earliest photometry epochs to understand the explosion physics governing

the initial rise of the SN Ia light curve. These early data points also provide a means of testing models to constrain the nature of the binary companion star. I do not find evidence for interaction between SN ejecta and a companion star, ruling out theories requiring a red giant as a companion in most cases. In Chapter 4, I combine the data presented in this thesis with other samples in the literature to place constraints on cosmological parameters. I reject a non-accelerating Universe with 99.999% confidence. In Chapter 5, I present a study of an individual peculiar SN Ia that is unlike any previously published object, bucking the relationships normally observed in SNe Ia. Studying extreme SNe Ia may provide insights into understanding the physics of normal SNe Ia.

Dedicated to my wife, Janice, whose warmth, love, and selflessness continues to be my guiding light

Contents

List of Figures

List of Tables

Preface

As humans we endeavor to understand our surroundings. Every culture has a story to describe the origins of the Universe and our relationship to the natural world. Although rooted in folklore and mysticism, their cosmologies are the result of a desire to make sense of a seemingly chaotic world. The advent of a methodical scientific approach gave humans a new means of explaining the natural world. Through careful observations, scientists could make testable hypotheses and incrementally expand the body of human knowledge in a systematic way.

Of the physical sciences, astronomy asks questions on the largest of possible scales. The dogged gazing at astronomical objects has led to (among other discoveries) the discovery that we are but one of many heavenly bodies orbiting the Sun, the realization we reside in a single galaxy amongst a Universe filled with billions of others, and the unexpected discovery that the Universe is expanding at an accelerating rate, probably due to an unexplained, unidentified dark energy.

It is humbling to step back and recognize that all of these discoveries took place by the somewhat simple act of looking at light. Unlike the experimental physicist or the biologist, the astronomer does not have a subject to manipulate, but rather analyzes the light that manages to find Earth within the vast expanse of space. By studying the properties of light, astronomers are able to determine the laws of physics that govern astronomical objects and piece together a narrative of the Universe firmly rooted in science.

This thesis is my contribution to the scientific narrative of our place in the Universe.

Acknowledgments

It is my pleasure to acknowledge the following wonderful people who have made this thesis possible.

This thesis was the brainchild of my advisor, Alex Filippenko, who presciently conceived of the idea of a robotic telescope to systematically find and follow supernovae. His continued guidance as an adviser and mentor has been invaluable. Of the many things I have learned from Alex, perhaps the most valuable has been that the best science discussions are over Zachary's pizza. Thank you for your advising and countless slices of pizza. And thanks to my thesis committee members, Josh Bloom and Steve Boggs, for taking the time to read and comment on this work.

A huge debt of gratitude must be paid to current and former members of Alex's supernova group. Black-belt spectroscopists Ryan Chornock, Ryan Foley, and Jeffrey Silverman have been a rich resource of great ideas and wisdom. I owe much to their insight into data analysis and supernova physics. In addition, I am thankful for the many conversations in the halls of Campbell I had with Brad Cenko, Kelsey Clubb, Saurabh Jha, Maryam Modjaz, Dan Perley, Dovi Poznanski, Ken Shen, and Nathan Smith. A special thanks to Frank Serduke for the delightful company during long nights of observing at Lick, the delicious wine recommendations, and the corny puns.

My heart sinks with sadness knowing that this thesis will never make it to the hands of Weidong Li. My introduction to supernova photometry (and the world of research) took place in Weidong's office in 2004 and he had been a pillar of support up until his untimely death in 2011. Any question, at any time of the day, was met with a thoughtful, detailed, and often humorous response within hours. Weidong was a dedicated mentor, a meticulous scientist, but most of all, a great friend. I miss you Weidong and hope this thesis lives up to your expectations.

Special thanks to Alex Conley for refereeing the journal versions of Chapters 2 and 3. His comments were especially thoughtful and much appreciated. In addition, his publicly available cosmology code was used in Chapter 4. It is safe to say that my work has benefited greatly from him.

My classmates Amber Bauermeister, Statia Cooke, Nicholas McConnell, and Peter K. G. Williams have always been a source of support, advice, and much merriment. I cannot image having a better cohort to share these past 6 years with. Thank you also to Adam Miller, Josh Shiode, Casey Stark, and Thea Steele, for being considerate, knowledgable officemates willing to be a sounding board for problems with code, data analysis, and LaTeX. In addition, there are the countless Berkeley graduate students whom I have had the pleasure to know and interact with. I extend special thanks to Louis-Benoit Desroches, John Johnson, Conor Laver, Evan Levine, Karin Sandstrom, and Kristen Shapiro.

A good fraction of the data presented in this thesis was due to the tireless observations of undergraduates on the 1-m Nickel telescope. I want to especially thank Carmen Anderson, Griffin Foster, Chris Griffith, Niels Joubert, Joel Leja, Brent Macomber, Tyler Pritchard, Patrick Thrasher, and Dustin Winslow.

I am grateful to Keith Baker, Wayne Earthman, Eleanor Gates, Bryant Grigsby, Thomas Lowe, Kris Miller, and Bernie Walp for their expertise in handling the telescopes at Lick Observatory. Even in the most difficult of circumstances they managed to keep the telescopes running.

And finally, I thank my two sisters, Usha and Bhavani, for keeping me in check, my mother for her unconditional support and love, and my dear departed father for instilling a passion and desire to question the obvious and seek the unknown. To my Berkeley family Ming, Jean, and Phyllis, "xie xie" for taking care of me and making me always feel like I had a home nearby. And it is to wife, Janice, I dedicate this thesis.

Chapter 1

Introduction

In this thesis, I present my efforts to study the properties and physics of supernovae (SNe) as part of the Lick Observatory Supernova Search (LOSS). SNe are the final, brilliant explosion of a star at the end of its life. These explosions make up some of the most energetic astronomical phenomena yet observed. At peak brightness these objects can outshine an entire galaxy of $\sim 10^{10}$ stars. These explosions occur at an estimated rate of about one per galaxy every 100 years, making them relatively common transients when observing a large number of galaxies. Looking at a large sample of SNe, I seek to better understand these events and use them to probe cosmology.

In this chapter I will motivate the study of SNe by giving a short introduction to the various types of exploding stars, how astronomers find and study SNe, and what astronomers can learn from SNe.

1.1 Supernovae

There are two major identified classes of SNe based on the physical method by which they explode: thermonuclear and core collapse. While this thesis is focused on thermonuclear SNe, I describe the two classes in the sections that follow.

1.1.1 Thermonuclear SNe

Stars that begin life with a mass < 8 $M_\odot$ will end their stellar evolution as a star called a white dwarf (WD). In the evolutionary phases leading up to this final stage, the star will shed its outermost layers leaving behind a naked core of inert carbon and oxygen. WDs have insufficient mass to fuse carbon and oxygen to higher-mass elements. Thermonuclear supernovae are believed to be the complete explosion of a WD accumulating matter from an

orbiting companion star. As the mass of the WD approaches the critical Chandrasekhar limit of 1.4 $M_\odot$, the temperature of the WD rises until a runaway thermonuclear reaction takes place that spreads across the entire star. The nuclear reaction fuses carbon and oxygen to higher-mass elements including radioactive nickel. The radioactive decay of nickel to cobalt and then cobalt to iron powers the supernova light output, producing a transient which can be as bright as an entire galaxy.

The specific circumstances by which a thermonuclear SN occurs (i.e., mass accretion up to nearly the Chandrasekhar limit) ensures a relatively standard luminosity from event to event. Coupled with extremely bright luminosities, these objects are good candidates for measuring distances on very large scales. However, the progenitor system for a thermonuclear SN has never been directly observed and thus the nature of the companion star remains an open question. Additionally, there are thermonuclear SNe that do not behave like the vast majority. Understanding the unexpectedly weird SNe given the relative uniformity of a majority of SNe Ia continues to be a challenge within the community.

1.1.2 Core-Collapse SNe

A core-collapse SN is the explosion of a massive star (> 8 $M_\odot$). Such stars are massive enough to fuse elements beyond carbon and oxygen in its core to power the luminosity of the star until reaching iron. The stability of the iron nucleus makes fusing two iron nuclei a reaction that requires energy rather than releasing it. An inert iron core builds at the center of the star until the core mass approaches the Chandrasekar limit. The pressure supporting the core cannot sustain the growing core mass and a collapse ensues. The collapse continues until the escalating core pressure produces a remnant supported by neutrons. The outer layers rebound off the core sending a shock that propagates through the star, but ultimately stalls. Neutrinos produced in the core carry away enough energy to unbind the outer layers of the star. Unlike thermonuclear SNe, core-collapse SNe come in a variety of observed subtypes depending the composition of the progenitor star prior to explosion.

1.1.3 Classification

Historically, the classification of SNe has been based on the observed elemental composition of the SN near peak brightness rather than the more physically motivated explosion mechanism. This results in a decision tree based on spectral observations as displayed in Figure 1.1. Originally SNe were classified as Type I (no hydrogen) or Type II (hydrogen). With the discovery of more SNe came a larger diversity in subtypes. Type Ia connotes objects with no hydrogen, but strong silicon. Type Ib have no hydrogen, weak or no silicon,

but some helium. Type Ic have no hydrogen or helium. In terms of physical explosion mechanism, Type Ia are thermonuclear explosions and the Type Ib/c and Type II are core collapse. This thesis is focused solely on SNe Ia.

1.2 Discovering and Monitoring SNe

SNe have been recorded by humans as early as 185 A.D. when Chinese astronomers noted the presence of a new "guest" star in the night sky. Discovery of SNe in our own galaxy continued to be noted by observant astronomers. The invention of the telescope allowed astronomers to extend the search for SNe in neighboring galaxies.

The recognition of SNe as a class of objects was first presented by Baade & Zwicky (1934). Noting the extreme brightness of these objects, their relative infrequency compared to nova explosions, and their presence in galaxies outside the Milky Way, these authors coined the term "super-nova" to describe the class of objects.

More recently, SNe have been found by systematically monitoring a large number of galaxies. A majority of SNe are found by dedicated telescope surveys that monitor large samples of galaxies periodically (typically within a week). Images are compared to previously observed template images. By subtracting the two images using sophisticated algorithms, new SN candidates are identified as bright point sources not present in previous images. In Figure 1.2, I show an example of an image before galaxy subtraction and after. Without galaxy subtraction (left panel) identifying the SN is nearly impossible. The SN becomes visible after subtracting off the galaxy light in the region surrounding the SN (right panel).

New SN candidates are classified using a telescope mounted with a spectrograph. Similar to a prism, a spectrograph spreads light out like a rainbow, allowing astronomers to analyze the SN spectrum. The features of the spectrum are an indiction of the elements present in the SN. Each SN is then classified using the decision tree in Figure 1.1.

In addition to taking spectra of SNe, astronomers measure the light output, or flux, of a SN with time by taking images of the supernova in different colors, or filters. By measuring the flux of a supernova against background stars with a constant flux, astronomers can measure the flux evolution of a SN and infer physical properties about the SN. This technique is referred to as photometry and is the main the concern of this thesis.

1.3 Why Study SNe Ia?

The thermonuclear variety of supernovae (SNe Ia) are of particular importance in astronomy because of their relatively standard luminosity. Having an object with a known

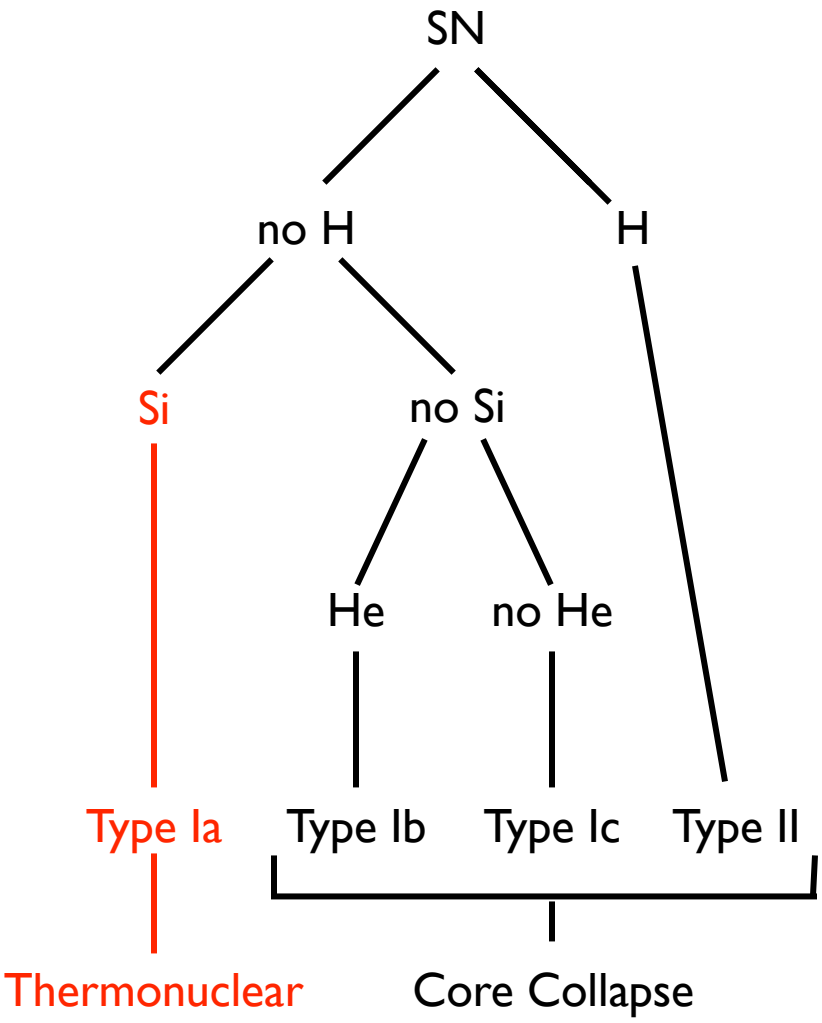

Figure 1.1: SN classification decision tree. Classification of SNe is based on the presence of elements in SN spectra observed near maximum light.

Figure 1.2: An example of galaxy subtraction used to identify a new SN. In the left panel is an image of a SN deeply embedded in the bulge of its host galaxy. The SN is indistinguishable from the light coming from the host galaxy. In the right panel is the SN with the surrounding galaxy light subtracted using a template image taken before the SN explosion. The SN is now clearly detected.

luminosity allows astronomers to determine distances by measuring the flux of the object and applying the inverse-square law.

Phillips (1993) analyzed a sample of SNe Ia and discovered a strong correlation between the characteristic width of a SN light curve and its luminosity. More luminous SNe Ia had broader light curves than less luminous SNe Ia. In Figure 1.3, I show an example of the diversity in SNe Ia light curves in the top panel of the figure. The SN luminosity is plotted as a function of time. The light curves are color coded by light-curve width. More luminous SNe appear higher on the plot and have broader light curves. By using this relationship between light-curve shape and luminosity found by Phillips (1993), we can standardize the luminosity using the measured light-curve width as shown in the bottom panel. SNe Ia are thus said to be "standardizable" candles.

Taking advantage of this correlation greatly improves the ability to standardize SN Ia luminosity, making SNe Ia significantly better distance indicators. Including another correction for the observed SN color allows SNe Ia to be accurate indicators of distance to within 10%. This correction accounts for the effects of host-galaxy dust and intrinsic color differences between SNe. Both effects have the same observed effect: redder SNe appear less luminous than bluer SNe. While these two parameters do a very good job of standardizing the luminosity of a SN Ia, astronomers continue to search for other parameters to make SNe Ia an even better distance indicator.

Edwin Hubble first used Cepheid variable stars (a less luminous standardizable candle) as a distance indicator to nearby galaxies to find the remarkable discovery that the Universe is expanding (Hubble 1929). As seen in Figure 1.4, Hubble found a linear relationship between the distance to a galaxy and the speed at which it is moving away from us. That is, at the present time, more distant galaxies are moving away from the Milky Way faster than nearby galaxies. The expansion rate measured by Hubble using Cepheid stars was a current measure of the gravity exerted by the mass content of the Universe. Hubble's discovery implies a dynamic Universe in motion guided by its mass-energy content. Encoded in SN Ia distance estimates, which probe a larger distance, is the expansion history of the Universe.

Accurate distances to SNe allow astronomers to start asking questions about the nature of the Universe. What is the energy density content of the Universe? Do we live in a Universe made up of only matter? Are there more exotic forces at work? How do cosmological parameters change with time? Answering these questions with SNe requires large samples of SNe Ia to refine relationships and find new ones to improve cosmological distance estimates. Samples of SNe from nearby galaxies are ideal because they can be observed with access to small-aperture telescopes.

In addition to cosmology, there are still outstanding questions regarding the progenitor

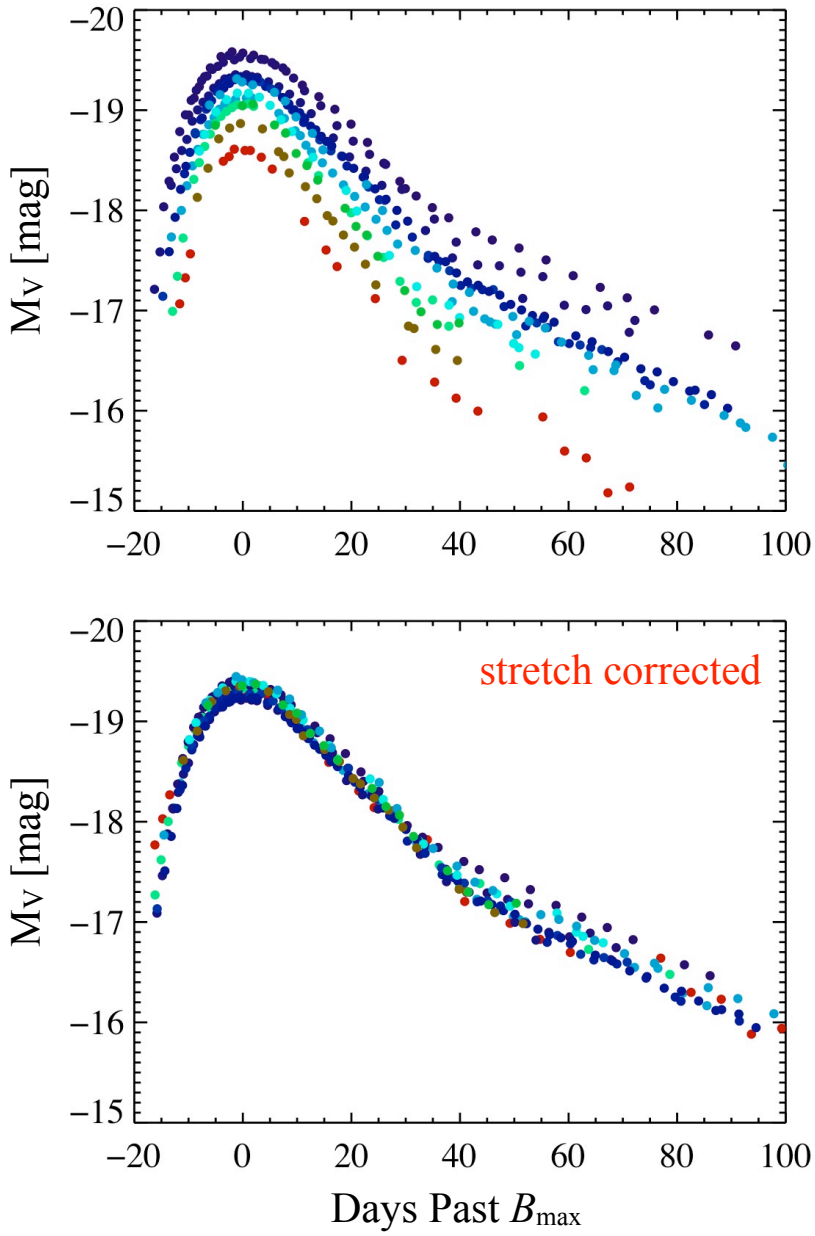

Figure 1.3: SN Ia light curves (i.e., luminosity as a function of time) before (top panel) and after (bottom panel) correcting for light-curve width. The light curves are color coded by light-curve width. Making a correction for this empirical relationship between luminosity and light-curve width allows SNe Ia to be standardizable candles.

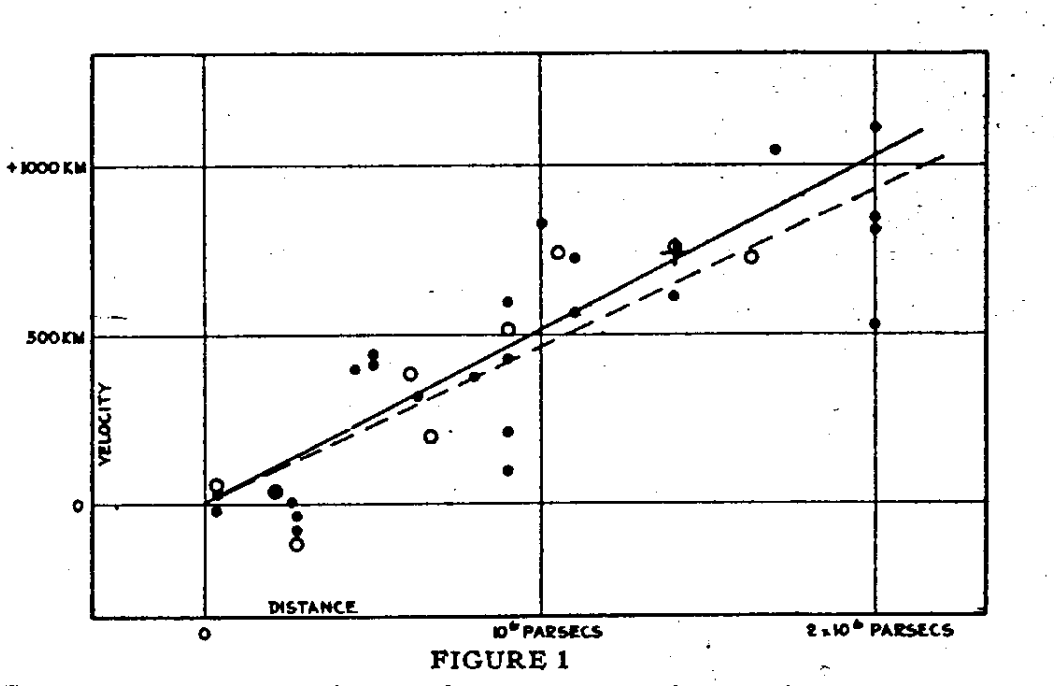

Figure 1.4: Original Hubble diagram using Cepheid variable stars from Hubble (1929). The abscissa displays distance and the ordinate is recession velocity (i.e., velocity moving away from the Milky Way). Measuring Cepheids in neighboring galaxies, Hubble found that more distant galaxies are moving away from the Milky Way faster than closer galaxies. Hubble was the first to discover that the Universe is expanding. Note that the ordinate axis has incorrect units. The axis should be labeled with km s^{-1} as opposed to km. Most of the galaxy velocities used for this plot were observed by Vesto Melvin Slipher at Lowell Observatory in Arizona although no credit is given to him in Hubble (1929). See Kirshner (2004) for an enjoyable article on the historical context of Hubble's discovery of the expanding Universe.

system of SNe Ia. Current theories suggest that a WD gains mass from a companion star although the nature of the companion star remains elusive. However, models by Kasen (2010) suggest that photometric observations of a SN Ia within days of explosion may contain the signature of the companion star.

1.4 The LOSS SN Ia Photometry Sample

This thesis is the presentation and analysis of data for 165 SNe Ia from the LOSS photometry sample. A collection of 10 years of data totaling over 16,000 images, the LOSS sample represents a well-sampled, high-precision collection of light curves in 4 optical broadband filters. The LOSS sample represents a significant contribution to the number of high-quality light curves of nearby SNe Ia. In Chapter 2, I present the data and reduction techniques used to construct the light curves. In Chapter 3, I make use of the earliest light-curve photometry epochs to study the explosion physics of SNe and place constraints on their progenitor system. Combining the LOSS sample with other samples published in the literature, I place constraints on cosmological parameters and search for physical systematics that may further improve SN Ia distance estimates in Chapter 4. Finally, in Chapter 5 I present data for a very peculiar SN Ia found as part of the LOSS survey unlike any other previously published SN Ia. Many of the properties associated with this SN defy normal relationships found for SNe Ia.

Chapter 2

Optical Light Curves for 165 SNe Ia

A version of this chapter was originally published in *The Astrophysical Journal Supplement Series* (Ganeshalingam, M., et al. 2010, ApJS, 190, 418).

Abstract

We present *BVRI* light curves of 165 Type Ia supernovae (SNe Ia) from the Lick Observatory Supernova Search follow-up photometry program from 1998 through 2008. Our light curves are typically well sampled (cadence of 3–4 days) with an average of 21 photometry epochs. We describe our monitoring campaign and the photometry reduction pipeline that we have developed. Comparing our dataset to that of (Hicken et al. 2009b), with which we have 69 overlapping SNe, we find that as an ensemble the photometry is consistent, with only small overall systematic differences, although individual SNe may differ by as much as 0.1 mag, and occasionally even more. Such disagreement in specific cases can have significant implications for combining future large datasets. We present an analysis of our light curves which includes template fits of light-curve shape parameters useful for calibrating SNe Ia as distance indicators. Assuming the $B-V$ color of SNe Ia at 35 days past maximum light can be presented as the convolution of an intrinsic Gaussian component and a decaying exponential attributed to host-galaxy reddening, we derive an intrinsic scatter of $\sigma = 0.076 \pm 0.019$ mag, consistent with the Lira-Phillips law.

2.1 Introduction

The importance of supernovae (SNe) in astrophysics cannot be overstated. Having luminosities that rival those of their host galaxies, SNe can be detected out to great distances. Type Ia supernovae (SNe Ia) have been shown to be accurate cosmological distance indicators, playing a critical role in the discovery and subsequent study of the accelerating expansion of the Universe and dark energy (Riess et al. 1998; Perlmutter et al. 1999; Riess et al. 2004, 2007; Wood-Vasey et al. 2007; Kowalski et al. 2008; Hicken et al. 2009a); see Filippenko (2005b) for a review.

Well sampled, high-precision light curves of nearby SNe Ia are required to better understand and calibrate SNe Ia at high redshift. Several groups have undertaken the project of collecting datasets of SN Ia light curves. The pioneering Calán/Tololo Supernova Survey acquired *BVRI* light curves of 29 SNe Ia (Hamuy et al. 1996b). The Harvard/Smithsonian Center for Astrophysics (CfA) Supernova Group has published *BVRI* light curves of 22 SNe Ia (Riess et al. 1999a) and *UBVRI* light curves of 44 SNe Ia (Jha et al. 2006b). These three datasets have proven invaluable in establishing and refining the important relationship between light-curve shape and peak luminosity that allows SNe Ia to be used as reliable distance indicators (Phillips 1993; Hamuy et al. 1996a; Riess et al. 1995, 1996; Perlmutter et al. 1997; Phillips et al. 1999). However, a larger sample of high-quality multi-color SN Ia light curves is required to further explore the luminosity-width relationship and perhaps find other nondegenerate parameters that will further improve the utility of SNe Ia as distance indicators.

The Lick Observatory Supernova Search (LOSS) follow-up program was initiated over 12 years ago with the goal of acquiring an extensive database of SN Ia photometry. This chapter focuses on the results of the first 10 years of our photometric efforts using the 0.76-m Katzman Automatic Imaging Telescope (KAIT) and the 1-m Nickel telescope at Lick Observatory. Over this period, we acquired data for 165 SNe Ia with an average cadence of 3–4 days in *BVRI* for a total of 13,778 images. We also developed an automated pipeline to reduce our data to produce final calibrated magnitudes.

The CfA Supernova group recently released their third extensive, high-quality dataset (Hicken et al. 2009b, hereafter CfA3), more than doubling the sample of published light curves of nearby SNe Ia. Their data span the years 2001–2008 and include $UBVRIr'i'$ light curves of 185 SNe Ia. While there is considerable overlap between the two datasets (69 SNe), and 17 SNe from the LOSS sample were published as part of CfA2 (Jha et al. 2006b), we contribute light curves of 79 unique SNe Ia. The Carnegie Supernova Project (CSP) has also published a set of $ugriBV$ light curves of 35 SNe Ia, and a smaller subset of $YJHK_s$ light

curves of 25 SNe Ia (Contreras et al. 2010). We share 14 overlapping SNe with the CSP dataset.

In Section 2.2, we describe the mechanics behind our photometry follow-up program, including how the SNe in this chapter are discovered and the resources used to observe them. In Section 2.3, we outline our data-reduction procedure. We address concerns of systematic errors in our reduction procedure in Section 2.3.5, finding that the systematic error in our dataset is 0.03 mag in *BVRI* after considering a number of possible sources. We present our results in Section 2.4. To ensure the quality of our photometry, we do extensive comparisons to previous manual reductions of data presented here and to results for the same SNe from different telescopes. In particular, we do an in-depth comparison to the CfA2 and CfA3 datasets, finding that in general the results are consistent with small overall systematic differences with a few notable exceptions. Comparisons to the CSP dataset have not been attempted because their results are given only in the natural system of the 1-m Swope telescope. Future studies of the overlap between these three datasets will be invaluable to studies of the systematics that plague SN Ia photometry from different telescopes and CCD/filter combinations. A discussion of light-curve properties from our sample is presented in Section 2.5, and our conclusions can be found in Section 2.6.

2.2 Observations

2.2.1 Discovery

Our photometric follow-up program is an extension of LOSS using KAIT (Li et al. 2000; Filippenko et al. 2001; Filippenko 2003, 2005a). KAIT is a robotic telescope which is dedicated to the search and monitoring of optical transients, with a priority placed on SNe. It is based on the earlier Berkeley Automatic Imaging Telescope (Richmond et al. 1993). The search strategy is designed to optimize the capabilities of a small, lightweight telescope, finding SNe within a week of explosion. KAIT typically visits the same galaxies every 3–7 days, taking a 16–20 s unfiltered exposure which on a good night probes down to ~ 19 mag ($\sim R$ band; Li et al. 2003a). New observations are automatically compared with archived galaxy template images. Human image checkers examine each SN candidate the next day, and the best candidates are flagged and reobserved that night. Confirmed SNe are promptly announced to the SN community through International Astronomical Union Circulars (IAUCs) and Central Bureau Electronic Telegrams (CBETs). We make an effort to spectroscopically classify and monitor newly discovered SNe with time allocated to us on the 3-m Shane telescope at Lick Observatory using the Kast double spectrograph (Miller

& Stone 1993). LOSS candidates are posted publicly to encourage other SN groups to use their resources to monitor and classify the objects spectroscopically, ultimately maximizing the scientific utility of our discoveries.

Supernovae discovered by LOSS are the dominant source for LOSS photometric follow-up efforts, making up 64% of the observed sample. Our own archival images provide constraints on the rise time of new transients, allowing us to start *BVRI* monitoring soon after discovery. The remaining discoveries come mostly from the dedicated efforts of amateur astronomers such as the Puckett World Supernova Search which accounts for $\sim 9\%$ of our sample.

Emphasis is placed on monitoring nearby SNe of all types that are found before maximum light, with a special effort to catch SNe Ia in the Hubble flow out to redshift $z \approx 0.05$. We try not to discriminate between SN Ia subclasses; however, our final sample of 165 most certainly suffers from observational bias and does not reflect the true demographics of SNe Ia (e.g., Li et al. 2001a,b). For a discussion on the observed luminosity function from a complete SN sample, see Li et al. (2011c).

Although the focus of this chapter is LOSS's contribution to studies of SNe Ia, LOSS's collection of SN II-P images has been reduced using the same photometry pipeline. The SN II-P light curves and spectra have been used by Poznanski et al. (2009) to refine their use as cosmological distance indicators. A more detailed analysis of ~ 60 SNe II is underway (Poznanski et al. 2012, in prep.) and will contain a public release of the data. In time, we will also make available our smaller dataset of SN Ib/c light curves.

2.2.2 Telescopes

The images in our dataset were acquired using the 0.76-m KAIT and the 1-m Nickel telescope, both at Lick Observatory located on Mt. Hamilton just outside of San Jose, CA. The site typically has an average seeing of $\sim 2''$, with some seasonal dependence.

A vast majority of our observations (94%) were taken with KAIT. KAIT is completely robotic, operating only via software. Observations of a SN are initiated by creating a request file which contains the right ascension and declination of the SN along with that of a nearby guide star. For a standard observation, we expose in *B* for 6 min and in *VRI* for 5 min each, and we set a cadence of 2–3 days. The request file is sent to a master scheduler program which determines the best time to observe the field in between observations conducted for the SN search. At night, KAIT automatically observes the field without the need for any human intervention.

Time on the the Nickel telescope was originally requested with the intent to calibrate SN fields against Landolt standard stars (Landolt 1983, 1992). Before 2006, the Nickel required

the observer to control the telescope locally from the control room adjacent to the dome, and the major constraint on the number of nights we could obtain was the amount of time observers were able to spend driving to and from Mt. Hamilton. After 2006, the forward-thinking staff of Lick Observatory initiated a program to enable remote observing, allowing our group to observe from the University of California, Berkeley campus (and other groups from UCB and other campuses as well). To take full advantage of this, we increased the number of active Nickel observers from 1 to 5 (including many undergraduate students), and expanded our observing campaign on the Nickel to include the monitoring of more distant SNe and to complement (primarily at late times) data taken with KAIT.

KAIT has a Ritchey-Chrétien mirror set with a focal ratio of $f/8.2$. It has been outfitted with three different CCDs during the interval 1998–2008. Prior to 2001 September 11, data were taken with an Apogee back-illuminated chip having 512×512 pixels. The CCD was then changed to a newer Apogee chip with the same number of pixels though with higher quantum efficiency redward of 4000 Å. On 2007 May 12, the camera was changed once again to a Finger Lakes Instrument (FLI) camera of the same size. All three CCDs have a scale of $0.8''$ pixel^{-1}, giving KAIT a field of view of $6.7' \times 6.7'$. The CCD is thermoelectrically cooled to 60° C below ambient temperature. Standard *BVRI* broad-band filters were used to obtain our images, though we switched *BVRI* filter sets on 1999 February 20. In total, we have had four combinations of CCD/filter sets on KAIT: Apogee/Old *BVRI* (KAIT1), Apogee/New *BVRI* (KAIT2), Apogee2/New *BVRI* (KAIT3), and FLI/New *BVRI* (KAIT4).

The 1-m Nickel is a Ritchey-Chrétien telescope with a primary mirror focal ratio of $f/5.3$. The CCD is a thinned, Loral, 2048×2048 pixel chip. Having a scale of $0.184''$ pixel^{-1}, the field of view of the Nickel is $6.3' \times 6.3'$. With a typical seeing of $2''$, our images are oversampled; thus, in practice, we bin the pixels by a factor of two to reduce the readout time.

Normalized throughput curves for our four KAIT combinations and the Nickel telescope are compared with the standard Bessell (1990) curves in Figure 2.1. The throughput curves are obtained by multiplying the transmission function of each filter by the quantum efficiency of the CCD and the atmospheric transparency at Lick Observatory. Filter transmission curves for the two different KAIT filter sets were measured in a laboratory using a Varian Cary 5000 spectrophotometer. The first Apogee CCD mounted on KAIT was also measured in a laboratory. The filter transmission for the Nickel was downloaded from the Mt. Hamilton Lick Observatory page[1]. The quantum-efficiency curves for the remaining CCDs are taken from the manufacturer's claims. In general, there is good agreement between each filter response and its corresponding Bessell curve. The largest deviations from the Bessell curves

[1] http://mthamilton.ucolick.org/techdocs/filters/phot_filt_curves.html.

appear in the RI bands for the old KAIT filter set (KAIT1) and for the I band at the Nickel telescope. Characteristics for each photometric band can be found in Table 2.1.

Table 2.1: Characteristics of Photometric Bands

System	Filter	Central Wavelength[a] (Å)	FWHM[b] (Å)
KAIT1	B	4369	954
	V	5402	914
	R	6720	2123
	I	8191	1760
KAIT2	B	4364	1022
	V	5389	911
	R	6297	1249
	I	8077	1493
KAIT3	B	4398	971
	V	5397	921
	R	6323	1297
	I	8076	1492
KAIT4	B	4445	907
	V	5389	909
	R	6273	1202
	I	8061	1471
Nickel	B	4369	898
	V	5329	828
	R	6259	1189
	I	8125	1673

[a] The central wavelength is defined as the wavelength between half-maximum transmission.

[b] FWHM is defined as the width between half-maximum transmission.

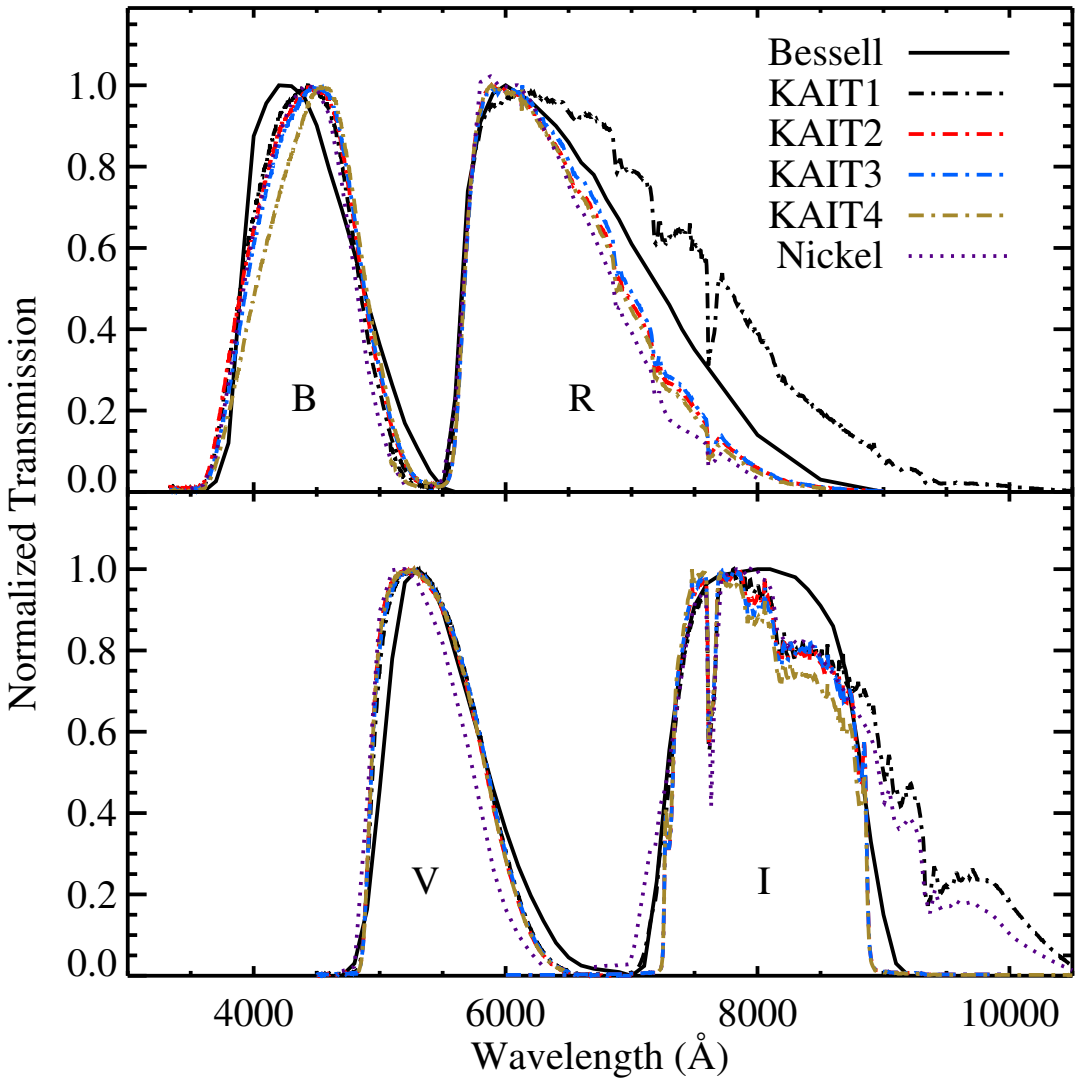

Figure 2.1: Transmission curve for the four different KAIT configurations and Nickel 1-m telescope compared with the standard Bessell (1990) *BVRI* curves plotted in solid black.

2.3 Data Reduction

High-precision light curves ($\sigma_{\rm mag} \lesssim 0.03$ mag) of nearby SNe are required to properly interpret SN data collected at high redshifts to derive cosmological parameters. Imperfections in data reduction can produce systematic errors which propagate into inaccurate measurements of cosmological parameters (e.g., Boisseau & Wheeler 1991). Our dataset is composed of *BVRI* images of 165 SNe with an average of 21 epochs per SN, making it impractical to manually reduce our data. Hence, we developed a software reduction pipeline that requires a minimal amount of human interaction yet provides an error-control flow system to deal with problematic data. Our reduction pipeline consists of three main processes: field calibration, galaxy subtraction, and differential photometry. Each of these will be described in the following sections.

2.3.1 The Calibration Pipeline

To calibrate the instrumental magnitudes of a SN to the Landolt system (Landolt 1983, 1992), the local standard stars in the SN fields need to be calibrated on photometric nights, so that differential photometry can be converted to absolute photometry. The importance of the accuracy of these photometric calibrations cannot be overlooked. As will be discussed in more detail in Section 2.3.5, one major source of the differences among published photometry for the same SNe comes from the differences in the calibrations. An error in the calibration will be directly transferred to the final photometry of a SN; thus, the goal of our calibration pipeline is to obtain reliable, self-consistent calibrations for each of the SN fields in our database.

We used both KAIT and the Nickel telescope for the calibrations of our SN fields. KAIT is a robotic telescope, so when we need to conduct calibrations on a promising photometric night, we override the automatic schedule with a manually prearranged calibration sequence. For the Nickel observations, we have a long-term project with the main goal of photometric calibration of the SNe in our photometry database. Over the years, the observations obtained with Nickel have evolved from on-site observing with a frequency of two nights per month to remote observing with a higher cadence (6–9 nights per month). In total, observations were performed over ~ 50 photometric nights at KAIT and ~ 100 at the Nickel telescope. Given the importance of field calibration, we try to visit fields *at least* twice and on average 5 times. SN 2008ar is the only SN in our sample which has just a single calibration. Calibrations for

other fields from that same night are consistent with previous results, giving us confidence that the night was indeed photometric. We plan, however, to obtain more calibrations for this particular field in the future, and we will update the photometry if necessary.

For the calibration sequence on each photometric night, we arrange observations of Landolt standard stars at different airmasses throughout the night. On each photometric night, usually about 20 Landolt fields are observed at KAIT or 12–18 at the Nickel telescope. The numerous standard-star observations enable us to derive a reliable calibration solution if the night is photometric, and to identify a nonphotometric night when the solution shows large scatter due to clouds. Whenever possible, the SN fields are observed at an airmass that is encompassed by that of the standard-star fields (airmass usually 1.0–2.0).

It was impractical to manually reduce the very large number of photometric calibration data, so a calibration pipeline was developed. The pipeline does the following processing, with manual interactions required for some of the steps.

1. **Pre-processing of the images.** This includes removal of the bias and dark current, and flatfielding.

2. **Reduction of the standard-star observations.** First, an astrometric solution is obtained for an image to identify Landolt stars based on their location in the database. Next, aperture photometry is performed on all of the standard stars with a small, optimal aperture of radius roughly the full width at half-maximum intensity (FWHM) to increase the signal-to-noise ratio (S/N). Finally, an aperture correction is derived using the brightest (but not saturated) stars to convert the small-aperture measurement to an aperture that is large enough to include all of the flux. In a majority of cases, we find that an aperture of $\sim 5\times$ FWHM is sufficient to account for the total flux of the star as demonstrated in Figure 2.2. The aperture corrections are visually inspected before they are applied to all of the standard stars.

3. **Finding the photometric solution.** The instrumental magnitudes from the absolute aperture-corrected photometry and the airmasses of the standards are input to the PHOTCAL package of IRAF[2], to solve for the extinction coefficients and color terms of the filters using equations of the form

[2]IRAF, the Image Reduction and Analysis Facility, is distributed by the National Optical Astronomy Observatory, which is operated by the Association of Universities for Research in Astronomy (AURA), Inc., under cooperative agreement with the National Science Foundation (NSF).

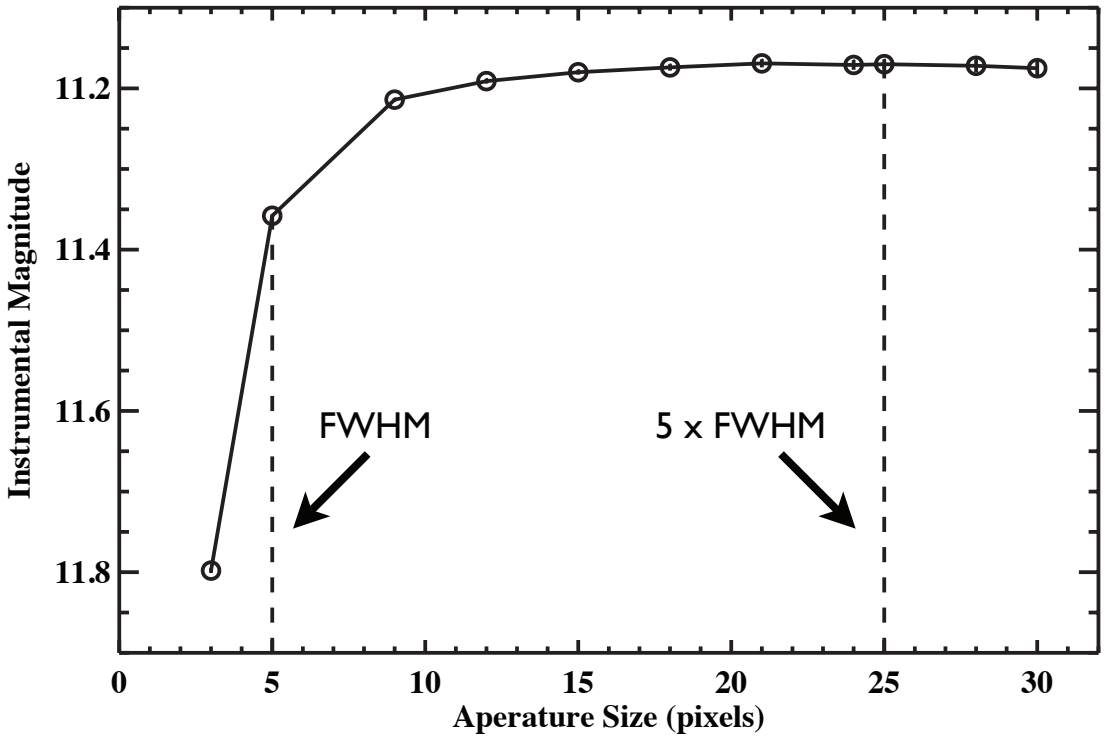

Figure 2.2: The instrumental magnitude of a Landolt standard star measured with aperture photometry as a function of aperture size. For this example, the FWHM of the image is approximately 5 pixels ($\sim 1.5''$). When performing absolute photometry to calibrate our SN fields, we use an aperture of $5 \times$ FWHM of the image to sum all of the flux. As shown in this example, the instrumental magnitude asymptotically approaches its total flux value. Using an aperture radius equal to $5 \times$ FWHM is sufficient to measure the total flux of our point sources.

$$
\begin{aligned}
b &= B + C_B(B-V) + k_B X_B + \text{ constant}, \\
v &= V + C_V(B-V) + k_V X_V + \text{ constant}, \\
r &= R + C_R(V-R) + k_R X_R, + \text{ constant, and} \\
i &= I + C_I(V-I) + k_I X_I + \text{ constant}.
\end{aligned}
$$

In the above set of equations, lower-case letters represent the magnitudes in the natural system of the telescope, upper-case letters are magnitudes in the Landolt system, X_i are the airmasses of the observation, C_i are linear color terms, and k_i are extinction coefficients. We tested the inclusion of a color term proportional to airmass, but found that it did not significantly improve the scatter in the fit.

This is an interactive process. Ideally, if the night is photometric, all standard stars should be used in the solution. However, due to cosmic rays, CCD defects, or poor S/N for some fainter standard stars, there are often outliers in the solutions. We carefully remove the outliers in an attempt to achieve solutions with the following precisions: root-mean square (RMS) < 0.04 mag for KAIT B, < 0.03 mag for KAIT VRI, < 0.03 mag for Nickel B, and < 0.02 mag for Nickel VRI. We also check the number and source of the outliers to identify nonphotometric nights. If a relatively large fraction ($\gtrsim 15\%$) of the data points are outliers, or if all stars in a particular image are outliers (a sign of cloud cover during the exposure), the night is marked as being nonphotometric.

4. **Reduction of the SN fields.** The instrumental magnitudes of the local standard stars are first measured with a small optimal aperture. Aperture corrections are then determined from several bright stars and applied to all of the stars. The photometric solution derived from the Landolt standard stars is applied to derive the magnitudes of the local standard stars in the standard system.

5. **Combining the calibrations from different photometric nights.** For the calibrated magnitudes of a star in any band, an iterative process is invoked to remove 3σ outliers until the final average value has RMS < 0.03 mag. The error of the calibrated magnitude is calculated as RMS$/\sqrt{N}$, where N is the total number of calibrations used in deriving the average (following the definition of the standard deviation of the mean). An example of this process is shown in Table 2.2.

Table 2.2: Example of the Calibration Pipeline Output

RA (hr)	Dec (deg)	B (mag)	V (mag)	R (mag)	I (mag)	Telescope
14.370000	-0.392374	17.261 X	16.687	16.295	15.868	20070616_kait
14.370002	-0.392362	17.354	16.731	16.280	15.862 X	20070617_kait
14.370001	-0.392341	17.289	16.711	16.282	15.917	20080118_kait
14.369999	-0.392355	17.291	16.679	16.263 X	15.918	20080119_kait
14.369999	-0.392362	17.367	16.725	16.342	15.954	20070609_40in
14.369999	-0.392362	17.367	16.706	16.370	15.950	20070616_40in
14.369998	-0.392348	17.350	16.708	16.345	15.945	20070617_40in
14.369999	-0.392355	17.354	16.706	16.333	15.958	20070708_40in
14.369998	-0.392345	17.427 X	16.750	16.386 X	15.927	20070805_40in
14.369999	-0.392362	17.370	16.748	16.344	15.954	20070804_40in
14.369999	-0.392341	17.265 X	16.660	16.292	15.963	20070811_40in
14.370000	-0.392328	17.357	16.736	16.359	15.963	20070812_40in
14.370001	-0.392346	17.372	16.761	16.340	15.971	20070820_40in
14.369999	-0.392326	17.359	16.528 X	16.355	16.032 X	20070821_40in
14.370002	-0.392346	17.376	16.752	16.327	15.956	20070824_40in
14.369999	-0.392333	17.375	16.731	16.337	15.901	20080112_40in
Average:						
14.369997 (15) 16	-0.392349 (05) 16	17.352 (008) 13	16.719 (008) 15	16.329 (008) 14	15.939 (008) 14	

Note. – This is for a star in the SN 2007af field, which has been observed on 15 photometric nights. The entries marked with an "X" are removed during the iterative process and are not used to calculate the final SN magnitude.

2.3.2 Galaxy Subtraction

A majority of SNe are found close to bright regions of their host galaxy, requiring galaxy subtraction to isolate the SN flux before photometry can be performed accurately. Template images of the host galaxy are obtained on a clear night during a dark run after the SN has faded beyond detection. Host-galaxy templates are visually inspected and chosen to have low background counts and a FWHM of $\leq 2.0''$. In cases where we had multiple high-quality templates, the images are registered and added together to produce a single deeper template.

Images are bias subtracted and twilight-sky flatfielded automatically at the telescope. Cosmic rays are removed using the `cosmicrays` procedure in the IRAF DAOPHOT package. We adopt parameters which ensure the replacement of obvious cosmic rays (objects with small FWHM compared to the average FWHM constrained by the nights with the best seeing) with background values while not affecting objects having stellar profiles.

Data images are registered to the template image by matching congruent triangles formed by objects which have a peak intensity value that is above the background in both images. The data image is then geometrically mapped to the template image using the `geomap` routine in IRAF.

Two independent template-subtraction routines were employed with our dataset, providing a consistency check for our photometry. Subtraction method 1 (SM1) is based on the ISIS package (Alard & Lupton 1998) as modified by Brian P. Schmidt for the High-z Supernova Search Team (Schmidt et al. 1998). The convolution kernel is computed as a function of position using stars in both images chosen automatically by ISIS. Ideally, the software avoids saturated stars, stars with nonstellar profiles, and cosmic rays. Our default parameters use three stamps in the x direction and three stamps in the y direction to determine the spatial variation in the kernel. The image with the better seeing (in most cases the template) is then convolved to match the seeing of the other image and the two images are subtracted. A 60×60 pixel square centered on the SN in the subtracted image is then copied onto the corresponding region in the observation image.

Subtraction method 2 (SM2) determines the convolution kernel with the IRAF task `psfmatch` (Phillips & Davis 1995) using three field stars chosen in the template image that are well above the background and are not saturated. Similar to SM1, the image with the better seeing is then convolved to the other image using using the averaged kernel. Unlike SM1, which automatically finds stars to compute the kernel, SM2 uses the same three stars for all of the data images associated with a particular template. The intensity of the two images is matched using a rectangular region of 60×60 pixels centered on the brightest star. The images are then subtracted. As in SM1, the SN in the subtracted image is pasted back onto the observation image. An example image from our subtraction pipeline is shown in

Figure 2.3.

As both of these subtraction methods are automated, it is inevitable that our software will produce poor subtractions for data taken under less than optimal conditions. In the worst of circumstances, such as data taken during taken during bad weather or poor seeing conditions, we are left with no choice but to eliminate data that fail both subtraction pipelines. To minimize the number of discarded images, we have implemented an error-control system to salvage images that initially cause the subtraction pipeline to fail.

The robustness of SM1 ensures that a subtracted image will always be output, though the quality of the subtracted image may be questionable if SM1 mistakenly uses a nonstellar source to construct the kernel. The most likely candidates for stamps that produce bad subtractions are cosmic rays which elude removal and galaxy nuclei from either the host galaxy or background galaxies. In such cases, our recourse is to identify suspect images and manually choose stamps until a satisfactory subtraction is obtained. The identification of such subtractions is done by the inspection of the final light curve. Comparison of the results of SM1 to SM2 generally indicates when one subtraction method fared better than the other. In cases where SM2 produces superior results, it is usually because the stamps chosen by SM2 are set *a priori* while SM1 chooses stamps on the fly.

For SM2, there are two main sources of potential failures: a bad point-spread function (PSF) for the kernel and an error in the intensity transformation. In the case of a bad PSF from one of the three stars, the convolution kernel is computed using the average of the remaining two stars. In the event that all three stars prove problematic (as in a case where none of the three stars is present in the data image), the pipeline exits without producing a subtraction. If the intensity matching first fails using the brightest star of the three stars, SM2 then uses a 60×60 pixel square about the next-brightest star.

An analysis of our finalized photometry shows that 81% of our data uses the results from both SM1 and SM2, 18% from only SM1, and 1% from just SM2. Of the two subtraction algorithms, SM1 produced the most robust results, yielding better subtractions in instances where our galaxy template was not optimal. In most instances where SM2 gave superior subtractions, better SM1 subtractions could be produced by manually choosing stars to compute the convolution kernel.

A minority of SNe in our dataset occurred far from the nucleus of the host galaxy and do not suffer from significant galaxy contamination as determined by inspection of late-time images. For these SNe, images were only registered before performing differential photometry. Table 2.3 contains a list of SNe which did not require galaxy subtraction, together with their offset from the host-galaxy nucleus.

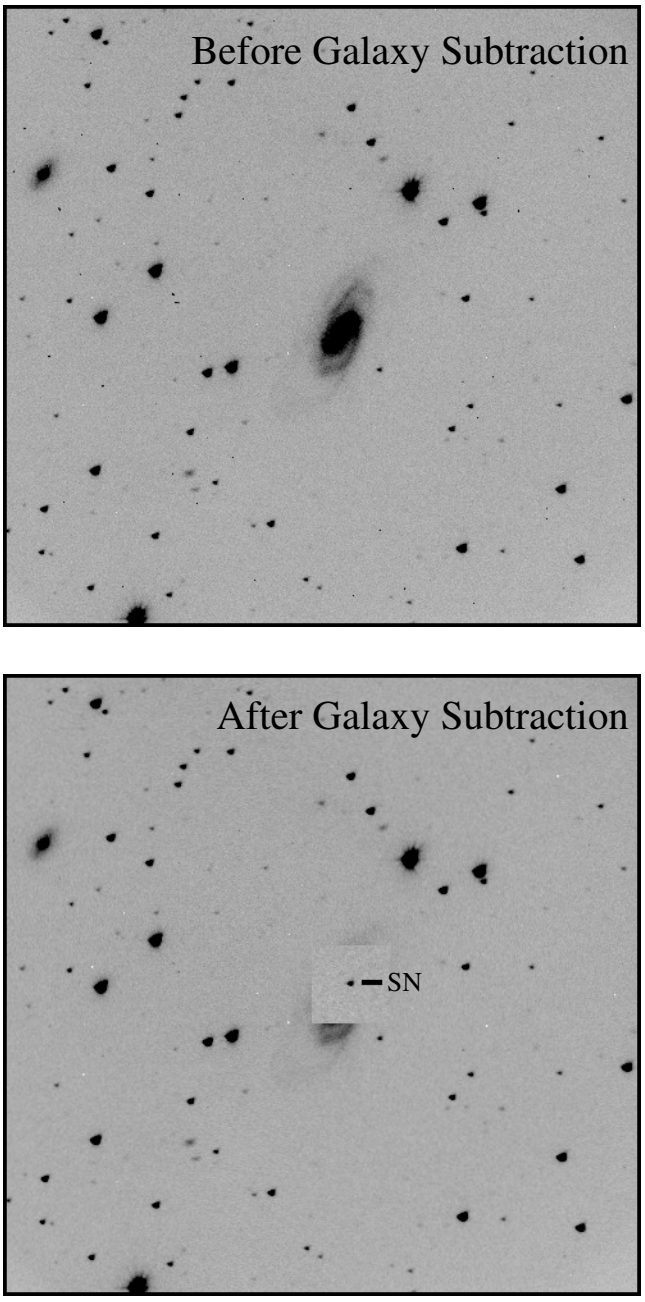

Figure 2.3: An example of our galaxy subtraction pipelines. The top image shows SN 2003gq on 1 August 2003 UT. The SN is embedded deep within the host galaxy. We can isolate the flux of the SN using our galaxy subtraction pipelines and paste a stamp of the subtracted image onto the data image at the position of the SN.

Table 2.3: SNe Not Requiring Galaxy Subtraction

SN	East (″)	North (″)
1998de	71.9	3.4
1999gh	52.0	15.8
2000cx	−23.0	−109.3
2001ah	−43.0	−32.4
2001cj	−7.6	35.2
2003fa	−9.5	48.9
2004E	3.2	20.4
2005cf	−15.7	123.0
2006bt	−44.4	−22.9
2006cp	19.9	−15.3
2006em	21.4	50.9
2007fr	5.5	−33.5

Note. – SN offsets from the host-galaxy nucleus are given.

2.3.3 Differential Photometry

Differential photometry was performed using the PSF-fitting method in the IRAF DAOPHOT package (Stetson 1987) to measure the SN flux relative to local standards in the field. Depending on the field, three or more of the brightest stars are chosen manually to construct a model PSF. Using a fitting radius equivalent to the FWHM of each data image (usually 3–5 pixels), the PSF is modeled out to 20 pixels. Instrumental magnitudes are measured for the SN and local standards of sufficient brightness found in the calibration pipeline.

The instrumental magnitudes are transformed into the standard Landolt system using

the following system of equations:

$$\begin{aligned} b &= B + C_B(B-V) + \text{constant}, \\ v &= V + C_V(B-V) + \text{constant}, \\ r &= R + C_R(V-R) + \text{constant, and} \\ i &= I + C_I(V-I) + \text{constant}. \end{aligned}$$

In the above set, the lower-case bandpass letters on the left-hand side are instrumental magnitudes and the upper-case bandpass letters are the transformed Landolt magnitudes. The coefficients C_i represent the averaged color terms found from multiple photometric nights. The zeropoint and effects of atmospheric extinction are absorbed into a constant which drops out in differential photometry.

A solution to this system of equations requires instrumental magnitudes for *BVRI*. Occasionally, data for one bandpass do not exist or are of such poor quality that galaxy subtraction or PSF-fitting photometry cannot be performed with confidence. As an initial zeroth-order solution, we use the instrumental magnitude from data taken within 10 days of the absent data. As our data are well sampled, this provides an adequate solution given that there is usually not a significant change in the SN flux between the two dates. As a check on this assumption, we compare the borrowed magnitude to the magnitude derived from a third-order polynomial fit to the final light curve 10 days before and after the date of the borrowed data. Instances in which the two differ by 0.1 mag are flagged. The borrowed data are then replaced by the magnitude derived from the fit (assuming a reasonable fit is found) and the transformation equations are again solved for the color-corrected Landolt standard magnitudes. As this is a second-order correction, we find that an uncertainty of 0.1 mag for the *B* band propagates into an error of < 0.01 mag for *VRI*. A summary of all of our averaged color terms can be found in Table 2.4.

Table 2.4: Summary of Color Terms

	Observed Color Terms[a]				Synthetic Color Terms[b]			
Telescope/Filter Set	C_B	C_V	C_R	C_I	C_B	C_V	C_R	C_I
KAIT1 (Apogee/Old *BVRI*)	−0.095	0.027	−0.181	−0.071	−0.035	0.029	−0.180	−0.049
KAIT2 (Apogee/New *BVRI*)	−0.085	0.032	0.062	−0.007	−0.043	0.040	0.066	−0.005
KAIT3 (Apogee2/New *BVRI*)	−0.057	0.032	0.064	−0.001	−0.073	0.034	0.056	−0.005
KAIT4 (FLI/New *BVRI*)	−0.134	0.051	0.107	0.014	−0.124	0.039	0.078	0.000
1-m Nickel	−0.092	0.053	0.089	−0.044	−0.004	0.084	0.123	−0.029

Continued on Next Page . . .

Table 2.4 –Continued

	Observed Color Terms[a]				Synthetic Color Terms[b]			
Telescope/Filter Set	C_B	C_V	C_R	C_I	C_B	C_V	C_R	C_I

[a]Observed color terms are averages from observations of Landolt standards over many photometric nights.
[b]Synthetic color terms are derived from synthetic photometry of spectrophotometric standards presented by Stritzinger et al. (2005) using the instrumental response curves found by multiplying the quantum efficiency of the CCD by the filter transmission and the atmospheric seeing at the telescope site.

Our goal is to perform differential photometry of the SN in comparison to those local standard stars which are sufficiently bright to be measured accurately, but do not saturate the detector, and to choose only those stars which give the most consistent results. The algorithm devised to satisfy both constraints goes as follows. The SN magnitude is calculated using all of the available local standard stars found with the calibration pipeline, an error-weighted mean is taken using the uncertainties in the calibrated magnitudes of the local standard stars (typically ≤ 0.02 mag), stars which give a SN magnitude more than 2.5 times the RMS in the scatter of the magnitudes are removed, and the error-weighted mean is recalculated. This is done for every data image for a particular SN, giving a different set of stars for each night's data. We then take the set of stars which are present in more than 2/3 of the individual sets of stars from each night's data. Subsequently, these local standard stars are visually inspected to ensure that they are not background galaxies and that they do not saturate the detector.

Our algorithm works well for cases in which there are many available local standards in the field, but can fail for sparse fields in which there are only two or three local standards. In such situations, the best we can do is manually choose local standards which are bright and give a consistent measurement for the SN magnitude.

The above procedure is applied to results from both SM1 and SM2. Light curves for SM1 and SM2 are visually reviewed. In cases where SM1 and SM2 both produce reliable subtractions, the mean is taken to be the final SN magnitude. If one subtraction method fared better than the other, the more reliable result was taken to be the final magnitude.

While we have chosen to provide our photometry in standard *BVRI* bands, other groups including Hicken et al. (2009b) have released their dataset of comparable size in both the standard system and the natural system of their telescope. There are benefits and detriments to photometry in either system. The standard system allows photometry from different telescopes to be easily compared and combined in cases where S-corrections (Stritzinger et al. 2002) are small. As we are using photometry from two different telescopes and four different KAIT CCD/filter combinations, putting our photometry in a standard system is

a sensible choice. However, this procedure assumes that the color terms derived from the color of our standard stars apply to the colors of a SN, which is not necessarily true as the spectral energy distribution of a standard star will differ from that of a SN. Photometry in a telescope's natural system avoids adding errors to the results from color corrections and should provide less scatter in SN flux measurements. The downside is that SN photometry from different telescopes is not readily comparable and requires accurate measurements of each telescope's transmission function. Currently, we rely on the quantum-efficiency curve supplied by the CCD manufacturer to construct our transmission curve. Although we have chosen to provide our photometry in the standard system, if there is sufficient demand for photometry in the natural system, we can make those data available.

2.3.4 Error Budget

Typically, we have multiple photometric observations of a given field for the purposes of calibrating the magnitude of local standards to Landolt standards. The error in the calibration of the local standard stars is taken to be the RMS of N observations divided by $\sqrt{N}$ (i.e., the uncertainty in the mean). To ascertain the error in our galaxy subtraction and PSF-fitting photometry routines, artificial stars with the same magnitude and PSF as the SN were added randomly to the data and re-extracted. Fifteen artificial stars were added within 60 pixels of the SN, often placing the artificial star in a background region of similar complexity to that of the SN. Another 15 were added randomly to the rest of the data image. The scatter in the magnitudes of the 30 recovered artificial stars was taken to be the uncertainty in our galaxy subtraction and photometry pipelines.

An implicit assumption in our treatment of this uncertainty is that we trust our galaxy subtraction and calculated PSF. In cases where our galaxy-subtraction pipeline performs less than optimally and host-galaxy light is improperly subtracted, our measured SN magnitude will be inaccurate. This leads to artificial stars which do not accurately represent the profile of the SN and hence an error which does not truly represent the error in our galaxy subtraction and photometry pipelines. In such cases, we benefit from having two independent subtraction pipelines. Since both subtractions are reducing the same data image, we expect the error from our artificial-star simulations to be similar, providing us with a check on the simulation's validity.

The final error for each subtraction method is taken to be the scatter from recovering the artificial stars added in quadrature with the calibration error. When data from both subtraction methods are combined, we take the final uncertainty to be the RMS in the two SN magnitude measurements added in quadrature with the quadrature addition of the error from the two subtraction pipelines, assuming the errors from the two pipelines are perfectly

correlated.

2.3.5 Systematic Errors

A major concern for large photometric datasets is the role of systematic errors. In this section we address possible sources of systematic errors and the possible impact such errors play on our final photometry for the LOSS dataset.

Color Terms

The observed color terms presented in Table 2.4 are averages of the color terms derived from observations of Landolt standards on photometric nights. Any evolution of the color terms as a function of season or over time will produce systematic errors in the final photometry correlated with the color of the SN and comparison stars. Plotted in Figure 2.4 and Figure 2.5 are the temporal evolution of our color terms for KAIT and the Nickel telescope, respectively. There have been no filter or CCD changes during our campaign on the Nickel, giving a large baseline to determine evolution in the color terms. We see no evidence of any significant evolution over the eight years of our observations. Discerning any trend in the evolution of the KAIT color terms is more difficult. Having four different CCD/filter combinations with varying tenures on KAIT, we do not have as long a baseline in comparison with the Nickel. We also do not have as many nights of photometric observations to determine the color terms. With the limited amount of available data, we do not detect any significant evolution in the color terms.

As a check on our color terms, we also derive the color terms needed to transform our natural-system magnitudes to the Landolt system using the total response curves for KAIT[1-4] and the Nickel. Armed with the atlas of spectrophotometric standards presented by Stritzinger et al. (2005), we calculate synthetic photometry for a number of standard stars over a range of colors using the transmission functions for KAIT[1-4] and the Nickel. The color terms derived from our synthetic phfotometry can be found in Table 2.4 along with the observered color terms derived from observations of Landolt standards on photometric nights.

Overall, the color terms derived from spectrophotometry match those derived from our observations of Landolt standards. The largest difference is in C_B for the Nickel telescope. The transmission functions for the Nickel filters are taken from the Mt. Hamilton Lick Observatory website and are the least well known, which could explain the rather significant difference. The other smaller differences are most likely due to other optical elements in the light path, such as the mirror reflectivity, which are not included in our transmission

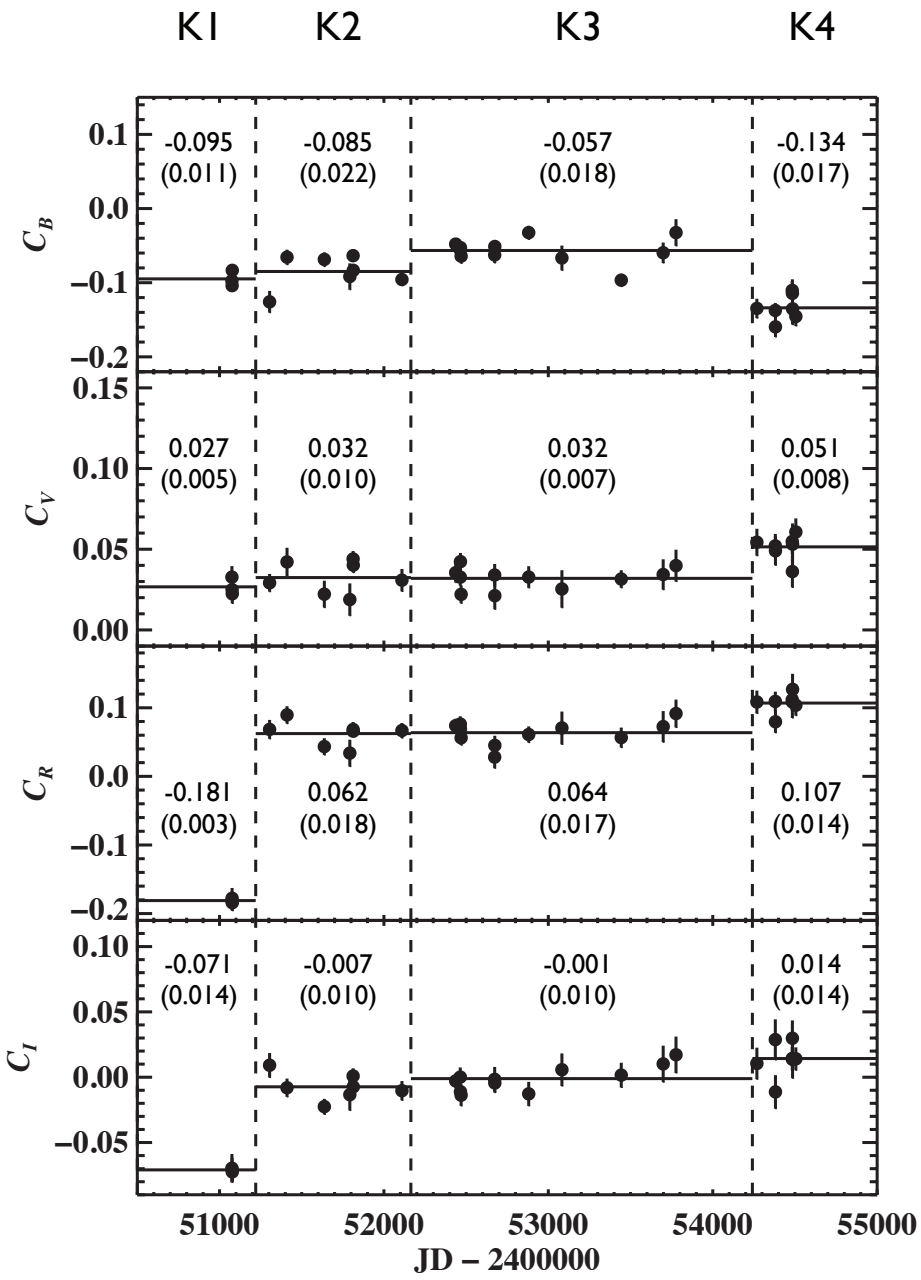

Figure 2.4: The KAIT color terms as a function of time. The dashed vertical lines indicate changes in the CCD/filter set (K1–K4). The solid horizontal lines indicate the mean color term for each set. The mean is also indicated along with the RMS in parentheses.

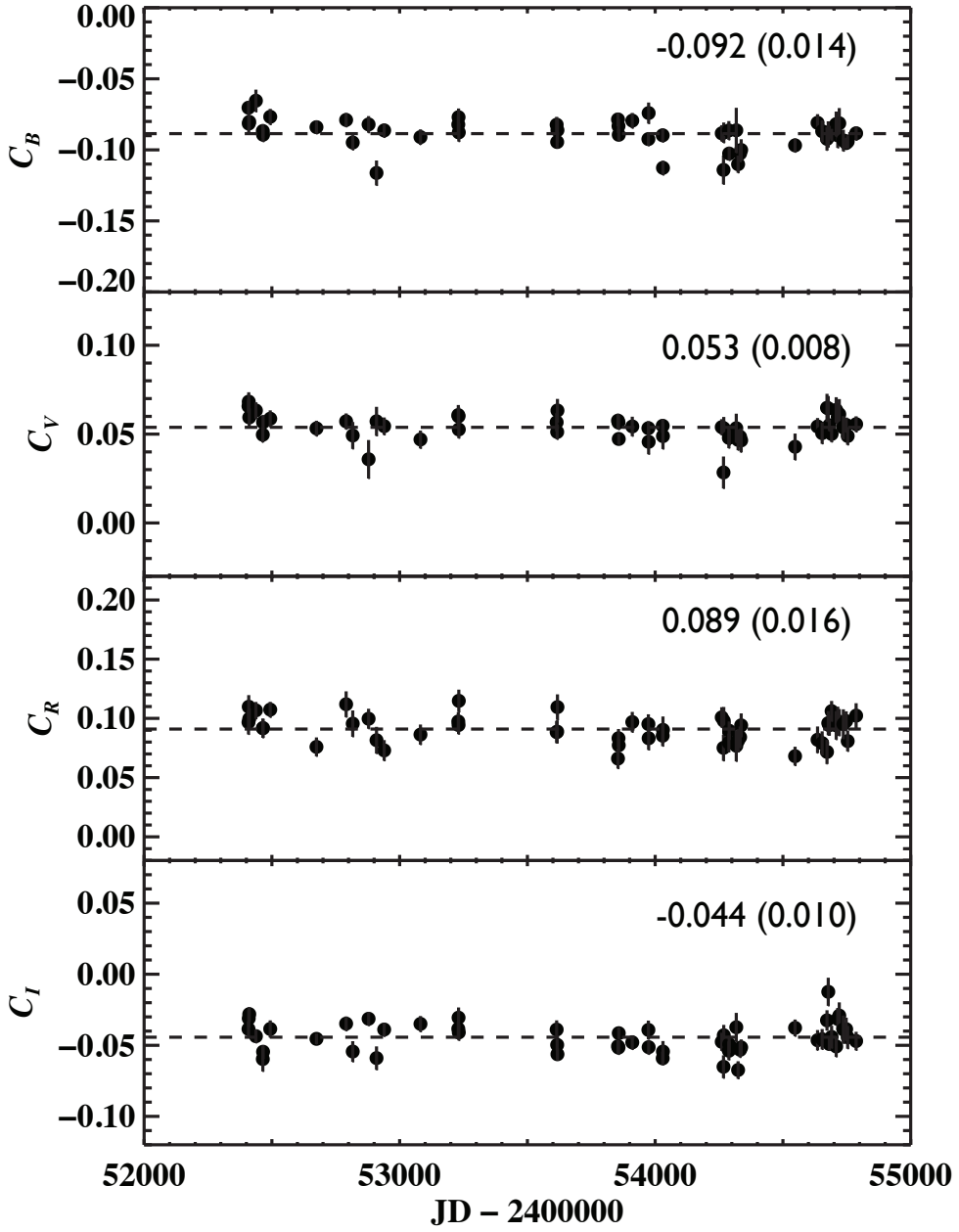

Figure 2.5: Same as Figure 2.4 except for the Nickel telescope.

curve. Following Stritzinger et al. (2002), we shifted the throughput curves in wavelength until we recovered the observed color terms. The required shifts can be found in Table 2.5. In general, relatively small shifts (< 100 Å) were required to match the observed color terms. The only exception is the I band of KAIT1 which required a shift of 140 Å.

Table 2.5: Wavelength Shifts to Instrumental Response Curves

Telescope/Filter Set	B	V	R	I
KAIT1 (Apogee/Old $BVRI$)	47 red	4 red	2 red	140 red
KAIT2 (Apogee/New $BVRI$)	35 red	12 red	2 red	0
KAIT3 (Apogee2/New $BVRI$)	15 blue	3 red	13 blue	21 blue
KAIT4 (FLI/New $BVRI$)	8 red	19 blue	41 blue	59 blue
1-m Nickel	66 red	46 red	38 red	80 red

Note. – All shifts measured in Angstroms.

Evolution of Atmospheric Term

For each photometric night, we derive the atmospheric correction term required to do absolute photometry for calibrating our fields. We plot this as a function of time in Figure 2.6. There is no clear evolution over time. As a function of season, however, we do see evidence for a weak sinusoidal trend. Curiously, the atmospheric term is larger in the summer and fall months compared to the winter and spring months, contrary to the expectation that summer brings clearer, more transparent nights; the presence of diffuse smoke from various wildfires in California is a possible cause. This trend is small and will not impact our final photometry. We also caution that the inhomogeneous sampling (we have more photometric nights during the spring and summer months) could lead to a spurious trend.

Combining Calibrations from KAIT and Nickel

Calibration of local standards in each SN field was done using both KAIT and the Nickel telescope. The results are combined using a sigma clipping routine to discard outliers. However, any systematic differences in photometry between different systems could translate into a systematic error in our final photometry depending on the ratio of the number of KAIT calibrations to Nickel calibrations. To quantify any differences in derived magnitudes

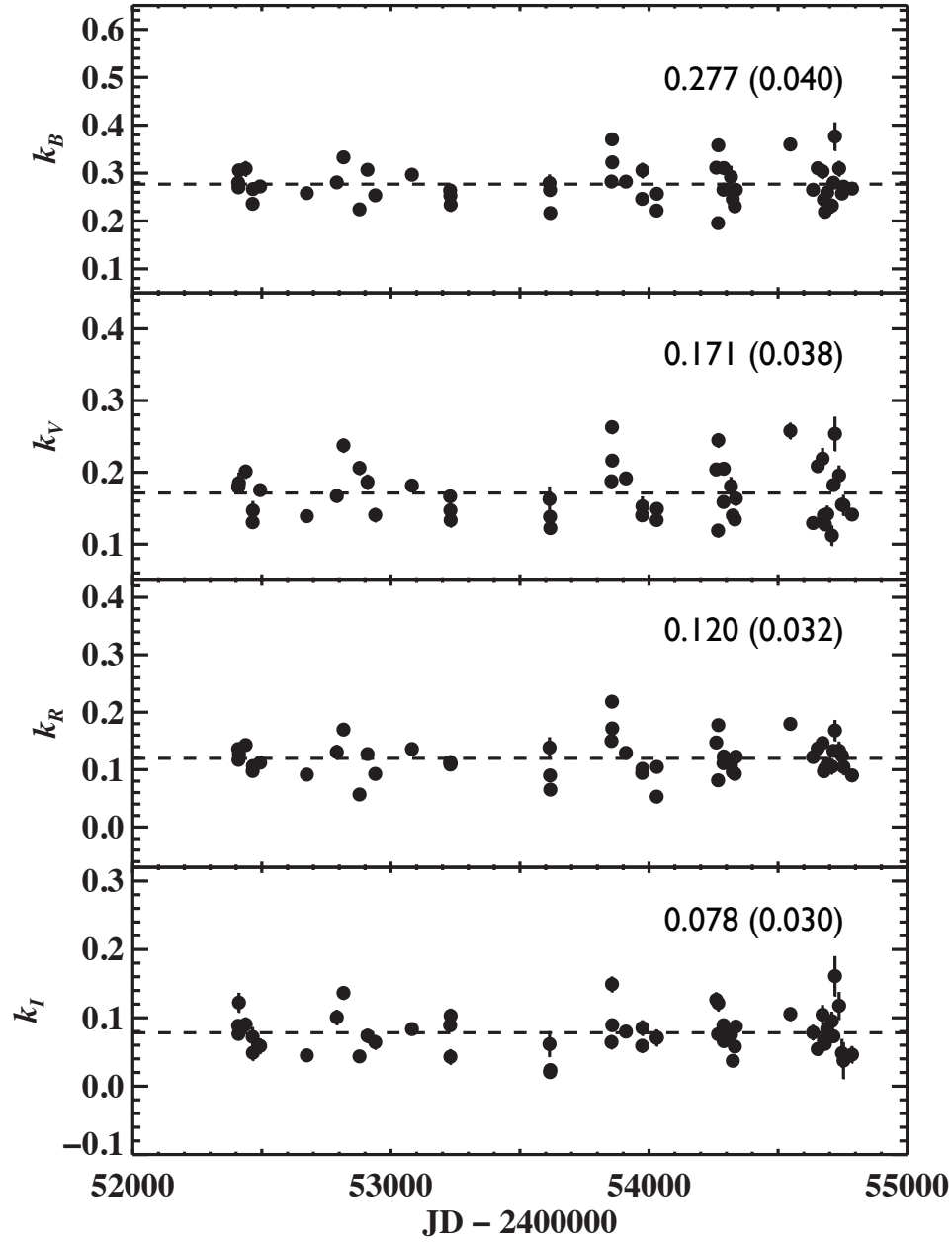

Figure 2.6: The atmospheric correction term for transforming Nickel natural-system magnitudes to the Landolt system as a function of time. We do not see a significant trend with time.

for local standards between different systems, we compared the mean magnitude of each local standard using unique filter/CCD/telescope combinations. We only use instances in which a star was observed by two different systems. We find that there is no significant systematic shift between any of our different systems. We find a typical scatter of ~ 0.03 mag in the distribution of mean magnitudes from different systems, which we adopt as our systematic uncertainty in all bands. Figure 2.7 shows the distribution in differences for local standard stars between Nickel and KAIT3, the two systems which share the most overlap in observed stars. The mean of the distribution for each filter is < 0.01 mag with a $\sigma \approx 0.03$ mag. We find similar results in comparisons with our other systems.

Galaxy Subtraction

Even under the assumption that our galaxy subtraction routines are perfect, our ability to measure the SN magnitude is limited by the finite S/N of the template image. This induces a correlated error between photometry epochs that will affect parameters measured from light curves (e.g., Δm_{15}). To estimate this effect, we examined a test case where the SN occurred in an early-type galaxy having isophotes that could be easily measured. Using algorithms developed by Krajnović et al. (2006), we determined the isophote along the position of the SN[3]. Artificial stars with the same PSF as the SN were injected along the isophote in each data image, and the image was then reprocessed by our pipeline. We find that the scatter in the re-extraction of the artificial stars is comparable to the scatter we find in placing the artificial stars randomly within 60 pixels of the SN.

The previous method to gauge the error in the amount of galaxy light subtracted relies on the original measurement of the SN magnitude being correct. If the initial measurement is inaccurate, then the derived error from the scatter in our artificial-star test will not be indicative of the error induced from a galaxy template of finite S/N. To further investigate the error in using only a single template, we reduced data for one SN with a deeper galaxy template having a higher S/N. The deeper template was made possible by searching through our photometry database for two SNe that exploded in the same galaxy spaced out by more than one year. KAIT followed both SN 2005ds and SN 2000cn which occurred in UGC 12177. We stacked 5–6 high-quality images (FWHM $< 1.5''$ with low sky background) of SN 2005ds to construct a deep galaxy template for UGC 12177, which we measure to be ~ 1 mag deeper than a typical image from KAIT. We then ran the data for SN 2000cn through our pipeline using the deeper template with the same parameters adopted to reduce the data with a single image.

[3]An IDL version of the software is available from http://www-astro.physics.ox.ac.uk/∼dxk/idl/.

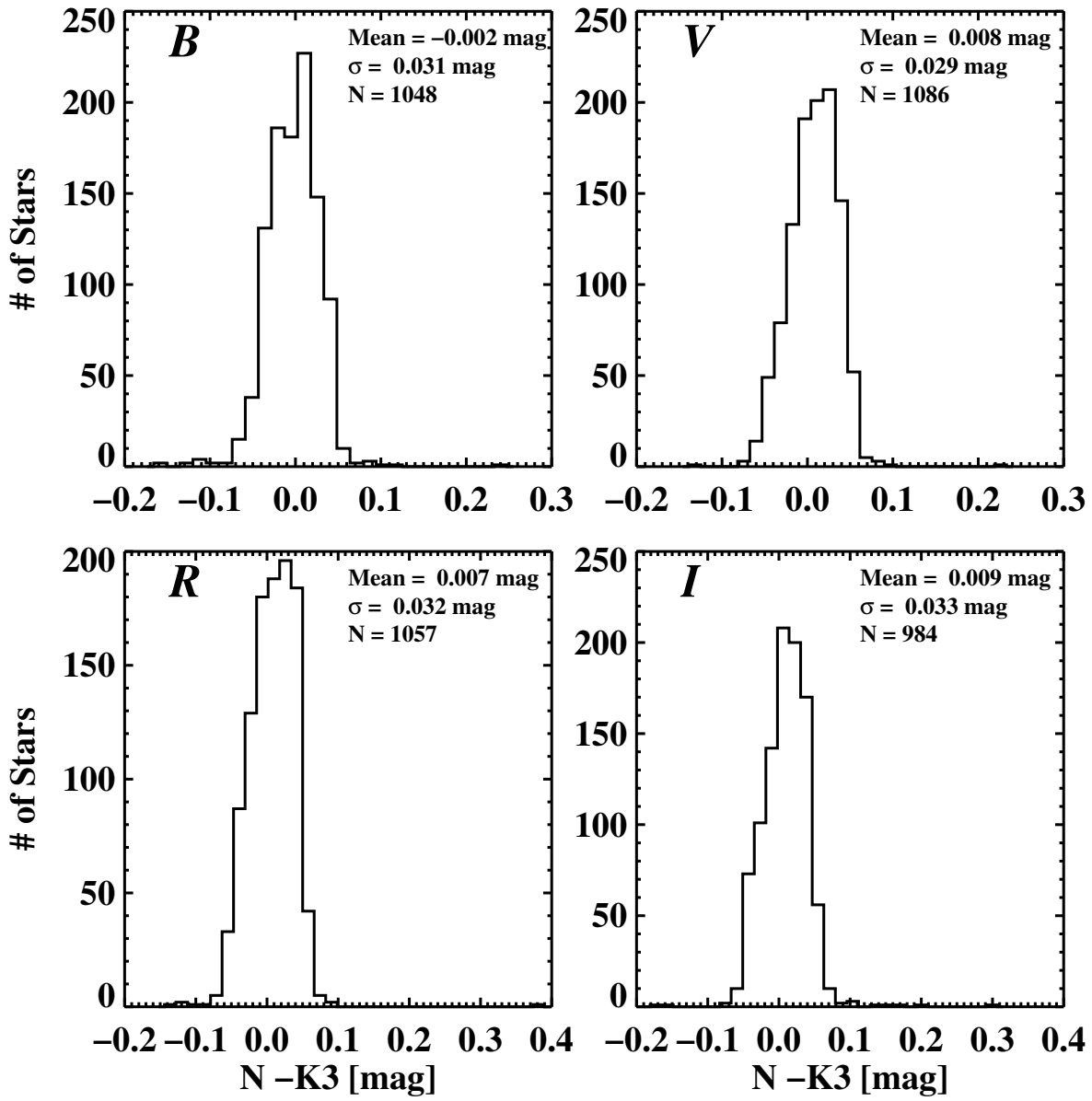

Figure 2.7: Distributions of residual differences in measurements of local standard stars observed with the Nickel telescope and KAIT3. The data are consistent with little to no offset in calibrations from these two different telescope systems in all observed bands. The scatter in the distributions leads us to adopt a systematic error of 0.03 mag.

Figure 2.8 shows the results, with the top plot giving a comparison of the two final light curves. The middle plot shows the residual between the two light curves in $BVRI$, in the sense of the single-image template subtracted from the stacked template. The bottom plot is the residual scaled by the photometry error. Overall, the results from the two different galaxy templates are consistent with the error bars found using our pipeline. We do note, however, a few systematic trends. On average, there is a systematic difference of ~ 0.04 mag in the I band, although this is almost always within 1σ. We also find that the B-band residuals increase with phase as the ratio of galaxy to SN flux increases at the position of the SN. However, the significance is reduced if we scale the residuals by the 1σ photometry error. We conclude from these tests that the correlated error induced from using a single image as a galaxy template is not negligible, but is taken into account by the error budget described in Section 2.3.4.

PSF as a Function of Color

We tested to see if there were variations of the PSF with the color of field stars. Using images of the open cluster M67, we measured the FWHM of stars taken from Chevalier & Ilovaisky (1991), which span a range of colors. A linear fit shows no convincing trend in either the KAIT or Nickel images. Figure 2.9 shows an example from data taken with the Nickel telescope. We rule out any strong dependence of the PSF on the color of field stars which would introduce a systematic error in our galaxy subtraction process.

Transformation into the Landolt System

A possible risk in transforming instrumental magnitudes into the Landolt system is correlating the SN magnitude with the color of the comparison local standard star. We check for any correlation in the post-transformation SN magnitude by calculating the χ^2 statistic defined as

$$\chi^2 = \sum_i \left(\frac{(m_i - \overline{m})}{\sigma_{m_i}} \right)^2,$$

where m_i is the SN magnitude found using the ith local standard star, $\overline{m}$ in the error-weighted average of SN magnitudes, and σ_{m_i} is the associated error in m_i (photometry and calibration error added in quadrature). We use the reduced χ^2, χ^2_ν, as an indicator to determine how well our final magnitudes are described by a constant (i.e., the error-weighted mean). We find that $\chi^2_\nu \approx 1$ in almost all cases, indicating that the error-weighted mean is an appropriate combination of individual measurements to produce a final SN magnitude. We do not see a

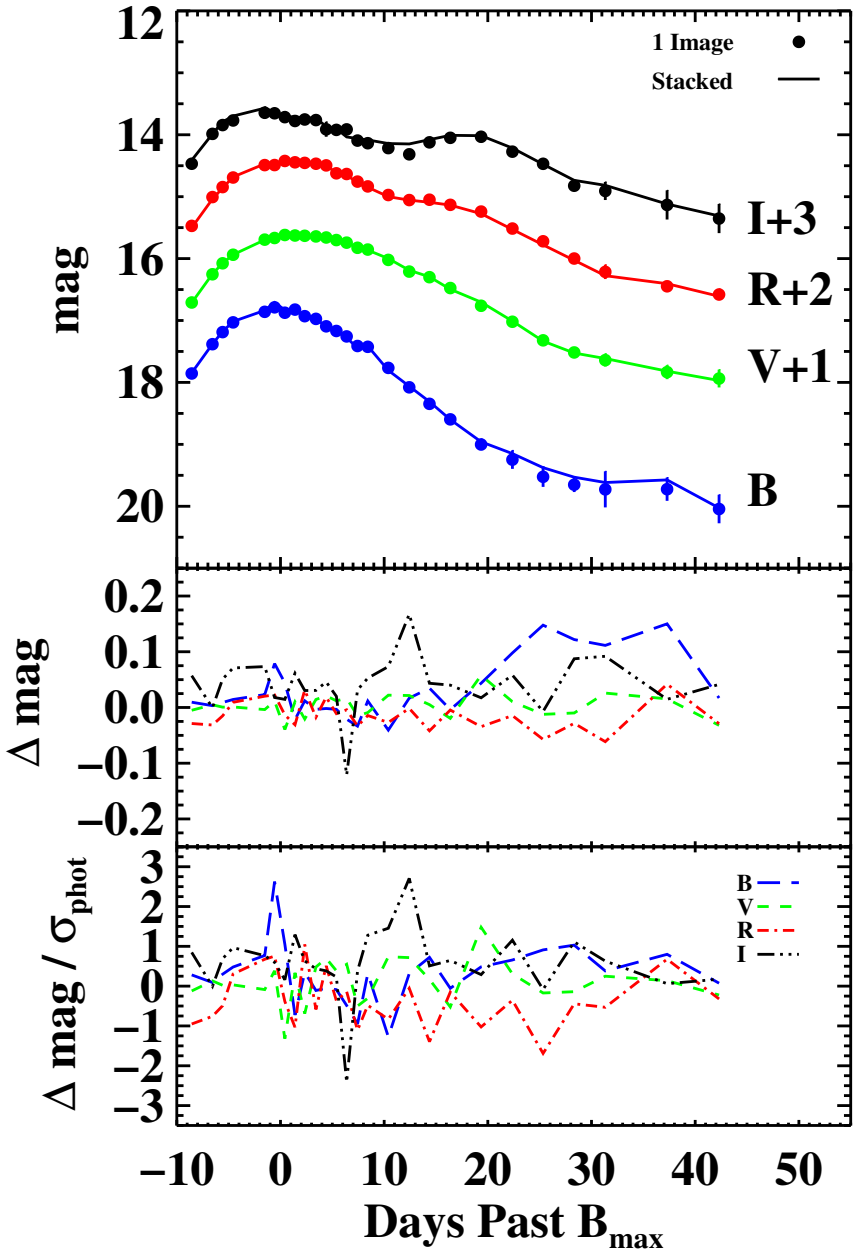

Figure 2.8: Comparison of reductions of SN 2000cn using a single template image and a stacked template of 5–6 images. The top plot is the two individual light curves. The middle portion shows the difference between the two reductions, in the sense of one template reduction minus the stacked template. The bottom plot shows the difference scaled by the photometry errors found from our pipelines.

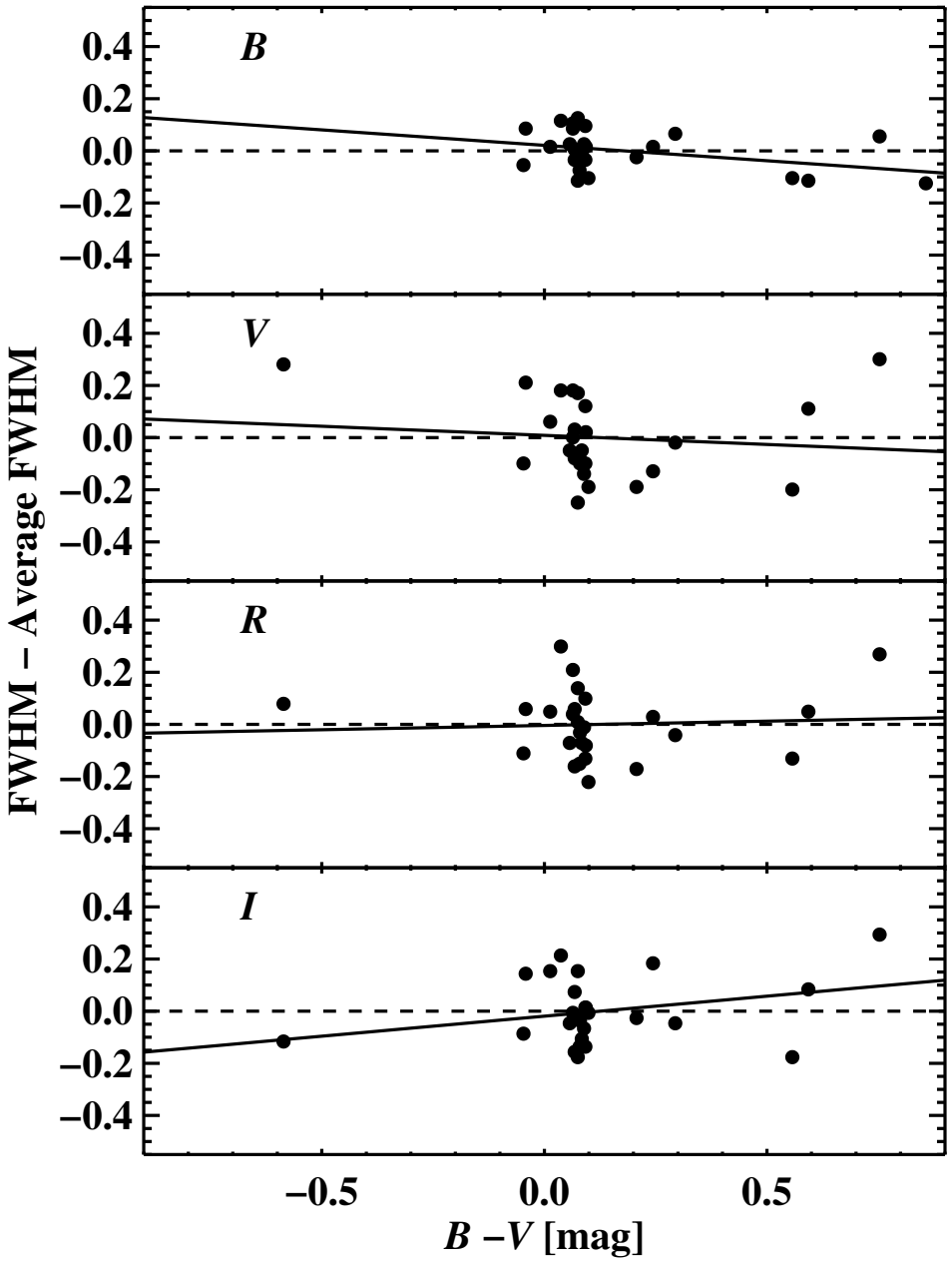

Figure 2.9: The FWHM of stars in the field of M67 as a function of their color from *BVRI* images taken with the Nickel telescope. The best-fit line is plotted in solid black for each filter. We do not measure a significant trend, indicating that the image PSF is independent of color.

convincing linear trend with the color of the comparison star; thus, we deem it unnecessary to correct our photometry for the possibility of this effect.

Summary

As a result of our study of possible systematic errors in our dataset, we adopt a final systematic uncertainty of 0.03 mag in *BVRI*. This error is not included in our photometry tables, but should be included when combining the LOSS sample with photometry from other datasets.

Table 2.6: Photometry of SN 2001dl

JD	B (mag)	V (mag)	R (mag)	I (mag)	Telescope
2452121.83	17.942 (083)	17.665 (052)	17.265 (029)	16.985 (039)	KAIT2
2452122.81	17.658 (040)	17.381 (051)	17.035 (028)	16.862 (031)	KAIT2
2452123.80	17.512 (037)	17.255 (029)	16.828 (019)	16.650 (031)	KAIT2
2452124.79	17.350 (062)	17.082 (033)	16.749 (028)	16.574 (035)	KAIT2
2452128.88	17.089 (038)	16.766 (021)	16.517 (020)	16.391 (032)	KAIT2
2452129.84	17.137 (049)	16.758 (028)	16.463 (021)	16.484 (040)	KAIT2
2452130.86	17.022 (034)	16.766 (024)	16.462 (016)	16.513 (025)	KAIT2
2452132.81	17.076 (025)	16.760 (025)	16.450 (015)	16.604 (066)	KAIT2
2452134.74	17.138 (031)	16.765 (018)	16.496 (013)	16.708 (038)	KAIT2
2452136.82	17.292 (027)	16.827 (017)	16.587 (022)	16.825 (049)	KAIT2
2452138.78	17.297 (030)	16.884 (022)	16.656 (013)	16.952 (038)	KAIT2
2452140.81	17.478 (048)	17.022 (020)	16.820 (015)	17.030 (043)	KAIT2
2452142.77	17.617 (026)	17.100 (029)	16.985 (031)	17.280 (081)	KAIT2
2452145.82	17.992 (086)	17.334 (042)	17.170 (023)	17.333 (061)	KAIT2
2452147.76	18.095 (064)	17.393 (025)	17.236 (034)	17.495 (078)	KAIT2
2452151.72	18.574 (092)	17.576 (043)	17.313 (040)	17.328 (065)	KAIT2
2452157.79	19.177 (129)	17.884 (065)	17.360 (030)	17.088 (044)	KAIT2
2452161.74	19.527 (124)	18.159 (056)	17.559 (029)	17.079 (049)	KAIT2
2452165.76	19.836 (058)	18.366 (035)	17.704 (030)	17.220 (034)	KAIT3
2452169.72	19.878 (097)	18.637 (052)	17.983 (030)	17.482 (038)	KAIT3
2452173.68	20.027 (123)	18.766 (067)	18.173 (035)	17.758 (040)	KAIT3
2452182.70	···	···	18.526 (131)	···	KAIT3
2452186.67	···	18.875 (081)	18.575 (044)	18.412 (082)	KAIT3

Continued on Next Page ...

Table 2.6 –Continued

JD	B (mag)	V (mag)	R (mag)	I (mag)	Telescope

Note. – Quoted errors in parentheses are in units of 0.001 mag.

Table 2.7: Comparison Stars for SN 2002de

Star	α(J2000)	δ(J2000)	B (mag)	V (mag)	R (mag)	I (mag)	$N_{\rm calib}$
1	16:16:33.47	+35:40:34.1	18.221(011)	16.775(014)	15.878(012)	15.038(010)	5
2	16:16:20.58	+35:45:32.8	16.595(011)	15.794(013)	15.379(013)	15.001(009)	4
3	16:16:38.51	+35:45:21.5	17.980(010)	17.454(014)	17.066(011)	16.781(014)	4
4	16:16:23.30	+35:45:16.9	17.442(013)	16.897(012)	16.556(011)	16.255(013)	5
5	16:16:18.33	+35:44:26.6	17.346(012)	16.710(011)	16.363(010)	16.053(013)	5
6	16:16:45.44	+35:43:20.6	16.332(007)	15.632(013)	15.244(010)	14.859(011)	4
7	16:16:30.30	+35:41:24.6	17.384(011)	16.770(013)	16.376(009)	16.099(016)	6

Note. – Quoted errors in parentheses are in units of 0.001 mag.

2.4 Results

We present the results of running the pipeline on SNe Ia from LOSS data taken during the interval 1998–2008. A representative sample of our light curves is shown in Figure 2.10. The light curves are shifted relative to the date of B-band maximum light found by using the light-curve fitting software MLCS2k2.v006 (Jha et al. 2007), or by direct polynomial fits for peculiar SNe that do not have representative templates in MLCS2k2.v006. An example of our photometry can be found in Table 2.6. We note that the uncertainty quoted in Table 2.6 only refers to the statistical error; a systematic error of 0.03 mag should be added when comparing to other datasets. Figure 2.11 shows an example of our finding charts, with comparison stars labeled. We include an example of our comparison-star photometry in Table 2.7. All of the remaining light-curve tables, finding charts, and comparison-star photometry are available online[4].

[4]http://hercules.berkeley.edu/database/public.

Basic information about each SN and galaxy was gathered from the NASA/IPAC Extragalactic Database (NED)[5]. Discovery and classification information for each SN can be found in Table 2.8. Table 2.9 presents host-galaxy properties. Information regarding our SNe (such as discoverers, classification references, etc.) was obtained from our private searchable MYSQL SN database (Silverman et al. 2012c), which collects information about each SN.

[5]http://nedwww.ipac.caltech.edu/.

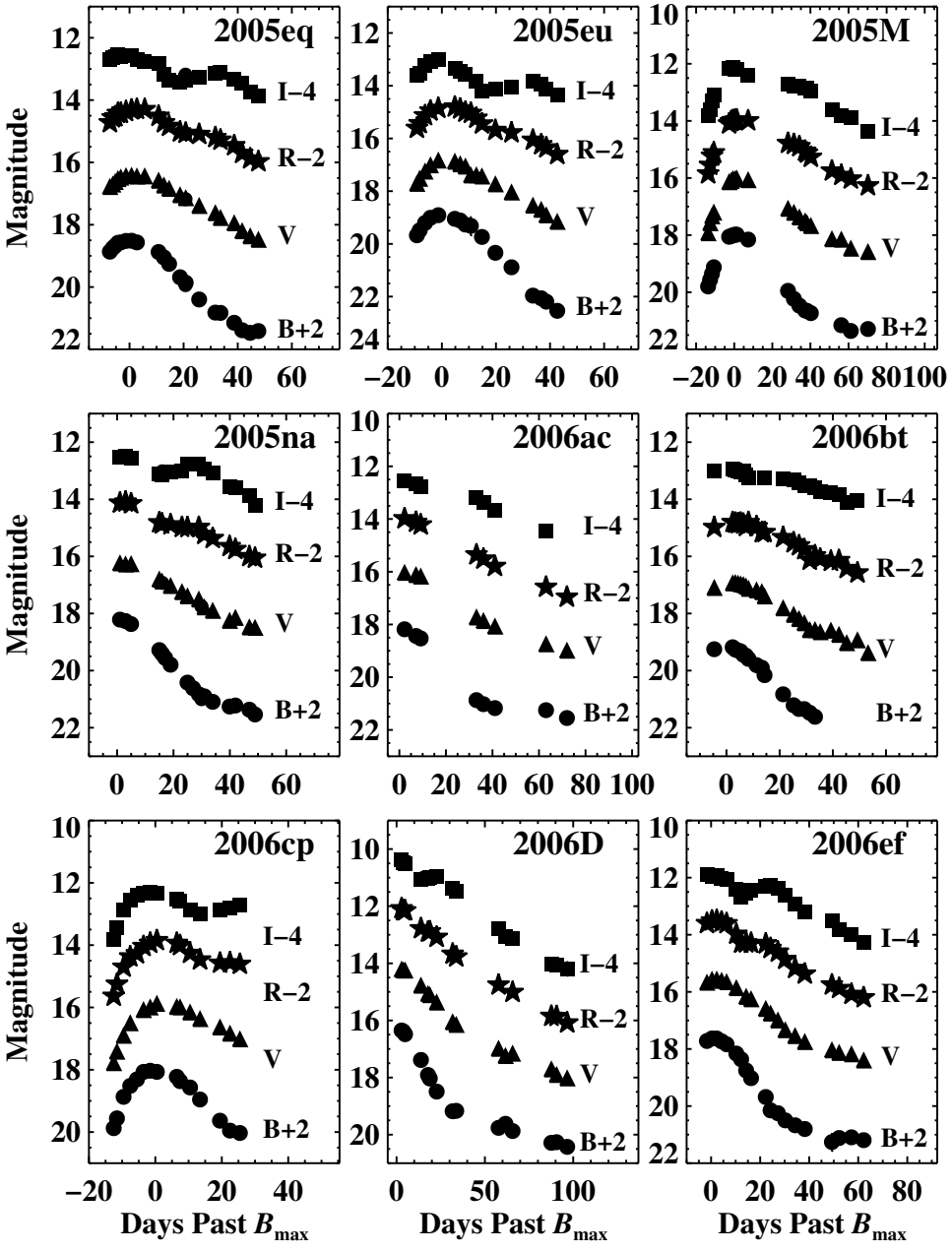

Figure 2.10: Representative *BVRI* light curves of nine SNe Ia from our sample. Dates have been shifted relative to $B_{\max}$.

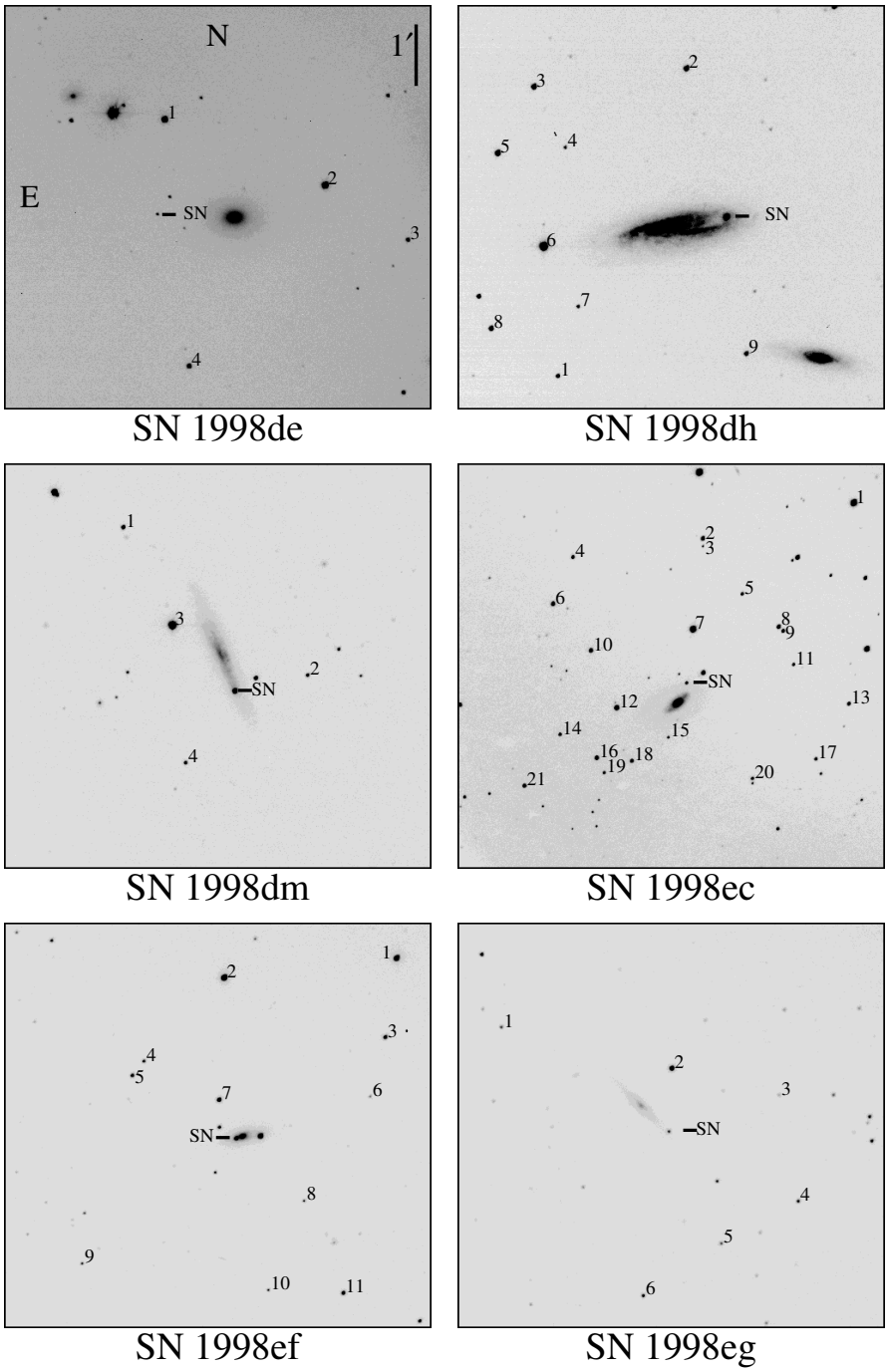

Figure 2.11: Finder charts for six SNe Ia from our sample. The vertical bar on the right edge of the top-left panel indicates 1′. North is up and east to the left. Finders for the rest of our sample are archived online.

Table 2.8: Discovery and Classification References for SNe Ia in the LOSS Sample

SN	Host Galaxy	UT Discovery Date	Discovery Ref.	Spectroscopic Ref.
SN 1998de	NGC 252	1998-07-23	IAUC 6977	IAUC 6980
SN 1998dh	NGC 7541	1998-07-20	IAUC 6978	IAUC 6980
SN 1998dm	MCG -01-4-44	1998-08-22	IAUC 6993	IAUC 6997
SN 1998ec	UGC 3576	1998-09-26	IAUC 7022	IAUC 7024
SN 1998ef	UGC 646	1998-10-18	IAUC 7032	IAUC 7032
SN 1998eg	UGC 12133	1998-10-19	IAUC 7033	IAUC 7037
SN 1998es	NGC 632	1998-11-13	IAUC 7050	IAUC 7054
SN 1999aa	NGC 2595	1999-02-11	IAUC 7108	IAUC 7108
SN 1999ac	NGC 6063	1999-02-26	IAUC 7114	IAUC 7122
SN 1999bh	NGC 3435	1999-03-29	IAUC 7135	IAUC 7138
SN 1999by	NGC 2841	1999-04-30	IAUC 7156	IAUC 7157
SN 1999cl	NGC 4501	1999-05-29	IAUC 7185	IAUC 7190
SN 1999cp	NGC 5468	1999-06-18	IAUC 7205	IAUC 7206
SN 1999da	NGC 6411	1999-07-05	IAUC 7215	IAUC 7219
SN 1999dg	UGC 9758	1999-07-23	IAUC 7229	IAUC 7239
SN 1999dk	UGC 1087	1999-08-12	IAUC 7237	IAUC 7238
SN 1999dq	NGC 976	1999-09-02	IAUC 7247	IAUC 7250
SN 1999ej	NGC 495	1999-10-18	IAUC 7286	IAUC 7298
SN 1999gh	NGC 2986	1999-12-03	IAUC 7286	IAUC 7328
SN 1999gp	UGC 1993	1999-12-23	IAUC 7337	IAUC 7341
SN 2000cn	UGC 11064	2000-06-02	IAUC 7436	IAUC 7437
SN 2000cp	2MFGC 12921	2000-06-21	IAUC 7441	IAUC 7442
SN 2000cu	ESO 525-G004	2000-07-12	IAUC 7453	IAUC 7454
SN 2000cw	MCG +05-56-7	2000-07-14	IAUC 7456	IAUC 7457
SN 2000cx	NGC 524	2000-07-17	IAUC 7458	IAUC 7463
SN 2000dg	MCG +01-1-29	2000-08-22	IAUC 7480	IAUC 7484
SN 2000dk	NGC 382	2000-09-18	IAUC 7493	IAUC 7494
SN 2000dm	UGC 11198	2000-09-24	IAUC 7495	IAUC 7497
SN 2000dn	IC 1468	2000-09-27	IAUC 7498	IAUC 7499
SN 2000dr	IC 1610	2000-10-05	IAUC 7505	IAUC 7506

Continued on Next Page . . .

Table 2.8 –Continued

SN	Host Galaxy	UT Discovery Date	Discovery Ref.	Spectroscopic Ref.
SN 2000fa	UGC 3770	2000-11-30	IAUC 7533	IAUC 7535
SN 2001C	CGCG 285-012	2001-01-04	IAUC 7555	IAUC 7563
SN 2001E	NGC 3905	2001-01-05	IAUC 7557	IAUC 7566
SN 2001V	NGC 3987	2001-02-19	IAUC 7585	IAUC 7585
SN 2001ah	UGC 6211	2001-03-27	IAUC 7603	IAUC 7604
SN 2001ay	IC 4423	2001-04-18	IAUC 7611	IAUC 7612
SN 2001bf	MCG +04-42-22	2001-05-03	IAUC 7620	IAUC 7625
SN 2001bg	NGC 2608	2001-05-08	IAUC 7621	IAUC 7622
SN 2001bp	SDSS J160208.91+364313.8	2001-05-15	IAUC 7626	IAUC 7626
SN 2001br	UGC 11260	2001-05-13	IAUC 7629	IAUC 7629
SN 2001cj	UGC 8399	2001-05-30	IAUC 7640	IAUC 7651
SN 2001ck	UGC 9425	2001-06-03	IAUC 7641	IAUC 7645
SN 2001cp	UGC 10738	2001-06-19	IAUC 7645	IAUC 7640
SN 2001da	NGC 7780	2001-07-09	IAUC 7658	IAUC 7664
SN 2001dl	UGC 11725	2001-07-30	IAUC 7675	IAUC 7676
SN 2001eh	UGC 1162	2001-09-09	IAUC 7714	IAUC 7714
SN 2001en	NGC 523	2001-09-26	IAUC 7724	IAUC 7732
SN 2001ep	NGC 1699	2001-10-03	IAUC 7727	IAUC 7731
SN 2001ex	UGC 3595	2001-10-16	IAUC 7735	IAUC 7736
SN 2001fh	2MASX J21204248+4423590	2001-11-03	IAUC 7744	IAUC 7748
SN 2002G	CGCG 189-024	2002-01-18	IAUC 7797	IAUC 7802
SN 2002aw	2MFGC 13321	2002-02-15	IAUC 7831	IAUC 7834
SN 2002bf	CGCG 266-031	2002-02-22	IAUC 7836	IAUC 7846
SN 2002bo	NGC 3190	2002-03-09	IAUC 7847	IAUC 7848
SN 2002cd	NGC 6916	2002-04-08	IAUC 7871	IAUC 7873
SN 2002cf	NGC 4786	2002-04-13	IAUC 7877	IAUC 7878
SN 2002cr	NGC 5468	2002-05-01	IAUC 7890	IAUC 7891
SN 2002cs	NGC 6702	2002-05-05	IAUC 7891	IAUC 7894
SN 2002cu	NGC 6575	2002-05-11	IAUC 7898	IAUC 7898
SN 2002cx	CGCG 044-035	2002-05-12	IAUC 7902	IAUC 7903

Continued on Next Page . . .

Table 2.8 –Continued

SN	Host Galaxy	UT Discovery Date	Discovery Ref.	Spectroscopic Ref.
SN 2002de	NGC 6104	2002-06-01	IAUC 7914	IAUC 7915
SN 2002dj	NGC 5018	2002-06-12	IAUC 7918	IAUC 7919
SN 2002dl	UGC 11994	2002-06-16	IAUC 7920	IAUC 7923
SN 2002do	MCG +07-41-1	2002-06-17	IAUC 7923	IAUC 7927
SN 2002dp	NGC 7678	2002-06-18	IAUC 7924	IAUC 7927
SN 2002eb	CGCG 473-011	2002-07-22	IAUC 7937	IAUC 7953
SN 2002ef	NGC 7761	2002-07-30	IAUC 7943	IAUC 7945
SN 2002el	NGC 6986	2002-08-12	IAUC 7953	IAUC 7954
SN 2002er	UGC 10743	2002-08-23	IAUC 7959	IAUC 7961
SN 2002eu	2MASXI J0149427+323730	2002-08-30	IAUC 7963	IAUC 7965
SN 2002fb	NGC 759	2002-09-06	IAUC 7967	IAUC 7967
SN 2002fk	NGC 1309	2002-09-17	IAUC 7973	IAUC 7976
SN 2002ha	NGC 6962	2002-10-21	IAUC 7997	IAUC 7999
SN 2002he	UGC 4322	2002-10-28	IAUC 8002	IAUC 8004
SN 2002jg	NGC 7253	2002-11-23	IAUC 8022	IAUC 8023
SN 2003D	MCG -01-25-9	2003-01-06	IAUC 8043	IAUC 8043
SN 2003W	UGC 5234	2003-01-28	IAUC 8061	IAUC 8061
SN 2003Y	IC 522	2003-01-29	IAUC 8062	IAUC 8063
SN 2003cg	NGC 3169	2003-03-21	IAUC 8097	IAUC 8099
SN 2003cq	NGC 3978	2003-03-30	IAUC 8103	IAUC 8106
SN 2003du	UGC 9391	2003-04-22	IAUC 8121	IAUC 8122
SN 2003fa	ARK 527	2003-06-01	IAUC 8140	IAUC 8142
SN 2003gn	CGCG 452-024	2003-07-22	IAUC 8168	IAUC 8170
SN 2003gq	NGC 7407	2003-07-24	IAUS 8168	IAUC 8170
SN 2003gs	NGC 936	2003-07-29	IAUC 8171	IAUC 8172
SN 2003gt	NGC 6930	2003-07-29	IAUC 8172	IAUC 8175
SN 2003he	MCG -01-1-10	2003-08-11	IAUC 8182	IAUC 8189
SN 2003hv	NGC 1201	2003-09-09	IAUC 8197	IAUC 8198
SN 2003kf	MCG -02-16-2	2003-11-27	CBET 53	CBET 53
SN 2004E	KUG 1314+318B	2004-01-15	IAUC 8271	IAUC 8271

Continued on Next Page . . .

Table 2.8 –Continued

SN	Host Galaxy	UT Discovery Date	Discovery Ref.	Spectroscopic Ref.
SN 2004S	MCG -05-16-21	2004-02-03	IAUC 8283	IAUC 8283
SN 2004as	SDSS J112538.81+224952.2	2004-03-11	IAUC 8302	IAUC 8302
SN 2004at	MCG +10-16-37	2004-03-12	IAUC 8302	IAUC 8304
SN 2004bd	NGC 3786	2004-04-07	IAUC 8316	IAUC 8317
SN 2004bg	UGC 6363	2004-04-07	IAUC 8317	IAUC 8321
SN 2004bk	NGC 5246	2004-04-22	IAUC 8329	IAUC 8331
SN 2004br	NGC 4493	2004-05-15	IAUC 8340	IAUC 8343
SN 2004bv	NGC 6907	2004-05-24	IAUC 8344	IAUC 8345
SN 2004bw	MCG +00-38-19	2004-05-26	IAUC 8345	IAUC 8353
SN 2004dt	NGC 799	2004-08-11	IAUC 8386	IAUC 8387
SN 2004ef	UGC 12158	2004-09-04	IAUC 8399	IAUC 8403
SN 2004eo	NGC 6928	2004-09-17	IAUC 8406	IAUC 8409
SN 2004ey	UGC 11816	2004-10-14	IAUC 8419	IAUC 8420
SN 2004fz	NGC 783	2004-11-14	IAUC 8437	IAUC 8440
SN 2004gs	MCG +03-22-20	2004-12-12	IAUC 8453	IAUC 8453
SN 2005M	NGC 2930	2005-01-19	IAUC 8470	IAUC 8474
SN 2005am	NGC 2811	2005-02-22	IAUC 8490	IAUC 8491
SN 2005bc	NGC 5698	2005-04-02	IAUC 8504	CBET 132
SN 2005bl	NGC 4070	2005-04-14	IAUC 8512	CBET 139
SN 2005bo	NGC 4708	2005-04-17	IAUC 8514	IAUC 8517
SN 2005cc	NGC 5383	2005-05-19	IAUC 8534	ATEL 502
SN 2005cf	MCG -01-39-3	2005-05-28	IAUC 8534	IAUC 8534
SN 2005de	UGC 11097	2005-08-02	IAUC 8580	IAUC 8581
SN 2005dm	IC 219	2005-08-26	IAUC 8589	CBET 204
SN 2005el	NGC 1819	2005-09-25	IAUC 8604	CBET 245
SN 2005eq	MCG -01-9-6	2005-09-30	IAUC 8608	IAUC 8610
SN 2005eu	NSF J022743.32+281037.6	2005-10-04	IAUC 8611	CBET 245
SN 2005na	UGC 3634	2005-12-31	IAUC 8655	CBET 351
SN 2006D	MCG -01-33-34	2006-01-11	CBET 362	CBET 366
SN 2006X	NGC 4321	2006-02-04	IAUC 8667	CBET 393

Continued on Next Page . . .

Table 2.8 –Continued

SN	Host Galaxy	UT Discovery Date	Discovery Ref.	Spectroscopic Ref.
SN 2006ac	NGC 4619	2006-02-09	IAUC 8669	CBET 398
SN 2006bt	CGCG 108-013	2006-04-26	CBET 485	CBET 485
SN 2006cp	UGC 7357	2006-05-28	CBET 524	CBET 528
SN 2006dm	MCG -01-60-21	2006-07-03	CBET 568	CBET 569
SN 2006ef	NGC 809	2006-08-18	CBET 597	CBET 604
SN 2006ej	NGC 191	2006-08-23	CBET 603	CBET 604
SN 2006em	NGC 911	2006-08-25	CBET 605	CBET 612
SN 2006en	MCG +05-54-41	2006-08-26	CBET 606	CBET 608
SN 2006eu	MCG +08-36-16	2006-09-03	IAUC 8745	CBET 622
SN 2006gr	UGC 12071	2006-08-21	CBET 638	CBET 642
SN 2006hb	MCG -04-12-34	2006-09-27	CBET 649	CBET 652
SN 2006je	IC 1735	2006-10-15	CBET 675	CBET 678
SN 2006le	UGC 3218	2006-10-26	CBET 700	CBET 702
SN 2006lf	UGC 3108	2006-10-26	CBET 704	CBET 705
SN 2007O	UGC 9612	2007-01-21	CBET 818	CBET 818
SN 2007af	NGC 5584	2007-03-01	CBET 863	CBET 865
SN 2007au	UGC 3725	2007-03-18	CBET 895	CBET 898
SN 2007bc	UGC 6332	2007-04-04	CBET 913	CBET 915
SN 2007bj	NGC 6172	2007-04-18	CBET 930	IAUC 8834
SN 2007ca	MCG -02-34-61	2007-04-25	CBET 945	CBET 947
SN 2007ci	NGC 3873	2007-05-15	CBET 966	IAUC 8843
SN 2007co	MCG +05-43-16	2007-06-04	CBET 977	CBET 978
SN 2007cq	2MASX J22144070+0504435	2007-06-21	CBET 983	CBET 984
SN 2007fr	UGC 11780	2007-07-14	CBET 1001	CBET 1001
SN 2007hj	NGC 7461	2007-09-01	CBET 1048	CBET 1048
SN 2007le	NGC 7721	2007-10-13	CBET 1100	CBET 1101
SN 2007sr	NGC 4038	2007-12-18	CBET 1172	CBET 1173
SN 2007qe	NSF J235412.09+272432.3	2007-11-13	CBET 1138	ATEL 1280
SN 2007ux	2MASX J10091969+1459268	2007-12-23	CBET 1187	CBET 1189
SNF20071021-000[a]	2MASX J00150006+1619596	2007-10-21	...	...

Continued on Next Page ...

Table 2.8 –Continued

SN	Host Galaxy	UT Discovery Date	Discovery Ref.	Spectroscopic Ref.
SN 2008A	NGC 634	2008-01-02	CBET 1193	CBET 1198
SN 2008C	UGC 3611	2008-01-03	CBET 1195	CBET 1197
SN 2008L	NGC 1259	2008-01-14	CBET 1212	CBET 1219
SN 2008Q	NGC 524	2008-01-26	CBET 1228	CBET 1232
SN 2008Z	SDSS J094315.36+361709.2	2008-02-07	CBET 1243	CBET 1246
SN 2008ar	IC 3284	2008-02-27	CBET 1273	CBET 1273
SN 2008bf	NGC 4055	2008-03-18	CBET 1307	CBET 1310
SN 2008cl	UGC 10261	2008-05-16	CBET 1378	CBET 1380
SN 2008dr	NGC 7222	2008-06-28	CBET 1419	CBET 1419
SN 2008dt	NGC 6261	2008-06-30	CBET 1423	CBET 1424
SN 2008dx	NGC 4898A	2008-06-24	CBET 1427	CBET 1427
SN 2008ec	NGC 7469	2008-07-14	CBET 1437	CBET 1438
SN 2008ei	UGC 11977	2008-07-23	CBET 1446	CBET 1447
SNF20080514-002[a]	UGC 8472	2008-05-16	ATEL 1532	ATEL 1532
SNF20080909-030[a]	...	2008-09-09	...	...

[a] Discovered and spectroscopically classified by the Nearby Supernova Factory (Aldering et al. 2002).

Table 2.9: Host-Galaxy References for SNe Ia in the LOSS Sample

SN	Host	$E(B-V)_{\rm MW}$ (mag)	$z_{\rm helio}$	E ($''$)	N ($''$)
SN 1998de	S0	0.059	0.016	72	3
SN 1998dh	Sbc	0.067	0.009	-54	10
SN 1998dm	Sc	0.045	0.007	-14	-37
SN 1998ec	Sb	0.085	0.020	-9	20
SN 1998ef	Sb	0.074	0.018	6	-2
SN 1998eg	Sc	0.121	0.025	-26	-25
SN 1998es	S0	0.032	0.011	0	11
SN 1999aa	Sc	0.040	0.014	2	31
SN 1999ac	Scd	0.046	0.009	24	-30
SN 1999bh	Sb	0.015	0.017	-10	-3
SN 1999by	Sb	0.016	0.002	-98	89
SN 1999cl	Sb	0.038	0.008	-46	23
SN 1999cp	Scd	0.025	0.009	-52	23
SN 1999da	E	0.051	0.013	-71	1
SN 1999dg	S0	0.039	0.022	5	5
SN 1999dk	Sc	0.050	0.015	4	26
SN 1999dq	Sc	0.109	0.014	-4	-6
SN 1999ej	S0a	0.072	0.014	18	-20
SN 1999gh	E	0.058	0.008	52	16
SN 1999gp	Sb	0.056	0.027	-11	10
SN 2000cn	Scd	0.057	0.023	-7	-7
SN 2000cp	Sb	0.050	0.034	-3	2
SN 2000cu	Sa	0.088	0.020	12	2
SN 2000cw	Sbc	0.072	0.030	8	-21
SN 2000cx	S0	0.082	0.008	-23	-109
SN 2000dg	Sb	0.092	0.038	-7	-1
SN 2000dk	E	0.070	0.017	-5	9
SN 2000dm	Sab	0.185	0.015	-4	-5
SN 2000dn	S0	0.048	0.032	-26	15
SN 2000dr	S0	0.021	0.019	21	-6
SN 2000fa	Sd/Irr	0.067	0.021	7	-4
SN 2001C	Sb	0.070	0.011	15	-6

Continued on Next Page ...

Table 2.9 –Continued

SN	Host	$E(B-V)_{\rm MW}$ (mag)	$z_{\rm helio}$	E ($''$)	N ($''$)
SN 2001E	Sc	0.039	0.019	1	-23
SN 2001V	Sb	0.020	0.015	52	28
SN 2001ah	Sbc	0.013	0.058	-4	-32
SN 2001ay	Sb	0.019	0.030	-10	9
SN 2001bf	···	0.099	0.015	5	-8
SN 2001bg	Sb	0.039	0.007	22	-19
SN 2001bp	···	0.023	0.095	4	-6
SN 2001br	Sa	0.065	0.021	2	2
SN 2001cj	Sb	0.014	0.024	-8	35
SN 2001ck	Sb	0.013	0.035	-6	3
SN 2001cp	Sbc	0.157	0.022	-49	-40
SN 2001da	Sab	0.058	0.017	9	-3
SN 2001dl	Sd/Irr	0.054	0.021	-2	11
SN 2001eh	Sb	0.064	0.037	-36	6
SN 2001en	Sd/Irr	0.054	0.016	6	-3
SN 2001ep	Sb	0.047	0.013	10	-16
SN 2001ex	Sb	0.053	0.026	-5	0
SN 2001fh	Sb	0.746	0.013	1	-6
SN 2002G	E	0.013	0.034	6	-7
SN 2002aw	Sb	0.007	0.026	-2	2
SN 2002bf	Sb	0.011	0.024	1	4
SN 2002bo	Sa	0.025	0.004	12	-14
SN 2002cd	Sbc	0.405	0.010	10	10
SN 2002cf	E	0.036	0.015	-16	9
SN 2002cr	Scd	0.025	0.009	41	50
SN 2002cs	E	0.108	0.016	25	-1
SN 2002cu	E	0.063	0.023	-91	-26
SN 2002cx	···	0.032	0.024	11	-18
SN 2002de	Sd/Irr	0.019	0.028	-4	1
SN 2002dj	E	0.095	0.009	-9	-3
SN 2002dl	Sc	0.078	0.016	10	-9
SN 2002do	E	0.314	0.016	0	8

Continued on Next Page ...

Table 2.9 –Continued

SN	Host	$E(B-V)_{\rm MW}$ (mag)	$z_{\rm helio}$	E ($''$)	N ($''$)
SN 2002dp	Sc	0.049	0.012	31	22
SN 2002eb	Sb	0.061	0.028	-15	-14
SN 2002ef	S0	0.032	0.024	10	7
SN 2002el	S0	0.087	0.029	-8	25
SN 2002er	Sa	0.161	0.009	-12	5
SN 2002eu	···	0.045	0.038	11	12
SN 2002fb	E	0.089	0.016	-18	-9
SN 2002fk	Sbc	0.040	0.007	-12	-4
SN 2002ha	Sab	0.102	0.014	-7	-29
SN 2002he	E	0.040	0.025	-20	-37
SN 2002jg	Sb	0.066	0.016	-20	-13
SN 2003D	E	0.065	0.022	2	-10
SN 2003W	Sc	0.048	0.020	0	3
SN 2003Y	S0	0.048	0.017	-4	19
SN 2003cg	Sa	0.031	0.004	14	5
SN 2003cq	Sbc	0.020	0.033	32	-2
SN 2003du	Sd/Irr	0.010	0.006	-9	-14
SN 2003fa	Sb	0.039	0.039	-10	49
SN 2003gn	Sab	0.050	0.034	16	-11
SN 2003gq	Sbc	0.069	0.021	-5	11
SN 2003gs	S0	0.035	0.005	13	-15
SN 2003gt	Sab	0.110	0.016	5	-5
SN 2003he	Sbc	0.039	0.025	-2	6
SN 2003hv	S0	0.015	0.006	17	-57
SN 2003kf	Sb	0.313	0.007	9	-14
SN 2004E	E/S0	0.015	0.030	3	20
SN 2004S	Sc	0.100	0.009	-47	-31
SN 2004as	Sd/Irr	0.015	0.031	0	-9
SN 2004at	···	0.012	0.023	-13	0
SN 2004bd	Sa	0.024	0.009	-2	-4
SN 2004bg	Sb	0.022	0.021	14	7
SN 2004bk	Sb	0.025	0.023	-10	-5

Continued on Next Page ...

Table 2.9 –Continued

SN	Host	$E(B-V)_{\rm MW}$ (mag)	$z_{\rm helio}$	E ($''$)	N ($''$)
SN 2004br	E	0.023	0.023	-9	-1
SN 2004bv	Sbc	0.063	0.011	-4	-21
SN 2004bw	Scd	0.141	0.021	22	-7
SN 2004dt	Sa	0.027	0.020	7	11
SN 2004ef	Sb	0.055	0.031	-7	-9
SN 2004eo	Sab	0.108	0.016	59	7
SN 2004ey	Sc	0.137	0.016	8	-13
SN 2004fz	Sc	0.061	0.017	-2	-13
SN 2004gs	S0	0.031	0.027	-10	-13
SN 2005M	Sb	0.031	0.022	-7	-11
SN 2005am	Sa	0.054	0.008	18	31
SN 2005bc	Sb	0.010	0.012	5	8
SN 2005bl	E	0.029	0.024	13	-11
SN 2005bo	Sab	0.046	0.014	-8	-13
SN 2005cc	Sd/Irr	0.007	0.008	-1	-5
SN 2005cf	S0	0.097	0.006	-15	123
SN 2005de	Sb	0.102	0.015	-17	33
SN 2005dm	E	0.026	0.017	7	2
SN 2005el	S0	0.114	0.015	39	-23
SN 2005eq	Scd	0.074	0.029	16	26
SN 2005eu	···	0.131	0.035	-1	-1
SN 2005na	Sa	0.078	0.026	-2	-7
SN 2006D	Sab	0.046	0.009	-13	6
SN 2006X	Sbc	0.026	0.005	-12	-48
SN 2006ac	Sb	0.016	0.023	4	22
SN 2006bt	S0a	0.050	0.032	-44	-23
SN 2006cp	Sc	0.026	0.022	20	-15
SN 2006dm	Sc	0.039	0.022	8	-6
SN 2006ef	S0	0.024	0.018	8	25
SN 2006ej	Sc	0.035	0.020	-6	-5
SN 2006em	E	0.059	0.019	21	-51
SN 2006en	Sc	0.064	0.032	11	-4

Continued on Next Page . . .

Table 2.9 –Continued

SN	Host	$E(B-V)_{\rm MW}$ (mag)	$z_{\rm helio}$	E ($''$)	N ($''$)
SN 2006eu	E	0.194	0.024	13	-9
SN 2006gr	Sb	0.085	0.035	-23	-24
SN 2006hb	E	0.027	0.015	9	18
SN 2006je	Sb	0.046	0.038	19	21
SN 2006le	Sb	0.449	0.017	-12	40
SN 2006lf	Sb	0.954	0.013	13	-12
SN 2007O	Sc	0.023	0.036	8	-2
SN 2007af	Scd	0.039	0.005	-40	-22
SN 2007au	S0	0.067	0.021	41	-31
SN 2007bc	Sa	0.022	0.021	-29	-16
SN 2007bj	E	0.118	0.017	4	2
SN 2007ca	Sc	0.067	0.014	25	-2
SN 2007ci	E	0.026	0.018	-4	-12
SN 2007co	···	0.113	0.027	8	-15
SN 2007cq	···	0.109	0.026	-3	6
SN 2007fr	···	0.061	0.051	6	-34
SN 2007hj	S0	0.088	0.014	-7	14
SN 2007le	Sc	0.033	0.007	-4	-17
SN 2007qe	···	0.038	0.024	12	1
SN 2007sr	Sd/Irr	0.047	0.005	-3	-379
SN 2007ux	···	0.045	0.031	4	5
SNF20071021-000	···	0.069	0.028	-3	7
SN 2008A	Sa	0.054	0.016	-15	19
SN 2008C	S0a	0.084	0.017	-3	0
SN 2008L	S0	0.159	0.019	-6	-10
SN 2008Q	S0	0.083	0.008	141	42
SN 2008Z	···	0.012	0.021	-2	-7
SN 2008ar	Sa	0.037	0.026	5	3
SN 2008bf	E	0.035	0.024	20	46
SN 2008cl	S0	0.021	0.063	3	8
SN 2008dr	Sb	0.043	0.041	-1	8
SN 2008dt	S0a	0.046	0.035	1	-6

Continued on Next Page ...

Table 2.9 –Continued

SN	Host	$E(B-V)_{\rm MW}$ (mag)	$z_{\rm helio}$	E ($''$)	N ($''$)
SN 2008dx	E	0.010	0.023	-45	-3
SN 2008ec	Sa	0.069	0.016	14	-7
SN 2008ei	Sd/Irr	0.085	0.038	-5	-3
SNF20080514-002	S0	0.034	0.022	-11	-12
SNF20080909-030	···	0.069	0.032	···	···

Note. – SN offsets from the host-galaxy nucleus are given.

2.4.1 The LOSS Sample

Precise measurements of cosmological parameters require multi-color light curves that are well sampled and range from before maximum light to a month past maximum to accurately correlate the width of the light curve to its luminosity. Figure 2.12 shows the average cadence between photometry epochs versus the number of photometry epochs for each SN in our sample. The plot reveals a significant clustering around a cadence of 3 days and ~ 25 epochs of photometry, indicating that our light curves are on average well sampled and cover an extensive range during the photometric evolution of the SN. A histogram of the number of photometry epochs can be found in Figure 2.13; we find a median of 21 epochs of photometry for the SNe. Figure 2.14 shows how many days after $B_{\rm max}$ we commence photometric monitoring. On average, we start observing 6 days before maximum light in B, with 125 SNe having data before maximum.

Cosmological studies of SNe Ia require follow-up observations of SNe that are within the Hubble flow to avoid substantial peculiar velocities induced by the gravitational attraction between galaxies, which produce deviations from a straight Hubble law. Adopting a typical peculiar velocity of 300 km s^{-1}, we define the lower limit of our cosmology sample at $cz =$ 3000 km s^{-1}, at which point peculiar motions will be $\lesssim 10\%$ of the expansion velocity. Our sample contains 135 SNe Ia in the Hubble flow. Figure 2.15 shows a histogram of the LOSS sample as a function of redshift. We find a median recession velocity of $cz_{\rm helio} = 5816$ km s^{-1} for our entire sample, and a median value of $cz_{\rm helio} = 6595$ km s^{-1} for our Hubble-flow sample.

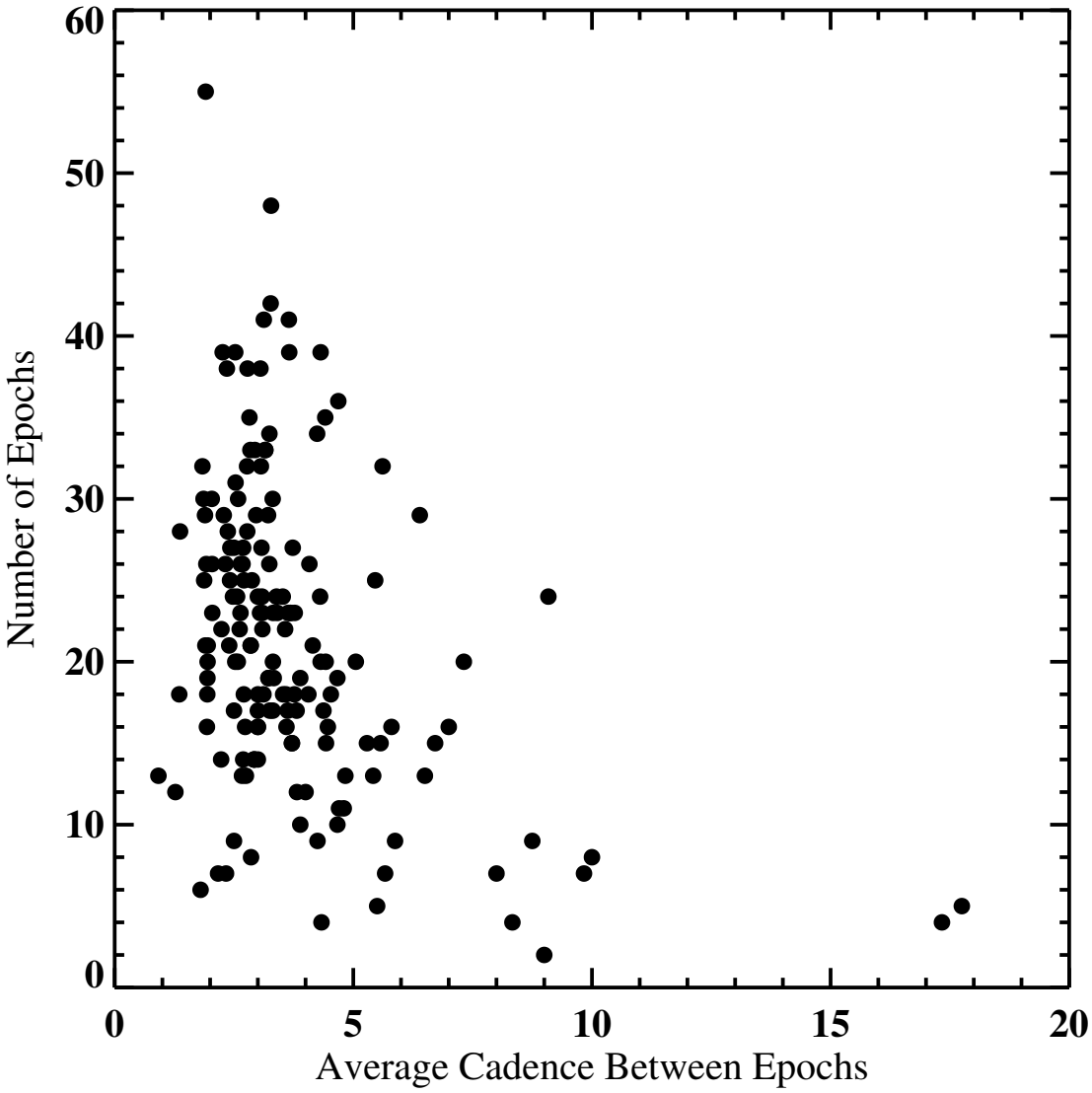

Figure 2.12: Scatterplot of the average cadence between epochs in days versus the number of epochs for each SN. The tight grouping of points indicates that a large majority of the SNe are well sampled and have over 20 epochs of photometry.

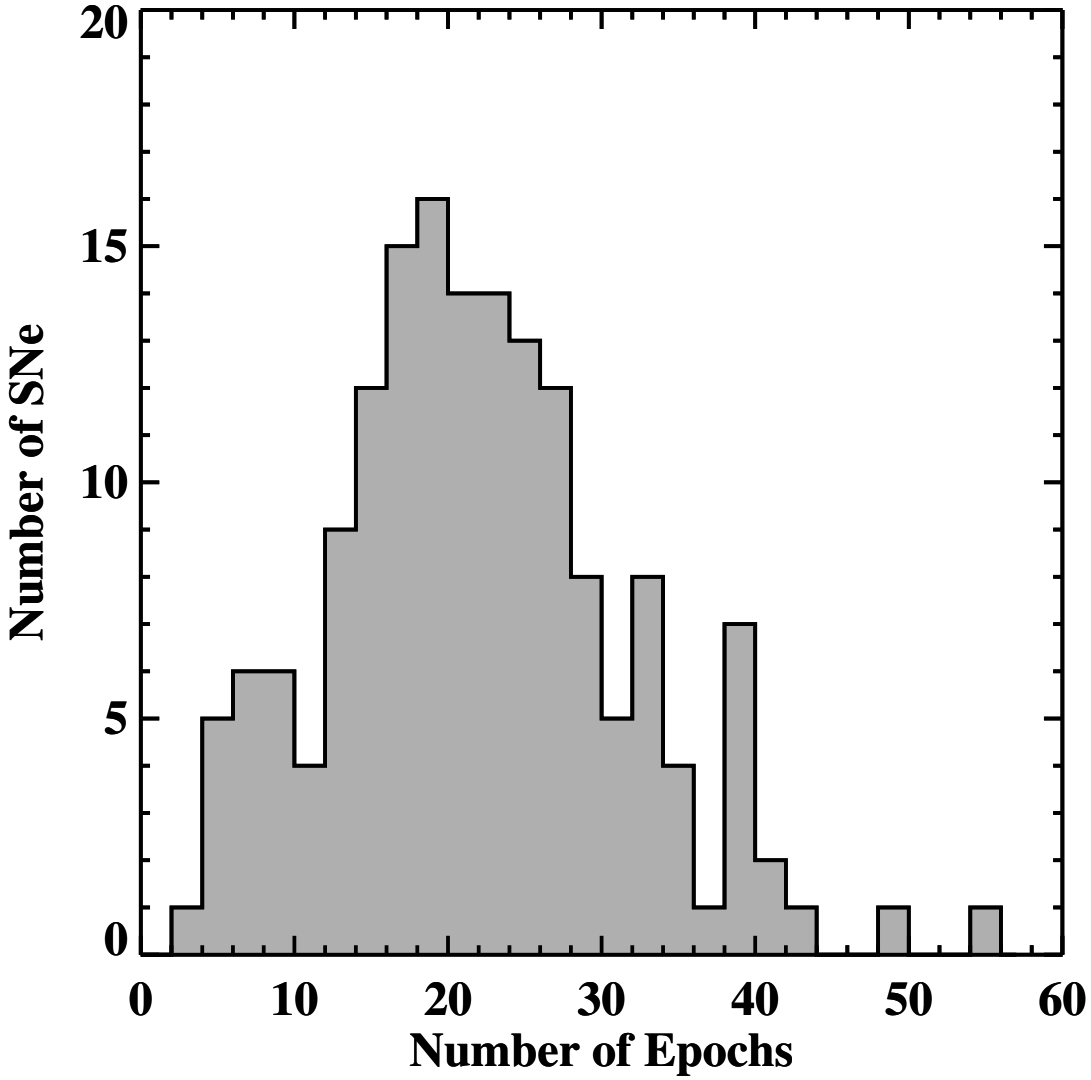

Figure 2.13: Distribution for the number of epochs per SN using the number of V-band observations. We find a median of 21 epochs of photometry per SN.

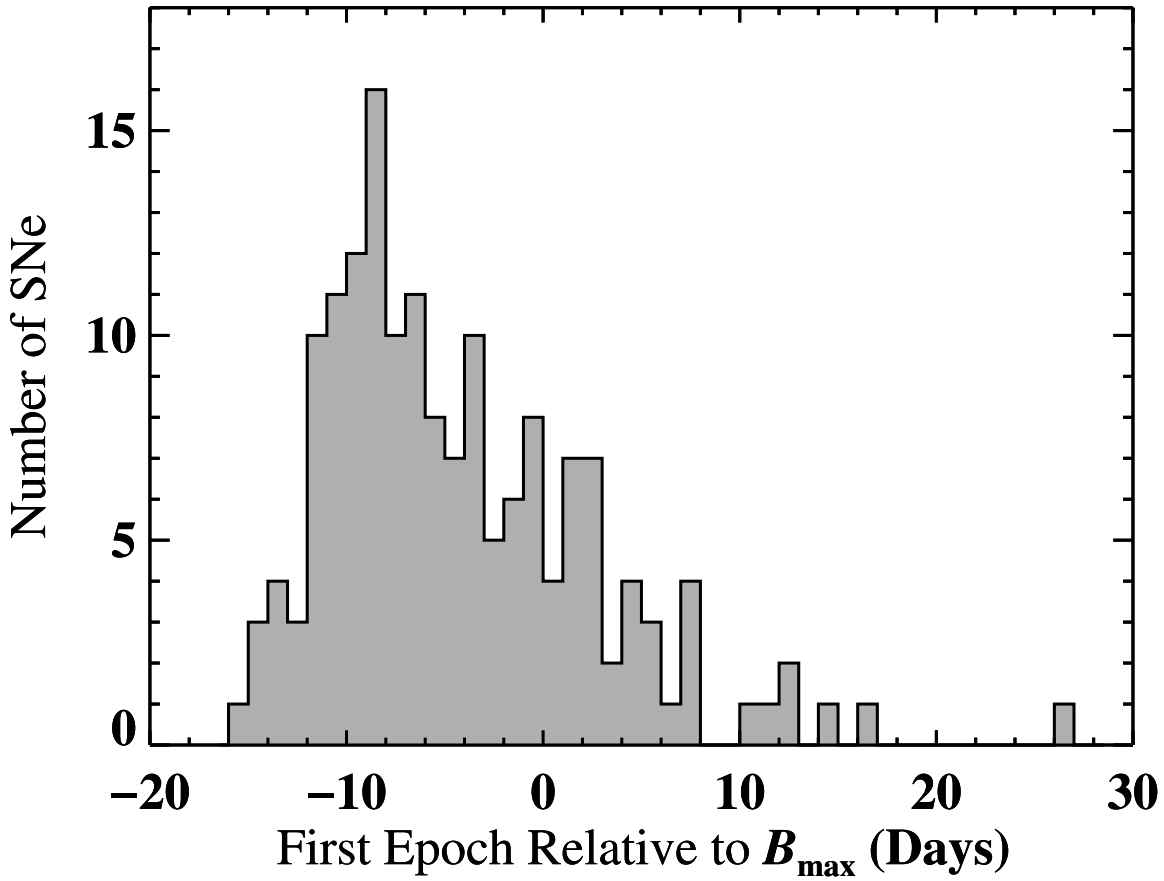

Figure 2.14: Distribution of first photometry epoch relative to $B_{\max}$. The median value for our sample is 6 days before $B_{\max}$.

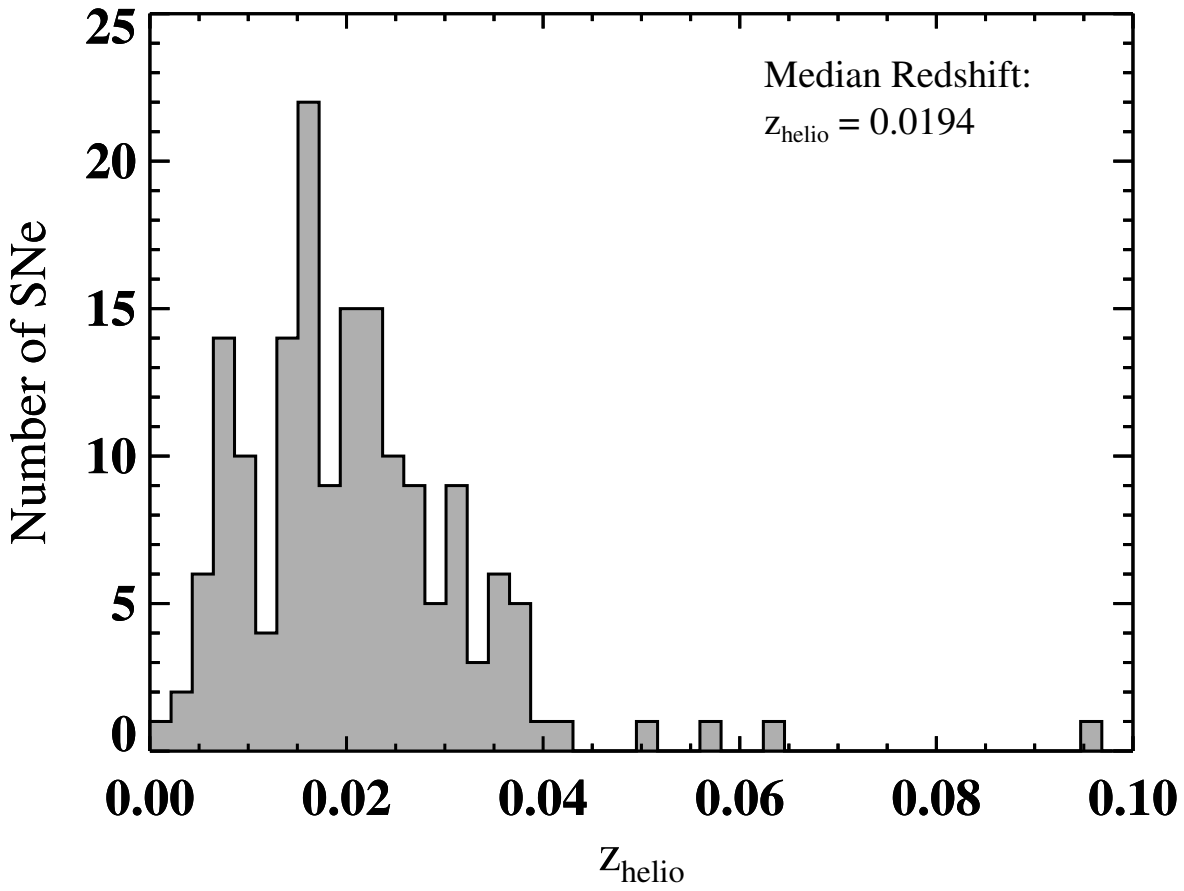

Figure 2.15: Redshift distribution for the LOSS sample. We find a median recession velocity of $cz_{\rm helio} = 5816$ km s^{-1} ($z_{\rm helio} = 0.0194$) for our sample.

2.4.2 Comparison with Published Data

In this chapter, we present a homogeneously observed and reduced dataset of SN Ia *BVRI* light curves. The most productive science will come from combining datasets collected from different telescopes (Kowalski et al. 2008; Hicken et al. 2009a). Understanding the underlying differences between these datasets will be crucial to improving the cosmological utility of SNe Ia. Wang et al. (2009b) have shown that photometry of a nearby bright SN ($B_{\rm max}$= 13.64 mag) having negligible host-galaxy contamination with different telescopes can exhibit systematic differences of $\sigma \approx 0.05$ mag prior to making S-corrections for instrumental response (Stritzinger et al. 2002). The situation becomes increasingly more complicated when galaxy subtraction must be performed.

While it is outside the scope of this chapter to conduct a detailed comparison to quantify systematic differences between reductions of common SNe, it is instructive to do a rough comparison to what has been published in the literature as a sanity check on our pipeline reductions. We classify the level or concordance by the following definitions: "good" is an average difference within 0.05 mag, "adequate" is between 0.05 mag and 0.1 mag, and "poor" is greater than 0.1 mag. In the following comparison, we include the systematic error of 0.03 mag found in Section 2.3.5.

Comparisons to Previous LOSS Reductions

A few of the SNe included herein have been reduced manually by other members of our research group. Comparing the results from our pipeline to previously published KAIT and Nickel data offers a unique check on our pipeline without having to worry about the difficulties that arise from comparing photometry from different telescopes.

Optical light curves of SN 1998de using KAIT data were published by Modjaz et al. (2001). SN 1998de was a subluminous SN 1991bg-like object (Filippenko et al. 1992b; Leibundgut et al. 1993) located 72″ from the nucleus of its host galaxy ($cz = 4990$ km s^{-1}) in a clean environment free of galaxy contamination. Neither reduction procedure used template subtraction and both utilized PSF-fitting photometry. Our comparison-star calibrations agree to within 0.01 mag in *BVR* although our *I*-band calibration is systematically 0.03 mag brighter. The photometry published by Modjaz et al. is K-corrected and cannot be compared directly to the data presented here. We obtained the original (not K-corrected) data directly from the lead author, M. Modjaz (2010, private communication). Our results agree to within 0.01 mag in *BVR*. Our *I*-band photometry is brighter by ~ 0.05 mag, which is not entirely unexpected since our field calibration is systemically brighter in *I* by 0.03 mag.

KAIT light curves for the peculiar SN 2000cx were published by Li et al. (2001c). A bright, nearby (but peculiar) SN Ia located far from the nucleus of its host galaxy, both reductions did not perform galaxy subtraction and used PSF-fitting photometry. The *BVRI* light curves agree to within 0.03 mag. It is also worth noting that the pipeline reduction brings the KAIT data to within 0.01 mag of *BVRI* data obtained at the Wise Observatory (Israel) that were also presented by Li et al..

SN 2002bf provides an excellent test of the abilities of our pipeline. The SN lies 4.1″ from its host galaxy's center. Leonard et al. (2005) present photometry from KAIT and the Nickel telescope which were rereduced with our photometry pipeline. As is noted by the authors of Leonard et al., "the galaxy subtraction procedure for SN 2002bf was particularly challenging." In Figure 2.16 we compare our reduction to that of Leonard et al. In general, we find a systematic offset of ~ 0.1 mag in all bands; it is most pronounced in the late-time data when proper galaxy subtraction is the most necessary. The final magnitudes for both sets of comparison stars show excellent agreement. The discrepancy can probably be traced back to the galaxy subtraction. Examining the results of our pipeline, we do not see any obvious results of oversubtraction which could explain why we systematically measure the SN to be fainter than found by Leonard et al.

Leonard et al. (2005) present *BVRI* light curves of SN 2003du taken by KAIT and the Nickel telescope, but reduced manually without the use of the pipeline. The two reductions are in excellent agreement, to within 0.01 mag in *BVR* and within 0.03 mag in *I*. Our *I*-band data are systematically brighter than those published by Leonard et al.. Although this is within our definition of "good," the difference in *I* is troubling. The solution is likely traced back to the calibrations of the local standards. While there is general agreement between the new and old calibrations in *I*, our star 7 is brighter than star 6 of Leonard et al. by 0.1 mag, and our star 9 is brighter by 0.03 mag, which would make our *I*-band photometry of SN 2003du brighter. This exercise highlights the importance of calibrations in producing reliable SN flux measurements.

SN 2005cf data taken with KAIT were reduced independently by Wang et al. (2009b). The SN is sufficiently far away from the host-galaxy nucleus that galaxy subtraction was not performed by either reduction. The two reductions are in excellent agreement, with *BVRI* photometry all within 0.01 mag.

Comparison to CfA2

Jha et al. (2006b) present *UBVRI* light curves of 44 SNe Ia from the CfA2 dataset, of which 17 can be found in the LOSS sample. Of the 17, 15 have overlapping data which can be compared. We compare the two datasets by interpolating a line between LOSS data

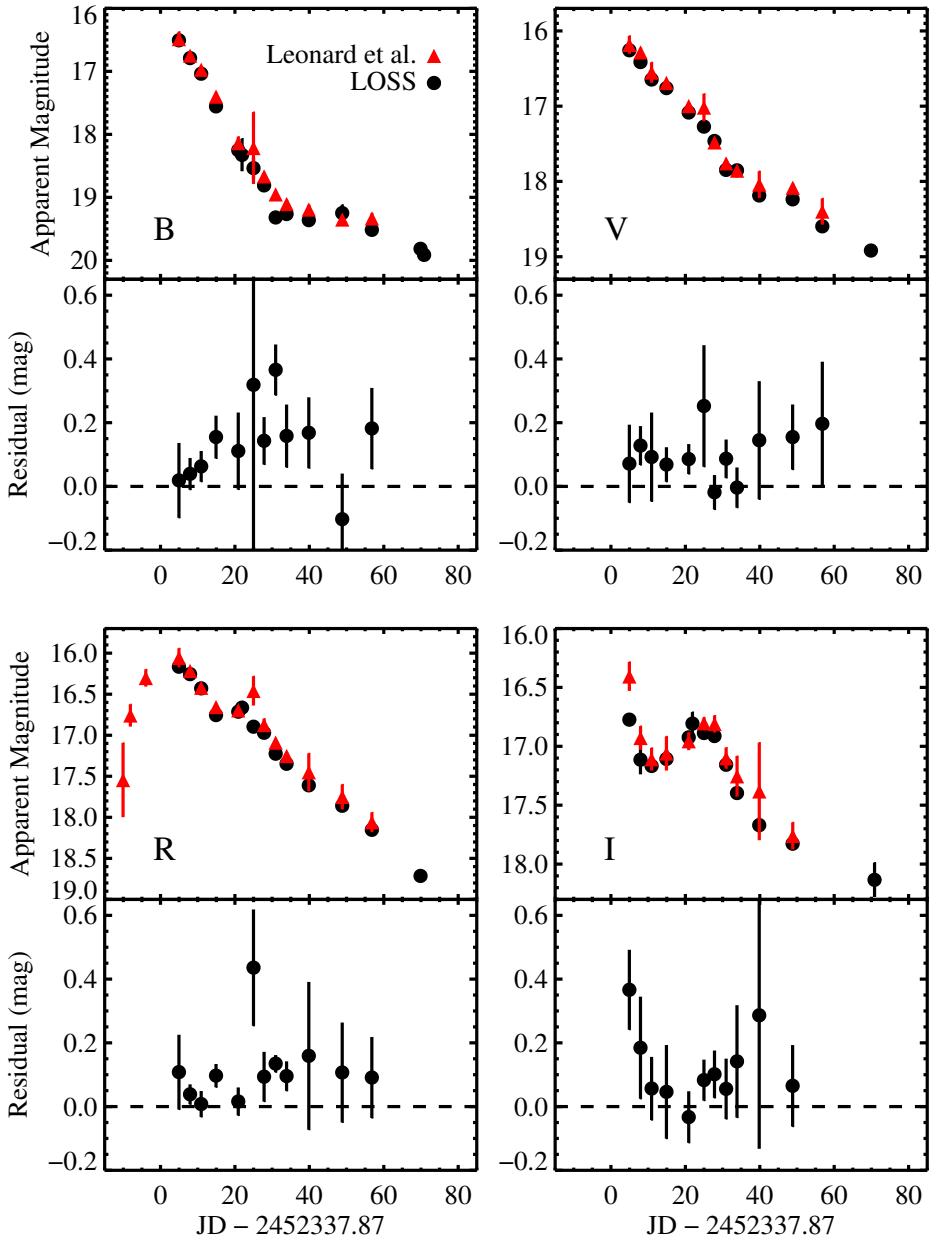

Figure 2.16: Comparison SN 2002bf photometry presented by Leonard et al. (2005) and by LOSS using the same KAIT data. SN 2002bf was only 4.1″ from the host-galaxy nucleus, providing an extreme test for our galaxy subtraction pipelines. The LOSS photometry is roughly 0.1 mag fainter in all bands. The first three *R*-band epochs from Leonard et al. (2005) are unfiltered observations which are not included in the LOSS photometry.

taken within at most 4 days from each CfA2 data point. We include a systematic error of 0.02 mag for the CfA2 data based on they systematic error found for CfA3 data (Hicken et al. 2009b).

Overall, we find good agreement between the two datasets with a few exceptions. In particular, SNe 1998dh, 1999aa, 2000cn, 1999ac, 1999dq, 1999ej, 1999gp, and 2000cn all agree to within 0.05 mag.

The worst cases of systematic differences are found in the I band. We find differences of ~ 0.1 mag for SNe 1998ef, 1998es, 1999cl, 1999gh, 2000dk, and 2000fa. With the exception of SN 1999cl, the LOSS data are systematically fainter than the CfA2 data. Comparing our derived magnitudes for the field stars to those of Jha et al., we find no discernible trend to explain the magnitude of the discrepancy.

In the case of SN 1999cl, the likely culprit is the calibration. We have only 3 comparison stars in our calibration (typically we have ~ 10 stars in a field), of which two overlap with the CfA2. Our star 2 is fainter than their star 4 by 0.07 mag. A summary of our comparison to Jha et al. can be found in Table 2.10.

The most likely solution is to apply S-corrections (Stritzinger et al. 2002) in order to account for the variation in transmission functions of different telescopes. Wang et al. (2009b) show that the scatter in the I-band light curve of SN 2005cf, combining data from 7 different telescopes, is reduced from 0.061 mag to 0.030 mag by applying S-corrections. If S-corrections are indeed the explanation of the differences between the LOSS and CfA2 data, we would expect the residual to be dependent on the spectral energy distribution of the SN. In Figures 2.17, 2.18, and 2.19, we compare the BRI residuals to $B-V$, $V-R$, and $V-I$ colors (respectively) for all of the data points in our overlapping set of SNe. In Figures 2.17 and 2.18, the B and R residuals are fairly independent of color. Subtracting the linear fit to the data points to remove any perceived linear correlation does not improve the scatter. However, doing so for the I-band residuals reduces the scatter from 0.084 to 0.075 mag, hinting that applying a color-dependent S-correction might slightly improve the situation.

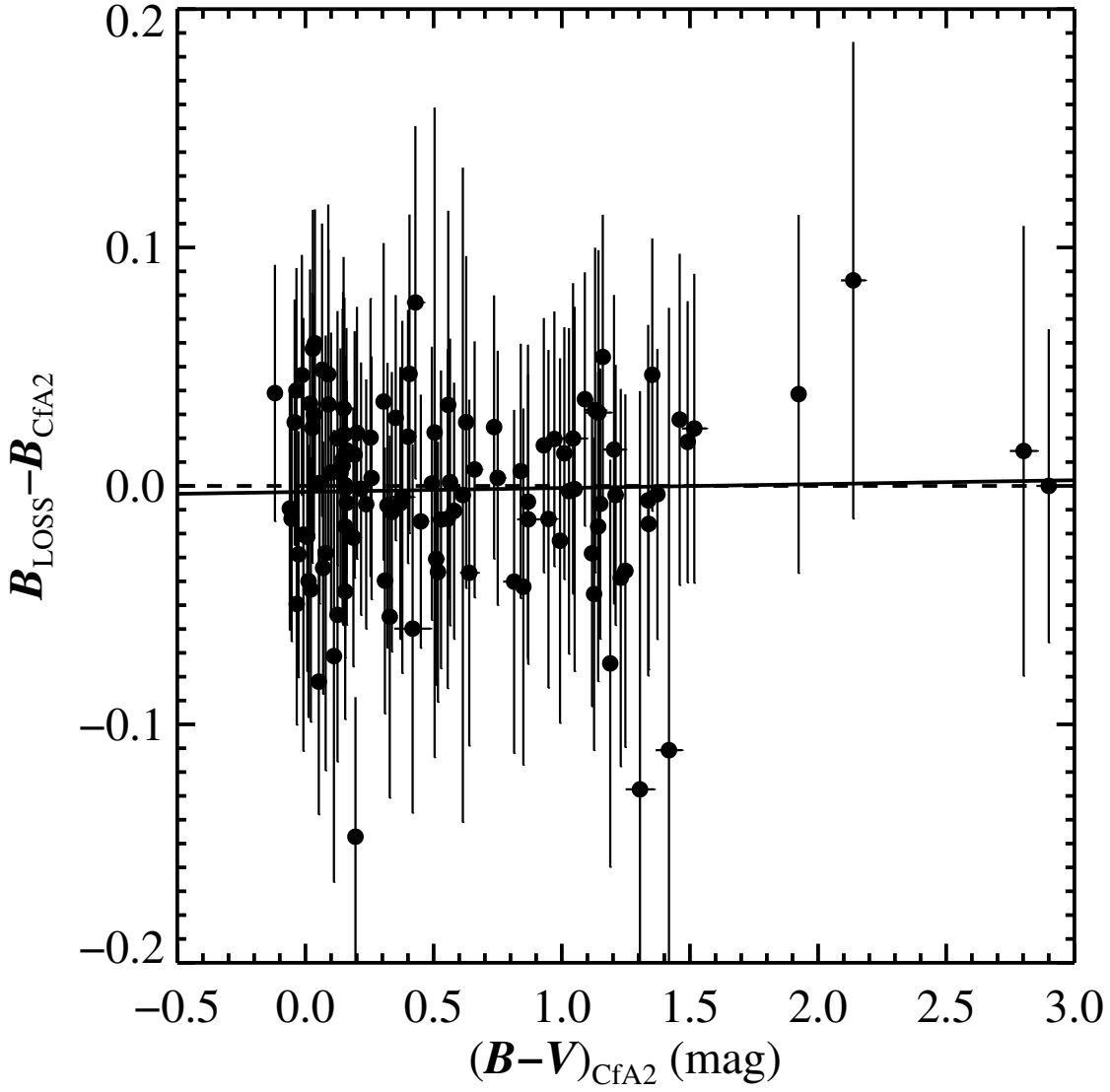

Figure 2.17: Residuals for overlapping LOSS and CfA2 data points as a function of $B-V$ color. A linear fit (solid line) to the data shows that there is not a strong relationship between the residuals and color, an indication that S-corrections will not substantially improve the agreement between data points.

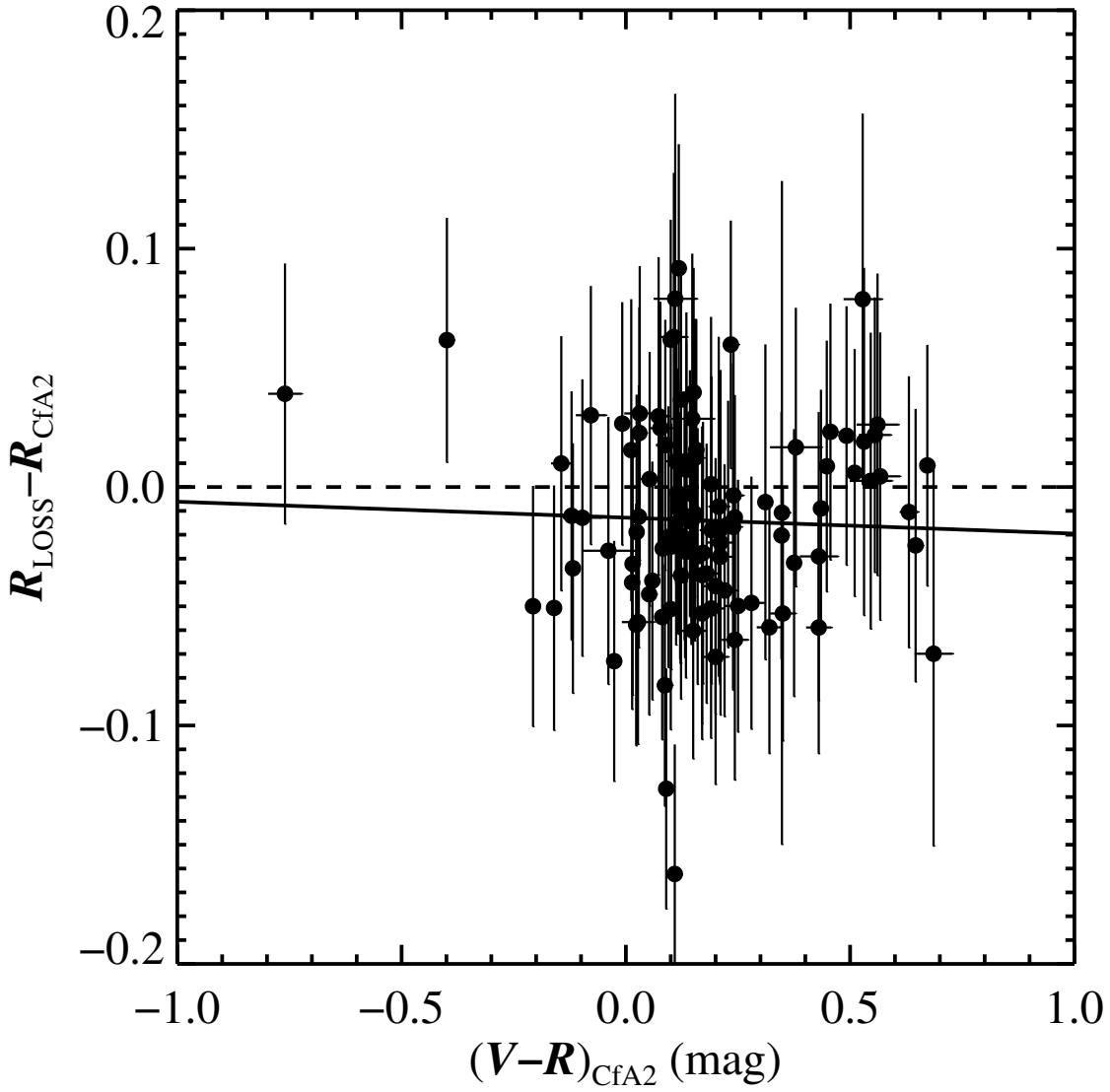

Figure 2.18: Residuals for overlapping LOSS and CfA2 data points as a function of $V - R$ color. A linear fit (solid line) to the data shows little to no relationship between residuals and color. A systematic shift of ~ 0.01 mag accounts for the difference.

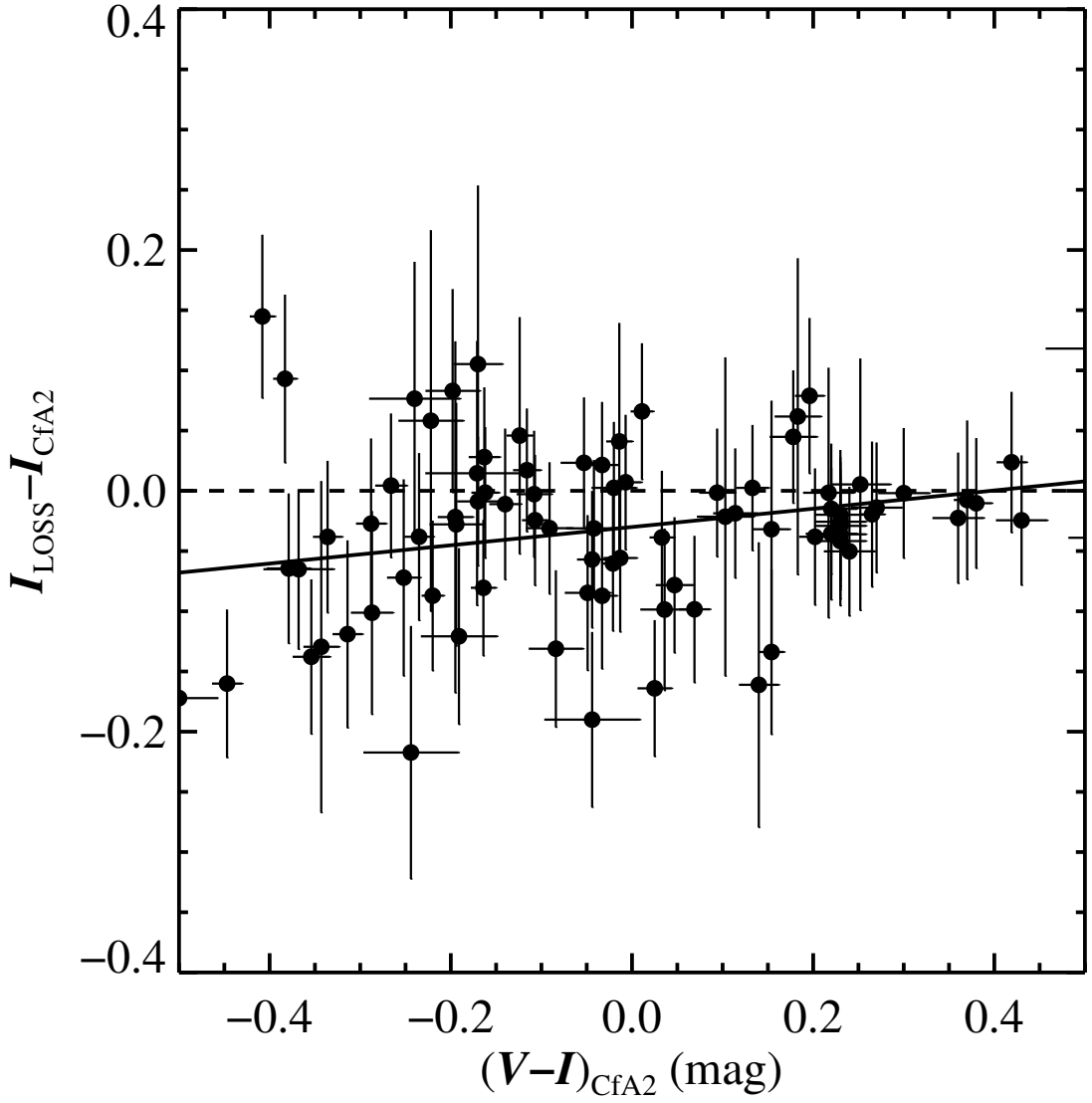

Figure 2.19: Residuals for overlapping LOSS and CfA2 data points as a function of $V - I$ color. A linear fit (solid line) to the data shows a correlation between the residuals and color, indicating that an S-correction could possibly improve the agreement between these two photometric datasets. Correcting for the linear fit reduces the scatter by 0.01 mag.

Table 2.10: Photometric Comparison with CfA2

SN	B Residual	RMS	N	V Residual	RMS	N	R Residual	RMS	N	I Residual	RMS	N
SN 1998dh	-0.003 ± 0.022	0.023	7	-0.022 ± 0.022	0.009	7	0.032 ± 0.022	0.025	6	-0.044 ± 0.022	0.066	7
SN 1998dm	-0.021 ± 0.037	0.016	4	-0.010 ± 0.037	0.030	4	0.060 ± 0.037	0.029	4	0.036 ± 0.037	0.065	4
SN 1998ef	0.001 ± 0.027	0.045	4	-0.035 ± 0.027	0.026	4	-0.074 ± 0.027	0.043	4	-0.099 ± 0.027	0.031	4
SN 1998es	0.010 ± 0.023	0.049	7	-0.043 ± 0.023	0.050	7	-0.004 ± 0.023	0.044	9	-0.126 ± 0.023	0.049	6
SN 1999aa	0.024 ± 0.021	0.022	8	-0.036 ± 0.021	0.037	8	-0.050 ± 0.021	0.011	4	-0.003 ± 0.021	0.107	5
SN 1999ac	-0.005 ± 0.022	0.021	8	-0.041 ± 0.022	0.012	8	-0.030 ± 0.022	0.025	8	0.030 ± 0.022	0.052	8
SN 1999by	0.001 ± 0.014	0.021	15	-0.022 ± 0.014	0.016	15	-0.048 ± 0.014	0.013	15	-0.023 ± 0.014	0.019	15
SN 1999cl	0.023 ± 0.027	0.028	7	0.019 ± 0.027	0.013	8	0.020 ± 0.027	0.028	6	0.105 ± 0.027	0.021	7
SN 1999dq	0.010 ± 0.013	0.019	18	-0.021 ± 0.013	0.027	19	-0.003 ± 0.013	0.023	20	-0.001 ± 0.013	0.026	19
SN 1999ej	0.026 ± 0.044	0.008	2	0.001 ± 0.044	0.014	2	-0.009 ± 0.044	0.029	2	0.021 ± 0.044	0.035	2
SN 1999gh	-0.055 ± 0.058	0.025	2	0.038 ± 0.058	0.018	2	0.016 ± 0.058	0.010	2	0.111 ± 0.058	0.025	2
SN 1999gp	-0.061 ± 0.027	0.048	6	-0.018 ± 0.027	0.056	6	-0.045 ± 0.027	0.059	6	-0.006 ± 0.027	0.035	6
SN 2000cn	0.026 ± 0.021	0.049	12	0.036 ± 0.021	0.018	12	0.014 ± 0.021	0.032	12	0.032 ± 0.021	0.049	12
SN 2000dk	-0.033 ± 0.020	0.025	8	-0.001 ± 0.020	0.026	8	-0.018 ± 0.020	0.026	8	-0.095 ± 0.020	0.051	8
SN 2000fa	-0.016 ± 0.027	0.055	6	-0.009 ± 0.027	0.042	6	-0.019 ± 0.027	0.020	6	-0.108 ± 0.027	0.030	6

The calculated mean residuals (mag) are LOSS minus CfA2.

SN 2002bo

Krisciunas et al. (2004b) present optical photometry of SN 2002bo. We find that our photometry is in good agreement; *VRI* measurements agree to within 0.03 mag while B is within 0.04 mag.

SN 2003du

Stanishev et al. (2007) present extensive *UBVRI* photometry of SN 2003du in the nearby galaxy UGC 09391. Our *BVRI* light curves start around $B_{\max}$, about ten days after those of Stanishev et al.. Overall, the agreement between the two datasets is excellent. We share over 20 epochs in common and find that our light curves are within 0.03 mag in *BVR* and 0.05 mag in I. The light curves from Stanishev et al. are S-corrected, perhaps explaining the measured difference in the I band.

Anupama et al. (2005) also present optical photometry of SN 2003du, and we share ~ 30 overlapping epochs. Our *BVR* light curves are systematically brighter by ~ 0.05 mag while I is in excellent agreement to within 0.01 mag. The discrepancy in *BVR* between the two reductions can be traced back to calibrations for the local field standards. There are four overlapping comparison stars which we measure to be systematically brighter by ~ 0.05 mag, once again underscoring the importance of consistent calibrations.

CfA3

The most recent release from the Center for Astrophysics, CfA3, roughly doubles the number of published nearby SN Ia light curves (Hicken et al. 2009b). CfA3 data obtained during 2001–2004 were taken in *UBVRI* , while subsequent data were in $UBVr'i'$. We share 69 SNe in common with CfA3. Combining the two datasets gives close to 260 SNe Ia with well-sampled light curves which could be used for cosmology. In this section we compare the LOSS dataset with the CfA3 dataset, the two largest existing samples of nearby SNe Ia, to study any trends that arise. We include a systematic error of 0.02 mag for CfA3 data as suggested by Hicken et al. (2009b).

Similar to our comparison with CfA2, we compare individual CfA3 points with a linear interpolation to adjacent LOSS points that are within 4 days of one another. Of the 69 SNe in common, we can compare 67 *BV* light curves and 33 *RI* light curves. Table 2.11 provides the error-weighted mean residuals for individual SNe. To study the residuals in more detail, we plot the residuals for all of our data-point comparisons as a function of SN phase in Figure 2.20. Ideally, if we are not plagued by systematic errors from differences in calibrations or galaxy subtraction, we expect the mean residual to be ~ 0 mag with a reasonable scatter

($\sigma \approx 0.05$ mag). We find the mean residual in B to be -0.013 mag with $\sigma = 0.114$ mag, in V to be 0.010 mag with $\sigma = 0.094$ mag, in R to be -0.014 mag with $\sigma = 0.071$ mag, and in I to be 0.018 mag with $\sigma = 0.074$ mag (see Table 2.12). This rather high level of scatter is fairly troubling considering that the sample is of bright, nearby SNe Ia! If we limit our comparison to data points brighter than mag 18, the scatter in all bands is reduced to a more reasonable $\sigma \approx 0.06$–0.07 mag (see Table 2.13 for details), implying that the two groups have a decent level of agreement around maximum light. The disagreement at later phases could be caused by the increased importance of proper galaxy subtraction, the inherent difficulty in measuring faint objects, or the growing importance of S-corrections at late times as the spectral energy distribution of the SN becomes increasingly nonstellar.

While restricting our comparison to points brighter than mag 18 provides a significant improvement, the question now becomes whether this level of scatter is randomly distributed over all data points for all of the overlapping SNe, or is a result of systematic differences in individual SNe which could be introduced through improper galaxy subtraction or differences in field calibrations. In Figure 2.21, we construct a histogram of mean residuals as a function of the number of SNe. We color code SN mean residuals computed with more than three data points blue and fewer reliable mean residuals computed with three or less data points red. The only distribution which appears Gaussian is the V band, although there are clearly outliers which indicate SNe that suffer from a systematic offset. The BI histograms are not centered at 0 mag, while the RI histograms do not seem convincingly Gaussian.

The following SNe deserve special attention as being clear outliers: SN 2001V in B and SN 2006eu in B and V. For SN 2001V, the disagreement is tied to the differences in the local standard stars. We share two overlapping stars with CfA3 which we measure to be systematically fainter by 0.15 mag in B, thus explaining why we find the SN to be fainter by ~ 0.13 mag in B. Surprisingly, comparing our local standards does not offer an explanation for the large discrepancies in SN 2006eu. We share four overlapping standards with CfA3 and we measure the stars to be fainter by ~ 0.106 mag in B and brighter by 0.01 mag in V. This does not explain why LOSS measures SN 2006eu to be systematically fainter by 0.30 mag in B and 0.46 mag in V.

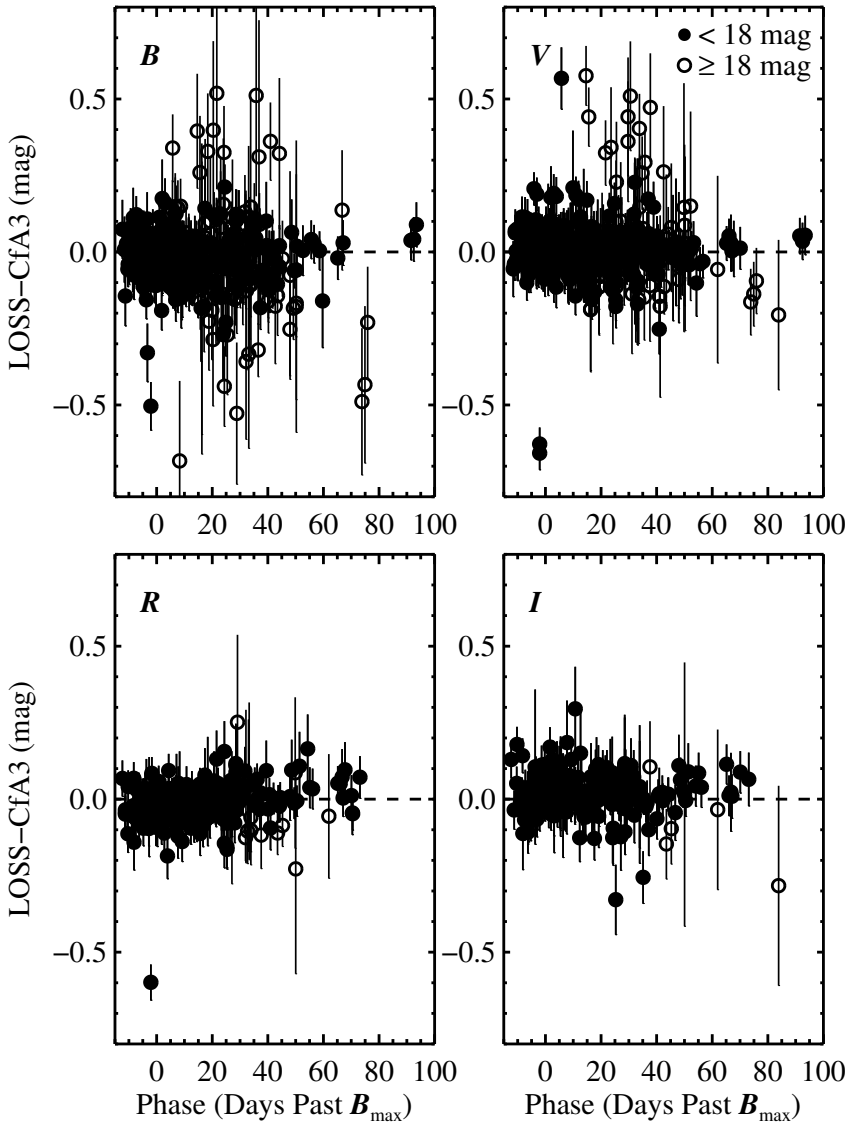

Figure 2.20: LOSS−CfA3 residuals for all comparison data points as a function of SN phase. Our data generally agree close to maximum light but grow discordant at late times. This is especially pronounced in B and V. If we restrict our comparison to points brighter than mag 18 (plotted in filled circles), we reduce the scatter significantly.

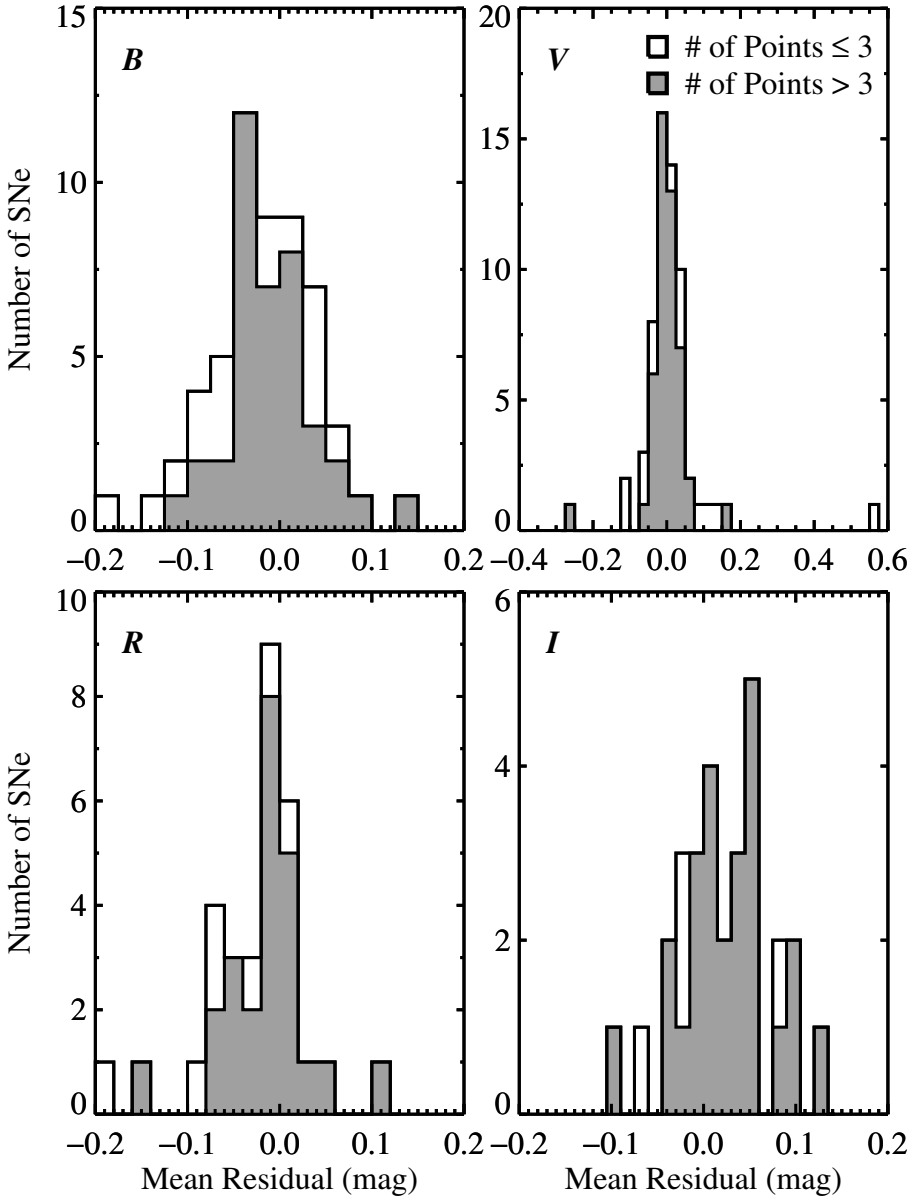

Figure 2.21: Histogram of the mean residual between CfA3 and LOSS data for individual SNe. Red indicates SNe with mean residuals calculated using three or fewer points and blue indicates SNe with mean residuals calculated using more than three points. The asymmetric shape and offset from zero indicate systematic differences between individual SNe.

Table 2.11: Photometric Comparison with CfA3

SN	B Residual	RMS	N	V Residual	RMS	N	R Residual	RMS	N	I Residual	RMS	N
SN 2001V	0.127 ± 0.028	0.040	9	-0.003 ± 0.025	0.044	11	0.102 ± 0.033	0.029	10	0.090 ± 0.029	0.018	7
SN 2001ah	···	···	0	0.101 ± 0.193	···	1	0.052 ± 0.124	0.130	4	···	···	0
SN 2001ay	-0.044 ± 0.037	0.055	5	-0.032 ± 0.027	0.010	8	-0.014 ± 0.027	0.021	8	0.053 ± 0.038	0.048	6
SN 2001bf	0.010 ± 0.021	0.013	7	0.008 ± 0.018	0.014	8	0.004 ± 0.019	0.013	8	0.007 ± 0.021	0.015	7
SN 2001cp	0.036 ± 0.066	···	1	-0.068 ± 0.036	0.125	3	-0.077 ± 0.035	0.109	3	-0.068 ± 0.063	0.266	2
SN 2001da	-0.009 ± 0.042	0.013	2	-0.067 ± 0.033	0.045	3	-0.082 ± 0.043	0.040	2	-0.019 ± 0.038	0.032	3
SN 2001eh	-0.012 ± 0.020	0.062	11	0.038 ± 0.017	0.038	13	-0.031 ± 0.017	0.025	12	-0.022 ± 0.023	0.111	11
SN 2001en	-0.040 ± 0.031	0.041	4	0.021 ± 0.027	0.023	4	-0.009 ± 0.028	0.011	4	0.056 ± 0.029	0.030	5
SN 2001ep	-0.031 ± 0.022	0.066	8	0.018 ± 0.016	0.022	12	0.007 ± 0.015	0.035	14	0.046 ± 0.017	0.016	12
SN 2001fh	-0.176 ± 0.043	0.268	3	-0.267 ± 0.025	0.360	5	-0.144 ± 0.029	0.302	4	-0.043 ± 0.030	0.017	4
SN 2002G	0.155 ± 0.215	···	1	-0.005 ± 0.097	···	1	-0.066 ± 0.082	···	1	0.086 ± 0.118	···	1
SN 2002bf	···	···	0	0.115 ± 0.062	···	1	0.019 ± 0.033	0.046	3	0.050 ± 0.041	0.133	5
SN 2002bo	-0.036 ± 0.018	0.066	12	-0.023 ± 0.017	0.027	10	-0.004 ± 0.015	0.048	14	0.024 ± 0.016	0.041	12
SN 2002cd	0.015 ± 0.037	0.057	5	-0.007 ± 0.026	0.028	5	-0.003 ± 0.026	0.014	5	0.081 ± 0.028	0.030	5
SN 2002cr	0.030 ± 0.019	0.021	8	0.001 ± 0.018	0.018	8	0.008 ± 0.018	0.032	8	-0.011 ± 0.018	0.023	8
SN 2002de	0.007 ± 0.028	0.011	4	0.059 ± 0.024	0.021	5	-0.042 ± 0.024	0.009	5	0.121 ± 0.029	0.036	5
SN 2002dj	-0.041 ± 0.017	0.012	12	0.018 ± 0.017	0.023	10	0.029 ± 0.019	0.037	8	0.090 ± 0.020	0.049	8
SN 2002do	0.038 ± 0.033	0.149	5	-0.025 ± 0.029	0.045	6	-0.012 ± 0.028	0.076	6	0.011 ± 0.027	0.027	7
SN 2002dp	-0.082 ± 0.023	0.059	7	-0.036 ± 0.018	0.056	10	-0.047 ± 0.020	0.035	9	0.038 ± 0.018	0.029	10
SN 2002eu	-0.067 ± 0.087	···	1	0.086 ± 0.068	···	1	-0.032 ± 0.044	0.004	2	0.027 ± 0.112	···	1
SN 2002fb	-0.105 ± 0.049	0.106	5	-0.009 ± 0.034	0.112	8	-0.042 ± 0.031	0.074	8	-0.014 ± 0.032	0.092	10
SN 2002fk	0.046 ± 0.020	0.052	8	0.019 ± 0.017	0.021	11	0.044 ± 0.015	0.029	15	0.015 ± 0.015	0.047	16
SN 2002ha	-0.031 ± 0.025	0.071	6	0.018 ± 0.024	0.030	6	0.011 ± 0.026	0.033	5	0.046 ± 0.024	0.038	6
SN 2002he	-0.021 ± 0.023	0.017	8	-0.045 ± 0.020	0.055	9	-0.052 ± 0.021	0.033	9	-0.093 ± 0.028	0.024	6
SN 2003D	···	···	0	-0.080 ± 0.154	0.073	2	-0.117 ± 0.110	···	1	0.106 ± 0.149	···	1
SN 2003W	0.021 ± 0.021	0.122	11	-0.029 ± 0.019	0.084	10	-0.005 ± 0.019	0.068	10	0.032 ± 0.019	0.062	14
SN 2003cg	0.013 ± 0.030	0.045	4	0.020 ± 0.022	0.012	6	0.007 ± 0.025	0.029	5	0.043 ± 0.026	0.025	4
SN 2003cq	···	···	0	-0.085 ± 0.061	0.131	3	-0.144 ± 0.060	0.139	3	···	···	0
SN 2003du	-0.001 ± 0.024	0.034	5	0.017 ± 0.015	0.022	12	-0.007 ± 0.013	0.026	18	0.017 ± 0.021	0.039	7
SN 2003fa	-0.067 ± 0.016	0.108	15	-0.008 ± 0.014	0.039	18	-0.063 ± 0.014	0.037	20	-0.041 ± 0.021	0.064	15
SN 2003kf	-0.041 ± 0.031	0.055	5	0.009 ± 0.028	0.019	4	-0.015 ± 0.027	0.015	4	0.001 ± 0.026	0.036	5
SN 2004as	-0.022 ± 0.036	0.017	3	-0.012 ± 0.027	0.040	6	-0.077 ± 0.026	0.048	6	-0.011 ± 0.036	0.034	6
SN 2004bg	-0.080 ± 0.027	0.110	7	-0.009 ± 0.019	0.038	11	-0.034 ± 0.020	0.041	10	-0.019 ± 0.042	0.021	3
SN 2004ef	-0.083 ± 0.041	0.167	3	-0.058 ± 0.033	0.055	5	···	···	0	···	···	0
SN 2005M	···	···	0	0.007 ± 0.041	0.006	2	···	···	0	···	···	0
SN 2005am	0.003 ± 0.015	0.082	16	-0.018 ± 0.013	0.033	18	···	···	0	···	···	0
SN 2005cf	0.017 ± 0.012	0.017	18	-0.020 ± 0.012	0.022	19	···	···	0	···	···	0
SN 2005el	-0.051 ± 0.018	0.061	17	0.026 ± 0.013	0.026	18	···	···	0	···	···	0

Continued on Next Page ...

Table 2.11 –Continued

SN	B Residual	RMS	N	V Residual	RMS	N	R Residual	RMS	N	I Residual	RMS	N
SN 2005eq	-0.084 ± 0.021	0.046	9	-0.046 ± 0.016	0.043	14	···	···	0	···	···	0
SN 2005eu	-0.089 ± 0.056	0.318	5	0.077 ± 0.021	0.154	15	···	···	0	···	···	0
SN 2005na	-0.109 ± 0.043	0.081	4	-0.060 ± 0.032	0.043	5	···	···	0	···	···	0
SN 2006D	-0.060 ± 0.054	0.081	2	0.038 ± 0.037	0.003	2	···	···	0	···	···	0
SN 2006X	0.081 ± 0.036	0.029	4	0.040 ± 0.023	0.049	7	···	···	0	···	···	0
SN 2006ac	-0.091 ± 0.065	0.180	2	-0.106 ± 0.071	0.063	2	···	···	0	···	···	0
SN 2006bt	-0.052 ± 0.036	0.045	9	-0.011 ± 0.031	0.063	10	···	···	0	···	···	0
SN 2006cp	-0.028 ± 0.036	0.034	5	-0.025 ± 0.039	0.024	4	···	···	0	···	···	0
SN 2006ef	0.041 ± 0.046	0.155	7	0.034 ± 0.042	0.054	5	···	···	0	···	···	0
SN 2006ej	0.055 ± 0.073	0.174	3	0.121 ± 0.040	0.101	3	···	···	0	···	···	0
SN 2006em	-0.483 ± 0.207	0.308	3	-0.078 ± 0.055	0.087	9	···	···	0	···	···	0
SN 2006en	-0.158 ± 0.039	0.151	6	-0.018 ± 0.034	0.041	7	···	···	0	···	···	0
SN 2006eu	0.285 ± 0.069	0.147	5	0.457 ± 0.043	0.118	9	···	···	0	···	···	0
SN 2006gr	-0.026 ± 0.021	0.018	9	-0.005 ± 0.019	0.033	10	···	···	0	···	···	0
SN 2006hb	···	···	0	-0.021 ± 0.021	0.036	13	···	···	0	···	···	0
SN 2006je	0.257 ± 0.126	0.156	3	0.000 ± 0.066	0.074	3	···	···	0	···	···	0
SN 2006le	-0.003 ± 0.017	0.034	15	0.029 ± 0.014	0.035	18	···	···	0	···	···	0
SN 2006lf	0.066 ± 0.025	0.065	13	-0.007 ± 0.017	0.070	18	···	···	0	···	···	0
SN 2007O	0.015 ± 0.045	0.173	3	0.088 ± 0.035	0.078	5	···	···	0	···	···	0
SN 2007af	0.008 ± 0.010	0.036	32	0.024 ± 0.011	0.021	23	···	···	0	···	···	0
SN 2007au	0.062 ± 0.027	0.098	8	0.029 ± 0.032	0.030	8	···	···	0	···	···	0
SN 2007bc	-0.032 ± 0.019	0.048	12	-0.008 ± 0.018	0.020	10	···	···	0	···	···	0
SN 2007ca	-0.104 ± 0.028	0.014	4	-0.065 ± 0.024	0.027	5	···	···	0	···	···	0
SN 2007ci	0.071 ± 0.024	0.034	7	0.065 ± 0.019	0.037	13	···	···	0	···	···	0
SN 2007co	-0.016 ± 0.014	0.052	20	0.021 ± 0.012	0.049	25	···	···	0	···	···	0
SN 2007cq	-0.015 ± 0.022	0.192	10	0.031 ± 0.017	0.081	12	···	···	0	···	···	0
SN 2007qe	0.027 ± 0.015	0.015	18	-0.001 ± 0.020	0.022	7	···	···	0	···	···	0
SN 2007sr	0.013 ± 0.013	0.022	19	-0.014 ± 0.015	0.026	12	···	···	0	···	···	0
SN 2008bf	-0.041 ± 0.020	0.096	15	0.173 ± 0.018	0.045	13	···	···	0	···	···	0

The calculated mean residuals (mag) are LOSS minus CfA3.

Table 2.12: Summary of CfA3 Comparison Analyzed as an Ensemble

Filter	Mean (mag)	Standard Deviation	Error-Weighted Mean
B	-0.016 ± 0.005	0.114	-0.009 ± 0.003
V	0.010 ± 0.004	0.094	0.006 ± 0.003
R	-0.014 ± 0.005	0.071	-0.015 ± 0.004
I	0.018 ± 0.005	0.074	0.022 ± 0.004

Note. – The calculated mean residuals (mag) are LOSS minus CfA3.

Table 2.13: Summary of Bright CfA3 Comparison Analyzed as an Ensemble

Filter	Mean (mag)	Standard Deviation	Error-Weighted Mean
B	-0.011 ± 0.006	0.069	-0.008 ± 0.003
V	0.006 ± 0.004	0.072	0.005 ± 0.003
R	-0.012 ± 0.005	0.067	-0.014 ± 0.004
I	0.021 ± 0.005	0.070	0.022 ± 0.004

Note. – The calculated mean residuals (mag) are LOSS minus CfA3. Only data points brighter than mag 18 are used.

2.4.3 LOSS in the Wild

A few individual SN Ia light curves presented here have already been published in other papers. LOSS data for SN 2004eo reduced with the pipeline appeared in Pastorello et al. (2007a) and data for SN 2002cx were supplied for Phillips et al. (2007). The LOSS reduction of SN 2002fk is in Riess et al. (2009) as a means to calibrate the SN distance ladder using Cepheid variables in NGC 1309. Data for SN 2003hv, reduced using our pipeline, were also presented by Leloudas et al. (2009).

2.5 Discussion

A major goal in SN Ia science is to use their multi-color light curves to calibrate SNe Ia as cosmological distance indicators. As discussed in Section 2.4.1, this requires a large number of objects with well-sampled light curves that cover from before $B_{\max}$ to a month past. Our sample presents a self-contained dataset which can be analyzed on its own and in comparison with other overlapping datasets to study the effects of systematics. In this section we explore the properties of our light curves in more detail. We note that the light-curve properties derived here do not include the systematic error of 0.03 mag found in Section 2.3.5.

2.5.1 Light-Curve Properties

The "width" of a light curve is an important parameter which has been shown to correlate very well with absolute peak brightness. One incarnation of this parameter is Δm_{15}, the difference between the SN magnitude at maximum light and 15 days past maximum light. We measure this quantity for both B and V using a template-fitting routine similar to that discussed by Prieto et al. (2006). We fit each band individually. Templates are constructed using light curves from our database that span the range of Δm_{15} and are well sampled. The data are K-corrected and corrected for Milky Way extinction (Schlegel et al. 1998). A fifth-order polynomial is fit to each template light curve to determine the date of maximum light. The light curves are shifted such that $t = 0$ is at maximum light and corrected for time dilation. Template light curves are constructed by fitting cubic splines between a range of -5 to 35 days past maximum light in each band. Lacking a SN 1991bg-like template, we augment our sample with the template of SN 1991bg from Prieto et al. (2006), which draws from photometry published by Hamuy et al. (1996b), Filippenko et al. (1992b), and Leibundgut et al. (1993). Our B templates are in the range $0.73 \leq \Delta m_{15} \leq 1.93$ mag and our V templates have $0.507 \leq \Delta m_{15} \leq 1.420$ mag.

We construct model light curves of varying Δm_{15} by taking linear combinations of our templates using the weighting scheme prescribed by Prieto et al. (2006) and calculating χ^2 to find the best fit. We use a triangle function to determine the weights of each template to construct models of varying Δm_{15}. For a given Δm_{15}^0, the weighting function is defined such that the triangle peaks at Δm_{15}^0 (the extinction-corrected value of Δm_{15}) with a weight of 1 and falls symmetrically to 0 linearly over a range of Δm_{15} of width γ,

$$w_i = \begin{cases} 1 - \frac{2}{\gamma}|\Delta m_{15,i} - \Delta m_{15}^0| & \text{for } |\Delta m_{15,i} - \Delta m_{15}^0| \leq \gamma/2 \\ 0 & \text{for } |\Delta m_{15,i} - \Delta m_{15}^0| > \gamma/2. \end{cases}$$

Templates with $\Delta m_{15,i} > \Delta m_{15}^0 + \gamma/2$ (that is, those templates that are the least like Δm_{15}^0)

are suppressed from contributing to the model. The model for a light curve of width Δm_{15}^0 in band X, $T^X(\Delta m_{15}^0)$, is given by

$$T^X(\Delta m_{15}^0) = \frac{\sum_{i=0}^{N} w_i T_i^X}{\sum_{i=0}^{N} w_i},$$

where T_i is the template light curve associated with $\Delta m_{15,i}$ in band X. We increase γ with increasing values of Δm_{15} to reflect the sampling of Δm_{15} in our light-curve templates. The results are visually inspected to ensure that a good fit is obtained. In cases where Δm_{15} runs close to endpoints in the template range of Δm_{15} or we could not obtain a good fit, we instead fit a fifth-order polynomial to the data. The final results of our template and polynomial fits are presented in Tables 2.14. As a check on the reliability of our template fits, we compare the results between polynomial fitting and template fitting and find that they agree to within the error bars in instances where good fits can be obtained for both.

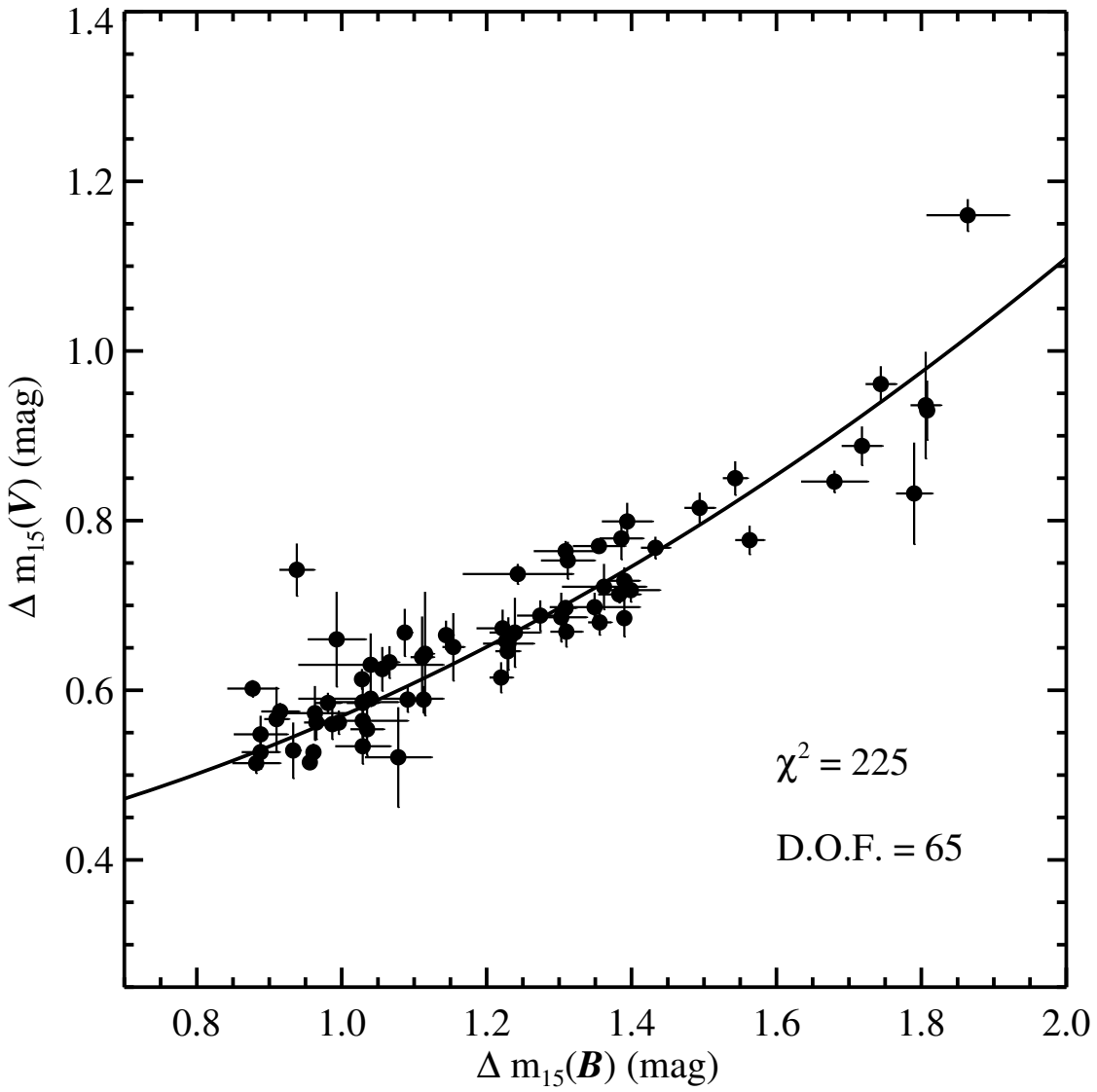

Figure 2.22: Measurements of $\Delta m_{15}(B)$ plotted against $\Delta m_{15}(V)$. We fit the data with a quadratic polynomial.

Table 2.14: Light-Curve Measurements

SN	$t_{B_{\max}} - 2400000$	$B_{\max}$	$\Delta m_{15}(B)$	$t_{V_{\max}} - 2400000$	$V_{\max}$	$\Delta m_{15}(V)$	$(B-V)_{B_{\max}}$	Fit[a]
SN 1998dh	51029.35(0.50)	13.847(031)	1.227(033)	51031.25(0.50)	13.789(030)	0.658(033)	0.034(031)	T
SN 1998dm	51060.45(0.55)	14.680(033)	0.848(049)	51061.58(0.51)	14.377(031)	0.570(032)	0.303(034)	P
SN 1998ef	51113.60(0.51)	14.810(034)	1.303(046)	51115.16(0.51)	14.864(033)	0.686(042)	−0.072(037)	T
SN 1998es	51143.79(0.51)	13.749(037)	0.978(032)	51144.30(0.51)	13.691(036)	0.575(033)	0.056(042)	T
SN 1999ac	51249.44(0.51)	14.051(032)	1.182(033)	51252.01(0.52)	14.054(031)	0.607(033)	−0.038(033)	P
SN 1999by	51308.21(0.50)	13.576(032)	1.899(031)	51310.90(0.50)	13.089(031)	1.259(030)	0.412(032)	T
SN 1999cl	51341.84(0.50)	14.882(031)	1.144(032)	51343.86(0.50)	13.735(031)	0.665(034)	1.123(032)	T
SN 1999cp	51363.83(0.50)	13.918(030)	1.028(032)	51364.65(0.50)	13.960(031)	0.613(032)	−0.047(031)	T
SN 1999da	51369.80(0.53)	16.570(034)	1.975(062)	51372.55(0.52)	16.020(031)	1.211(054)	0.450(039)	P
SN 1999dg	51393.26(0.62)	15.907(037)	1.414(112)	51395.30(0.59)	15.956(037)	0.815(064)	−0.083(043)	T
SN 1999dk	51415.02(0.52)	14.754(034)	1.154(034)	51416.74(0.53)	14.730(034)	0.651(050)	0.003(037)	T
SN 1999dq	51436.45(0.50)	14.367(031)	0.961(031)	51437.66(0.50)	14.316(030)	0.527(032)	0.040(032)	T
SN 1999ej	51483.74(0.52)	15.355(031)	1.582(034)	51485.10(0.50)	15.389(030)	0.832(035)	−0.050(031)	T
SN 1999gp	51550.99(0.54)	15.930(031)	0.908(040)	51552.24(0.52)	15.976(031)	0.534(034)	−0.056(032)	T
SN 2000cn	51707.39(0.51)	16.526(032)	1.680(055)	51708.83(0.50)	16.444(031)	0.846(033)	0.063(033)	T
SN 2000cu	51744.68(0.51)	15.877(034)	1.563(036)	51746.11(0.51)	15.887(031)	0.777(034)	−0.027(034)	T
SN 2000cw	51748.55(0.50)	16.651(031)	1.310(037)	51750.29(0.51)	16.702(031)	0.669(035)	−0.072(031)	T
SN 2000cx	51752.27(0.50)	13.036(030)	0.960(032)	51754.45(0.52)	12.967(030)	0.835(031)	−0.952(031)	P
SN 2000dk	51812.68(0.50)	15.260(031)	1.718(041)	51813.96(0.50)	15.322(031)	0.888(038)	−0.079(032)	T
SN 2000dm	51816.39(0.57)	14.995(036)	1.562(051)	51817.46(0.51)	15.093(030)	0.803(036)	−0.111(037)	T
SN 2000dn	51824.80(0.51)	16.569(033)	1.115(032)	51826.65(0.52)	16.642(033)	0.643(079)	−0.092(036)	T
SN 2000dr	51833.98(0.54)	15.932(033)	1.744(037)	51836.40(0.52)	15.867(031)	0.961(037)	0.019(033)	T
SN 2000fa	51891.47(0.54)	15.827(033)	0.910(034)	51893.38(0.67)	15.803(035)	0.566(048)	0.007(037)	T
SN 2001bf	52045.32(0.50)	14.642(031)	0.933(032)	52045.95(0.52)	14.695(032)	0.529(045)	−0.058(034)	T
SN 2001br	52053.02(0.55)	16.235(032)	1.346(058)	52054.43(0.55)	16.147(031)	0.776(038)	0.067(033)	T
SN 2001cj	52066.04(0.53)	15.802(031)	0.965(034)	52067.33(0.52)	15.935(031)	0.562(036)	−0.141(032)	T
SN 2001ck	52073.02(0.70)	16.693(039)	1.058(122)	52073.98(0.59)	16.771(034)	0.595(067)	−0.085(044)	P
SN 2001cp	52089.26(0.53)	15.602(032)	0.915(040)	52089.89(0.51)	15.634(031)	0.575(032)	−0.035(033)	T
SN 2001da	52107.72(0.53)	15.482(032)	1.230(046)	52109.89(0.51)	15.325(031)	0.655(043)	0.130(032)	T
SN 2001dl	52131.47(0.53)	16.833(034)	0.981(035)	52132.38(0.51)	16.590(031)	0.585(032)	0.239(034)	T

Continued on Next Page . . .

Table 2.14 –Continued

SN	$t_{B_{\max}} - 2400000$	$B_{\max}$	$\Delta m_{15}(B)$	$t_{V_{\max}} - 2400000$	$V_{\max}$	$\Delta m_{15}(V)$	$(B-V)_{B_{\max}}$	Fit[a]
SN 2001eh	52168.93(0.56)	16.556(032)	0.811(042)	52171.01(0.54)	16.656(031)	0.504(034)	−0.110(033)	P
SN 2001en	52193.02(0.50)	15.009(031)	1.274(044)	52194.24(0.50)	15.046(031)	0.688(035)	−0.050(031)	T
SN 2001ep	52199.85(0.50)	14.839(030)	1.356(034)	52201.71(0.50)	14.833(030)	0.680(034)	−0.019(031)	T
SN 2002G	52299.52(0.91)	17.621(039)	1.384(116)	52302.21(0.74)	17.323(048)	0.825(067)	0.243(054)	T
SN 2002bo	52357.50(0.52)	13.924(041)	1.194(053)	52359.20(0.52)	13.526(034)	0.702(036)	0.374(044)	T
SN 2002cd	52383.66(0.67)	15.574(034)	0.794(034)	52386.40(0.58)	14.941(034)	0.526(060)	0.601(037)	T
SN 2002cf	52384.90(0.55)	16.639(036)	1.864(064)	52387.12(0.56)	16.244(042)	1.160(036)	0.353(047)	T
SN 2002cr	52408.83(0.51)	14.160(031)	1.229(034)	52410.22(0.52)	14.206(031)	0.646(042)	−0.061(032)	T
SN 2002cs	52409.64(0.52)	15.047(033)	1.029(048)	52411.55(0.51)	15.096(032)	0.534(037)	−0.066(034)	T
SN 2002cu	52416.60(0.50)	16.097(032)	1.433(036)	52418.21(0.50)	16.090(031)	0.768(033)	−0.016(033)	T
SN 2002de	52433.61(0.50)	16.653(030)	0.996(031)	52435.20(0.51)	16.595(031)	0.562(033)	0.043(031)	T
SN 2002dj	52450.74(0.50)	13.903(031)	1.087(032)	52452.63(0.51)	13.828(032)	0.668(041)	0.053(033)	T
SN 2002dl	52452.57(0.50)	15.780(031)	1.808(031)	52454.30(0.50)	15.677(030)	0.930(046)	0.077(031)	T
SN 2002do	52442.69(1.44)	15.481(109)	1.708(159)	52445.47(0.70)	15.507(032)	0.989(039)	−0.096(110)	T
SN 2002dp	52451.34(0.51)	14.452(031)	1.296(036)	52452.87(0.51)	14.427(031)	0.676(036)	0.009(033)	T
SN 2002eb	52494.59(0.50)	15.961(030)	0.987(030)	52496.14(0.50)	16.074(030)	0.531(031)	−0.125(031)	T
SN 2002ef	52491.51(0.57)	16.666(031)	1.040(104)	52492.65(0.51)	16.351(030)	0.630(048)	0.309(032)	T
SN 2002el	52508.76(0.50)	16.082(032)	1.390(037)	52510.03(0.50)	16.175(032)	0.729(034)	−0.107(034)	T
SN 2002er	52524.77(0.50)	14.174(031)	1.309(034)	52526.64(0.50)	14.066(031)	0.697(031)	0.084(031)	T
SN 2002fk	52548.15(0.50)	13.129(031)	1.075(031)	52548.84(0.51)	13.251(031)	0.607(032)	−0.123(031)	P
SN 2002ha	52581.43(0.51)	14.689(032)	1.355(047)	52582.64(0.50)	14.782(030)	0.770(031)	−0.104(033)	T
SN 2002he	52586.40(0.51)	16.183(035)	1.494(037)	52587.38(0.50)	16.224(032)	0.815(035)	−0.050(037)	T
SN 2002jg	52610.19(0.50)	17.150(032)	1.475(039)	52611.82(0.51)	16.538(031)	0.778(034)	0.589(033)	T
SN 2003W	52679.37(0.51)	15.874(032)	1.113(031)	52681.69(0.52)	15.745(032)	0.589(034)	0.096(034)	T
SN 2003Y	52676.59(0.59)	17.734(042)	1.727(093)	52679.26(0.51)	16.827(032)	1.234(043)	0.830(047)	P
SN 2003du	52766.13(0.55)	13.486(034)	0.950(031)	52766.86(0.59)	13.588(031)	0.556(032)	−0.106(034)	T
SN 2003fa	52807.53(0.50)	16.554(031)	0.956(030)	52808.48(0.50)	16.706(031)	0.515(031)	−0.160(031)	T
SN 2003gn	52853.09(0.55)	17.315(036)	1.243(082)	52854.59(0.50)	17.308(031)	0.737(032)	−0.011(037)	T
SN 2003gq	52848.41(0.61)	17.824(041)	1.693(188)	52852.50(0.63)	17.621(034)	1.013(067)	0.075(052)	P
SN 2003gt	52862.17(0.50)	14.887(031)	1.056(031)	52863.55(0.51)	14.895(032)	0.625(040)	−0.019(032)	T

Continued on Next Page . . .

Table 2.14 –Continued

SN	$t_{B_{\max}} - 2400000$	$B_{\max}$	$\Delta m_{15}(B)$	$t_{V_{\max}} - 2400000$	$V_{\max}$	$\Delta m_{15}(V)$	$(B-V)_{B_{\max}}$	Fit[a]
SN 2003he	52876.46(0.51)	16.183(031)	0.987(032)	52878.22(0.52)	16.176(032)	0.560(035)	−0.010(033)	T
SN 2003hv	52892.67(0.52)	12.482(034)	1.637(037)	52893.12(0.63)	12.544(036)	0.868(034)	−0.065(040)	T
SN 2003kf	52980.36(0.58)	13.254(042)	0.873(082)	52981.19(0.53)	13.322(031)	0.507(030)	−0.080(042)	T
SN 2004as	53084.98(0.51)	16.912(034)	1.111(034)	53087.11(0.50)	16.865(031)	0.639(057)	0.021(034)	T
SN 2004at	53092.26(0.50)	15.641(030)	1.091(031)	53093.56(0.51)	15.807(032)	0.589(034)	−0.176(032)	T
SN 2004br	53146.96(1.60)	15.456(031)	0.683(155)	53151.68(0.63)	15.502(031)	0.636(044)	−0.097(046)	P
SN 2004bv	53161.01(0.50)	13.893(032)	0.888(040)	53162.14(0.51)	13.802(031)	0.527(036)	0.082(033)	T
SN 2004bw	53163.55(0.52)	15.758(032)	1.312(048)	53164.88(0.52)	15.823(031)	0.753(037)	−0.079(034)	T
SN 2004dt	53240.40(0.51)	15.155(032)	1.286(053)	53241.40(0.51)	15.228(032)	0.641(057)	−0.080(034)	T
SN 2004ef	53264.36(0.51)	16.823(032)	1.383(042)	53265.93(0.50)	16.756(031)	0.713(032)	0.048(033)	T
SN 2004eo	53278.34(0.50)	15.019(030)	1.390(031)	53280.16(0.50)	15.035(031)	0.685(037)	−0.042(031)	T
SN 2004ey	53304.30(0.55)	14.731(035)	0.963(056)	53305.09(0.60)	14.838(035)	0.573(044)	−0.110(039)	T
SN 2004fz	53333.87(0.50)	14.833(037)	1.399(050)	53335.71(0.50)	14.933(033)	0.718(033)	−0.127(039)	T
SN 2004gs	53356.34(0.51)	17.106(031)	1.775(036)	53358.41(0.53)	17.035(031)	0.692(072)	0.046(032)	T
SN 2005M	53405.90(0.55)	15.854(031)	0.827(039)	53407.49(0.61)	15.922(032)	0.507(049)	−0.082(032)	P
SN 2005am	53437.71(0.51)	13.679(032)	1.667(035)	53438.63(0.53)	13.607(031)	0.856(032)	0.065(034)	T
SN 2005bc	53470.58(0.52)	16.256(032)	1.394(046)	53471.72(0.51)	15.860(031)	0.799(037)	0.382(033)	T
SN 2005cf	53533.70(0.51)	13.254(032)	1.029(037)	53535.34(0.50)	13.252(031)	0.585(031)	−0.012(032)	T
SN 2005de	53598.85(0.50)	15.347(031)	1.220(034)	53600.33(0.50)	15.324(031)	0.615(035)	0.010(032)	T
SN 2005el	53647.08(0.51)	14.822(034)	1.309(053)	53647.98(0.50)	14.928(031)	0.764(032)	−0.114(035)	T
SN 2005eq	53654.90(0.51)	16.201(033)	0.882(045)	53655.80(0.52)	16.214(032)	0.514(032)	−0.021(034)	T
SN 2005eu	53660.57(0.52)	16.369(036)	0.938(038)	53661.18(0.51)	16.435(035)	0.742(043)	−0.072(040)	T
SN 2005na	53741.93(0.67)	15.905(037)	1.239(060)	53742.50(0.91)	16.030(036)	0.639(070)	−0.128(042)	T
SN 2006bt	53857.51(0.61)	16.924(036)	0.877(046)	53859.67(0.51)	16.756(031)	0.602(032)	0.146(037)	T
SN 2006cp	53897.07(0.61)	15.908(038)	0.993(050)	53899.23(0.55)	15.813(032)	0.660(064)	0.063(039)	T
SN 2006dm	53928.96(0.50)	15.982(032)	1.543(034)	53930.35(0.50)	15.987(032)	0.850(036)	−0.022(034)	T
SN 2006ef	53970.02(0.56)	15.530(033)	1.384(052)	53970.68(0.53)	15.519(031)	0.717(036)	0.004(034)	T
SN 2006ej	53976.28(0.64)	15.729(054)	1.397(154)	53977.95(0.58)	15.749(042)	0.770(048)	−0.046(062)	T
SN 2006eu	53987.35(0.85)	17.318(048)	1.309(144)	53987.03(0.79)	16.827(036)	0.707(051)	0.501(053)	P
SN 2006gr	54012.60(0.52)	16.843(045)	1.029(057)	54014.36(0.52)	16.863(038)	0.586(040)	−0.036(051)	T

Continued on Next Page . . .

Table 2.14 –Continued

SN	$t_{B_{\max}} - 2400000$	$B_{\max}$	$\Delta m_{15}(B)$	$t_{V_{\max}} - 2400000$	$V_{\max}$	$\Delta m_{15}(V)$	$(B-V)_{B_{\max}}$	Fit[a]
SN 2006le	54047.85(0.62)	14.738(037)	0.888(048)	54049.46(0.52)	14.858(034)	0.548(037)	−0.134(040)	T
SN 2006lf	54045.21(0.54)	13.800(043)	1.308(084)	54046.26(0.56)	13.857(042)	0.783(045)	−0.068(052)	T
SN 2007af	54174.50(0.56)	13.103(034)	1.222(047)	54176.13(0.53)	13.099(032)	0.673(037)	−0.014(036)	T
SN 2007au	54184.18(0.51)	16.519(036)	1.806(037)	54185.76(0.57)	16.389(054)	0.936(070)	0.108(057)	T
SN 2007bc	54200.14(0.53)	15.803(034)	1.349(069)	54201.94(0.51)	15.898(031)	0.698(034)	−0.120(034)	T
SN 2007ci	54246.55(0.52)	15.914(039)	1.744(038)	54248.60(0.52)	15.877(034)	0.880(053)	0.003(042)	T
SN 2007co	54264.68(0.53)	16.436(032)	1.040(104)	54266.48(0.50)	16.426(030)	0.590(031)	−0.008(032)	T
SN 2007cq	54280.43(0.52)	15.820(032)	1.066(033)	54282.38(0.50)	15.852(030)	0.633(036)	−0.053(033)	T
SN 2007fr	54302.51(0.52)	18.061(036)	1.790(039)	54303.96(0.58)	18.136(041)	0.832(067)	−0.095(045)	T
SN 2007hj	54350.13(0.55)	15.542(034)	1.953(058)	54352.27(0.51)	15.419(031)	1.027(033)	0.090(038)	P
SN 2007le	54398.94(0.52)	13.859(034)	1.015(041)	54400.11(0.73)	13.572(036)	0.554(038)	0.280(039)	T
SN 2007qe	54429.07(0.50)	16.003(032)	1.035(038)	54431.20(0.61)	15.989(044)	0.554(043)	−0.011(045)	T
SNF20071021-000	54407.83(0.52)	16.443(031)	1.239(046)	54409.60(0.55)	16.489(032)	0.668(051)	−0.066(033)	T
SN 2007sr	54448.34(0.75)	12.713(045)	1.053(066)	54448.97(1.64)	12.628(071)	0.542(057)	0.081(078)	T
SN 2007ux	54464.98(1.61)	17.229(100)	1.744(073)	54467.16(0.89)	17.269(032)	0.841(069)	−0.076(101)	T
SN 2008Q	54506.26(0.50)	13.481(030)	1.250(084)	54507.37(0.50)	13.483(031)	0.757(038)	−0.012(031)	T
SN 2008Z	54515.81(0.54)	16.399(036)	0.910(059)	54516.78(0.63)	16.284(056)	0.554(048)	0.109(059)	T
SN 2008ar	54534.57(0.70)	16.228(042)	1.078(055)	54536.21(0.63)	16.314(037)	0.521(066)	−0.101(047)	T
SN 2008bf	54555.14(0.53)	15.672(036)	1.029(069)	54556.05(0.53)	15.874(033)	0.564(036)	−0.207(038)	T
SN 2008dt	54646.73(3.05)	18.068(119)	0.958(135)	54649.15(1.25)	17.523(040)	0.613(057)	0.514(122)	T
SN 2008ec	54674.28(0.55)	15.491(033)	1.362(065)	54676.12(0.53)	15.386(032)	0.722(040)	0.081(034)	T
SNF20080514-002	54613.01(0.53)	15.834(034)	1.386(042)	54613.90(0.53)	15.992(033)	0.779(039)	−0.167(037)	T

[a] T(T)emplate or (P)olynomial fit.

Note. – 1σ uncertainties (mag) including both statistical and systematic errors noted in parentheses. Those for $B_{\max}$, $\Delta m_{15}(B)$, $V_{\max}$, $\Delta m_{15}(V)$, and $(B-V)_{B_{\max}}$ are reported in units of 0.001 mag.

Figure 2.22 shows $\Delta m_{15}(B)$ plotted against $\Delta m_{15}(V)$. We only use SNe which have $\Delta m_{15}(B)$ and $\Delta m_{15}(V)$ whose template and polynomial fits agree to within the derived error bars, reducing our sample to 68. There is a clear monotonic relationship indicating that the decline rates in bands behave similarly. Using a nonlinear least-squares fitting routine, we fit a quadratic polynomial to find our best fit by the functional form

$$\Delta m_{15}(V) = 0.17(\Delta m_{15}(B))^2 + 0.04(\Delta m_{15}(B)) + 0.36.$$

This fit has $\chi^2 = 225$ for 65 degrees of freedom. The scatter in the fit increases significantly for rapidly declining objects.

Figure 2.23 shows a histogram of the distribution of $(B-V)_{B_{\max}}$ values for our sample. We find a median value of $(B-V)_{B_{\max}} = -0.02$ mag. We further explore the distribution of $(B-V)_{B_{\max}}$ values by plotting them against $\Delta m_{15}(B)$ in Figure 2.24. We break our sample into three categories: SN 1991T-like, Normal, and SN 1991bg-like. These categories are defined spectroscopically and are either taken from the literature or from running the SuperNova IDentification (SNID) code (Blondin & Tonry 2007) on our spectroscopic database; see Silverman et al. (2012c) for more details on our implementation of SNID to our spectroscopic database. SNe that are SN 1991T-like are characterized by a lack of Si II and Ca II in premaximum spectra, have broader lights curves, and are more luminous than the typical SNe Ia (Filippenko et al. 1992a; Phillips et al. 1992). Objects that are SN 1991bg-like show strong Ti II and weak Fe II features at maximum light, and are intrinsically underluminous compared with normal SNe Ia (Filippenko et al. 1992b; Leibundgut et al. 1993). For a general review of the spectroscopic diversity of SNe Ia, see Filippenko (1997).

Of 18 SN 1991bg-like objects in our sample, we are able to measure Δm_{15} for 7. It is interesting to note that 5 of the 7 have $(B-V)_{B_{\max}} > 0.3$ mag. Of the 16 objects with $(B-V)_{B_{\max}} > 0.2$ mag, almost a third are SN 1991bg-like. Similar results have been presented by Garnavich et al. (2004) in the case of SN 1999by and Hicken et al. (2009b) for SN 1991bg-like rapid decliners in the CfA3 dataset. The 9 SN 1991T-like SNe (including similar SN 1999aa-like objects (Krisciunas et al. 2000; Li et al. 2001b)) share an even tighter grouping of $(B-V)_{B_{\max}}$ values with an average of -0.055 mag. The 91 spectroscopically normal SNe Ia are mostly clustered a little below $(B-V)_{B_{\max}} \approx 0$ mag with a few exceptions. There are 11 SNe that have $(B-V)_{B_{\max}} \geq 0.2$ mag, hinting that they may suffer from significant host-galaxy extinction. Using MLCS2k2 to fit our light curves (see Section 2.5.2 below for details), our suspicion is confirmed; MLCS2k2 finds that these SNe have $A_V \geq 0.4$ mag.

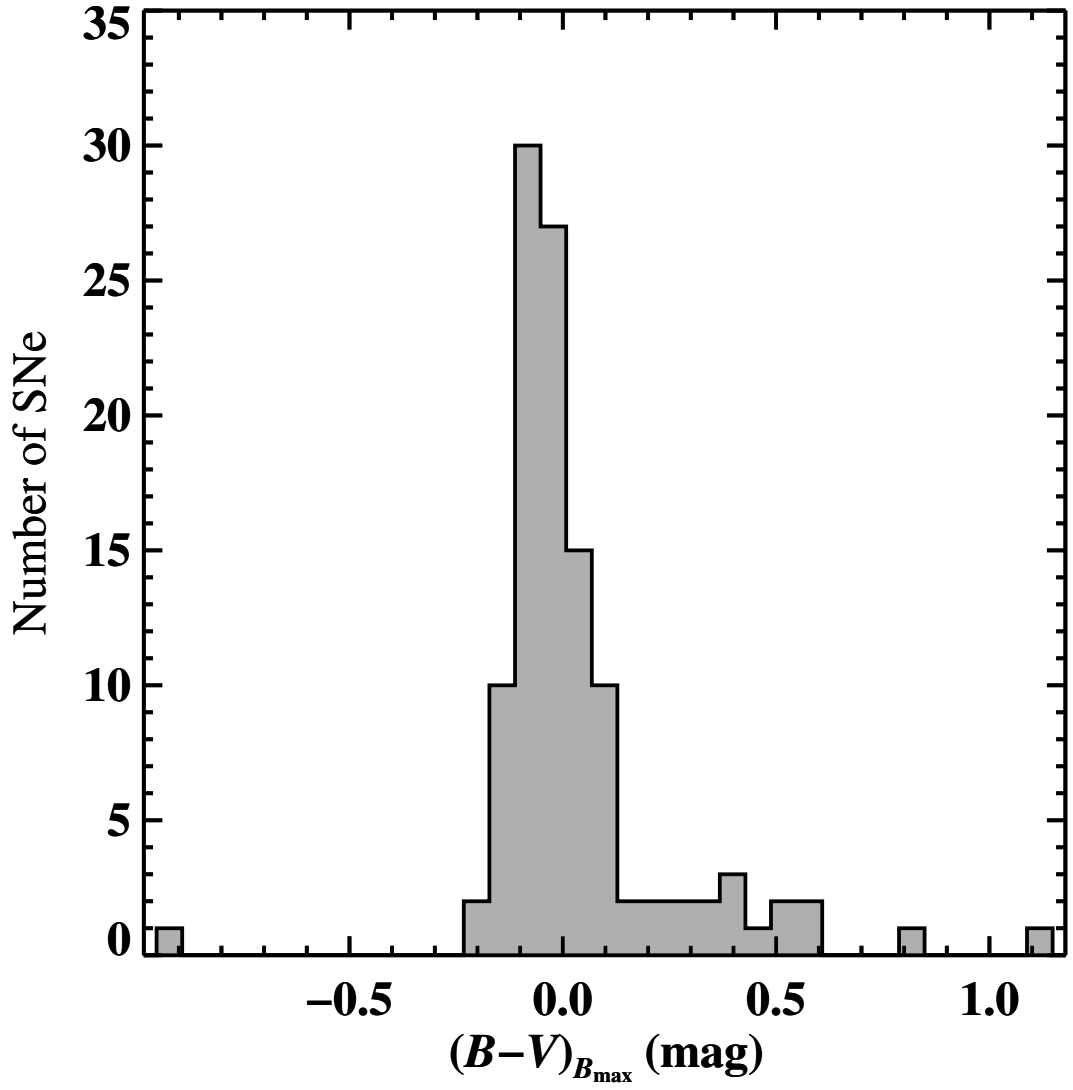

Figure 2.23: Distribution of $B-V$ values at $B_{\max}$. There is a clear peak at $B-V \approx 0$ mag with a tail that extends out to larger $B-V$ values. We find that SNe in the tail of the distribution are those that exhibit a significant amount of host-galaxy reddening and SN 1991bg-like objects. The bluest object that lies far to the left of the rest of the distribution in the peculiar SN 2000cx.

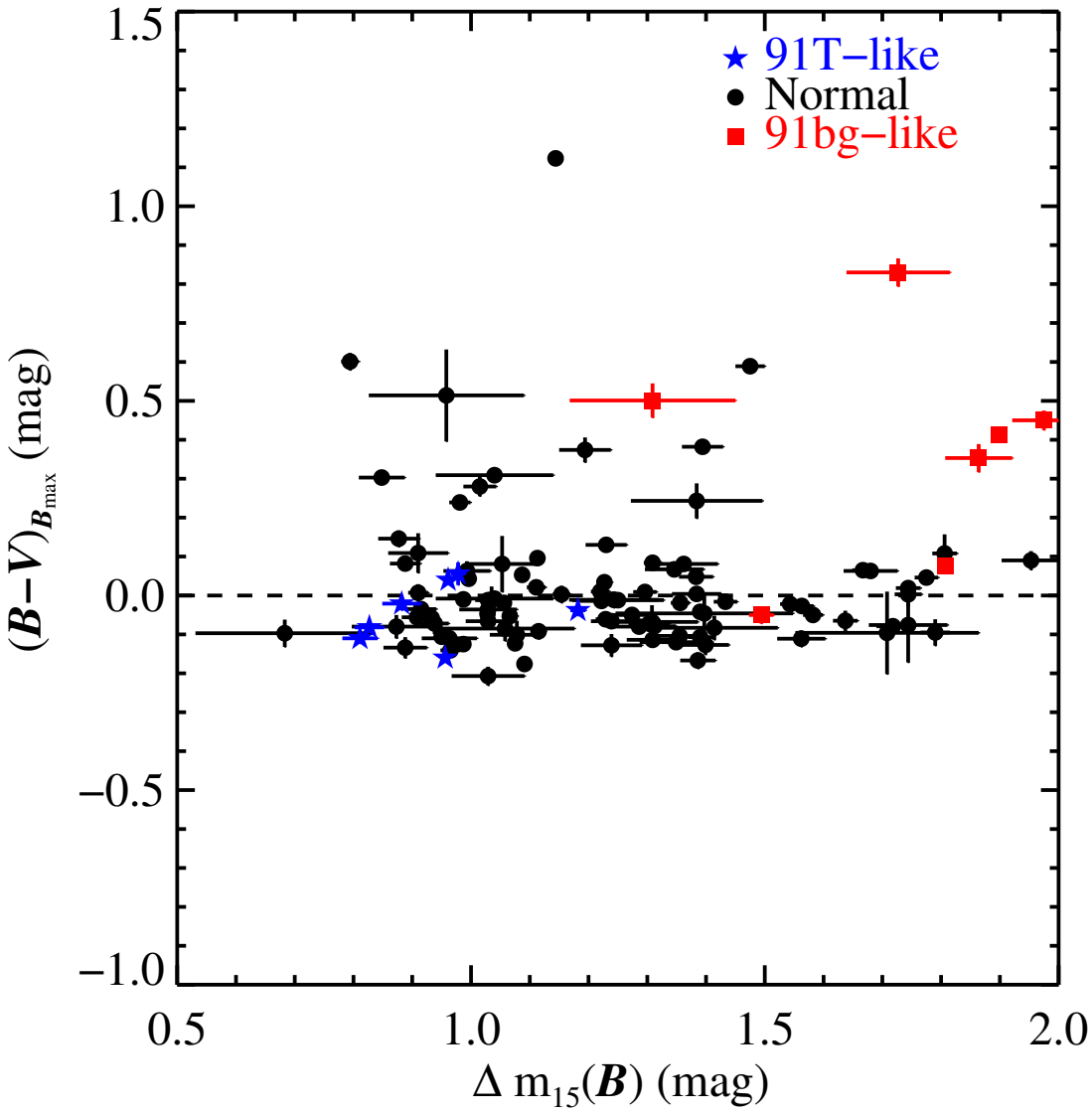

Figure 2.24: Comparison of $\Delta m_{15}(B)$ to $(B-V)_{B_{\max}}$. Objects have been coded by color and shape to highlight where different SN subclasses lie on the plot. SN 1991T-like objects are blue stars, normal SNe Ia are black circles, and SN 1991bg-like objects are red squares. Note that 6 of the 18 reddest objects are SN 1991bg-like.

2.5.2 Late-Time Colors

We have run the MLCS2k2.v006 distance fitter (Jha et al. 2007) on our dataset. Following the path set by Hicken et al. (2009a), we have run MLCS2k2 using two sets of priors for host-galaxy extinction: $R_V = 3.1$ and $R_V = 1.7$. For the purposes of this chapter, in which we simply wish to characterize our dataset, we will adopt the results of setting $R_V = 3.1$; using $R_V = 1.7$ does not affect the results below. For example, we find that the values derived for the MLCS2k2 Δ parameter for both sets of priors are within the 1σ errors for SNe with $A_V < 1.0$ mag. However, we do caution that there is a noticeable systematic trend between Δ residual and A_V (derived either using $R_V = 1.7$ or $R_V = 3.1$) which may slightly change the appearance of a few plots, but not the qualitative results presented below.

MLCS2k2 derives improved distances to SNe by parameterizing the absolute magnitude of a SN in the form of Δ, a measurement of how luminous a SN is compared to some fiducial value (with smaller Δ indicating an intrinsically brighter SN). This is done by attempting to separate intrinsic reddening in a SN from reddening from the host galaxy and then fitting to a training set of SN templates which are deemed to be free of host-galaxy extinction. Corrections for reddening are modeled as an intrinsic component governed by a Gaussian distribution of $B-V$ color 35 days past $B_{\max}$ that is uncorrelated with peak brightness and host-galaxy extinction given by a falling exponential peaking at $A_V = 0$ mag. The measured value of $(B-V)_{35}$ is drawn from the distribution formed by the convolution of the two different probability functions.

The explicit assumption is that the reddening can be disentangled into an intrinsic reddening component and a host-galaxy reddening component. Lira (1996) noted that the late-time $B-V$ color evolution for SNe with negligible host-galaxy extinction is strikingly similar, independent of $\Delta m_{15}(B)$. Phillips et al. (1999) used this observation to derive host-galaxy reddening estimates by determining the intrinsic late-time $B-V$ color behavior of four SNe in dust-free environments to correct the observed $B-V$ color of SNe that suffer from host-galaxy reddening. The authors measured an average slope of -0.0118 mag day^{-1} in the $B-V$ color curve in the interval 30 d $< t <$ 90 d, which has come to be known as the Lira-Phillips law.

The LOSS sample offers a significantly larger sample with which to test the Lira-Phillips law. In Figure 2.25, we plot $B-V$, $V-R$, and $V-I$ color curves for 133 SNe from our sample color-coded by the MLCS parameter Δ. Our sample excludes SNe which have an $A_V > 1.0$ mag as measured by MLCS. All light curves have been corrected for Milky Way extinction, K-corrected, corrected for time dilation, and shifted relative to the date of $B_{\max}$. What starts out as a dissonant tidal wave of data points marking quite distinct evolution at early times, converges to a similar evolution in the range 30 d $< t <$ 90 d similar to the

results found by Lira (1996); Phillips et al. (1999) and most recently Folatelli et al. (2010).

We measure $(B-V)_{35}$ for our sample by fitting a line with a fixed slope of -0.0118 mag day^{-1} to SNe with $B-V$ color curves having data at 30 d $< t <$ 90 d. We require that SNe have four or more data points in this range and are reliably fit. The results for 76 SNe from our sample can be found in Table 2.15. We also fit our $B-V$ color curves at this phase allowing the slope to vary. The error-weighted mean slope for our sample is -0.0115 ± 0.0001 mag day^{-1}, in excellent agreement with Phillips et al. (1999).

As was done by Jha et al. (2007), we fit a convolution of the two-component reddening model using a maximum-likelihood analysis. The parameters being fit are the peak and standard deviation (σ_{B-V}) of a Gaussian distribution of $(B-V)_{35}$ representing the intrinsic redness of SNe Ia at late times, and the scale length (τ_{B-V}) of a decaying exponential which models the probability distribution for host-galaxy reddening. The decaying exponential is truncated at the peak of the Gaussian to prevent negative-extinction measurements. To derive uncertainties for our fit, we performed a bootstrap analysis of the distribution.

Our results are shown in Figure 2.26. We find a mean $(B-V)_{35} = 1.006 \pm 0.022$ mag, $\sigma_{B-V} = 0.076 \pm 0.019$ mag, and $\tau_{B-V} = 0.161 \pm 0.036$ mag. Jha et al. find $(B-V)_{35} = 1.054 \pm 0.018$ mag, $\sigma_{B-V} = 0.062 \pm 0.012$ mag, and $\tau_{B-V} = 0.138 \pm 0.023$ mag using 82 objects, which mostly agree with the results presented here within the 1σ uncertainties. A Kolmogorov-Smirnoff test indicates that there is a 6% probability that the $(B-V)_{35}$ distribution presented here and that of Jha et al. (2007) are drawn from the same overall distribution. This rather small probability most likely reflects the different observational bias in each sample. The Lira-Phillips law as given by Phillips et al. (1999) predicts a mean $(B-V)_{35} \approx 1.044$ mag with a scatter of 0.05 mag. More recently, Folatelli et al. (2010) found an observed scatter about the Lira-Phillips law of 0.077 mag using a subset of the CSP sample with low host-galaxy reddening, although their analysis was done in the natural system of the Swope+CSP bands. Our values are in good agreement with these previously derived results.

Our larger value of τ is caused by the inclusion of SN 2006X and SN 1999cl, two SNe that appear to have extreme reddening properties. However, even with this value of τ, SNe having such extreme reddening are expected to be rare. Wang et al. (2009a) found both of these SNe to be members of a spectroscopic subclass that displayed a high-velocity Si II feature around maximum light in comparison with normal SNe Ia. On average, Wang et al. found that high-velocity SNe Ia are redder than spectroscopically normal SNe Ia and may be described by a different reddening distribution. While the prescription of a Gaussian convolved with a decaying exponential does a good job of modeling the late-time color distribution of most of our sample, it does not explain extremely reddened SNe such as SN 2006X and SN 1999cl.

Table 2.15: Lira-Phillips Fits for $(B-V)_{35}$

SN	$(B-V)_{35}$	$\sigma_{(B-V)_{35}}$
SN 1998dh	1.195	0.032
SN 1998dm	1.439	0.036
SN 1998ef	1.267	0.042
SN 1999aa	1.097	0.036
SN 1999ac	1.156	0.032
SN 1999cl	2.176	0.061
SN 1999dk	1.172	0.040
SN 1999dq	1.281	0.035
SN 1999ej	1.089	0.043
SN 1999gh	1.062	0.041
SN 2000cu	1.235	0.102
SN 2000cx	0.839	0.030
SN 2000dk	0.963	0.056
SN 2000dr	1.073	0.081
SN 2001V	1.245	0.040
SN 2001bf	1.087	0.036
SN 2001cj	1.012	0.058
SN 2001cp	0.967	0.085
SN 2001da	1.163	0.043
SN 2001dl	1.349	0.060
SN 2001en	1.132	0.040
SN 2001ep	1.278	0.040
SN 2002aw	1.257	0.047
SN 2002bf	1.307	0.045
SN 2002bo	1.407	0.031
SN 2002cr	1.138	0.032
SN 2002cu	1.113	0.060
SN 2002de	1.179	0.057
SN 2002dl	1.072	0.044
SN 2002dp	1.199	0.031
SN 2002eb	1.189	0.043
SN 2002er	1.282	0.037

Continued on Next Page ...

Table 2.15 –Continued

SN	$(B-V)_{35}$	$\sigma_{(B-V)_{35}}$
SN 2002fk	1.069	0.032
SN 2002ha	0.967	0.036
SN 2002he	1.091	0.044
SN 2003du	1.028	0.030
SN 2003gs	1.063	0.032
SN 2003gt	1.224	0.033
SN 2003he	1.100	0.042
SN 2003hv	0.969	0.031
SN 2003kf	1.071	0.032
SN 2004S	1.000	0.036
SN 2004at	1.076	0.048
SN 2004bg	1.062	0.040
SN 2004bk	1.204	0.036
SN 2004bv	1.201	0.032
SN 2004bw	1.018	0.057
SN 2004dt	1.130	0.035
SN 2004ef	1.176	0.116
SN 2004eo	1.111	0.042
SN 2004ey	1.142	0.034
SN 2005M	1.053	0.037
SN 2005am	1.115	0.032
SN 2005bc	1.369	0.045
SN 2005cf	1.215	0.031
SN 2005de	1.222	0.038
SN 2005el	0.905	0.036
SN 2005eq	1.075	0.054
SN 2005eu	1.214	0.067
SN 2005na	1.016	0.045
SN 2006D	0.985	0.034
SN 2006X	2.334	0.040
SN 2006dm	0.906	0.050
SN 2006ef	1.083	0.042

Continued on Next Page ...

Table 2.15 –Continued

SN	$(B-V)_{35}$	$\sigma_{(B-V)_{35}}$
SN 2006ej	1.063	0.050
SN 2006hb	1.055	0.048
SN 2007af	1.196	0.031
SN 2007bj	0.840	0.036
SN 2007co	1.108	0.054
SN 2007cq	1.050	0.038
SN 2007hj	1.117	0.041
SN 2007le	1.455	0.032
SN 2008A	1.424	0.047
SN 2008bf	1.061	0.043
SN 2008ec	1.320	0.045

The prescribed reddening treatment fails for the emerging class of SN 2002cx-like objects (Li et al. 2003b; Jha et al. 2006a; Phillips et al. 2007). As we have noted throughout this chapter, since we manually select SNe Ia to monitor, there is no reason our sample should reflect the true population of SNe Ia, and we emphasize that the sample is most likely biased. For example, our sample may have a relative excess of bluer SNe Ia which are easier to discover and hence more likely to be selected for photometric monitoring.

2.5.3 Galaxy Distribution

Using Δ as a proxy for the absolute magnitude of a SN and thus its decline rate, we can break our sample into three sets: fast decliners ($\Delta > 0.3$), normal ($-0.15 \leq \Delta \leq 0.3$), and slow decliners ($\Delta < -0.15$). In Figure 2.27, we show a histogram of the number of SNe found as a function of galaxy morphology for the three sets of SNe. We caution the reader from drawing extensive conclusions from this figure, as our sample may suffer from significant observational biases. However, it is interesting to note that our sample follows many relationships that have been previously noticed. Fast decliners in our sample are more likely to be found in early-type galaxies, while normal and slow decliners seem to favor later types (Della Valle & Livio 1994; Hamuy et al. 1996a; Howell 2001). While it is tempting to

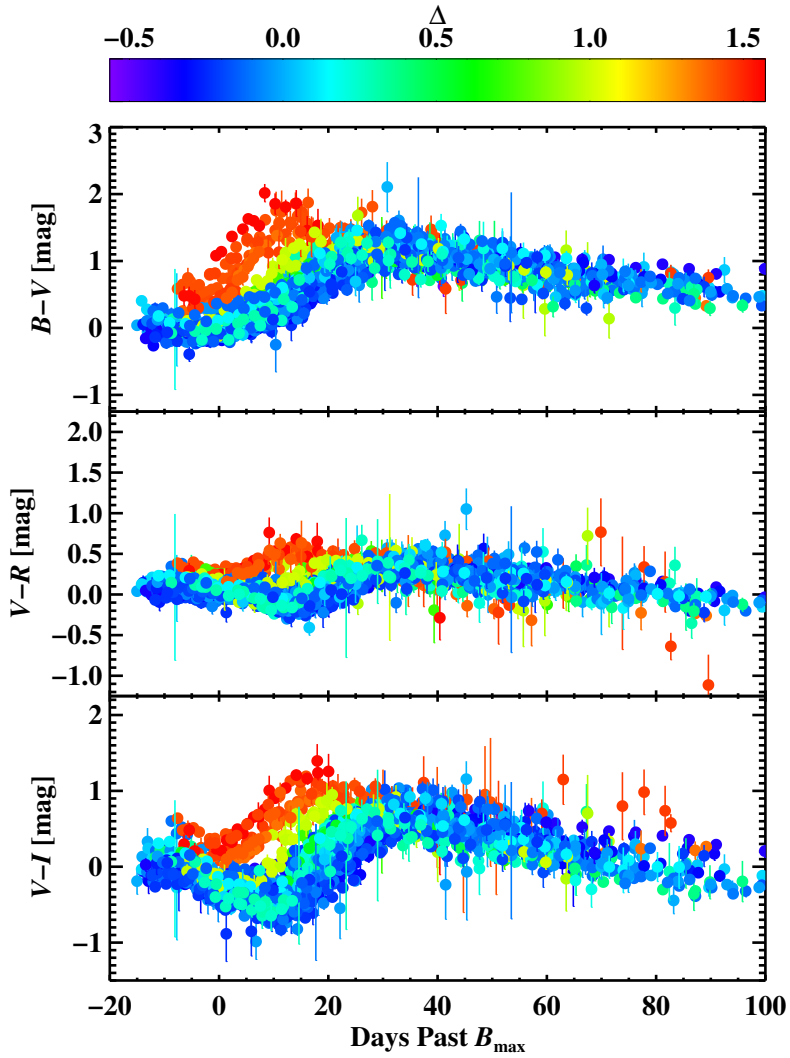

Figure 2.25: Color curves for 133 SNe from the LOSS sample color coded by the MLCS parameter Δ, which quantifies the width of the light curve in the sense that smaller Δ corresponds to a broader light curve. The top panel shows the $B-V$ color curve, the middle $V-R$, and the bottom $V-I$. The color curves have been shifted relative to maximum light in the B band and corrected for time dilation. All curves have been corrected for Milky Way reddening. We use only SNe that have $A_V \leq 1.0$ mag as found with MLCS. Despite SNe with various Δ values having very distinct color evolution for $t < 30$ days after $B_{\max}$, there is a remarkable convergence to similar evolution in the interval 30 d $< t <$ 95 d, mostly independent of Δ, as was first noted by Lira (1996). We measure an average slope that is in good agreement with the Lira-Phillips relation (Phillips et al. 1999)

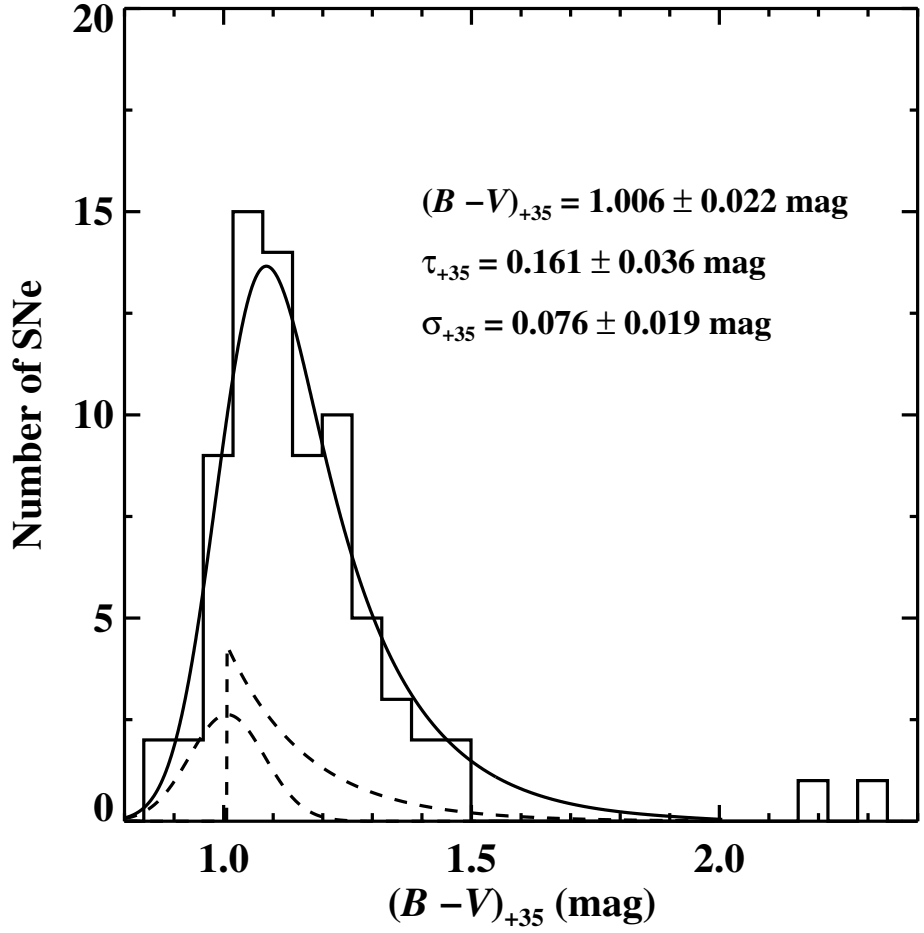

Figure 2.26: Distribution of $B-V$ values at 35 days past $B_{\rm max}$. We fit a Gaussian convolved with a decaying exponential to the distribution to determine the intrinsic scatter in SN color at late times. An example of the two functions is shown with broken lines, although not to scale. The best-fit convolution of the two distributions is overplotted as a solid line.

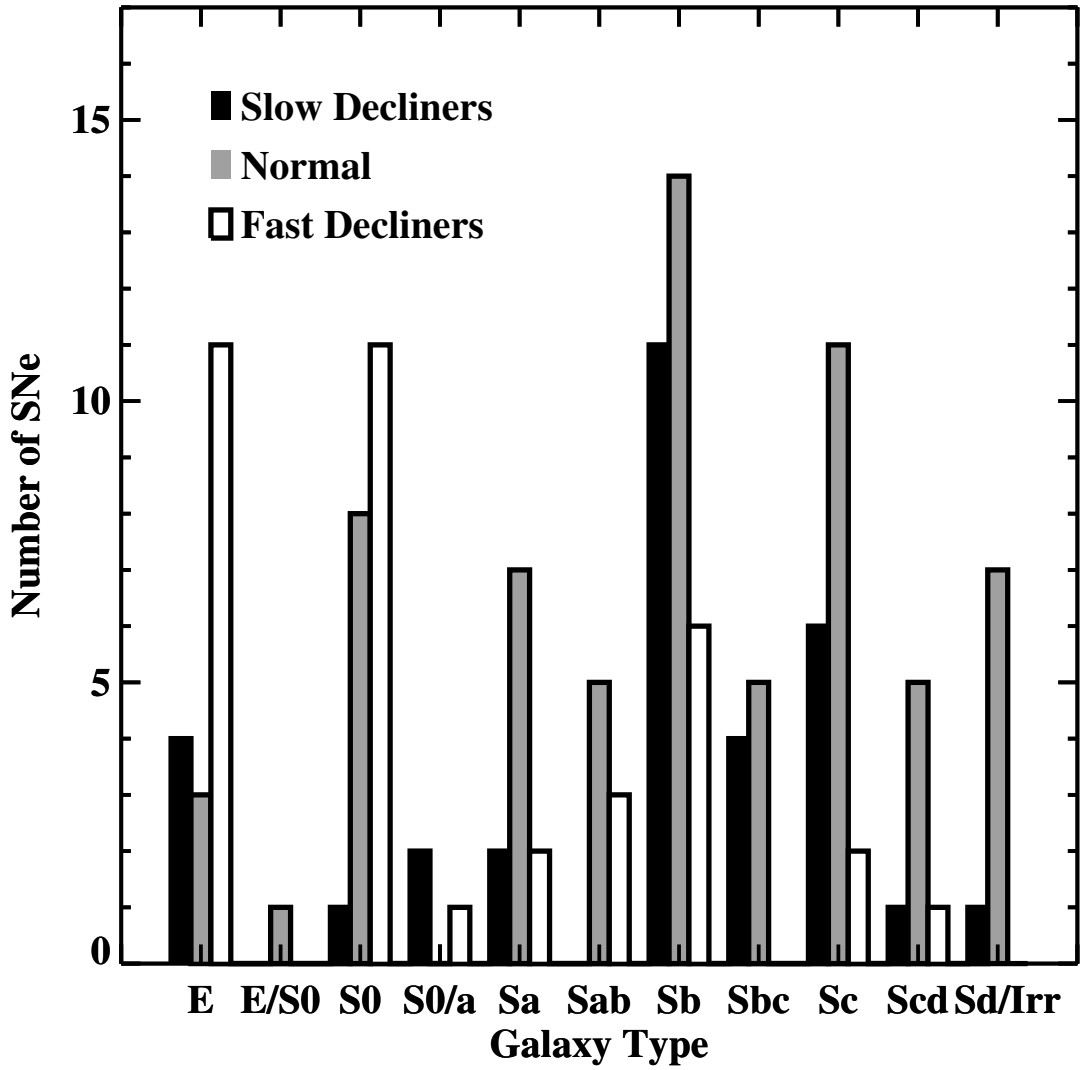

Figure 2.27: Histogram of galaxy morphologies for the LOSS sample broken up by decline rate. Blue bars indicate slow decliners, normal SNe Ia are black, and fast decliners are orange. We define decline rates by using the MLCS2k2 parameter Δ. Slow decliners have $\Delta < -0.15$, normal SNe Ia have $-0.15 \leq \Delta \leq 0.3$, and fast decliners have $\Delta > 0.3$. Fast decliners in our sample are preferentially found in early-type galaxies, while normal SNe Ia and slow decliners are in later-type galaxies.

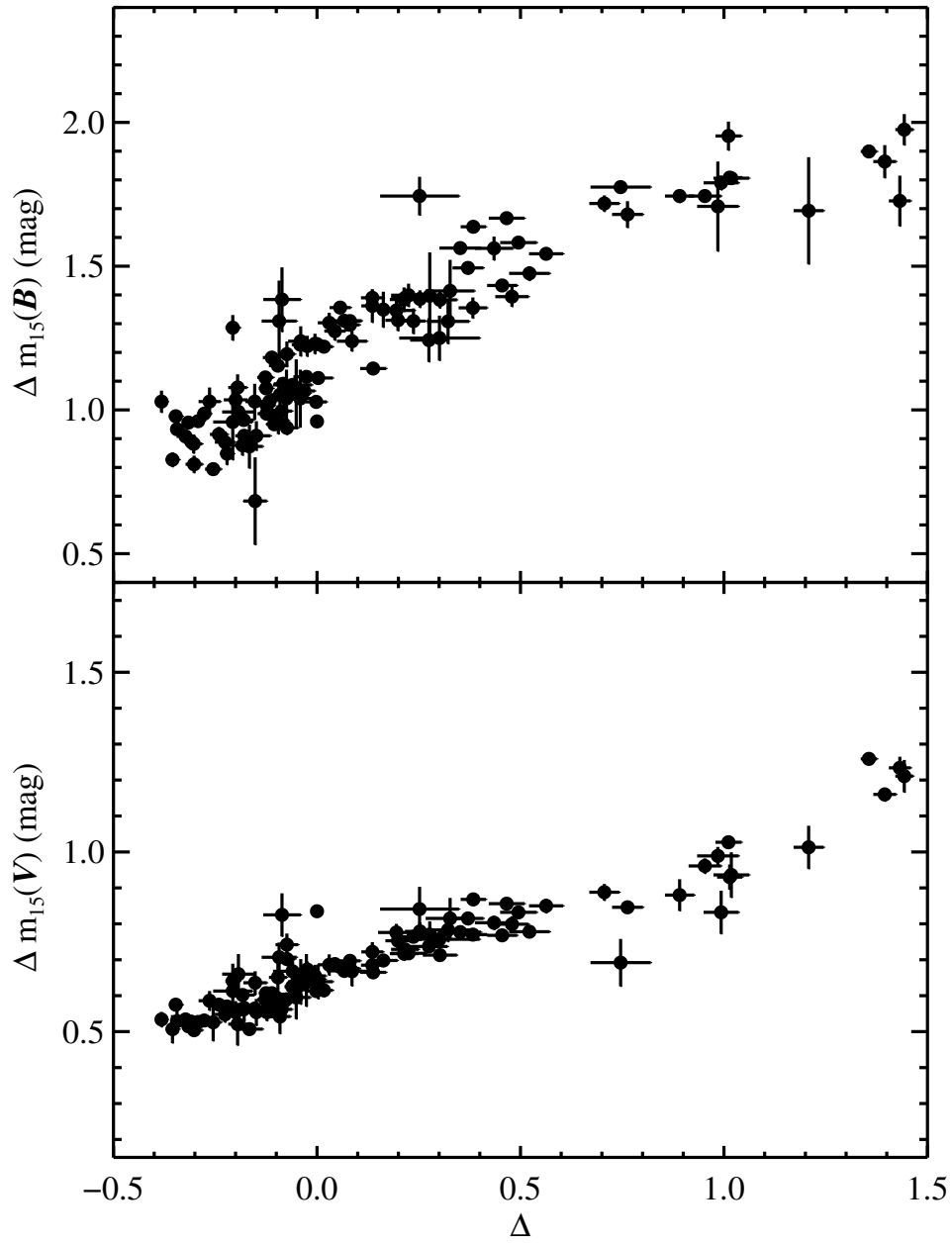

Figure 2.28: Comparisons of Δ to $\Delta m_{15}(B)$ and $\Delta m_{15}(V)$. Both Δ and Δm_{15} are measurements that correlate light-curve shape with intrinsic luminosity. A linear correlation holds for most of the SNe in the sample. Fast declining SNe ($\Delta \gtrsim 0.8$) do not seem to follow the trend set by rest of the sample.

conclude that more than one population of stars gives rise to SNe Ia, the observational bias in our photometric dataset must be kept in mind.

2.5.4 Δ and Δm_{15}

We compare Δ with our direct fits to $\Delta m_{15}(B)$ and $\Delta m_{15}(V)$ in Figure 2.28. As both are a proxy for the absolute magnitude of a SN, there is clearly a trend between the two. In both plots, the fastest decliners ($\Delta \geq 0.75$) do not seem to lie on the linear trend set by the rest of the sample.

2.6 Conclusion

We have presented *BVRI* light curves of 165 SNe Ia, most of which are of high quality and well sampled. This represents a homogeneously observed and reduced dataset. We estimate the systematic error in our photometry dataset to be 0.03 mag in *BVRI*.

As a consistency check on our reduction procedure, we compared our results with previous manual reductions of LOSS data and with data from other telescopes. We find that in general there is very good agreement between the results presented here and those already in the literature.

A major goal in SN Ia photometry must be to understand the systematics that arise from combining large datasets. We have shown that by analyzing the overlapping CfA3 and LOSS photometry as a single ensemble, the average residual is within 0.02 mag in *BVRI*. However, the scatter is surprisingly large ($\sigma \approx 0.1$ mag). If we limit our analysis to overlapping points brighter than mag 18, we can reduce the scatter to within 0.06–0.07 mag, which is still quite high. This scatter is due to systematic offsets in individual SN datasets and could be the result of calibration differences or galaxy-subtraction inconsistencies.

We have measured various light-curve parameters for our dataset that are useful in characterizing the light-curve shape vs. luminosity relationship, including $\Delta m_{15}(B)$ and $\Delta m_{15}(V)$. We have also run MLCS2k2 on our dataset, setting $R_V = 3.1$ to determine the parameter Δ. Our upcoming cosmology chapter will use this dataset to add to the existing literature on SN Ia cosmology. In particular, comparisons of MLCS2k2 with other distance fitters such as SALT, SALT2 (Guy et al. 2007), and a simple two-parameter fit will be used to attempt to disentangle the best method for handling reddening and for determining distances to SNe.

Understanding the effects of reddening is necessary in order to derive reliable distances to SNe Ia using distance fitters. We measured the distribution of $(B-V)_{35}$ for 76 SNe in our

sample by fitting the late-time colors with the Lira-Phillips slope. Fitting the distribution with a normally distributed component modeling Gaussian variations in SN color convolved with a decaying exponential host-galaxy component, we found that are results are consistent with the priors used by MLCS2k2 at the 1σ level. Future studies will examine the validity of assuming a decaying exponential as the probability distribution function of galactic reddening and the observational bias included in our sample.

The true potential of our extensive photometric dataset will be realized when analyzed in conjunction with the Berkeley Supernova Ia Program (BSNIP) spectroscopic database. We have ~ 1400 spectra of ~ 600 objects published in Silverman et al. (2012c). The overlap with the photometry is ~ 120 objects with a median of 3 spectra per object. A detailed analysis combining our spectra with derived parameters from our photometry, such as Δ and Δm_{15}, can be found in Silverman et al. (2012a).

The future of SN Ia science remains promising. In combination with other large low-redshift datasets being released by the CfA and the CSP, the extensive sample of light curves will push studies of SN Ia cosmology to the limit of our understanding of these objects as distance indicators. The next step will be to combine the new nearby SN Ia datasets by accounting for S-corrections, putting all of the datasets on the same photometric system. This will require a vigilant comparison between in the intersection of published datasets to understand systematic differences.

Chapter 3

The Rise-Time Distribution of Nearby Type Ia Supernovae

A version of this chapter was published in *The Monthly Notices of the Royal Astronomical Society* (Ganeshalingam, M., Li, W., & Filippenko, A. V. 2011, MNRAS, 416, 2607).

Abstract

We present an analysis of the B-band and V-band rise-time distributions of nearby Type Ia supernovae (SNe Ia). Drawing mostly from the Lick Observatory Supernova Search sample of SNe Ia presented in Chapter 2, together with other published nearby SNe Ia with data starting at least one week before maximum light, we use a two-stretch template-fitting method to measure the rise and decline of BV light curves. Our analysis of 61 SNe with high-quality light curves indicates that the longer the time between explosion and maximum light (i.e., the rise time), the slower the decline of the light curve after maximum. However, SNe with slower post-maximum decline rates have a faster rise than would be expected from a single-parameter family of light curves, indicating that SN Ia light curves are not a single-parameter family of varying widths. Comparison of the B-band rise-time distribution for spectroscopically normal SNe Ia to those exhibiting high-velocity spectral features indicates that high-velocity (HV) SNe Ia have shorter B-band rise times compared to their spectroscopically normal counterparts. After normalizing the B-band light curves to $\Delta m_{15}(B) = 1.1$ mag (i.e., correcting the post-maximum decline to have the same shape as our template), we find that spectroscopically normal SNe Ia have a rise time of 18.03 ± 0.24 d, while HV SNe have a faster B-band rise time of 16.63 ± 0.29 d. Despite differences in

the B band, we find that HV and normal SNe Ia have similar rise times in the V band. Furthermore, the initial rise of a SN Ia B-band light curve follows a power law with index $2.20^{+0.27}_{-0.19}$, consistent with a parabolic rise in flux predicted by an expanding fireball toy model. We compare our early-time B-band data to models for the predicted signature of companion interaction arising from the single-degenerate progenitor scenario. There is a substantial degree of degeneracy between the adopted power-law index of the SN light-curve template, the rise time, and the amount of shock emission required to match the data.

3.1 Introduction

Type Ia supernovae (SNe Ia) are believed to be the result of a thermonuclear runaway explosion of a C/O white dwarf (WD) approaching the Chandrasekhar limit (see Hillebrandt & Niemeyer 2000 for a review). Explosive nucleosynthesis up to ^{56}Ni releases $\sim 10^{51}$ erg, unbinding the progenitor. The subsequent light curve is powered by injection of energy from the radioactive decay of ^{56}Ni; the γ rays degrade to longer wavelengths as they diffuse out through the expanding ejecta.

The well-established relationship between the light-curve width and the luminosity at peak brightness allows SNe Ia to be "standardizable candles" at optical wavelengths (Phillips 1993), and possibly almost standard candles in the infrared (Krisciunas et al. 2004b; Wood-Vasey et al. 2008; Folatelli et al. 2010). Application of the width-luminosity relation along with color information to SNe Ia over cosmological scales has led to the discovery of the accelerating expansion of the Universe (Riess et al. 1998; Perlmutter et al. 1999; see also Astier et al. 2006; Riess et al. 2007; Wood-Vasey et al. 2007; Kowalski et al. 2008; Hicken et al. 2009a; Amanullah et al. 2010), indicating either the presence of "dark energy" having a negative pressure or a failure of general relativity on the largest scales. Recent work has also shown that including spectral flux ratios may also aid in reducing Hubble-diagram residuals (Bailey et al. 2009; Blondin et al. 2011).

Despite the successful cosmological application of SNe Ia, the SN community lacks a clear understanding of the nature of their progenitor systems. Possible scenarios include a single-degenerate WD paired with a red-giant post-main-sequence star undergoing stable mass transfer until $M_{\rm WD}$ approaches $M_{\rm Ch} \approx 1.4$ M$_\odot$ (Whelan & Iben 1973; Livio 2000), a double-degenerate WD merger that reaches or surpasses $M_{\rm Ch}$ (Webbink 1984; Iben & Tutukov 1994), or the result of a sub-Chandrasekhar explosion of a WD steadily burning helium accreted from a companion (Shen & Bildsten 2009). Each scenario carries with it tentative observational evidence and hardships imposed by unrealized theoretical predictions.

While considerable attention has been focused on the post-maximum decline of the

SN Ia light curve, less has been paid to the rise of the SN Ia from explosion to maximum brightness. This is due to the dearth of data in the days following the SN explosion and the intrinsic difficulty of finding SNe Ia shortly after explosion. The Lick Observatory Supernova Search (LOSS) has been successful at finding SNe in the nearby Universe (redshift $z < 0.05$) and the Sloan Digital Sky Survey (SDSS) Supernova Survey (Frieman et al. 2008) has found and monitored 391 SNe at moderate redshift ($0.03 \leq z \leq 0.35$). Higher redshift searches such as the SuperNova Legacy Survey (Astier et al. 2006) and ESSENCE (Wood-Vasey et al. 2007) benefit from cosmological time dilation, allowing the SN rise to be spread out over more days in the observer's frame.

A first attempt at quantifying SN Ia rise times by Pskovskii (1984) analyzed 54 historical light curves gathered from photographic plates and visual B magnitude estimates, finding a typical rise of 19–20 d. Recent attempts have made use of more reliable data taken with charge-coupled devices (CCDs) which are linear in translating photons to counts over a large dynamic range. A seminal paper by Riess et al. (1999b, hereafter R99) used observations of nearby SNe Ia to find a B-band rise time of 19.5 ± 0.2 d for a normal SN Ia having a decline of 1.1 mag between maximum light and 15 d after maximum in the B band (i.e., $\Delta m_{15}(B) = 1.1$ mag; Phillips 1993). Studies using data on higher redshift SNe Ia have found a rise time in concordance with that of R99 (Aldering et al. 2000; Conley et al. 2006), advancing the notion that there is limited, if any, evolution in SN Ia properties from high to low redshifts. Most recently, (Conley et al. 2006, hereafter C06) found a rise of $19.10^{+0.18}_{-0.17}$ (stat)± 0.2(sys) d using SNLS data.

In an analysis of B- and V-band photometry of eight nearby SNe Ia with excellent early-time data, Strovink (2007, hereafter S07) found tentative evidence for two populations of B-band rise times. After correction for light-curve decline rate, S07 found that three SNe rise in 18.81 ± 0.36 d and five SNe rise in 16.64 ± 0.21 d. More recently, Hayden et al. (2010b, hereafter H10) analyzed B- and V-band photometry 105 SNe Ia from the SDSS sample and found that SNe Ia come from a rather broad distribution of B-band rise times, with evidence indicating that slower declining events (e.g., more luminous SNe) have some of the fastest rise times. This result has significant implications for light-curve fitting techniques that rely on a single-parameter family of light curves and theoretical modeling of SNe Ia. H10 find an average B-band rise time of 17.38 ± 0.17 d, a departure from the results of R99 and C06 which H10 trace back to differences in fitting methods.

In this chapter, we analyze available data on nearby SNe Ia to measure the rise times, relying heavily on the recently released LOSS sample presented in Chapter 2. Previous analyses such as those of S07 and H10 use combined results from both B- and V-band photometry to measure the B-band rise time. In this chapter, we compare the B-band

rise time measured in the B and V bands and find that such a combination may not be appropriate. Instead, we present independent analysis of the B and V bands. Specifically, we define the rise time in a photometric band as the elapsed time between explosion and maximum light for that particular band. Nearby SNe offer the advantage of being able to be monitored by small-aperture telescopes and benefit from not requiring significant K-corrections, which at early times are ill defined because of a lack of available spectra to model the SN spectral energy distribution (SED).

3.2 Data

3.2.1 LOSS Light Curves

LOSS is a transient survey utilizing the 0.76-m Katzman Automatic Imaging Telescope (KAIT) at Lick Observatory (Li et al. 2000; Filippenko et al. 2001; see also Filippenko, Li, & Treffers 2011, in prep.). KAIT is a robotic telescope that monitors a sample of $\sim 15,000$ galaxies in the nearby Universe ($z < 0.05$) with the goal of finding transients within days of explosion. Fields are imaged every 3–10 d and compared automatically to archived template images, and potential new transients are flagged. These are subsequently examined by human image checkers, and the best candidates are reobserved the following night. Candidates that are present on two consecutive nights are reported to the community using the International Astronomical Union Circulars (IAUCs) and the Central Bureau of Electronic Telegrams (CBETs). Time allotted to our group on the Lick Observatory 3-m Shane telescope with the Kast double spectrograph (Miller & Stone 1993) is used to spectroscopically identify and study candidates. Between first light in 1997 and 2010 September 30 UT, LOSS found over 865 SNe, 382 of which have been spectroscopically classified as SNe Ia. The statistical power of the LOSS SNe is well demonstrated by the series of papers deriving the nearby SN rates (Leaman et al. 2011; Li et al. 2011c,a).

In addition to the SN search, KAIT monitors active SNe of all types in broad-band *BVRI* filters. The first data release of *BVRI* light curves for 165 SNe Ia along with details about the reduction procedure have been presented in Chapter 2. In summary, point-spread function (PSF) fitting photometry is performed on images from which the host galaxy has been subtracted using templates obtained > 1 yr after explosion. Photometry is transformed to the Landolt system (Landolt 1983, 1992) using averaged color terms determined over many photometric nights. Calibrations for each SN field are obtained on photometric nights with an average of 5 calibrations per field.

The LOSS light curves represent a homogeneous, well-sampled set of *BVRI* light curves.

The average cadence is 3–4 d between observations, with a typical light curve having 22 epochs. Of the 165 *BVRI* light curves in the sample, 70 have data starting at least one week before maximum light.

3.2.2 Light Curves from Other Nearby Samples

In addition to the LOSS sample, here we include data from the following previously published SN Ia samples: the Calán-Tololo sample (Hamuy et al. 1996b), the Center for Astrophysics (CfA) Data Releases 1–3 (Riess et al. 1999a; Jha et al. 2006b; Hicken et al. 2009b), and the Carnegie Supernova Project (CSP) dataset (Contreras et al. 2010). In cases where there are data from multiple samples, we chose the dataset with the best-sampled light curve to avoid introducing systematic calibration error. With the exception of the CSP sample, all light curves are in the Landolt photometric system. The CSP light curves are in the natural system of the Swope telescope at Las Campanas Observatory. Comparing LOSS B-band light curves (in the Landolt system) with CSP B-band light curves (in the Swope natural system), we find differences of ~ 0.03 mag which do not appear to be correlated with SN color. We adopt 0.03 mag as the systematic uncertainty of the CSP Swope system light curves.

We also include individual light curves for SN 1990N (Lira et al. 1998), SN 1992A (Altavilla et al. 2004), SN 1994D (Patat et al. 1996), SN 1998aq (Riess et al. 2005), SN 1999ee (Stritzinger et al. 2002), SN 2003du (Stanishev et al. 2007), SN 2007gi (Zhang et al. 2010), and a preliminary reduction of SN 2009ig which was found by LOSS about 15 d before maximum light. In total, we have BV light curves for 398 SNe.

3.3 Methods

In this section we detail the method used to measure the rise times of our sample. Most previous measurements of the SN Ia rise time have used a single-stretch fit (see R99, C06). These studies "stretched" the template light curve along the time axis to determine the stretch value, s, that best fit the data. A light curve narrower than the template would have $s < 1$, a wider light curve $s > 1$, and a light curve that matched the template perfectly $s = 1$. Explicit in this formalism is that a single stretch value applies to both the rising and falling portions of the light curve. Instead, we adopt a two-stretch fitting procedure first introduced by H10 to fit our B- and V-band data; we fit each band independently. Here we discuss our implementation of the two-stretch fitting routine with a template created mostly from LOSS data.

3.3.1 The Two-Stretch Fitting Method

In our two-stretch fitting routine, pre-maximum and post-maximum data are decoupled, allowing the two portions of the light curve to take on different stretch values to match a template. We define s_r to be the "rise stretch" and s_f to be the "fall stretch." The template has $s_r = s_f = 1.00$ by construction. The two stretched light-curve portions are joined at peak where the first derivative is 0, ensuring a continuous function with a continuous first derivative at maximum light.

Mathematically, the time axis is stretched such that

$$\tau = \begin{cases} \frac{t-t_0}{s_r(1+z)} & t \leq t_0 \\ \frac{t-t_0}{s_f(1+z)} & t > t_0, \end{cases} \tag{3.1}$$

where τ represents the effective "stretch-corrected" rest-frame epoch, t_0 is the time of maximum light, and z is the SN redshift.

Similar to other implementations of stretch (e.g., Goldhaber et al. 2001), we model each light curve as a function of time by

$$f(t) = f_0 S(\tau), \tag{3.2}$$

where f_0 is the peak flux and S is our normalized template light curve. We perform a χ^2 minimization to the quantity

$$\chi^2 = \sum_i \frac{(F(t_i) - f(t_i))^2}{\sigma^2_{\rm phot} + \sigma^2_{\rm template}}, \tag{3.3}$$

where i is an index summed over all observations, $F(t_i)$ are individual flux measurements, $\sigma_{\rm phot}$ is the photometric uncertainty including systematic error, and $\sigma_{\rm template}$ is the uncertainty in our template as described in Section 3.3.2. Our χ^2 minimization fits for the values of f_0, t_0, s_r, and s_f. We restrict the fit to data within $\tau < +35$ d relative to maximum light, after which SNe enter the nebular phase where the stretch parametrization is no longer applicable (Goldhaber et al. 2001).

The rest-frame rise time of a light curve (i.e., the elapsed time between explosion and maximum light in that band) is obtained by multiplying the measured s_r by the fiducial rise time of the template. Following S07, we define the B-band fall time to be the amount of time required for the B-band light curve to decline by 1.1 mag starting at maximum light in B. We define the fall time for the V band to be the required time for a V-band light curve to fall by 0.66 mag; the fall time of a light curve is $15\,s_f$ d. By construction, both templates with $s_f = 1$ have a fall time of 15 d.

The B-band fall stretch s_f is directly related to $\Delta m_{15}(B)$ by the simple, empirical formula

$$\Delta m_{15}(B) \approx 1.1 - 1.70(s_f(B) - 1.0) + 2.30(s_f(B) - 1.0)^2, \quad (3.4)$$

which was found by stretching our B-band template and reading off the resulting value of $\Delta m_{15}(B)$ mag. Similarly, for our V-band template, we find

$$\Delta m_{15}(V) \approx 0.66 - 0.83(s_f(V) - 1.0) + 0.94(s_f(V) - 1.0)^2. \quad (3.5)$$

Note that Equations 3.4 and 3.5 are only valid for the LOSS templates, and that $s_f(B) = 1$ and $s_f(V) = 1$ respectively correspond to $\Delta m_{15}(B) = 1.1$ mag and $\Delta m_{15}(V) = 0.66$ mag.

K-corrections are computed with the spectral series of Hsiao et al. (2007) which provides the spectral evolution of a SN Ia with a one-day cadence. Using all available multi-color photometry for a SN, the spectrum for the phase nearest the photometry epoch is warped to match the colors in the observer's frame using a third-order spline with knots placed at the effective wavelength of each available filter. K-corrections are computed from the warped spectrum and are typically < 0.05 mag.

For a single SN, our fitting procedure gives the date of maximum light, maximum flux, rise stretch, and fall stretch for both the B- and V-band light curves. For the purpose of comparing our results to those of H10, we compute the B-band rise time (i.e., the time between explosion and maximum light in B) found using both B- and V-band photometry. To determine the B-band rise time using V-band photometry, we measure the V-band rise time (the time between explosion and maximum light in V) and subtract off the time between maximum light in V and maximum light in B. We employ this determination of the B-band rise time using V-band photometry to compare the rise-time behaviour of the two bandpasses over the same time period. Consequently, the determination of the B-band rise time using the V band typically has larger uncertainties than using the B-band photometry, since we must also include the error from both the times of B and V maximum. We emphasize that the V-band rise time is defined to be the elapsed time between explosion and maximum light in the V band.

3.3.2 Template

The template plays an important role in measuring light-curve properties. A template which does not reflect the data will lead to fits with systematically incorrect measurements of light-curve properties (H10; Aldering et al. 2000). Here we discuss the sample of objects and the method used to construct our light-curve templates for the B and V band.

We construct our templates from a sample of well-observed "normal" SNe Ia. Most of the objects come from the set of SNe Ia observed by LOSS from Chapter 2, but we also

include several objects published previously. SNe Ia with excellent light curves but known peculiarities, such as SN 1999ac (Phillips et al. 2006), SN 2000cx (Li et al. 2001b; Candia et al. 2003), SN 2002cx (Li et al. 2003b; Jha et al. 2006a), SN 2004dt (Leonard et al. 2005; Wang et al. 2006; Altavilla et al. 2007), SN 2005hk (Phillips et al. 2007), and SN 2009dc (Yamanaka et al. 2009; Silverman et al. 2011), are avoided. The underluminous SN 1991bg-like objects show distinctly different photometric behaviour compared with the rest of the SN Ia population, so they are excluded from the sample as well. In total, the set includes 60 objects, many of which are also in the rise-time SN Ia sample discussed in Section 3.3.4.

For the zeroth-order template light curve, we adopt the fiducial $\Delta = 0$ ($\Delta m_{15}(B) = 1.1$ mag) template from the Multi-color Light-Curve Shape (MLCS2k2) fitter (Jha et al. 2007).[1] Light-curve data are then fit using a two-stretch fitting parametrization. The parameters being fit via a χ^2 minimization technique are the time of maximum light t_0, the flux at maximum light f_0, the rise stretch s_r, and the fall stretch s_f (see Section 3.3.1 for details) after correcting the light curves for time dilation using redshifts obtained from the NASA/IPAC Extragalactic Database.[2] The light-curve data are then normalized using the best-fit parameters to have a peak flux of 1.0 at $\tau = 0$ and de-stretched, using s_r and s_f, along the time axis to match the template. After normalizing and de-stretching all of our light-curve data to match the shape of the template, we study the mean residuals between the data and the template.

While we find that even though the $\Delta = 0$ templates do a reasonable job in fitting the data, there are still small systematic trends in the fit residuals. For each band, we fit a smooth curve to the residuals and use it as a correction to the input template. These "refined" templates are then used to fit the light-curve data from our template sample again and the fit residuals are studied. This process is iterated until convergence is reached — that is, no systematic trend is observed in the fit residuals. Convergence is achieved within 5 iterations. We restrict this part of the template training procedure to data where the MLCS2k2 template is well defined, but before the SN enters the nebular phase. For the B band this is within the range $-10 < \tau < +35$ d with respect to maximum light in B. For the V band this is $-11 < \tau < +35$ d with respect to maximum light in V.

To estimate the uncertainties of our templates, we bin the fit residuals in 3 d intervals and calculate their root-mean square (RMS). Because a particular light-curve fit can have systematic residuals relative to the input template (i.e., several data points in one portion of the light curve all show negative residuals, while data in another portion all show positive residuals), the residuals at different epochs are correlated, and the RMS measurements are

[1] Downloaded from www.physics.rutgers.edu/∼saurabh/mlcs2k2/ on October 7, 2010.

[2] http://nedwww.ipac.caltech.edu/

an overestimate of the true uncertainties. It is difficult to quantify how the residuals are correlated because different light-curve fits have different patterns of residuals. We assume that the residuals are equally affected by the correlated errors in all portions of the template, and apply a constant scaling factor to the RMS measurements so that the overall fit to all of the data has a reduced $\chi^2 \approx 1$. These scaled RMS measurements are adopted as the uncertainties of our templates.

Suffering from a dearth of early-time data, we adopted an expanding fireball model to describe the SN light curve for $\tau < -10$ d relative to maximum light based on the arguments presented by R99 and employed in most rise-time studies thereafter. After explosion of the progenitor, the SN undergoes free, unimpeded expansion such that its radius, R, expands proportionally with time, τ. Approximating the SN as a blackbody, the optical luminosity through a broad-band filter on the Rayleigh-Jeans tail of the SED is given by $L \propto R^2T \propto (v\tau)^2T$. Despite recent observations indicating that T may actually change substantially over this period (Pastorello et al. 2007b; Hayden et al. 2010b), if we assume that changes in v and T are modestly small, then $L \propto \tau^2$. Wrapping our ignorance into a "nuisance parameter" α, we can write the flux in the rise-time region as $f = \alpha(\tau + t_r)^2$, where t_r is the rise time of the template.

To determine the rise time for our template, we restrict our sample to light curves with data starting at $\tau \leq -10$ d relative to B-band maximum and at $\tau \leq -11$ d for the V band. The following approach was adopted.

1. Create a random realization of the light curves in our sample using reported photometry uncertainties for each data point and systematic calibration uncertainties for each light curve in our template section (see Section 3.3.3 for details on how this is implemented).

2. Perform the two-stretch fitting routine, restricting the fits to data within the range $-10 < \tau < 35$ d for B or $-11 < \tau < 35$ d for V. The fit is restricted to this range to avoid imposing a shape in the region where we will fit for the rise time.

3. Normalize and two-stretch correct the light curves in the sample.

4. Fit a parabola to the ensemble of light-curve points with $\tau \leq -10$ d for B or $\tau \leq -11$ d for V with the constraint that the parabola is continuous with the template.

The procedure outlined above was performed 1000 times for the B- and V-band data independently. We find a best-fit rise time of 17.92 ± 0.19 d for the B band and 19.12 ± 0.19 d for the V band.

We also attempted to find the best rise time for our template using the approach outlined by H10, except on a finer grid. We tested templates with different rise times in the range

$15 \leq t_r \leq 21$ d in 0.1 d increments (as opposed to the 0.5 d increments of H10). For each template, light curves with data starting at least ten days before maximum light were fit using the two-stretch method (see Section 3.3.1 for more details). Unlike the previous procedure to determine the rise time, all data at $\tau < +35$ d are used in the fit. We calculated the χ^2 statistic for all stretch-corrected data in the region $\tau \leq -10$ d for each template. We fit a fourth-order polynomial to the curve of reduced χ^2 as a function of t_r. The minimum of the polynomial is taken to be the rise time that best fits our data.

Performing a Monte Carlo simulation of this procedure to draw 500 unique realizations of our dataset, we find a best-fit rise time of 17.11 ± 0.09 d for our B-band template and 18.07 ± 0.11 d for our V-band template. These rise times disagree at the 4–5σ level with what we found above. It is unclear why these two procedures find such different results for the best-fit rise time for our template. However, when comparing a B-band template with a rise time of 17.11 d to the data after they have been two-stretch corrected using stretches found with fits restricted to $-10 < \tau + 35$ d, we see a significant systematic trend for data $\tau < -13$ d. Similar results are found in a V-band comparison with a template rise time of 18.07 ± 0.11 d. While the nature of the discrepancy eludes us, we use a B-band rise time of 17.92 ± 0.19 d and a V-band rise time of 19.12 ± 0.19 d to avoid introducing any systematic error. As a precaution, we have run our analysis using both sets of template rise times and find that while some of the final numbers change, they change systematically (by ~ 0.50–0.75 d) and do not affect any of our qualitative results or final conclusions. In Section 3.4.5, we discuss using different rise times in the context of searching for signatures of interaction with the companion star in the single-degenerate scenario.

We caution the reader from interpreting the above template rise times as the "typical" rise time of a SN Ia or even the rise time of a SN with $\Delta m_{15}(B) = 1.1$ mag. The rise time found above should be viewed as the rise time required to match the *shape* of our template light curve in the region $-10 < \tau < 0$ d. The rising portion ($\tau < 0$ d) of our template light curve based on the MLCS2k2 template does not *a priori* reflect a light curve with a decline $\Delta m_{15}(B) = 1.1$ mag. Thus far, the goal of constructing our template was to find a light-curve shape that will fit our sample by applying independent stretches to the rising and falling portions of the light curve. To that extent, the actual number associated with the template rise time is meaningless; the significance is in the *shape* of the light curve. For example, we could construct an equivalent B-band template with a rise time of 35.84 d by stretching the rising portion ($\tau < 0$ d) of our 17.92 d template by a factor of 2. Using a template with a rise time of 35.84 d would decrease the measured rise stretches by a factor of 2. The final rise time for each SN found by multiplying the rise stretch by the fiducial rise time of the template will be the same for both templates. In Section 3.4.1, we will use

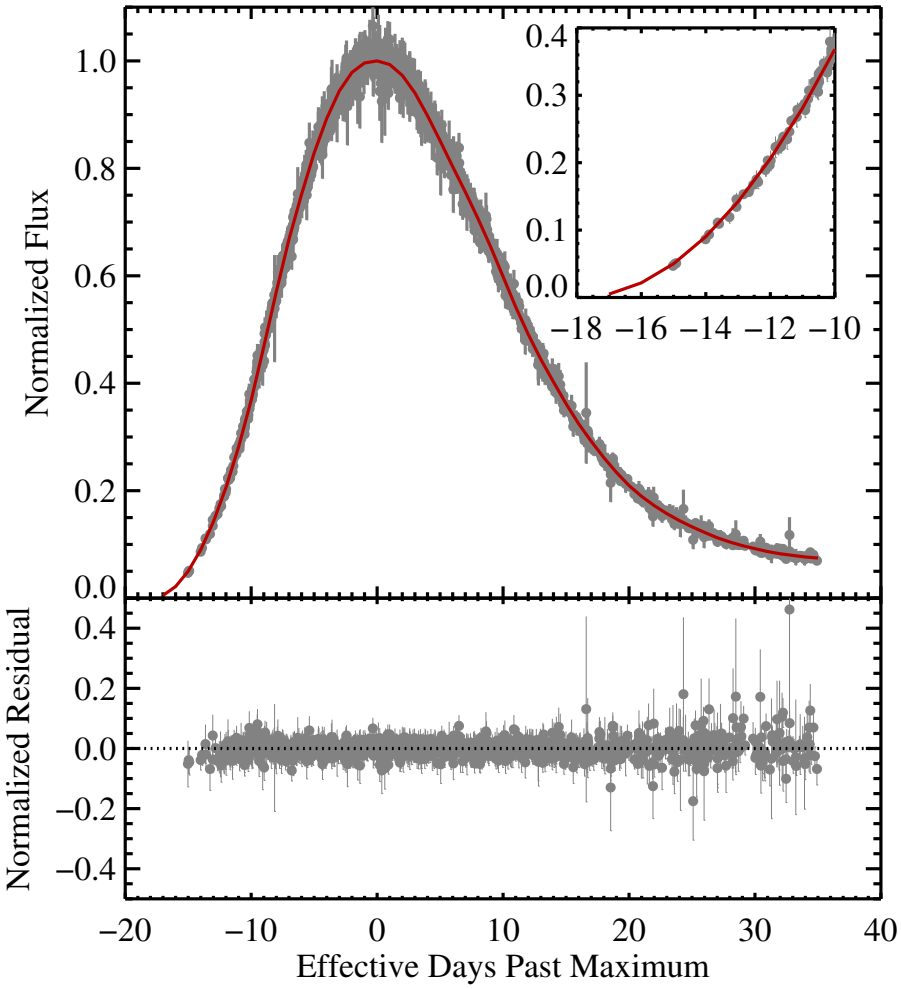

Figure 3.1: Stretch-corrected B-band light curves for 61 objects using the two-stretch method. All light curves have been shifted such that $\tau = 0$ d is at maximum light and they have the same peak flux. Overplotted in red is the LOSS template. We restrict our fits to data within 35 d of maximum light. The inset panel is a detailed view of the early-time rise of the SN. The bottom panel shows the residuals between the stretch-corrected data and the template normalized by the template flux.

the shapes of our template light curves to measure the rise and fall of our data sample and we will address the fall stretch-corrected rise time of SNe Ia in our sample.

Figure 3.1 compares our template light curve to the stretch-corrected light-curve data. Residuals to the fit scaled by the template flux are plotted in the bottom panel of the figure. The template fits all portions of the light curve, without any systematic trends in the residuals.

3.3.3 Estimating Uncertainties

To estimate the uncertainties in our fitting procedure, we use a Monte Carlo procedure including the effects of systematic calibration error from different photometric surveys, the uncertainty in rise time of our template, and the statistical photometric error. The prescription for one simulation for our Monte Carlo procedure is as follows.

1. For each survey, model calibration uncertainties by choosing a random photometric offset, and change all photometry from that survey by that random amount. The random offset is chosen for each survey assuming a Gaussian distribution with a mean offset of 0.0 mag and $\sigma = 0.03$ mag. SNe from the same survey will have the same photometric offset while SNe from a different survey may have a different offset.

2. Model the photometric error by perturbing every photometric point for each SN randomly based on its reported uncertainty, assuming the uncertainty is Gaussian.

3. Modify the LOSS template to have a rise time given by a random draw from a Gaussian distribution defined by the mean of 17.92 d and $\sigma = 0.19$ d for B or 19.12 d and $\sigma = 0.19$ d for V (see Section 3.3.2 for how these values were derived).

4. Fit simulated data with the modified template.

We perform 1000 Monte Carlo simulations for our B- and V-band photometry independently. We take the parameter uncertainties to be the standard deviation in our 1000 trials and keep track of the covariance matrix between fit parameters.

3.3.4 The Rise-Time Sample

We restrict our final sample to objects that have $\sigma_{t_{r,f}} \leq 1.5$ d in both the B and V bands to ensure that we are using objects where the rise and fall of the light curve are being fit well. By the nature of our Monte Carlo procedure, each light curve does not have a single value of χ^2 associated with it. We instead identify SN light curves which have a median

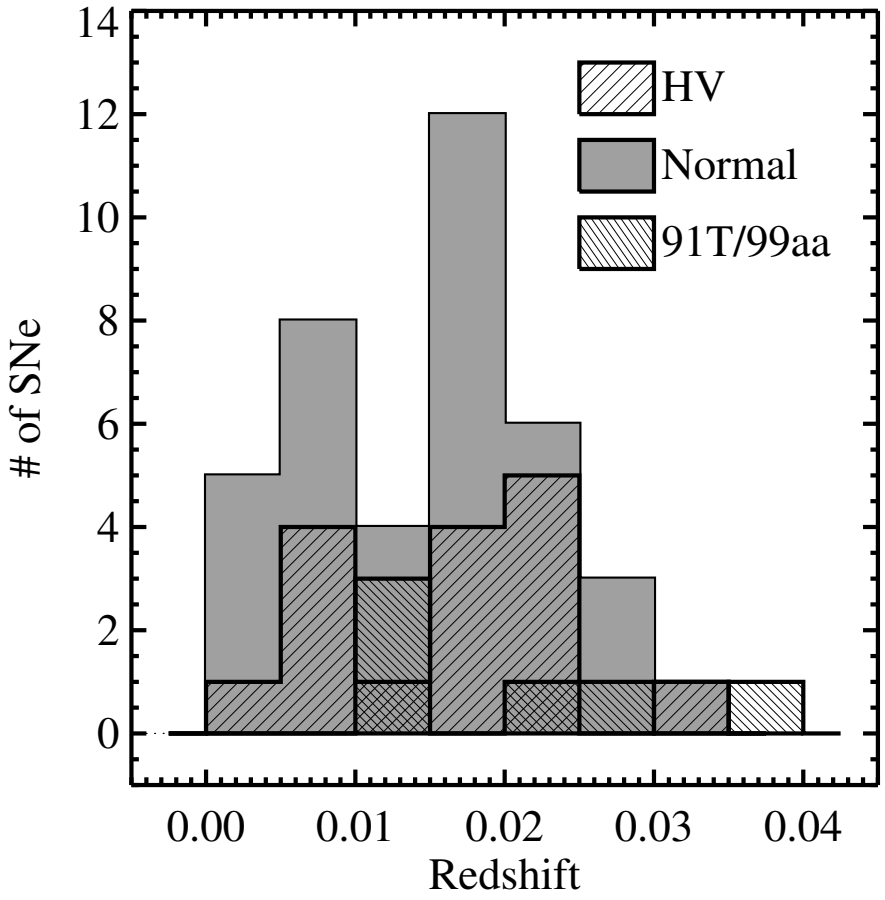

Figure 3.2: The redshift distribution of our sample broken into the three spectroscopic subclassifications: Normal, High Velocity, and SN 1991T/1999aa-like. The median redshift for the entire sample of 61 objects is 0.016.

reduced $\chi^2 < 1.5$ over the 1000 trials. Fits are visually inspected to identify the poor ones, which are excluded from our sample. We also place the somewhat strict requirement that the SN have data starting 7 *effective* days before maximum (defined by Equation 3.1) to anchor the measurement of s_r. We explore the effects of relaxing or tightening these requirements in Section 3.4.7 and find that changing the requirements does not affect our final results.

Objects similar to the subluminous SN 1991bg (Filippenko et al. 1992b; Leibundgut et al. 1993) were unable to be fit satisfactorily by our fitting routine. This is not surprising given the significant differences in light-curve shape and spectral evolution between the SN 1991bg-like SNe Ia and "Branch-normal SNe Ia" (Branch & Tammann 1992). In Section 3.4.6 we discuss our attempt to measure the rise times of SN 1991bg-like objects. We also exclude SN 2005hk, which is of the peculiar SN 2002cx subclass (Li et al. 2003b; Jha et al. 2006a; Phillips et al. 2007).

Of the initial BV light curves for 398 SNe, 95 have data starting at least 7 effective days before maximum light that could be fit with our two-stretch routine. Of the 95, 63 have good fits with rise and fall times that be can reasonably measured to within an uncertainty of 1.5 d.

For the purposes of analysing the rise time of different spectroscopic subclasses, we further break our sample into three groups: Normal, High Velocity (HV), and SN 1991T/1999aa-like (Filippenko et al. 1992a; Li et al. 2001b; Garavini et al. 2004). For the classification of HV objects, we adopt the criterion of Wang et al. (2009a) that the average $v_{\rm Si}$ for spectra taken within one week of maximum light is $\geq 1.2 \times 10^4$ km s^{-1}. Objects which have $v_{\rm Si} \leq 10^4$ km s^{-1} (more typical Si velocities for a normal SN Ia) are classified as normal SNe Ia.

We also spectroscopically identify SN 1991T/1999aa-like objects in our sample. The combination of SN 1991T-like and SN 1999aa-like objects is based off of previous studies which note the similar photometric and spectroscopic properties of the two subtypes (Li et al. 2001b; Strolger et al. 2002). In particular, both exhibit broad light curves ($\Delta m_{15}(B) \approx$ 0.8–0.9 mag) and spectra indicative of higher photospheric temperatures than normal SNe Ia (see Filippenko 1997 for a review of the spectroscopic diversity of SNe Ia).

Our subclass information comes from spectra taken within one week of maximum light observed as part of the Berkeley SuperNova Ia Program (BSNIP; Silverman et al. 2012c). Using a modified version of the SuperNova IDentification (SNID) code (Blondin & Tonry 2007), we are able to classify SN spectra using a cross-correlation algorithm against a spectral database of know subtypes. Classification of SN 1991T/1999aa-like objects requires a spectrum within a week of maximum light to avoid confusion with normal SNe Ia (Li et al. 2001b).

In instances where a SN in our sample has a classification in Wang et al. (2009a), we

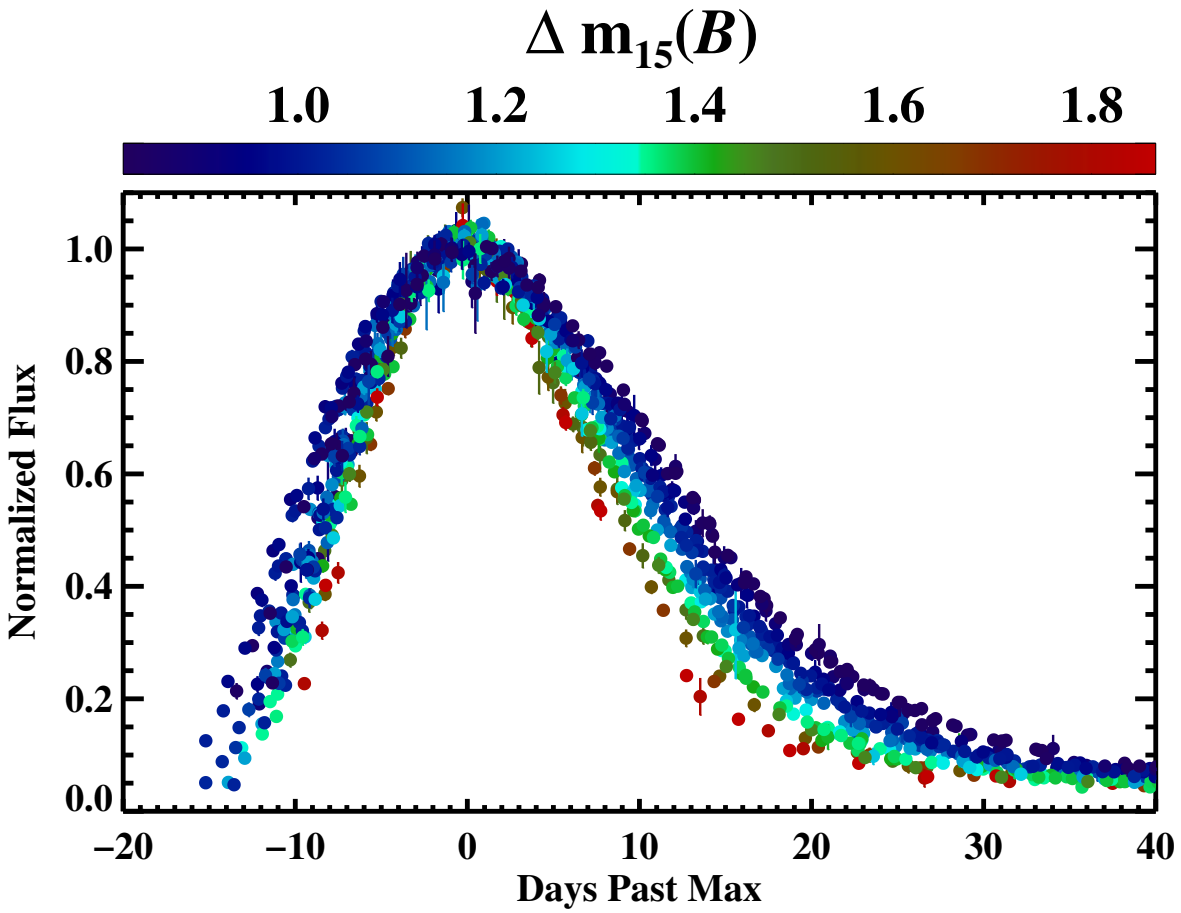

Figure 3.3: B-band light curves for the SNe used in this analysis. The light curves have been shifted such that they share the same peak flux and $t = 0$ is the time of maximum light. The light curves are well sampled and start at least one week before maximum light. The SNe are coded by $\Delta m_{15}(B)$ which measures the the post-maximum decline. The collection of light curves strongly suggests that SNe with slow rise also have a slow decline.

adopt their subclassifications. Otherwise, our subclassifications are based on BSNIP spectra. We are left without subclass identifications for only SNe 1992bo and 1992bc; hence, these two objects are excluded from our subsequent analysis. Our final sample consists of 61 SNe, including 39 normal, 16 HV, and 6 SN 1991T/1999aa-like SNe. Figure 3.2 shows the redshift distribution of our sample for each of the three spectroscopic subclassifications.

We plot the B-band light curves for the 61 SNe that passed our cuts in Figure 3.3. The SNe are shifted relative to the time of maximum light and normalized to have the same peak flux. Qualitatively, objects with slower post-maximum declines (i.e., smaller $\Delta m_{15}(B)$) have slower rise times. In Section 3.4.1, we explore this relationship in more depth.

H10 analyze a sample of 41 nearby SNe Ia drawn from S07, R99, and the CfA3 sample (Hicken et al. 2009b). Our analysis benefits from the addition of the LOSS SN Ia sample which has BV data starting at least a week before maximum light for 70 SNe. Data from the LOSS sample make up $\sim$70% of the objects that pass our cuts.

3.3.5 B- and V-Band Results: To Combine or Not to Combine?

In similar analyses of the B-band rise-time distribution, S07 and H10 combine stretches in the B and V bands using an error-weighted mean to produce a final single B-band rise time and fall time for each SN. H10 found evidence for a weak trend between the difference in stretch values for B and V as a function of $\Delta m_{15}(B)$ using measurements for 105 SDSS-II SNe Ia.

We take a different approach and independently measure the B-band and V-band rise times from the corresponding photometric data. However, we can use the results of our fitting routine to look for similar trends in the B-band rise time. In this section, we compare the B-band rise time derived from the B band to that derived from the V band. The B-band rise time found using the V-band data is measured by taking the V-band rise time and subtracting the time between maximum light in the V and B bands.

Comparisons by H10 are done in stretch space, while ours are between the measured rise/fall time. H10 use a single template rise time of 16.5 d for both the B and V bands for fitting the rise stretch of their data light curves. Going from rise stretch to rise time only requires multiplying the measured rise stretch by the rise time of their fiducial template. Our fitting routine measures the rise and fall values of stretch using a Monte Carlo simulation which randomly chooses a template rise time based on the best-fit template rise time and its Gaussian uncertainty (see Section 3.3.3 for details). The measured rise-stretch values are tied to the template rise time used for the fit, making the rise time a more appropriate quantity to compare.

Table 3.1: Mean Differences in B-Band Rise Time Derived using B- and V-Band Photometry by Spectroscopic Subclassification

Subclassification	$t_r(B)(B) - t_r(B)(V)$
Normal	-0.79 ± 0.13 d
High Velocity	-1.08 ± 0.16 d
SN 1991T/1999aa-like	-1.17 ± 0.45 d
All	-0.91 ± 0.10 d

B-band Rise-Time Comparison

In Table 3.1, we show the differences in B-band rise time derived using the B band, $t_r(B)(B)$, and the V band, $t_r(B)(V)$, for our sample divided by spectroscopic subclassification.

For our entire sample of 61 SNe, we find a mean difference of -0.91 ± 0.10 d (standard error of the mean), in the sense that the B-band rise time is shorter using B-band photometry compared to that derived using V-band photometry. Breaking our objects by spectroscopic subclassification, the difference in B-band rise time found using B- and V-band photometry is -0.79 ± 0.13 d for normal SNe, -1.08 ± 0.16 d for HV SNe, and -1.17 ± 0.45 d for SN 1991T/1999a-like objects. We find evidence for a systematic difference of ~ 1 d between the 2 determinations of the B-band rise time.

In Figure 3.4 we plot difference in B-band rise time as a function of $\Delta m_{15}(B)$. There appears to be a small trend in the B-band rise time difference with increasing $\Delta m_{15}(B)$. Fitting a line results in a slope of -0.54 ± 0.44 d mag^{-1}. The slope is computed by bootstrap resampling our sample to give 1000 realizations of our dataset. The mean and standard deviation of the distribution of the fit slopes are adopted as the most probable slope value and 1σ uncertainty. We do not find evidence of a significant trend.

Our comparison shows evidence for a slight systematic trend that the rise time is ~ 1 d longer when measured with the V band. At least part of such a shift can be hidden by uncertainties in measuring the time of maximum flux of a light curve where the derivative slowly approaches 0 within a day of maximum light. Combining the two measurements will introduce systematic errors into an analysis.

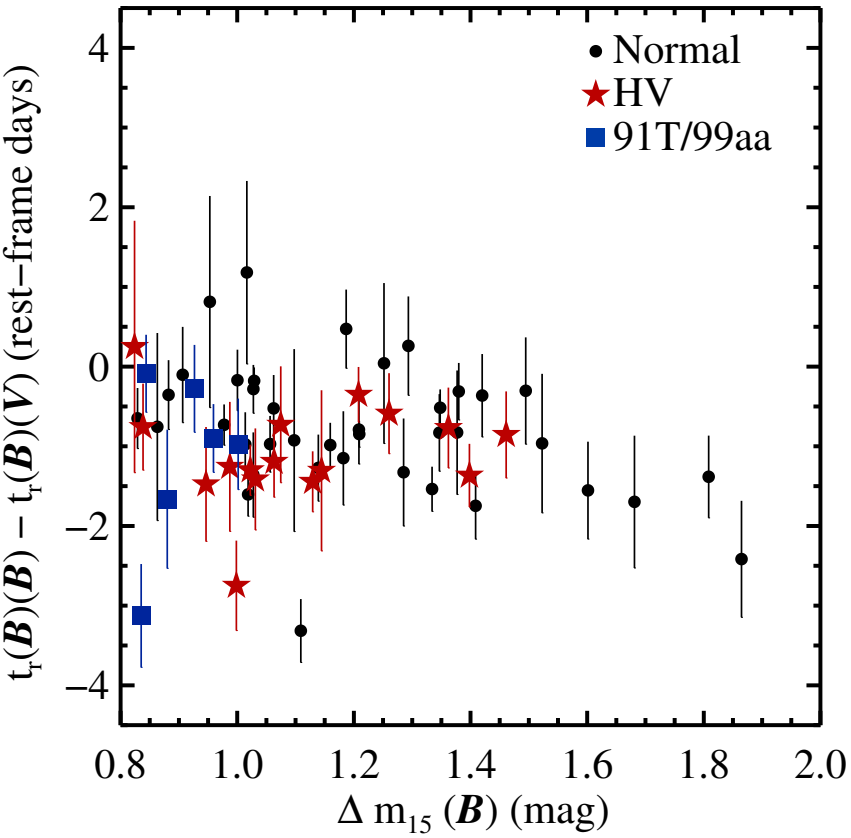

Figure 3.4: Difference in the rest-frame B-band rise time derived from the B band, $t_r(B)(B)$, and the V band, $t_r(B)(V)$, as a function of $\Delta m_{15}(B)$. Differences are generally small, although there appears to be a small trend in the rise time as a function of $\Delta m_{15}(B)$. We find evidence for a systematic difference between the two measurements.

Table 3.2: Mean Differences in B- and V-Band Fall Times by Spectroscopic Subclassification

Subclassification	$t_r(B)(B) - t_r(B)(V)$
Normal	-0.20 ± 0.08 d
High Velocity	-0.19 ± 0.22 d
SN 1991T/1999aa-like	-0.32 ± 0.39 d
All	-0.21 ± 0.09 d

Fall-Time Comparison

In a comparison of fall-time stretches derived from the B and V bands by H10, the authors found that objects with small $\Delta m_{15}(B)$ had a larger B-band fall stretch than V-band fall stretch (i.e., $t_f(B) > t_f(V)$). We look for a similar trend in our data.

Recall that the B-band fall time is defined as the amount of time it takes for the B-band light curve to fall by 1.1 mag after maximum light in B, and the V-band fall time is defined as the amount of time it takes for the V-band light curve to fall by 0.66 mag after maximum light in V. By construction, our templates both have a fall time of 15 d.

In Table 3.2 we show the difference in fall times between the B and V bands (i.e., $t_f(B) - t_f(V)$). A comparison of the fall times for all 61 objects gives a mean difference of -0.21 ± 0.09 d (standard error in the mean) between the B and V bands for all objects. There is no significant mean difference in the fall time measured between the B and V bands across all subclassifications.

We plot the difference in fall times as a function of $\Delta m_{15}(B)$ in Figure 3.5. The mean fall-time difference is consistent with 0 d. Fitting a line to the data, we measure a slope of -0.47 ± 0.36 d mag^{-1}, finding no significant evidence for a trend.

3.4 Analysis

In this section we present our analysis of the B- and V-band rise-time distribution of our nearby sample. Given the results found in Section 3.3.5, we treat the B and V bands separately. In the following analysis, the rise time for a given band is defined as the elapsed time between explosion and maximum light in that band. Note that the results are not

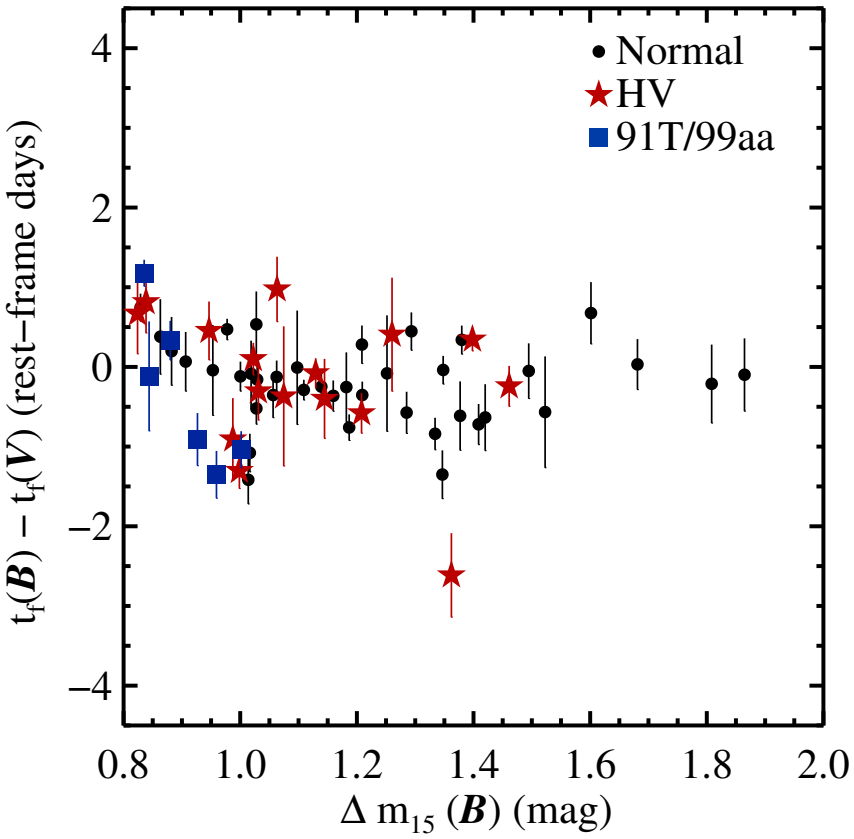

Figure 3.5: Difference in the fall times in the B band, $t_f(B)$, and the V band, $t_f(V)$. The difference is consistent with 0 d.

corrected for stretch unless indicated by a $'$ symbol, in which case the quantity is corrected for fall stretch.

3.4.1 Rise Times Correlated with Decline

In Figure 3.6, we plot the rest-frame B-band rise time as a function of $\Delta m_{15}(B)$ and the rest-frame V-band rise time as a function of $\Delta m_{15}(V)$ for our nearby sample of 61 objects. In both bands, there is a strong correlation between the rise time and the post-maximum decline, although the scatter indicates that the situation is more complicated than a simple one-to-one mapping between light-curve decline and the rise time. In general, SNe with slower post-maximum declines (e.g., small $\Delta m_{15}(B)$/ $\Delta m_{15}(V)$) have longer rise times. This correlation is evident in B, but shows more scatter in V. Using 61 objects, we calculate a Pearson correlation coefficient of -0.69 ± 0.03 for B and -0.49 ± 0.04 for V. The probability of a Pearson coefficient < -0.49 for two uncorrelated variables and 61 measurements is $< 0.01\%$, indicating a highly significant correlation in both B and V. The correlation remains strong even when excluding SN 1991T/1999aa-like objects.

Figure 3.6 indicates that SN 1991T/SN 1999aa-like SNe (i.e., overluminous SNe Ia) have the longest rise times. In contrast, H10 find that overluminous events have some of the shortest B-band rise times in their sample. However, H10 have few overluminous events and spectroscopic identifications were not included in their analysis. Instead, identifications of overluminous objects were based on $\Delta m_{15}(B)$.

In Table 3.3, we give the fall-stretch corrected rise times, t_r', for the various spectroscopic subclassifications in our sample for the B and V bands. When B-band light curves are fall-stretch corrected to a light curve with $\Delta m_{15}(B) = 1.1$ mag (i.e., $s_f = 1$), the rise time of normal SNe Ia and HV objects is (respectively) 18.03 ± 0.24 d (uncertainty in the mean) and 16.63 ± 0.29 d, a $\sim 3\sigma$ difference. H10 found an average B-band rise of 17.38 ± 0.17 d for the SDSS sample, consistent to 2.2σ with our rise time for normal SNe Ia.

Table 3.3: Rest-frame, fall-stretch corrected B- and V-band rise times

Subclassification	$t_r(')(B)$	$t_r(')(V)$
Normal	18.03 ± 0.24 d	20.23 ± 0.44 d
HV	16.63 ± 0.29 d	19.43 ± 0.33 d
SN 1991T/1999aa-like	18.05 ± 0.69 d	20.00 ± 0.68 d

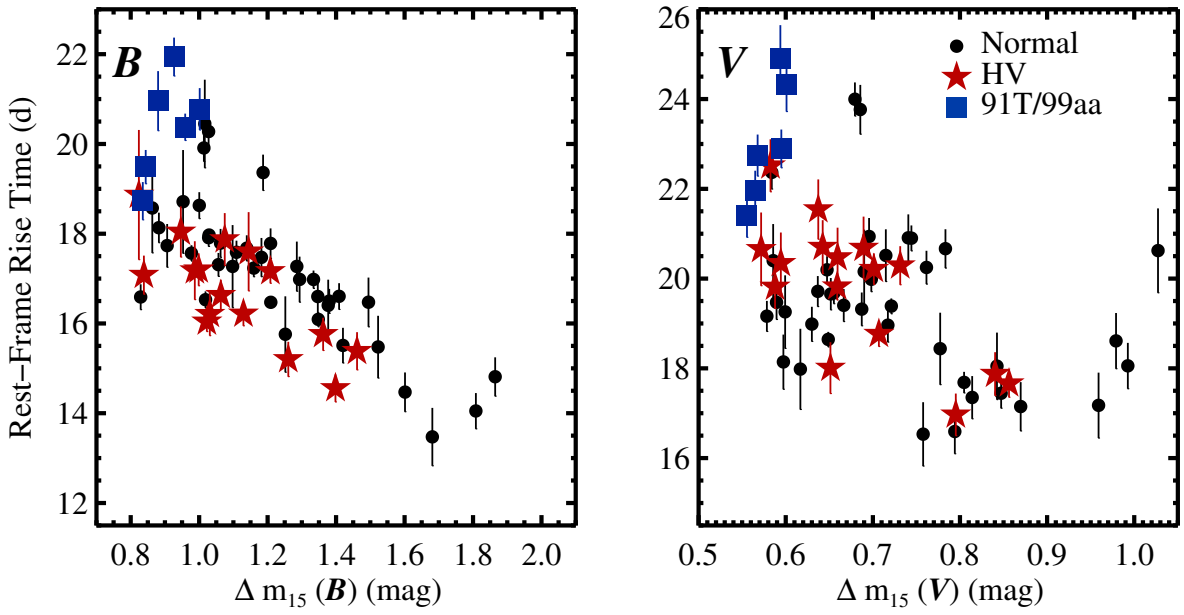

Figure 3.6: The rest-frame B-band rise time plotted as a function of $\Delta m_{15}(B)$ (left), and the rest-frame V-band rise time as a function of $\Delta m_{15}(V)$ (right). Note that the rise time is not stretch corrected. Using the two-stretch fitting method, we find a correlation between $\Delta m_{15}(B)$ (calculated from $s_f(B)$ and Equation 3.4) and rise time. SNe with smaller $\Delta m_{15}(B)$ (i.e., a slower post-maximum decline rate) have longer rise times. SNe that have been identified as HV are plotted as red stars. For fixed $\Delta m_{15}(B)$, HV SNe appear to have shorter rise times than their normal counterparts in the B band. Overluminous SN 1991T/1999aa-like objects are plotted as blue squares. These objects have the smallest values of $\Delta m_{15}(B)$ and the longest rise times. A less prominent, but similar correlation exists in $\Delta m_{15}(V)$ (calculated from $s_f(V)$ and Equation 3.5) and the V-band rise time.

When we correct our V-band rise times to $\Delta m_{15}(V) = 0.66$ mag by dividing by the V-band fall stretch for normal objects, we find a fall-stretch corrected, rest-frame V-band rise time of 20.23 ± 0.44 d (uncertainty in the mean). The fall-stretch corrected rise time of HV objects is 19.43 ± 0.33 d, consistent with the V-band rise time of normal objects. If we assume that a normal SN Ia with $\Delta m_{15}(B) = 1.1$ mag corresponds to $\Delta m_{15}(V) = 0.66$ mag, then the fall-stretch corrected V-band rise time is 2.20 ± 0.50 d longer than the B-band rise time. This is within 1.5σ of the 1.5 d difference reported by R99 despite our disagreement on the actual measured B-band and V-band rise times for a $\Delta m_{15}(B) = 1.1$ mag SN (R99 measure 19.5 ± 0.2 d and 21 ± 0.2 d for their B- and V-band rise times, respectively). For the HV objects, we measure a fall-stretch corrected rise-time difference of 2.80 ± 0.44 d. The larger difference (in absolute terms) in the B- and V-band rise times for HV objects compared to normal objects indicates that HV objects have a faster rise in the B band than in the V band (compared to normal objects).

3.4.2 The Rise Time of High-Velocity SNe

Plotted as red stars in Figure 3.6 are objects spectroscopically subclassified as HV, while normal SNe Ia are plotted as filled circles. In the B band, HV objects appear to lie along a locus of points below that of normal SNe. For a fixed $\Delta m_{15}(B)$ in the B band, HV objects have a shorter rise than normal SNe. Analysing smaller samples, Pignata et al. (2008) and Zhang et al. (2010) previously found that HV SNe Ia appear to have a faster B-band rise for a given $\Delta m_{15}(B)$. This result is not evident in the V band, where HV objects do not differ significantly from their normal counterparts.

The $\sim 3\sigma$ difference in fall-stretch corrected rise time between HV and normal objects in B and the lack of a significant difference in V provides evidence for subtle differences in the photometric evolution of these two subclassifications. Recent work by Wang et al. (2009a) and Foley & Kasen (2011) has shown that the two subclassifications have different $B_{\rm max} - V_{\rm max}$ pseudocolor[3] distributions, with HV objects typically having a redder pseudocolor. Furthermore, these studies have shown that separating HV and normal objects in cosmological analyzes reduces the scatter in a Hubble diagram from 0.18 mag to 0.12 mag.

Foley & Kasen (2011) provide a model which offers a possible explanation for why HV objects have a redder $B_{\rm max} - V_{\rm max}$ color at maximum light. The two dominant sources of opacity in the atmosphere of a SN are electron scattering and line opacity from Fe-group elements. Electron scattering opacity is wavelength independent, while line opacity from Fe-

[3]Note that $B_{\rm max} - V_{\rm max}$ is the B-band magnitude at maximum light in the B band minus the V-band magnitude at maximum light in the V band. The dates of maximum light are typically offset by $\sim$2 d, making this quantity not an actual observed color of the SN at a discrete time.

group elements is most significant at wavelengths shorter than 4300 Å (Kasen & Plewa 2007, hereafter KP07). The transition from electron scattering to Fe-group line opacity occurs near the peak of the B band. SNe with high-velocity ejecta will have broader Fe-group absorption features, which will decrease flux in the B band while having little effect on V-band flux.

Foley & Kasen (2011) analyze models of an off-center failed deflagration to detonation from KP07 to explore the expected differences in observables of HV and normal SNe. The KP07 models studied a single SN with an off-center ignition viewed from different angles. When viewed on the side nearest the ignition, the KP07 models produce a SN with HV features. When viewed from the side opposite the ignition, we will view a normal SN. Although the models presented in KP07 were intended to study the observational consequences of off-center explosions, their model spectra and light curves conveniently produce a similar distribution of ejecta velocities to that observed between normal and HV SNe depending on viewing angle. The set of models predicts that HV objects should have redder colors at maximum light in comparison to normal objects (see Fig. 8 of Foley & Kasen 2011) on theoretical grounds.

Using the model light curves of KP07, we can explore how the rise time of HV objects will differ from that of normal objects. If all other parameters are equal (i.e., Nickel mass, kinetic energy, etc.), the KP07 model predicts that HV SNe should have shorter rise times in B compared to normal SNe (as indicated by the model light curves in their Fig. 11) due to the enhanced line opacity from Fe-group elements. Although not specifically stated by KP07, one would expect the V-band rise time of the two subclasses to be similar, since the opacity in this wavelength range is dominated by electron scattering.

Consequently, the KP07 models also predict that the enhanced opacity at blue wavelengths from HV components in the SN ejecta reduce the peak absolute B-band magnitude and hasten the evolution of the B-band light curve, producing a larger $\Delta m_{15}(B)$. This complicates a direct comparison between the rise time of HV and normal SNe and does not necessarily predict the observed result in the left panel of Figure 3.6, that HV SNe lie on a locus of points below that of normal SNe in the $\Delta m_{15}(B)$–t_r plane. One expectation of the KP07 models is a $\Delta m_{15}(B)$ distribution for HV objects that is pushed to larger values in comparison to normal objects. We find a median $\Delta m_{15}(B)= 1.09$ mag for the HV objects and a median $\Delta m_{15}(B)= 1.11$ mag for the normal objects. However, our sample is most likely not representative of a complete sample of SNe Ia and suffers from observational bias.

Without quantifying how HV ejecta change both $\Delta m_{15}(B)$ and t_r, we cannot definitively claim that the models of KP07 explain our result. While it is beyond the scope of this chapter to match theoretical models to our observations, the KP07 models offer a possible qualitative explanation for why there are significant differences between HV and normal SNe in the B

band, but not in the V band.

Recent work by Maeda et al. (2010) finds evidence that SNe with a high velocity gradient (HVG) in the Si II line may be the natural result of viewing an asymmetric explosion. HVG SNe are defined by Benetti et al. (2005) as SNe that exhibit a time derivative in the velocity of the Si II line > 70 km s^{-1} d^{-1} around maximum light. Benetti et al. provide evidence that the HV and HVG subclassifications are highly correlated. Looking at the Fe II λ7155 and Ni II λ7378 nebular emission in late-time spectra that trace the deflagration ashes, Maeda et al. find that HVG SNe tend to exhibit redshifted lines while low-velocity gradient (LVG) SNe show a blueshift. The authors attribute this observational distinction to the difference between viewing an asymmetric explosion from the side nearest the site of initial deflagration (LVG) and the opposite side (HVG). The models of asymmetric explosions of SNe Ia presented by Maeda et al. (2011, hereafter M11) indicate that viewing a SN from the far side, one expects HVG SNe to have longer bolometric rise times and smaller $\Delta m_{15}(B)$ than comparable LVG SNe. This effect is more prominent in SNe with less ^{56}Ni (for instance, compare models A0.3 and A0.6 in Fig. 11 of M11). The longer rise times in HVG objects is attributed to an increased optical depth for optical photons when viewing the explosion from the side opposite the explosion site (i.e., the site of ^{56}Ni synthesis).

This is not necessarily inconsistent with our observational result that the HV SNe have a different rise-time distribution than normal SNe. If we view the SN from the side nearest the initial explosion site, we will see a LVG SN, and if we view the SN from the opposite side, we will see a HVG SN. Assuming HVG implies HV, we will measure a longer rise time and a smaller $\Delta m_{15}(B)$ for a high-velocity object assuming the B band roughly traces the bolometric behaviour. This will move the HV object up and to the left of a normal SN in the $\Delta m_{15}(B)$–t_r plane (Fig. 3.6). Depending on how the viewing angle affects both rise time and $\Delta m_{15}(B)$, the models of M11 could put the locus of HV points below that of normal SNe. However, the models presented in M11 do not outright predict a difference in rise times of HV objects in the B and V bands.

The models of KP07 and M11 offer opposite theoretical predictions for the rise time of HV SNe in comparison to normal SNe. KP07 predict that HV SNe should have larger $\Delta m_{15}(B)$ and shorter rise times than normal SNe, while M11 predict smaller $\Delta m_{15}(B)$ and longer rise times. The differences are rooted in the nature of the SN asymmetry (i.e., the distribution of intermediate-mass elements and ^{56}Ni) and the treatment of opacity. KP07 use an expansion opacity formalism which sums over individual lines, while M11 use a frequency averaged gray opacity. A better test of the HV models may possibly be found by looking at the $\Delta m_{15}(B)$ distributions of a complete SNe Ia sample, since both models predict that that asymmetries should influence the measured $\Delta m_{15}(B)$. Wang et al. (2009a) found the

$\Delta m_{15}(B)$ distribution of HV and normal SNe to be strikingly similar despite different $B_{\max} - V_{\max}$ distributions, although it is not clear that their sample is complete.

Despite evidence that HV objects have different rise-time properties than normal SNe, a clear physical picture remains elusive. Further efforts in modeling HV objects may shed light on the rise-time distribution of the different spectroscopic subclassifications.

3.4.3 The Rise Minus Fall Distribution

In the top two panels of Figure 3.7, we compare the rise time minus the fall time (RMF) as a function of $\Delta m_{15}(B)$ for the B band (left panel) and $\Delta m_{15}(V)$ for the V band (right panel). Note that the RMF has not been stretch corrected. As in Figure 3.6, blue squares refer to SN 1991T/SN 1999aa-like objects, red stars refer to HV SNe Ia, and black circles refer to spectroscopically normal SNe Ia. Overplotted in a broken line is the expectation from a one-to-one mapping of rise time to fall time using a single-stretch parametrization. For the B band we use a fiducial 18.03 d rise time and for the V band we use a rise time of 20.23 d based on the fall-corrected rise times found in Section 3.4.1. Clearly, our sample does not strictly follow a single-stretch parametrization. Similar to the results of H10, a number of slowly declining objects have a faster rise time (i.e., a smaller RMF) than expected from a one-stretch parametrization in both B and V. We reiterate that based on the results of Figure 3.6, more luminous SNe have longer rise times than less luminous SNe; however, Figure 3.7 indicates that more luminous SNe have faster rise times than expected based on a single-stretch parametrization.

In the bottom two panels of Figure 3.7, we plot the rest-frame B- and V-band distributions of RMF for the various subclass identifications. In B, HV objects have a mean RMF of 1.55 ± 0.27 d (uncertainty in the mean) in comparison to normal SNe that have an RMF of 2.77 ± 0.20 d. The 4σ difference in mean RMF offers evidence that the two distributions may be drawn from different populations. The mean RMF for our sample by subclassification can be found in Table 3.4. Despite significant differences in the B band, the mean V-band RMFs for the spectroscopic subclassifications are consistent with one another.

A Kolmogorov-Smirnoff (K-S) test finds that the two groups of SNe have a $\sim 0.01\%$ probability of being drawn from the same B-band RMF distribution and a $\sim 44\%$ probability of being draw from the same V-band RMF distribution. The lone SN with RMF < -1 d in B is SN 1999ee. Mazzali et al. (2005) find evidence of high-velocity features in spectra taken before maximum light. However, we retain the classification of Wang et al. (2009a) and regard SN 1999ee as being normal.

Our application of the K-S test indicates that HV and normal objects have a high probability of being drawn from different populations. However, the K-S test does not

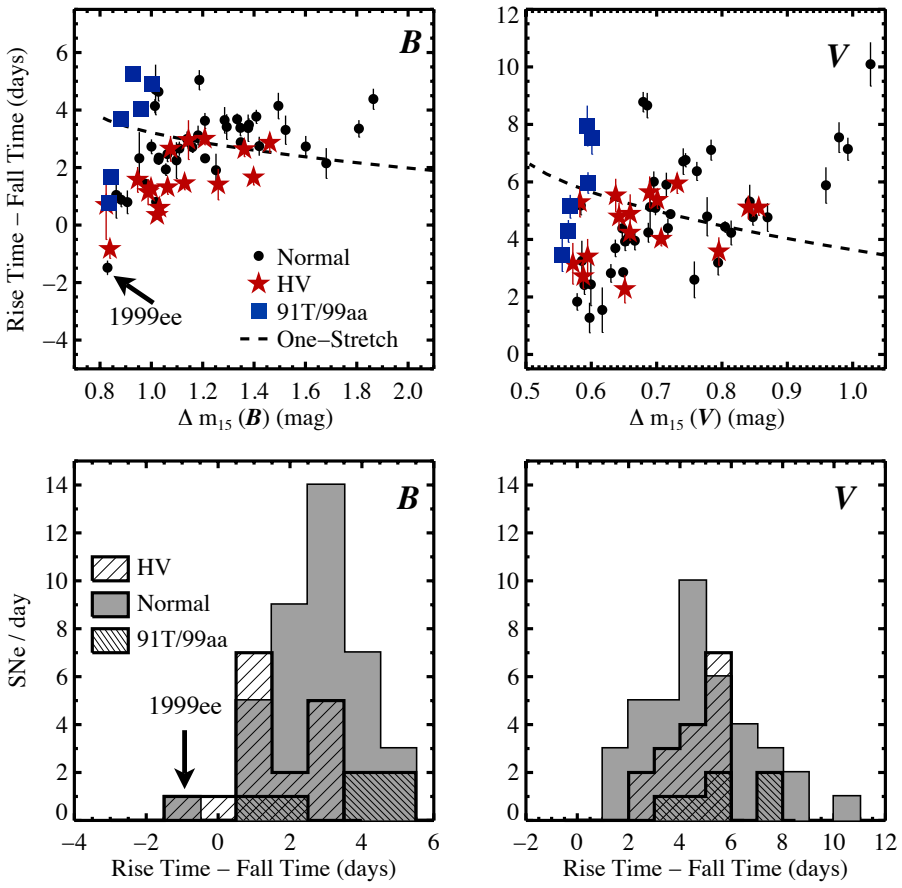

Figure 3.7: *Top panels:* The rest-frame corrected rise time minus the fall time (RMF) as a function of $\Delta m_{15}(B)$ for the B band (left) and of $\Delta m_{15}(V)$ for the V band (right). These quantities are not stretch corrected. Plotted as a dashed black line is the prediction using a single-stretch prescription where there is a one-to-one mapping of rise time to fall time. The nonlinearity in the prediction is due to the quadratic relationship between s_f and $\Delta m_{15}(B)$ in Equation 3.4. There is significant scatter about the line. We find that slowly declining SNe tend to have a faster rise than predicted by the single-stretch model. *Bottom panels:* The RMF distribution in the B and V bands. HV objects have a shorter B-band RMF in comparison to objects which are spectroscopically normal. A K-S test indicates a $< 0.01\%$ chance that the two distributions are drawn from the same parent distribution. No significant difference is seen in the V-band RMF distribution. SN 1999ee is the only normal SN with B-band RMF < -1 d, although a previous study noted HV features in spectra of this object (Mazzali et al. 2005).

reveal whether this difference is physical in origin or a reflection of observational bias. For instance, the difference in RMF between the two populations may also be a result of different stretch distributions. Such differences cannot be disentangled without knowledge of the observational bias in each of the photometric surveys used in our sample. Future surveys with proper spectroscopic follow-up observations and understanding of biases will aid in exploring the difference in RMF distribution for HV and normal SNe.

Our sample also includes 6 objects which show spectroscopic similarities to the overluminous SN 1991T or SN 1999aa. Based on the B- and V-band distribution of RMF for SN 1991T/1999a-like objects, these objects have slightly larger RMFs compared to normal and HV objects, however, the mean of the 1991T/1999aa-like distribution is consistent with the normal objects within 1σ.

S07 find evidence for two distinct RMF distributions using eight SNe. While we have presented evidence for distinct HV and normal populations, S07 only have a single HV object in their sample (SN 2002bo). The other seven SNe are classified as normal by the criterion of Wang et al. (2009a). We do not see evidence for two populations of rise times within our spectroscopically normal SNe.

Similar to the results of H10, we find that our sample does not follow the expectation from a one-stretch parametrization of light-curve shape. This is especially evident in V, where the trend appears to go in the opposite direction predicted by a single-stretch fit.

Table 3.4: Mean Rise Minus Fall Times for Different Spectroscopic Subclassifications

Subclassification	RMF (B)	RMF (V)
Normal	2.77 ± 0.20 d	4.83 ± 0.33 d
High Velocity	1.55 ± 0.27 d	4.45 ± 0.28 d
SN 1991T/1999aa-like	3.38 ± 0.73 d	5.72 ± 0.73 d

Note. – Quantities have not been corrected for stretch.

3.4.4 Rise-Time Power Law

Previously, we assumed the rise in flux took the form of a parabola, $n = 2$, based on physical arguments presented in Section 3.3.1. In this section, we fit for the functional form of the rising portion of the light curve ($\tau \leq -10$ d) as a power law of the form $f = A(\tau + t_r)^n$,

where t_r is the rise time. Allowing n to vary, we perform a χ^2 minimization to find the best-fit power law to our B-band photometry. However, unlike the analysis in previous sections, we restrict our two-stretch fitting procedure to $-10 < \tau < +35$ d in order to avoid imposing a shape on the region we plan to fit. We find a best fit of $n = 2.20^{+0.27}_{-0.19}$, consistent (1σ) with the expanding fireball modeled by a parabola. The uncertainty in the power-law index is found using a Monte Carlo simulation similar to that outlined in Section 3.3.3 except modified to only fit within the region $-10 < \tau < 35$ d.

Our result is in agreement with that of C06, who find $n = 1.8 \pm 0.2$, and H10, who find $n = 1.80^{+0.23}_{-0.18}$. However, H10 show evidence of significant color evolution during this period of light-curve evolution, challenging our assumption of modest temperature change. They find a linear $B - V$ color evolution of 0.5 mag between 15 d and 9 d before maximum light, leading to a temporal dependence closer to $n \approx 4$ rather than the $n = 2$ predicted by an expanding fireball.

We check for similar evidence of color evolution in the expanding fireball phase in our sample. Using the color curves for SNe in the range of $-15 < \tau < -9$ d relative to maximum light, we create a median $B - V$ color curve similar to the analysis presented by H10. We divide the data into 1 d interval bins and take the median $B-V$ color for each bin. Corrections for Milky Way extinction were made using the dust maps provided by Schlegel et al. (1998). No corrections were attempted for possible host-galaxy extinction. Our median color curve shows a small change of 0.05 mag over the 6 d interval. However, inspecting the $B - V$ color curve for SN 2009ig in this range, we find a drop of 0.5 mag over the same interval, similar to what is reported by H10. This leads us to suspect that our median color curve does not necessarily reflect the full sample, and at least in individual SNe, there can be significant color change at $\tau < -9$ d. The discrepancy between the median color curve and that of SN 2009ig may be a result of using noisy data in the earliest time bins for the median color curve.

3.4.5 Companion Interaction

Recently, Kasen (2010) proposed using emission produced from the collision of the SN ejecta with its companion star to probe the progenitor system. Similar to the shock break-out in core-collapse SNe that is theoretically well understood (e.g., Klein & Chevalier 1978; Matzner & McKee 1999) and observed (e.g., Soderberg et al. 2008; Modjaz et al. 2009), in the single-degenerate progenitor scenario the expanding SN ejecta are expected to collide with the extended envelope of the mass donating companion. In the case of a companion undergoing Roche-lobe overflow, the radius of the companion is on the same order of magnitude as the separation distance. The timing and luminosity emitted from

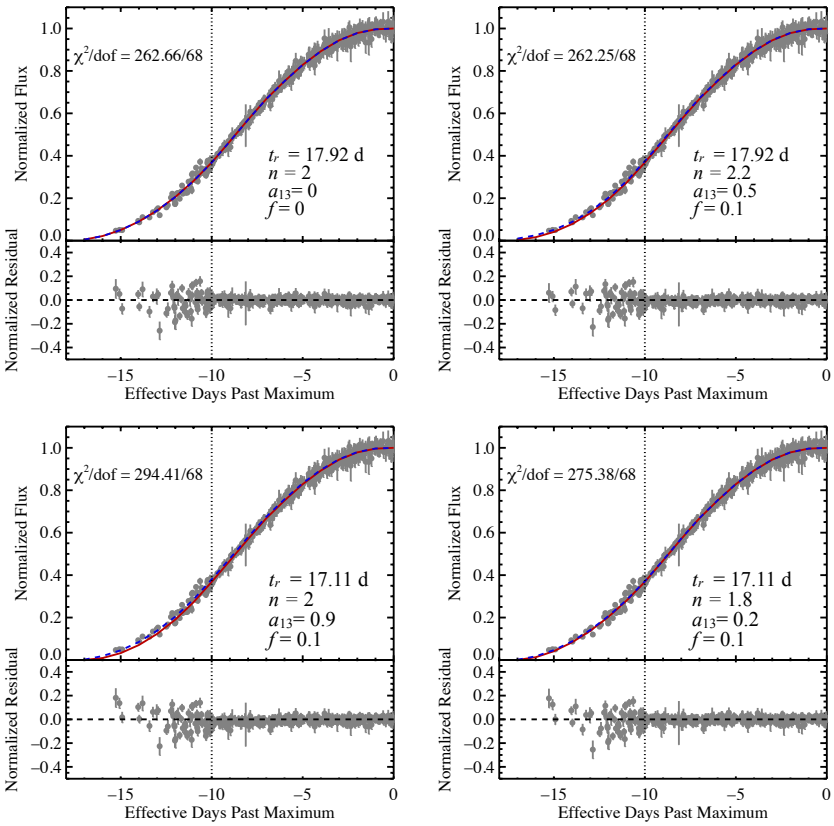

Figure 3.8: Two-stretch corrected B-band light curves compared to the expected flux of a collision between the SN ejecta and a 1 $M_\odot$ companion assuming the companion is undergoing Roche-lobe overflow. Only data in the range $-10 < \tau < +35$ d are used to stretch correct the light curves, to avoid imposing a shape onto data at $\tau \leq -10$ d. Plotted as a red line is the light-curve template with no shock interaction assuming various power laws for the initial rise, indicated by n, and rise times, t_r. Plotted as a blue dashed line is the expected "shocked template," which is the expected shock emission added to the template assuming different separation distances a_{13} and the fraction of SN explosions that show signs of interaction, f. The expected flux from the companion is estimated using the analytic models of Kasen (2010). The bottom plot for each panel shows the resulting normalized residual curve between the data and the "shocked template." We find a considerable degree of degeneracy between the adopted rise time, the power-law index for the initial rise, and the shock emission. As the four plots indicate, a similar minimum reduced χ^2 can be achieved with $n = 2$, $t_r = 17.92$ d and no shock emission (top left) or by varying the rise time, power-law index, and amount of shock emission (top right, bottom left, and bottom right, respectively).

the interaction will depend on the mass of the companion and the separation distance. The shock emission is expected to be brightest in the ultraviolet, but detectable in the B band. Hayden et al. (2010a) looked for this signal in the rising portion of the B-band light curves of 108 SDSS SNe Ia, finding no strong evidence of a shock signature in the data. Using simulated light curves produced with `SNANA` (Kessler et al. 2009b) and a Gaussian to model the shock interaction, the authors constrain the companion in the single-degenerate scenario to be less than a 6 $M_\odot$ main-sequence star, strongly disfavoring red giants (RGs) undergoing Roche-lobe overflow.

For this analysis, we focus on our B-band data where we have the best chance of detecting the signs of shock emission. Kasen (2010) predicts that in the initial few days after explosion, the luminosity produced by the interaction with the companion will dominate the luminosity powered by ^{56}Ni decay. Inspection of individual light-curve fits with the two-stretch fitting routine do not show the tell-tale signs of strong interaction. To take advantage of the power in numbers, we analyze all of the light curves as an ensemble. We then compare data from the earliest light-curve epochs to the models of Kasen (2010) to place constraints on the mass and distance to the companion.

We start by applying our two-stretch fitting routine again, but limiting the fit to data $-10 < \tau < +35$ d in order to avoid forcing a shape on the earliest data and possibly suppressing the signature of interaction. We construct models of "shocked" template light curves including contributions from companion interaction using the analytic solutions for the properties of the emission found by Kasen (2010). Using equations for $L_{\rm c,iso}$ and $T_{\rm eff}$ from Kasen (2010) (Eq. 22 and 25, respectively) and assuming the emission is that of a blackbody, we calculate the expected flux density at the peak of the B band ($\lambda_{\rm eff} = 4450$ Å) at a distance of 10 pc. We normalize the flux density from the shock to a peak SN Ia magnitude of $M_B = -19.3$ mag.

Based on the opening angle of the shock interaction, Kasen (2010) predicts that the interaction signature should be visible in $\sim 10\%$ of SN Ia explosions. Ideally, one should account for the viewing angle dependence of the detected shock emission. We make the simplification that we are either looking along the axis or we are not. Our light-curve models including the effects of interaction are the un-shocked template plus a fraction, f, of the collision flux calculated using the analytic model of Kasen (2010). A model with $f = 0$ represents a situation in which shock emission is never detectable (and reduces to the unshocked template) and $f = 1$ is a scenario in which shock emission is detectable in every SN explosion.

For most of the analysis in this chapter, we adopted an expanding fireball model for the early rise of the light curve ($\tau \leq -10$ d) which assumed a power-law index of $n = 2$.

Under this assumption, we found that our early-time data were best fit by a rise time of 17.92 d. However, as discussed in Section 3.4.4, the assumption that the initial rise of the light curve has $n = 2$ may be somewhat questionable given rather significant changes in SN color at early phases. As a test of the degeneracies between the added shock emission and the assumptions that go into constructing an unshocked template, we consider a number of different templates with different rise times and power-law indices. In addition to our nominal template with $t_r = 17.92$ d and $n = 2$, we also try templates with $t_r = 17.11$ d and $n = 2$, $t_r = 17.92$ d and $n = 2.2$, and $t_r = 17.11$ d and $n = 1.8$.

The parameters free to vary in the model for shock interaction are a_{13}, the distance to the companion normalized to 10^{13} cm, M_c, the companion mass, and f, the fraction of SN explosions that produce detectable shock emission. For this simple analysis the probed mass is fixed at $M_c = 1$ $M_\odot$, to explore RGs as a possible companion, and we set f equal to either 0 (i.e., no emission is detected) or 0.1, the expected fraction of SNe with detectable shock emission based on the opening angle of the shock. For each of our four different unshocked templates, we calculate the minimum χ^2 statistic for models by varying a_{13} to find the best-fit shocked template. The fit is restricted to data within the range of $-16 \leq \tau \leq -10$ d.

We note that the minimum reduced χ^2 in all of our fits for a_{13} exceeds 1 and is usually closer to 3–4. This is not completely unexpected since data at $\tau \leq -10$ d were not included in the two-stretch fitting procedure used to normalize the light curves, and this may induce correlated errors into the data at $\tau \leq -10$ d. We also suspect that the reported errors for the earliest photometry epochs may be underestimated. Furthermore, the scatter in the data points may even be the physical result of a distribution of companion masses, separation distances, and viewing angles contributing to the emitted flux from shock interaction. Unfortunately, we are not in a position to disentangle what is contributing to the scatter.

Our final results for each template are shown in Figure 3.8. Plotted in red are the unshocked templates and in blue are the shocked templates including some contribution of companion interaction. In each case of an unshocked template, we can find an acceptable fit with similar χ^2 by varying the separation distance. There is a significant degree of degeneracy between the parameters, making the task of disentangling the true sign of companion interaction at this level extremely difficult. For instance, for our template with $n = 2$ and $t_r = 17.92$ d, we do not see signs of any interaction. However, had we used a template with $n = 2$ and $t_r = 17.11$ d, we would find that if the fraction of SNe that showed signs of shock interaction is $f = 0.1$, then χ^2 is minimized with $a_{13} = 0.9$. Similarly, when varying n and t_r in the unshocked template, suitable matches to the data can be found by adjusting the amount of shock interaction.

The degeneracy is partially broken by increasing the contribution of companion inter-

action to the "shocked template" by either increasing f or a_{13}. Fixing $f = 0.1$ based on the expected opening angle of the shock, $a_{13} = 2$ increases the reduced χ^2 by more than 1 for all of our unshocked templates.

In summary, we find that with our limited sample of early-time data, we cannot completely disentangle the behaviour of the power-law index, the adopted rise time, and the amount of companion interaction. This result makes use of all of the light-curve data at $\tau \leq -10$ d as an ensemble. Better constraints could be placed on individual, excellently sampled light curves in the rise region. In particular, efforts to obtain data at bluer wavelengths, where the shock interaction is stronger and more easily detectable, will greatly help to break degeneracies in the fitting process.

Recently, Justham (2011) and Di Stefano et al. (2011) have argued that the transfer of angular momentum from the companion donor star to the C/O white dwarf acts to increase the critical mass required to explode and the time required for the white dwarf to explode. Consequently, the donor star may possibly evolve past the red giant phase, vastly reducing the cross section for interaction with SN ejecta. The subsequent shock emission for a RG would decrease beyond current detection limits, thus saving RGs as a possible donor in the single-degenerate scenario. The increased time to explosion allows the mass ejected from the envelope of the donor star time to diffuse to the density of the ambient interstellar medium, offering an explanation for the tight constraints placed on the presence of Hα in nebular spectra of SNe Ia (Leonard 2007, and references therein).

3.4.6 SN 1991bg-Like Objects

The analysis presented thus far has excluded SN 1991bg-like objects due to fits which had unacceptably large χ^2 per degree of freedom. To investigate what was causing the poor fits, we focus on the B-band light curve of the SN 1991bg-like SN 1999by from the LOSS sample, which has data starting about -10 d before maximum light in the B band. As seen in Figure 3.9, the largest difference in light-curve shape between SN 1999by and our template occurs at $t > +10$ d, where the light curve of SN 1999by transitions to a slower linear decline not seen until $t > +30$ d in normal SNe Ia. Similar differences in light-curve shape for SN 1991bg are found by Filippenko et al. (1992b) and Leibundgut et al. (1993). The fit parameters of s_f and s_r are correlated; thus, a bad fit for s_f will propagate into an incorrect determination of s_r. Given the different light-curve shapes for SN 1991bg-like objects and normal objects for $t > 10$ d, we are unable to acceptably fit s_f and thus s_r. For the purposes of exploring the rise time of SN 1991bg-like objects, we restrict our fit to the pre-maximum portion of the light curve using the date of maximum found with a low-order polynomial fit. For SN 1999by, we find a best-fit rise time of 13.33 ± 0.40 d (overplotted

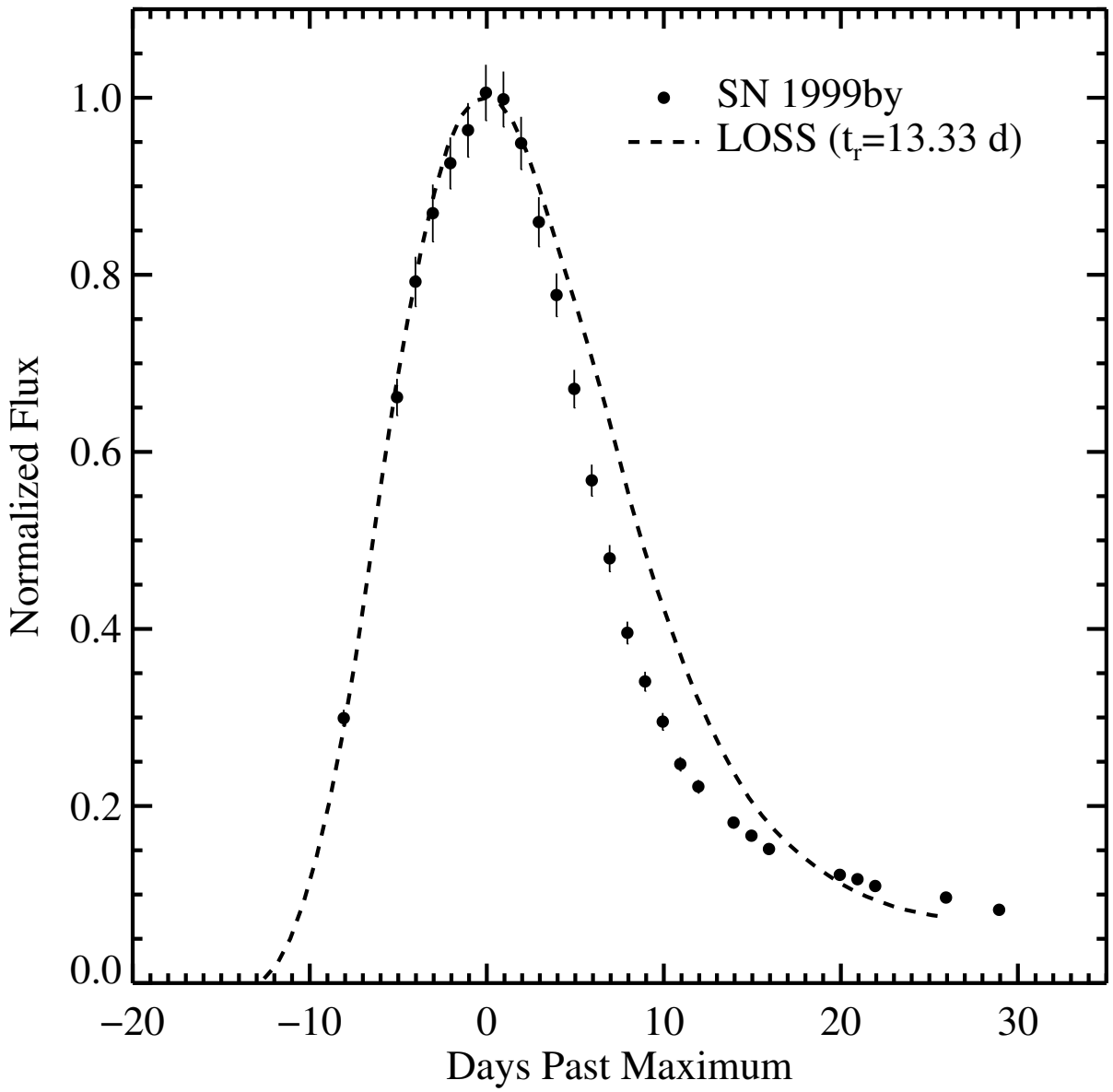

Figure 3.9: Comparison of the B-band light curve for the SN 1991bg-like SN 1999by (solid circles) and the LOSS template (black dashed line) stretched along the time axis by 0.74 to match the rise portion of the light curve. The light-curve evolution of SN 1999by for $t > 10$ d past maximum makes it impossible to find a reasonable fit using our two-stretch fitting routine. If we restrict our fit to the pre-maximum portion of the light curve, we find a rise time of 13.33 ± 0.40 d.

as dashed lines in Fig. 3.9), indicating that they join other objects with large $\Delta m_{15}(B)$ as the fastest risers in our sample. This matches the qualitative results found by Modjaz et al. (2001) for the SN 1991bg-like SN 1998de.

3.4.7 Impacts of Fitting Cuts

To ensure that the results described in the previous sections are not a result of the cuts made in Section 3.3.4, we reanalyze our data, both tightening and relaxing the constraints on the uncertainty in t_r and t_f, $\sigma_{t_{r,f}}$. Most of the reported results are not highly sensitive to fitting cuts. Restricting acceptable fits to reduced $\chi^2 = 1.5$, a first epoch at $\tau = -10$ d, and $\sigma_{t_{r,f}} = 1$ d decreases the number of available objects to 26 normal, 9 HV, and 3 SN 1991T/SN 1999aa-like SNe Ia. The probability that the B-band RMF populations are drawn from the same parent population increases to $\sim 4\%$. The difference in the B-band fall-time corrected rise time, $t_r{}'$, between HV and normal SNe remains significant at -1.44 ± 0.49 d, indicating a faster rise for HV objects. Relaxing constraints to a reduced $\chi^2 = 2$, first epoch at $\tau = -5$ d relative to maximum light, and $\sigma_{t_{r,f}} = 1.5$ d increases the difference in fall-stretch corrected B-band rise time between HV and normal objects to -1.86 ± 0.49 d. The V-band rise times remain consistent between HV and normal objects, as do the V-band RMF distributions. Overall, changing what we define as an "acceptable" fit does not impact our results.

3.5 Discussion

We have presented an analysis of the rise-time distribution of nearby SNe Ia in the B and V bands. Using a two-stretch fitting technique, we find that the SN rise time is correlated with the decline rate in the sense that SNe with broader light curves post-maximum (i.e., light curves with small $\Delta m_{15}(B)/\Delta m_{15}(V)$) have longer rise times. While SN 1991bg-like objects could not be fit well by our two-stretch fitting procedure, we found that restricting our analysis to the pre-maximum data for the SN 1991bg-like SN 1999by gives a rise time of 13.33 ± 0.40 d. This follows the expected trend of a fast rise leading to a fast decline.

Using a sample of 105 SDSS SNe at intermediate redshifts ($0.037 \leq z \leq 0.230$), H10 find that there is a great diversity in B-band rise times for a fixed $\Delta m_{15}(B)$, and that the slowest declining SNe tend to have the fastest rise times. While we do see evidence for scatter in rise times with $\Delta m_{15}(B)$, we find a strong correlation between $\Delta m_{15}(B)$ and rise time in the sense that slowly declining SNe Ia have longer rise times. This correlation is strong in the B band, but weaker in the V band. The discrepancy with H10 may be a result of combining

B- and V-band stretches which was avoided in this analysis.

We find that a single value of the stretch does not adequately describe the rising and falling portions of our light curves. Similar to the results in H10, more luminous SNe with longer fall times have shorter rise times than one would expect from a single-stretch prescription for light curves. This is especially evident in our analysis of V-band light curves. However, we reiterate that while luminous SNe have shorter rise times than expected from a single-stretch prescription, they still have longer rise times than less luminous SNe, contrary to the findings of H10.

R99 and C06 found a fiducial B-band rise time of ~ 19.5 d for a "typical" SN Ia. In a departure from previous results, H10 report an average rise time of 17.38 ± 0.18 d. We find a fall-stretch corrected (i.e., corrected to have a post-maximum fall of $\Delta m_{15}(B) = 1.1$ mag) B-band rise time of 18.03 ± 0.24 d for spectroscopically normal SNe and 16.63 ± 0.30 d for HV SNe. Our B-band rise time for spectroscopically normal SNe with $\Delta m_{15}(B) = 1.1$ mag is in agreement with the average rise time found by H10 at the 2.2σ level. When correcting our V-band light curves to a post-maximum fall of $\Delta m_{15}(V) = 0.66$ mag, we find a fall-stretch corrected V-band rise time of 20.23 ± 0.44 d.

After correcting for post-maximum decline rate, HV SNe Ia have faster rise times than normal SNe Ia in the B band, but similar rise times in V. We find a $\sim 3\sigma$ difference in the fall-stretch corrected rise time between HV and normal SNe in the B band. The rise minus fall (RMF) distributions (not corrected for stretch) of the two subclassifications show significant differences in the two populations. The peak values of the distributions are offset by 1.22 ± 0.34 d in the B band, with HV objects having a faster rise time. A K-S test indicates a $\sim 0.01\%$ probability that HV SNe come from the same parent RMF population as normal SNe in the B band. Despite differences in the B band, we see no evidence of a difference in the RMF populations in the V band.

Based on the model presented by Foley & Kasen (2011) and the models of KP07, we offer a possible qualitative explanation for why HV SNe should have a different B-band rise-time distribution than normal SNe, but similar V-band distributions. The physical origin of the difference is possibly rooted in the different opacity mechanisms at work in the B and V bands. Line blanketing from Fe-group elements is the dominant source of opacity for wavelengths shorter than ~ 4300 Å, the peak of the B band. At longer wavelengths, such as the V band, electron scattering is the dominant source of opacity. Rapidly moving ejecta, as is the case with HV objects, will broaden absorption features, diminishing the B-band flux without affecting the V-band flux. Models from KP07 show that all other things being equal (e.g., Ni mass, kinetic energy), this leads to faster light curves with larger $\Delta m_{15}(B)$ for HV objects. However, the enhanced opacity at short wavelengths also affects $\Delta m_{15}(B)$,

complicating the application of the models to our result. Further modeling and observations of HV SNe Ia are required to shed light on the photometric differences of this spectroscopic subclass.

We fit the earliest data in our sample ($\tau \leq -10$ d) to find that the flux rises as a power law with index $2.20^{+0.27}_{-0.19}$. This is consistent with the unimpeded, free expansion of the expanding fireball toy model that predicts an index of 2. However, a preliminary analysis of SN 2009ig in the range $-15 < \tau < -9$ d shows evidence of significant color evolution, contrary to the assumption of little to no color evolution in the expanding fireball model. H10 find similar color evolution in an analysis of the $B - V$ color curve of SDSS SNe Ia and derive an expected power-lax index of 4.

We compare our early-time B-band data as an ensemble to models (Kasen 2010) of shock interaction produced from SN ejecta colliding with the mass-donating companion in the single-degenerate progenitor scenario. When relaxing our assumptions on the functional form of the early-time template light-curve behaviour (i.e., changing the rise time or power-law index of the rise), we find that our data require some amount of shock interaction to remove systematic trends. This indicates a level of degeneracy between the adopted template rise time, the power-law index, and the amount of shock interaction required to match the data.

Future surveys with high-cadence search strategies will provide well-sampled SN light curves starting days after explosion, substantially adding to the sample of rise-time measurements. Complemented with spectroscopic follow-up observations, analysis of the RMF distribution can be further broken into different spectroscopic classes to provide insights into the underlying populations and the physics that differentiates them.

Chapter 4

Constraints on Dark Energy with the LOSS SN Ia Sample

Abstract

We present a cosmological analysis of the Lick Observatory Supernova Search (LOSS) Type Ia supernova (SN Ia) photometry sample introduced in Chapter 2. These SNe provide an effective anchor point to estimate cosmological parameters when combined with datasets at higher redshift. The data presented in Chapter 2 have been re-reduced in the natural system of the KAIT and Nickel telescopes to minimize systematic uncertainties. We have run the light-curve fitting software SALT2 on our natural-system light curves to measure light-curve parameters for LOSS light curves and available SN Ia datasets in the literature. We present a Hubble diagram of 586 SNe in the redshift range $z = 0.01$-1.4 with a residual scatter of 0.176 mag. Of the 226 low-z objects in our sample, 91 objects are from LOSS, including 45 SNe without previously published distances. Assuming a flat Universe, we find a best-fit $w = -0.86^{+0.13}_{-0.16}$ (stat) ± 0.11 (sys) from SNe only; consistent with a cosmological constant. Our data prefer a Universe with an accelerating rate of expansion with 99.999% confidence. When looking at Hubble residuals as a function of host-galaxy morphology, we do not see evidence for a significant trend, although we find a somewhat reduced scatter in Hubble residuals from SNe residing within a projected distance < 10 kpc of the host-galaxy nucleus ($\sigma = 0.156$ mag). Similar to the results of Blondin et al. (2011) and Silverman et al. (2012a), we find that Hubble residuals do not correlate with the expansion velocity of Si II λ6355 measured in optical spectra near maximum light. Our data are consistent with no presence of a "Hubble bubble." Improvements in cosmological analyses within low-z

samples can be achieved by better constraining calibration uncertainties in the zero points of photometric systems.

4.1 Introduction

Type Ia supernovae (SNe Ia) are believed to be the thermonuclear explosion of a white dwarf undergoing mass transfer from a companion star; see Hillebrandt & Niemeyer (2000) for a review. At peak brightness, the luminosity of a SN Ia ($M_B \approx -19.2$ mag) can rival that of its host galaxy and is reasonably standard from event to event ($\sigma \approx 0.5$ mag). Observed correlations between light-curve properties and luminosity further allows SN Ia to be standardized to within ∼0.2 mag (∼10% in distance) (Phillips 1993; Tripp 1998; Phillips et al. 1999). These properties make SNe Ia a ideal distance indicator on extragalactic scales.

Application of large samples of SNe Ia led to the discovery that the Universe is accelerating in its expansion (Riess et al. 1998; Perlmutter et al. 1999). Subsequent application of large samples of SNe Ia out to high redshifts (Riess et al. 2004; Astier et al. 2006; Riess et al. 2007; Wood-Vasey et al. 2007; Hicken et al. 2009a; Kessler et al. 2009a; Amanullah et al. 2010; Sullivan et al. 2011a; Suzuki et al. 2012) has led to precise estimates of cosmological parameters when combined with measurements of baryon acoustic oscillations (BAO) and anisotropy in the cosmic microwave background (CMB); see Filippenko (2005a) for a review.

Reconstructing the expansion history of the Universe with SN Ia requires datasets spanning the widest possible range in redshift. Nearby SNe are less sensitive to cosmological parameters, but provide an anchor on a Hubble diagram to determine the relative brightness of a SN without the influence of cosmological parameters. Leverage on cosmological parameters comes from the luminosity distance to higher redshift SNe sensitive to the details of cosmological evolution. To this end, datasets at both ends of the redshift range play relatively important roles in determining cosmological parameters.

Many groups have taken on the challenge of collecting large samples of SNe Ia light curves. The first sample of 29 low-z objects was presented by the Calán/Tololo Supernova Survey (Hamuy et al. 1996b). The SN group at the Harvard/Smithsonian Center for Astrophysics (CfA) has produced 4 large samples of low-z SN Ia light curves (Riess et al. 1999a; Jha et al. 2006b; Hicken et al. 2009b, 2012) comprising a significant bulk of published low-z light curves. The Carnegie Supernova Project (CSP) has released two datasets of SN Ia light curves (Contreras et al. 2010; Stritzinger et al. 2011) with an impressive wavelength coverage of $ugriBV$ along with $YJHK$ for a fraction of the objects. Soon the Nearby Supernova Factory (SNFactory) will also release their dataset of spectrophotometric observations that can be used to synthesize measurements in any arbitrary optical broadband filter (Aldering

et al. 2002).

At intermediate redshifts ($0.05 < z < 0.35$), the Sloan Digital Sky Survey (SDSS) has released light curves for 146 SNe Ia in *ugriz* (Holtzman et al. 2008) from observations of Stripe 82. At higher redshifts ($0.15 < z < 1.1$), the Supernova Legacy Survey (SNLS) has released the results of the three-year rolling survey (Guy et al. 2010) netting a total of 252 objects with *griz* photometry. ESSENCE (Equation of State: SupErNovae trace Cosmic Expansion) has published their first set of R- and I-band light curves for 102 objects (Miknaitis et al. 2007) and will soon publish photometry of their 6-year sample of 228 SNe Ia (Narayan et al., in prep.). The search for SNe Ia extends out to space with programs utilizing the *Hubble Space Telescope (HST)* to find even more-distant SNe to probe epochs of cosmic expansion the most sensitive to cosmological parameters (Riess et al. 2007).

SN Ia cosmological analyses make use of an observed correlation between light-curve width and intrinsic luminosity to standardize SN Ia luminosity (i.e., the "Phillips relation"; Phillips 1993; Phillips et al. 1999). In addition to applying corrections to light-curve width, distance fitters also make assumptions about SN color and host-galaxy extinction to further standardize SN Ia luminosity to improve distance estimates (Tripp 1998; Tripp & Branch 1999). Many tools have been developed using well-observed SNe as a training set to refine these relationships and produce reliable distance estimates, including Multicolor Light-Curve Shape (MLCS; Riess et al. 1996; Jha et al. 2007), Spectral Adaptive Light-curve Template (SALT2; Guy et al. 2007), SiFTO (Conley et al. 2008), and BayeSN (Mandel et al. 2009, 2011).

With the success of the light-curve width and color parameters, the question has turned to what other observables correlate with intrinsic luminosity (but remain uncorrelated with light-curve width and SN color) to further improve distance estimates. Many studies have tried to correlate Hubble residuals with other light-curve (Folatelli et al. 2010), spectral (Bailey et al. 2009; Blondin et al. 2009; Silverman et al. 2012a), and host-galaxy properties (Kelly et al. 2010; Sullivan et al. 2010; Lampeitl et al. 2010). The relative ease of access to small- or medium-aperture telescopes makes low-z samples an ideal choice for pursuing a third parameter.

In this chapter, we present a cosmological analysis highlighting the addition of the Lick Observatory Supernova Search (LOSS) sample of nearby SNe Ia ($z < 0.05$). LOSS is an ongoing survey to find and monitor optical transients in the nearby Universe within days or weeks of explosion (Filippenko et al. 2001; Li et al. 2003a). The LOSS SN Ia sample is the first data release of high-quality *BVRI* light curves of 165 objects observed in the years 1998–2008 (see Chapter 2 for details). The light curves of these objects are well sampled (typical cadence of one epoch every 3–4 days) and on average start a week before maximum

light. The LOSS sample has been used to measure the rise-time distribution of SNe Ia (see Chapter 3), correlate photometric properties with spectral features (Silverman et al. 2012a), and identify specific subsets of SNe Ia that may prove to be more precise distance indicators (Wang et al. 2009a; Foley & Kasen 2011).

The aim of this chapter is to combine the LOSS sample with previously published samples to derive constraints on cosmological parameters $\Omega_{\rm m}$, $\Omega_{\rm DE}$, and the dark energy equation-of-state, $w = P/(\rho c^2)$. In addition, we study the effects of systematic uncertainties, and look for trends underlying residuals in our cosmology fits. The ultimate goal is to find another parameter (be it photometric, spectroscopic or host property) that correlates with luminosity and is uncorrelated with light-curve width and SN color to further standardize SN luminosity.

This chapter is organized as follows. In Section 4.2, we introduce the datasets from various photometric samples across a wide range of redshifts. Section 4.3 describes the methods by which we measure light-curve properties to estimate distances. Our results from our sample of 586 SNe Ia along with joint constraints from other cosmological probes are presented in Section 4.4. Additionally, we explore the impacts of systematic calibration uncertainties on our ability to measure cosmological parameters. In Section 4.5, we focus on the low-z sample (a significant fraction from LOSS) to search for physical systematics which may hint at the long-sought after third parameter for improving SNe Ia distance estimates.

4.2 Data

In an idealized SN Ia cosmological analysis, the entire dataset would comprise SN Ia photometry over the entire range of redshifts taken with a perfectly homegenous telescope network with well-characterized throughput curves. Currently, the single largest contribution to systematic uncertainties in SN Ia distance estimates and cosmological parameters is the photometry zero point (Conley et al. 2011). Future datasets from LSST and Pan-STARRS will bypass this issue by providing a standalone, self-consistent dataset with well understood throughput curves that will replace existing low, intermediate, and high-redshift datasets. However, until the realization of such a dataset, we must rely on combining datasets from multiple observing programs covering the largest possible redshift range. Here, we describe the LOSS dataset, as well as the other published datasets used for our cosmological analysis.

4.2.1 The LOSS Sample

The LOSS sample is the first data release of 165 *BVRI* light curves of nearby (median $z_{\rm CMB} = 0.0194$) SNe Ia presented in Chapter 2. A majority of the light curves in LOSS are well sampled and start a week before maximum light in the *B* band. The main discovery engine for the SNe Ia in our sample was the 0.76-m Katzman Automatic Imaging Telescope (KAIT) as part of a targeted search for nearby SNe (Filippenko et al. 2001; Li et al. 2003a; Leaman et al. 2011). KAIT discoveries account for ∼70% of the objects in the LOSS sample. Our photometric follow-up data were acquired with KAIT and the 1-m Nickel telescope at Lick Observatory.

The processing of data is described in detail in Section 2.3. In summary, point-spread function (PSF) fitting photometry is performed on images from which the host galaxy has been subtracted using templates obtained > 1 yr after explosion. Following the convention set by previous photometry data releases (Hamuy et al. 1996b; Riess et al. 1999a; Jha et al. 2006b), data were transformed to the Landolt system (Landolt 1983, 1992) using averaged color terms determined over many photometric nights. Calibrations for each SN field are obtained on photometric nights with an average of 5 calibrations per field.

The motivation to publish light curves on the Landolt system is to allow light curves from multiple sources to be easily compared. However, the simple color corrections used to transform natural-system magnitudes to a given standard photometry system is based on coefficients derived from stellar spectral energy distributions (SEDs) which do not accurately describe the SED of a SN (especially when the SN becomes nebular). Applying such color corrections does not guarantee that the SN photometry will necessarily be on the Landolt system. To properly account for the SN SED, second-order "S-corrections" (Stritzinger et al. 2002; Wang et al. 2009b) must be performed using a representative spectral series. In the case of SN 2005cf (a nearby, well-observed SN Ia caught well before maximum light), S-corrections improved the discrepancy between photometry systems from an a root-mean square (RMS) of 0.06 mag to 0.03 mag (Wang et al. 2009b).

However, there is a changing tide in how large datasets of low-z SN Ia photometry are being released. Starting with the CfA3 dataset (Hicken et al. 2009b) and CSP datasets (Contreras et al. 2010; Stritzinger et al. 2011), groups have begun to release SN photometry in the natural system of their telescope along with transmission curves of their photometry system, avoiding color corrections altogether. This has the obvious disadvantage that photometry from two telescope systems cannot be readily compared. Instead, photometry must be transformed from one system to the other using a SN spectral series coupled with the transmission functions of the telescope system.

The true advantage of natural-system photometry is only realized when the transmission

function of the telescope system is well characterized. Using natural-system photometry reduces systematic errors in cosmological fits and better constrains cosmological parameters (Conley et al. 2011; Sullivan et al. 2011a). The necessary requirement is precise and accurate measurements of the transmission curves to properly characterize their properties which low-z SN groups have started to undertake (Stritzinger et al. 2011; Hicken et al. 2012).

The original data release of the LOSS SN Ia light curves (see Chapter 2) was in the Landolt system. To better take advantage of our dataset, we re-release our data in the natural system of the KAIT and Nickel telescopes[1]. We caution that during our follow-up photometry campaign, KAIT went through a change in filter set and three different CCDs with different quantum-efficiency curves. In total, there are four different KAIT transmission curves for each bandpass; these configurations are referred to as KAIT[1-4] (see Chapter 2.2.2 for details on the characteristics of the bandpasses). Analyzing the dataset as a whole without accounting for differences in the photometry system is ill advised. We recommend either using the results on the Landolt system or transforming all of the data to a common system using an appropriate spectral series (e.g., Hsiao et al. 2007). We document the procedure for transforming our SN photometry into the telescope natural-photometry system in Appendix A.

4.2.2 Additional Low-Redshift Datasets

In addition to the LOSS dataset, we also include contributions from the Calán/Tololo sample (29 SNe; Hamuy et al. 1996b), CfA1 (22 SNe; Riess et al. 1999a), CfA2 (44 SNe; Jha et al. 2006b), CfA3 (185 SNe; Hicken et al. 2009b), CSP (35 SNe; Contreras et al. 2010), and light curves of individual SNe available in the literature. The Calán/Tololo, CfA1, CfA2, and individually published light curves are in the Landolt system, while all of the other samples are presented in the natural system. We will combine all light curves on the Landolt system into the "Lit" sample for the purposes of our analysis. We analyze all other light curves in the natural system of the telescope using published transmission curves.

The common practice within SN cosmology analyses is to combine low-z samples from different observing programs. There is significant overlap between the CSP, CfA3, and LOSS samples. Instead of combining data for SNe in common, we choose the light curves that have the best temporal coverage and are best sampled.

The overlapping SNe among the datasets offers an opportunity to study systematics between these programs. In Chapter 2.4.2, an analysis between the CfA3 and LOSS datasets found that individual SNe could suffer from systematic offsets of up to $\sim$0.05 mag, likely due

[1]Data in both the natural and standard photometric systems can be currently downloaded from http://hercules.berkeley.edu/database.

differences in calibrations. In Chapter 3.2.2, we found a typical scatter of 0.03 mag between CSP and LOSS datasets. Hicken et al. (2012), found a similar level of disagreement between the three datasets. In Section 4.4.4, we will study the impact that calibration zero-point uncertainties have on our measurement of cosmological parameters.

Throughout the rest of this chapter, we will refer to the combined sample of LOSS + CfA3 + CSP + Lit as the "low-z" sample.

4.2.3 SDSS SNe

The dataset of 146 SNe Ia released by the Sloan Digital Sky Survey (Holtzman et al. 2008; Kessler et al. 2009a) fills in the once sparsely populated intermediate redshift range ($0.1 < z < 0.4$). The data are in the natural system of the SDSS filter system on the AB photometry system (Oke 1974). Following Holtzman et al. (2008) and Conley et al. (2011), we only use data flagged < 1024 and SNe that do not show signs of peculiarity (e.g., SN 2002cx; Li et al. 2003b; Phillips et al. 2007). We omit u- and z-band photometry which have been shown to suffer from obvious systematic errors that are not well understood (Kessler et al. 2009a; Conley et al. 2011).

4.2.4 SNLS SNe

For higher redshifts ($0.4 < z < 1$), we use the third-year data release from SNLS (SNLS3; Guy et al. 2010). SNLS released *griz* photometry of 252 spectroscopically confirmed SNe Ia in the natural system of the Megacam instrument of the Canada-France-Hawaii telescope (CFHT)[2]. We do not include other older high-z samples such as those of the Supernova Cosmology Project (SCP; Perlmutter et al. 1999) and High-z SN Search Team (Riess et al. 1998) which do not have as strong a handle on systematics and could bias results when combined with the SNLS3 sample. Similarly, we do not include R- and I-band photometry of 102 SNe from the ESSENCE program (Miknaitis et al. 2007). While the ESSENCE sample is large, the systematics are not as well characterized. The SNLS3 sample represents a large sample of high-z SNe with a well-controlled handle on systematic errors (Conley et al. 2011).

4.2.5 HST SNe

Differentiating different models of dark energy requires sampling the expansion history at $z > 1$ where optical features have been shifted into the near-infrared. Searching for SNe Ia at these redshifts is more feasible from a space based telescope such as *HST*. Targeted searches

[2]Downloaded from http://hdl.handle.net/1807/26549.

for higher-z SNe have produced a sample in the redshift range $0.2 < z < 1.55$ (Riess et al. 2007).

The sample consists of observations using the Advanced Camera Survey (ACS) and the Near-Infrared Camera and Multi-Object Spectrograph (NICMOS). Following Conley et al. (2011), we omit SNe at $z < 0.7$ with F606W observations that will include both U- and B-band features due to the broad wavelength range covered by the filter. To limit the effect of biasing light-curve parameter estimates, we also place the constraint that if there is an early observation at $-20 < t_{B_{\max}} < -15$ d, then there must be an observation at $-8 < t_{B_{\max}} < +9$ d. If there is no early-time observation, then we require an observation at $-8 < t_{B_{\max}} < +5$ d. These requirements minimize the biasing of light-curve parameter estimates (Guy et al. 2010; Conley et al. 2011).

4.3 Distance Fitting

The method by which one turns SNe Ia light curves into a distance estimate is a topic of some debate. There is universal agreement regarding a strong correlation between light-curve width and luminosity (Phillips 1993; Phillips et al. 1999) that can be used via a linear (or quadratic) correction to standardize SN Ia luminosity. However, debate continues on how to correct SN luminosity for the effects of variations in intrinsic color and host-galaxy extinction. In the absence of host-galaxy extinction, SNe Ia with redder colors are intrinsically fainter (Riess et al. 1996; Jha et al. 2007). Similarly, SNe Ia that suffer from host-galaxy extinction will also have redder colors and a diminished observed brightness. Both effects act in the same direction (i.e., a redder SN is fainter), making it difficult to disentangle the two effects.

The Bayesian optimist would say, all is not lost: we have prior information on host-galaxy extinction. Host-galaxy extinction can only act to make the SN color redder and is likely drawn from a distribution we can infer (e.g., the galactic line of sight prior; Hatano et al. 1998). Making simple assumptions, we can place constraints on what we think is the probability distribution function of host-extinction extinction. If we then train a model on a sample of low-extinction SNe light curves, we can apply our model to data light curves to estimate an extinction value within a Bayesian framework. This is the approach taken by the MLCS fitter (Riess et al. 1996; Jha et al. 2007). BayeSN (Mandel et al. 2009, 2011) takes a similar approach, but also incorporates SN Ia infrared data to infer properties of host-galaxy extinction.

An alternative viewpoint is that the two effects cannot be disentangled and we should deal with the combined effect. The relationship that governs intrinsic color and luminosity appears to act in the same way that host-galaxy extinction diminishes brightness. Similar

to the linear correction between light-curve width and luminosity, another linear correction for the observed SN color (which includes contributions from both intrinsic and host-galaxy extinction) can be applied to further standardize the SN luminosity. This is the approach of two-parameter empirical fits like SALT2 and SiFTO.

MLCS has been successful at predicting distance estimates. However, there are indications that the framework by which it treats host-galaxy reddening may have systematic problems. Using the updated MLCS2k2.v006, Jha et al. (2007) found the existence of a somewhat sharp discontinuity in the Hubble expansion rate suggesting that the region within $H_0 d_{\rm sn} < 7400$ km s^{-1} is underdense compared to the global average–the so-called "Hubble bubble." Conley et al. (2008) found that this result may be due to how MLCS2k2.v006 treats dust extinction and using MLCS2k2 with a lower R_V value may be more appropriate (Hicken et al. 2009a).

Kessler et al. (2009a) found that MLCS2k2.v006 produced distance estimates that favored a Universe with $w = -0.72 \pm 0.07({\rm stat}) \pm 0.11({\rm sys})$ assuming a spatially flat Universe (i.e., $\Omega_{\rm m} + \Omega_{\rm DE} = 1$). This is in strong disagreement with other distance fitters consistent with $w = -1$ and it was traced back to how MLCS2k2.v006 treats U-band observations. The MLCS2k2.v006 U-band model was trained on low-z U-band observations which are notoriously hard to calibrate. Other distance fitters such as SALT2 were trained on high-z rest-frame U-band observations which fall into redder optical bandpasses, typically the g band. Alternatively, the discrepancy could be attributed to intrinsic differences between low-z and high-z SNe Ia in the UV rather than calibrations (Ellis et al. 2008; Cooke et al. 2011; Foley et al. 2012a). However, Conley et al. (2011) point out that the direction of this evolutionary difference between low-z and high-z SNe runs in the opposite direction, exacerbating the difference in U-band photometry of low-z and high-z SNe. We note that the root of this problem is not the methodology of MLCS2k2, but the implementation of the training process. Current analyses opt to exclude observer frame U-band observations to avoid the issue entirely.

For the purpose of deriving SN Ia distances, we will adopt the empirical approach of fitting coefficients to linear corrections for light-curve width and SN color. We will use SALT2 (Guy et al. 2007, 2010) to derive light-curve parameters. Then, using a χ^2 minimization and marginalization process, we will fit for linear-correction coefficients that minimize the Hubble residuals. Below we discuss our implementation of this procedure.

4.3.1 SALT2

The first version of SALT was developed by SNLS (Guy et al. 2005). SALT2 is an updated version of SALT with an larger training set of light-curve templates; it is the version

implemented in this work. SALT2 is trained on data from low-z SNe from the literature and SNe from the first two years of the SNLS (Guy et al. 2007, 2010). Light-curve parameters are measured using a time-varying spectral series of SNe along with an adopted exponential color law to model light-curve data given the bandpass of that data. SALT2 measures a parametrization of the light-curve width (x_1), the SN color (c), and the apparent B-band magnitude at maximum light (m_B). The parameter x_1 is similar in concept to the stretch parametrization of light-curve width (Perlmutter et al. 1997; Goldhaber et al. 2001), with increasing x_1 values corresponding to broader (and more luminous) SNe Ia. The parameter c is a measurement of the $B_{\max} - V_{\max}$ pseudocolor relative to the average pseudocolor of the SALT2 training set.

For our implementation of SALT2 on the LOSS data, we do our fitting in the natural photometry system of LOSS using the KAIT[1-4] and Nickel throughput curves presented in Chapter 2.2.2. The LOSS throughput curves are obtained by multiplying the transmission function of each filter by the quantum efficiency of the CCD and the atmospheric transparency at Lick Observatory. The quantum-efficiency curves for the remaining CCDs are taken from the manufacturer's claims. Filter transmission curves for the two different KAIT filter sets were measured in a laboratory using a Varian Cary 5000 spectrophotometer.

Transformations of natural-system magnitudes derived from spectrophotometry of standard stars with our transmission curves from Stritzinger et al. (2005) into the Landolt system produced slightly different color terms than those determined from our multiple nights of photometric observations. Following Stritzinger et al. (2002), we shift our transmission curves along in wavelength until we recover our observed color terms. These shifts can be found in Table 2.5 of Chapter 2 and are reflected in our transmission curves.

The zero point adopted in the most recent version of SALT2 is the flux standard BD $+17^\circ$ 4806 which has well measured Landolt magnitudes as opposed to Vega, which is too bright for most photometric systems and consequently does not have well-measured Landolt magnitudes. Since fitting is done using the transmission curves of the LOSS photometry system, we estimate the magnitudes of BD $+17^\circ$ 4806 in the the KAIT[1-4] and Nickel systems by transforming the Landolt magnitudes (Landolt & Uomoto 2007) using the color terms in Table 2.5 of Chapter 2.

With light-curve parameters for our full SNe Ia sample obtained, a model for the corrected apparent magnitude of a SN, $m_{B,\mathrm{corr}}$, is adopted which applies linear corrections for the light-curve width and color at peak brightness to the measured apparent magnitude, m_B. The corrected apparent magnitude has the form

$$m_{B,\mathrm{corr}} = m_B + \alpha \times (\text{light-curve width}) - \beta \times (\text{color}), \tag{4.1}$$

or in terms of the distance modulus and SALT2 parametrizations of light-curve width, x_1,

and color, c,

$$\mu_{\rm SN} = m_{B,\rm corr} - M, \tag{4.2}$$
$$= m_B + \alpha x_1 - \beta c - M. \tag{4.3}$$

The constants α, β, and M (the fiducial absolute magnitude of a SN Ia) are determined using a large sample of SNe Ia fit to minimize residuals against a cosmological model. We marginalize over M in our cosmological fits, while including α and β in our fitting process. Marginalizing over α and β has been shown to produce biased results (Kowalski et al. 2008; Conley et al. 2011).

The χ^2 statistic of interest given N SNe is

$$\chi^2 = \sum_{s=1}^{N} \frac{[\mu(z_s, \Omega_{\rm m}, \Omega_{\rm DE}, w) - \mu_{{\rm SN},s}]^2}{\sigma^2_{{\rm m},s} + \sigma^2_{{\rm pec},s} + \sigma^2_{\rm int}}, \tag{4.4}$$

where $\mu(z_s, \Omega_{\rm m}, \Omega_{\rm DE}, w)$ is the luminosity distance modulus of the SN in the CMB rest frame given cosmological parameters $(\Omega_{\rm m}, \Omega_{\rm DE}, w)$, $\sigma_{\rm m}$ is the measurement error in light-curve properties accounting for covariances between measured parameters, $\sigma_{\rm pec}$ is the uncertainty due to deviations from Hubble's law induced by gravitational interactions from neighboring galaxies, and $\sigma_{\rm int}$ is a constant intrinsic scatter added to each SN to achieve a reduced $\chi^2 \approx 1$. Errors are assumed Gaussian, although there are likely slight departures from this assumption in the light-curve parameter error estimates. We adopt 300 km s^{-1} as the peculiar velocity for each SN. Changing this value has little effect on the final cosmological results, although increasing $\sigma_{\rm pec}$ decreases the leverage of the lowest redshift objects.

Following Conley et al. (2011), we adjust $\sigma_{\rm int}$ for each photometry sample (low-z, SDSS, SNLS, and HST) such that the reduced χ^2 for that sample is ~ 1 using the best-fit values for ($\Omega_{\rm m}$, w) in a flat Universe. We fix $\sigma_{\rm int}$ to the values found in Table 4.1 for all subsequent fits. The $\sigma_{\rm int}$ term captures both the intrinsic dispersion in SN Ia luminosity (after correcting for light-curve width and color), unaccounted photometric uncertainties within a survey, and possible selection biases. As noted by Conley et al. (2011), this comes at the cost of the ability to discern subtle differences in cosmological models. However, the goal of this chapter is to study more common cosmological models, in which case we are willing to accept the increased uncertainty in our distance measurements.

Table 4.1: Intrinsic Dispersion and RMS of SN Samples

Sample	$\sigma_{\rm int}$ (mag)	RMS (mag)
Low-z	0.113	0.176
SDSS	0.097	0.160
SNLS	0.088	0.182
HST	0.105	0.247
ALL		0.176

Cosmological parameters are estimated using two complementary techniques: χ^2 minimization and χ^2 marginalization. Both techniques were used by Conley et al. (2011) and are described in their Appendix B. The χ^2 minimization approach uses the `Minuit` minimization package (James & Roos 1975) to find the cosmological parameters and linear coefficients that minimize Equation 4.4. Parameter errors are estimated using standard assumptions that uncertainties are Gaussian and the model is linear over those uncertainties. The χ^2 marginalization procedure calculates Equation 4.4 over a grid of possible cosmological and linear-coefficient values and then converts χ^2 into a relative probability via $P \propto e^{-\chi^2/2}$. Confidence intervals are constructed by finding the bounds covering the desired fraction of the total probability. The two different methods will not generally produce exactly the same results since they have different mathematical meanings (Upadhye et al. 2005; Conley et al. 2011). Both codes were downloaded from the SNLS 3-year data release website[3].

Recent cosmological analyses of SNe Ia (Conley et al. 2011; Sullivan et al. 2011a; Suzuki et al. 2012) have taken into account a correlation found between Hubble residual and host-galaxy mass (Kelly et al. 2010; Sullivan et al. 2010; Lampeitl et al. 2010). Sullivan et al. (2010) find that SNe in galaxies more massive than 10^{10} $M_\odot$ are $\sim$0.075 mag brighter than SNe hosted in less massive galaxies. Conley et al. (2011) implement this by essentially fitting for two M values[4] depending on a cutoff host-galaxy mass (10^{10} $M_\odot$ in the SNLS analysis; Conley et al. 2011; Sullivan et al. 2011a). We are currently in the unfortunate position of not having host-galaxy measurements for a majority of the LOSS objects. We are in the process of combining *BVRI* photometry of our host galaxies taken as part of the LOSS follow-up program with SDSS (Abazajian et al. 2009) and GALEX (Martin et al. 2005) photometry

[3]Downloaded from https://tspace.library.utoronto.ca/handle/1807/26549.

[4]Note that Conley et al. (2011) instead refer to $\mathcal{M}$, which is related to the fiducial absolute mag of a SN Ia, M, by $\mathcal{M} = M - 5\log_{10} h + 5\log_{10} c$. Here, c is the speed of light.

to produce estimates of host-galaxy properties (Tucker et al., in prep). In this work, we do not make any corrections for host-galaxy mass and instead fit for a single M value.

Table 4.2: Summary of SN Samples

Sample	Redshift Range	$N_{\rm SN}$	$N^{\rm a}_{\rm points}$
Low-z	0.01–0.13	226	43
SDSS	0.04–0.42	122	42
SNLS	0.12–1.03	230	37
HST	0.84–1.34	8	13
Low-z			
LOSS	0.01–0.10	91	51
CfA3	0.01–0.07	55	32
CSP	0.01–0.08	22	77
Lit	0.01–0.13	58	31

[a]Median number of photometry epochs used in SALT2 fit.

4.3.2 Fitting

For a given SN, we fit all photometry simultaneously within the range of 3000 – 7000 Å excluding observer-frame U- and u-band observations (due to the U-band anomaly discussed in Section 4.3). SN rest-frame I, i, and z bands are not well represented in the SALT2 training set of SNe and are also excluded.

4.3.3 Selection Criteria

We employ selection criteria to ensure that we are only including SNe Ia that are adequately fit by the SALT2 model. We require SALT2 fits to have a reduced $\chi^2 < 2$, although each fit is also visually inspected. Many of the low-z objects have spectroscopic identifications from Silverman et al. (2012c) or Blondin et al. (2012), allowing us to securely eliminate peculiar SNe that are not represented in the SALT2 model training set. These include objects similar to SN 2000cx (Li et al. 2001c), SN 2001ay (Krisciunas et al. 2011), SN 2002cx

(Li et al. 2003b), SN 2002es (Chapter 5), SN 2006bt (Foley et al. 2010b), or SN 2009dc (Yamanaka et al. 2009; Silverman et al. 2011; Taubenberger et al. 2011).

Cuts on c and x_1 are required to ensure that we are within a parameter space described by the SALT2 training set. This also helps eliminate peculiar objects that are either subluminous (e.g., SN 1991bg-like objects; Filippenko et al. 1992b; Taubenberger et al. 2008), super Chandrasekar-mass candidates (Howell et al. 2006; Hicken et al. 2007; Yamanaka et al. 2009; Scalzo et al. 2010; Silverman et al. 2011; Taubenberger et al. 2011), or highly reddened objects that may follow a different host-galaxy extinction law (e.g., SN 2006X; Wang et al. 2008). We restrict our sample to objects with $c < 0.50$ and $-3 < x_1 < 2$.

A minimum redshift cutoff is employed to minimize the impact of peculiar velocities. Previous analyses have used cutoffs in the range of $z = 0.01 - 0.02$. More conservative cutoffs have been used to eliminate any influence of a Hubble bubble. Our analysis does not find evidence for a Hubble bubble, consistent with what is found by Conley et al. (2007) and Hicken et al. (2009a) (see Section 4.5.1). To maximize the number of objects in the low-z sample we adopt a cutoff of $z = 0.01$. Increasing our minimum redshift does not significantly alter our results.

Objects along a line of sight with Milky Way reddening of $E(B - V) > 0.20$ mag as measured by the dust maps of Schlegel et al. (1998) are also excluded due to concerns that $R_V \neq 3.1$ (Conley et al. 2011).

The number of objects contributing to our final cosmology sample, the redshift range, and the typical number of points used in our SALT2 fit can be found in Table 4.2. Figure 4.1 shows the redshift distribution for each of the samples in our final cosmology sample totaling 586 objects. The inset to Figure 4.1 reflects the LOSS contribution of 91 out of 226 objects (45 without previously published distances) to the low-z SNe used in this analysis.

In Figure 4.2, we plot the x_1 (left panel) and c (right panel) distribution for our different samples. The low-z sample has the clearest differences compared to other higher redshift samples. This is not unexpected since most low-z SN discoveries are from targeted searches like LOSS or by amateur astronomers which are biased compared to an untargeted sample. SDSS and SNLS, on the other hand, are rolling searches which do not target preselected galaxies. The low-z sample has significantly more underluminous objects (i.e., smaller x_1) and redder objects (i.e., larger c) compared to the other samples.

Table 4.3 shows our SALT2 light-curve parameter values as well as distance estimates using fitting coefficients derived from our best-fit cosmology (see Section 4.4 for details).

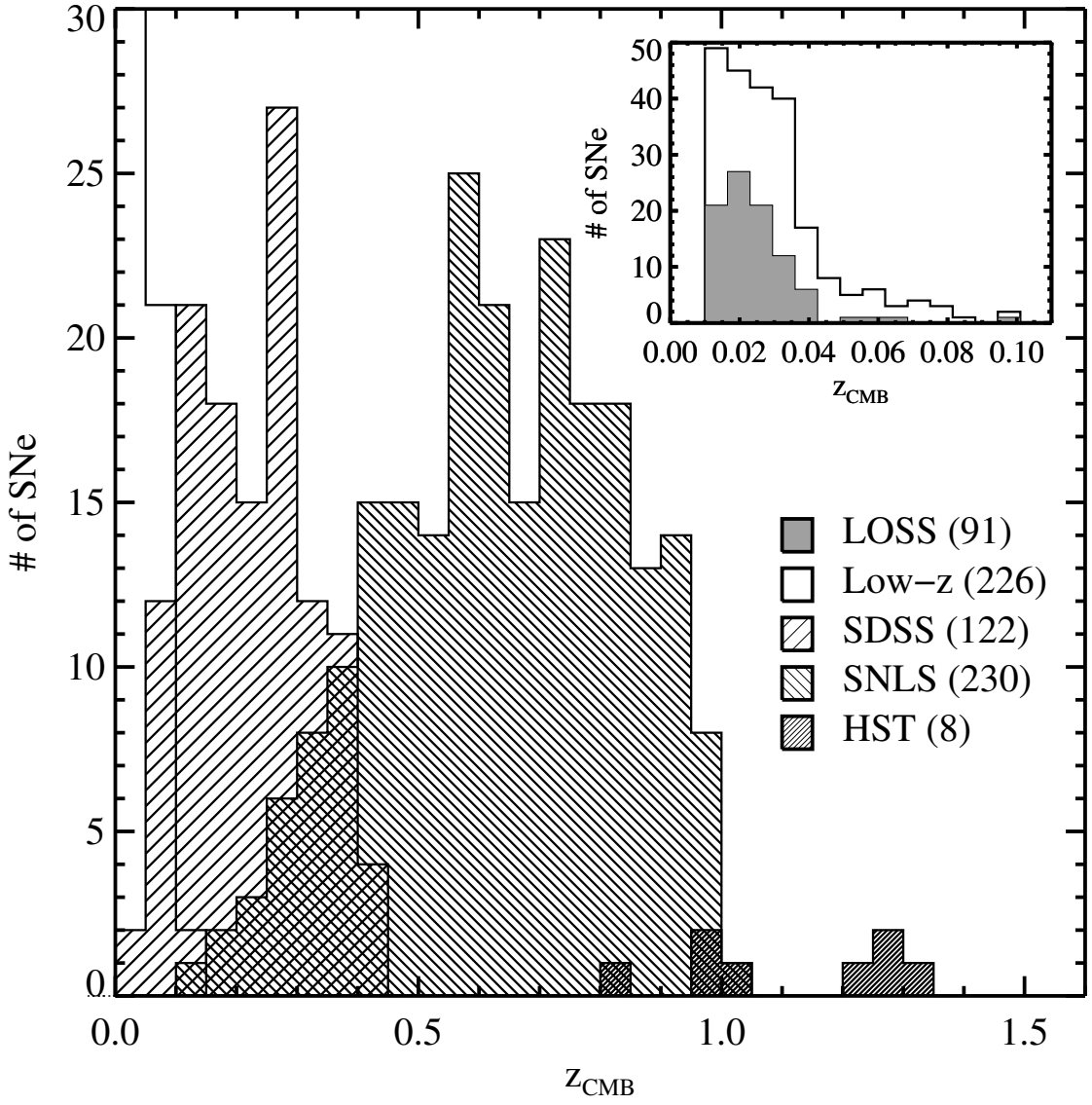

Figure 4.1: The redshift distribution for the SN sample presented in this work. Each photometric sample is shaded according to the pattern indicated in the legend. Note that the first bin of the low-z sample extends beyond the bounds of the plot. The inset plot shows the redshift distribution for the low-z sample with the LOSS contribution shaded in gray.

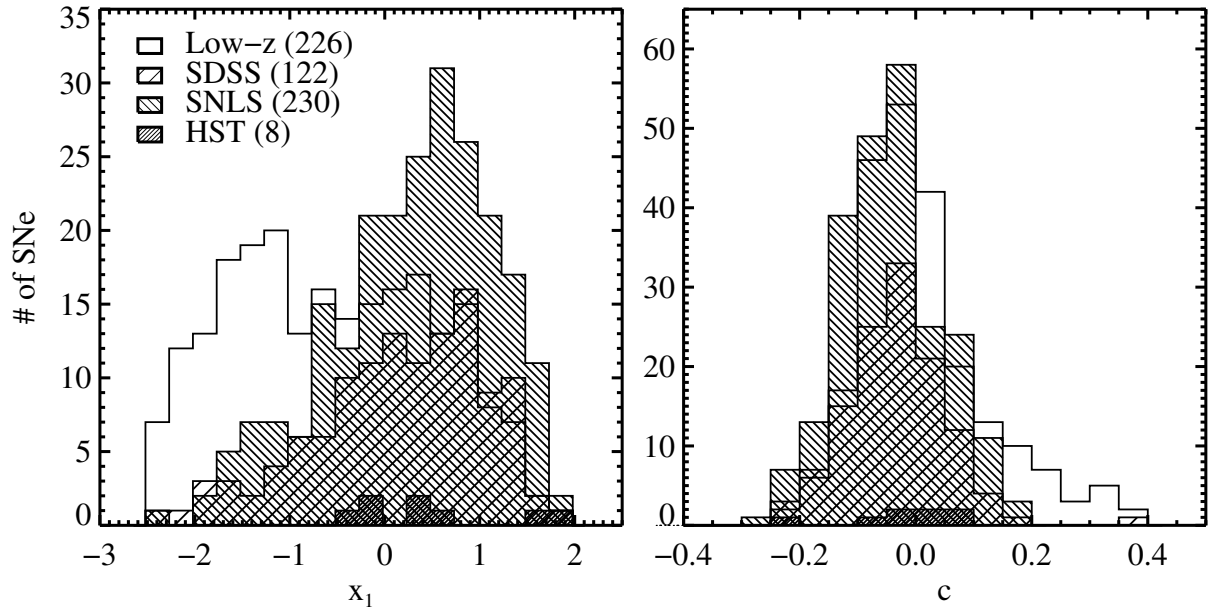

Figure 4.2: The SALT2 parameter distribution for the SN sample presented in this work. The left panel shows the x_1 distribution for our photometric samples and the right panel shows the c distribution. The low-z sample has more underluminous (smaller x_1) and redder (higher c) objects compared to other samples.

Table 4.3: SALT2 Parameters and Distances for SNe

SN	$z_{\rm CMB}$	m_B (mag)	x_1	c	μ (mag)	Sample	Reference
SN 1998bp	0.010	15.294 (0.035)	-2.520 (0.180)	0.197 (0.033)	33.363 (0.261)	Low-z	1
SN 2002dj	0.010	13.880 (0.028)	-0.276 (0.075)	0.004 (0.026)	32.889 (0.249)	Low-z	2
SN 2002cr	0.010	14.178 (0.020)	-0.601 (0.040)	-0.047 (0.019)	33.299 (0.246)	Low-z	2
SN 1999cp	0.010	13.927 (0.027)	-0.084 (0.043)	-0.045 (0.026)	33.119 (0.249)	Low-z	2
SN 2002dp	0.010	14.456 (0.022)	-0.830 (0.047)	0.020 (0.021)	33.333 (0.246)	Low-z	2
SN 2006bh	0.011	14.344 (0.023)	-1.561 (0.047)	-0.063 (0.024)	33.377 (0.247)	Low-z	3
SN 1999ee	0.011	14.872 (0.027)	0.719 (0.041)	0.237 (0.025)	33.289 (0.246)	Low-z	4
SN 2001fh	0.012	14.062 (0.039)	-2.412 (0.353)	-0.230 (0.035)	33.498 (0.234)	Low-z	2
SN 2005bc	0.013	16.236 (0.022)	-1.652 (0.117)	0.348 (0.022)	33.954 (0.216)	Low-z	2
SN 1999ej	0.013	15.378 (0.029)	-1.723 (0.087)	-0.018 (0.028)	34.244 (0.219)	Low-z	2
SN 2001ep	0.013	14.853 (0.028)	-0.855 (0.058)	0.018 (0.026)	33.732 (0.215)	Low-z	2
SN 2006lf	0.013	13.721 (0.031)	-1.304 (0.072)	-0.211 (0.028)	33.260 (0.217)	Low-z	5
SN 2002ha	0.013	14.679 (0.021)	-1.373 (0.055)	-0.086 (0.020)	33.813 (0.211)	Low-z	2
SN 2005al	0.013	14.848 (0.022)	-1.174 (0.044)	-0.093 (0.024)	34.033 (0.212)	Low-z	3
SN 1997E	0.014	15.097 (0.030)	-1.612 (0.139)	0.014 (0.029)	33.877 (0.214)	Low-z	1
SN 1999dq	0.014	14.397 (0.028)	0.836 (0.051)	0.045 (0.026)	33.438 (0.210)	Low-z	1
SN 1991ag	0.014	14.448 (0.041)	0.697 (0.136)	-0.042 (0.031)	33.744 (0.212)	Low-z	6
SN 2005kc	0.014	15.493 (0.022)	-0.670 (0.057)	0.161 (0.024)	33.947 (0.206)	Low-z	3
SN 1999dk	0.014	14.783 (0.029)	-0.171 (0.069)	0.001 (0.026)	33.816 (0.206)	Low-z	2
SN 1992al	0.014	14.461 (0.030)	-0.226 (0.084)	-0.111 (0.027)	33.840 (0.206)	Low-z	6
SN 2006N	0.014	15.091 (0.031)	-1.939 (0.104)	-0.041 (0.029)	33.998 (0.206)	Low-z	5
SN 2001bt	0.014	15.271 (0.029)	-0.874 (0.070)	0.157 (0.027)	33.707 (0.203)	Low-z	7
SN 2001fe	0.014	14.658 (0.030)	0.704 (0.129)	-0.053 (0.028)	33.991 (0.206)	Low-z	5
SN 2000dm	0.015	15.029 (0.031)	-1.853 (0.124)	-0.058 (0.030)	34.003 (0.206)	Low-z	2
SN 2004ey	0.015	14.704 (0.021)	0.008 (0.027)	-0.131 (0.022)	34.181 (0.199)	Low-z	3

Only a portion of this table is shown here for guidance regarding its form and content. Uncertainties are 1σ.
References. (1) Jha et al. (2006b); (2) Chapter 2; (3) Contreras et al. (2010); (4) Stritzinger et al. (2002); (5) Hicken et al. (2009b); (6) Hamuy et al. (1996b); (7) Krisciunas et al. (2004b); (8) Riess et al. (1999a); (9) Krisciunas et al. (2004a); (10) Krisciunas et al. (2001); (11) Holtzman et al. (2008); (12) Guy et al. (2010); (13) Riess et al. (2007).

4.4 Cosmological Results and Systematics

In this section, we present the results from our cosmological analysis using the full cosmological sample, with the inclusion of the LOSS sample which contributes 91 SNe, 45 having distance measurements published for the first time. We present both the results of our χ^2 minimization and marginalization procedures (see Section 4.3.1) and discuss the significance of our results. We will then discuss the impact of systematic uncertainties and their effect on our ability to measure cosmological parameters.

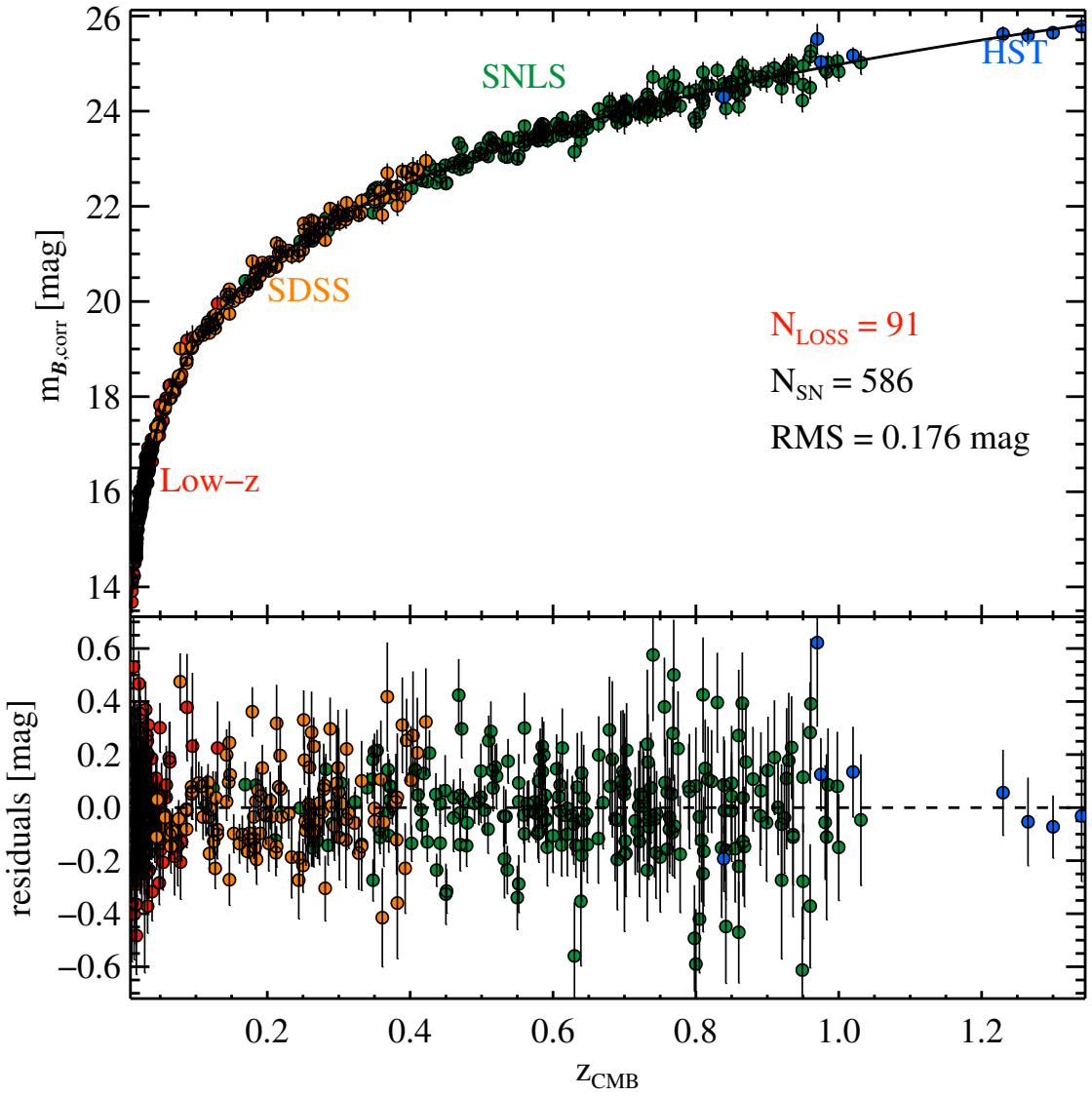

Figure 4.3: Hubble diagram for 586 SNe Ia. Each photometric sample is coded by the indicated color. Overplotted as a solid line is the best-fit cosmology. In the bottom panel we show the residuals for the fit. Residuals are measured as $\mu_{\rm SN} - \mu(z, \Omega_{\rm m}, \Omega_{\rm DE}, w)$.

4.4.1 Best-Fit Cosmology

In Figure 4.3, we show our best-fit Hubble diagram for our entire cosmological sample of 586 SNe. Our sample covers the redshift range 0.01–1.34. Overplotted is the best-fit cosmology assuming a cosmological constant (i.e., $w = -1$). We find a scatter of 0.176 mag for the entire sample. Objects are color coded by the sample to which they belong. Plotted in the bottom panel are the residuals as a function of redshift. We define the Hubble residual as $\mu_{\rm SN} - \mu(z, \Omega_{\rm m}, \Omega_{\rm DE}, w)$. SNe that are too bright for their luminosity distance will produce a negative residual. No significant trend is found as a function of redshift (see Section 4.4.2 for further discussion on tensions between datasets).

Table 4.4: Best-Fit Cosmological Parameters for a Flat Universe.

	χ^2 Minimization	χ^2 Marginalization
	SNe only	
$\Omega_{\rm m}$	$0.151^{+0.087}_{-0.117}$	$0.159^{+0.077}_{-0.086}$
w	$-0.813^{+0.155}_{-0.170}$	$-0.855^{+0.125}_{-0.164}$
α	0.146 ± 0.007	$0.147^{+0.010}_{-0.006}$
β	$3.168^{+0.079}_{-0.078}$	$3.2288^{+0.088}_{-0.070}$
	SNe + CMB + BAO	
$\Omega_{\rm m}$	$0.270^{+0.014}_{-0.013}$	$0.270^{+0.018}_{-0.012}$
w	$-1.055^{+0.047}_{-0.050}$	$-1.067^{+0.050}_{-0.046}$

Table 4.5: Best-Fit Cosmological Parameters for a Universe with $w = -1$.

	χ^2 Minimization	χ^2 Marginalization
	SN only	
$\Omega_{\rm m}$	$0.163^{+0.079}_{-0.083}$	$0.161^{+0.079}_{-0.074}$
Ω_Λ	$0.635^{+0.121}_{-0.127}$	$0.641^{+0.117}_{-0.113}$
α	0.146 ± 0.007	$0.147^{+0.010}_{-0.006}$
β	$3.169^{+0.079}_{-0.078}$	$3.229^{+0.088}_{-0.070}$

Continued on Next Page ...

Table 4.5 –Continued

	χ^2 Minimization	χ^2 Marginalization
	SN + CMB + BAO	
$\Omega_{\rm m}$	$0.265^{+0.013}_{-0.012}$	$0.264^{+0.019}_{-0.011}$
Ω_Λ	$0.737^{+0.012}_{-0.013}$	$0.738^{+0.015}_{-0.011}$

We measure cosmological parameters in the context of two scenarios. First, we consider a flat Universe dominated by matter and dark energy. We fit for $\Omega_{\rm m}$ and the dark energy equation-of-state parameter, w. Second, we relax the assumption of flatness and consider a Universe with matter and a cosmological constant, Λ. We will fit for $\Omega_{\rm m}$ and Ω_Λ. We present the results of both scenarios in Tables 4.4 and 4.5. Results for both χ^2 minimization and marginalization are presented and are consistent within 1σ uncertainties. In the results that follow, we present our χ^2 marginalization results which produce more reliable uncertainty estimates.

Assuming a flat Universe dominated by matter and dark energy, we find using only SNe Ia data that $\Omega_{\rm m} = 0.159^{+0.077}_{-0.086}$ and $w = -0.855^{+0.125}_{-0.164}$. We are able to reject a Universe without dark energy at the $> 4\sigma$ level (99.999% confidence) using the SNe Ia dataset. Including BAO measurements from Percival et al. (2010) and measurements of anisotropy in the CMB from Komatsu et al. (2011), we find significantly tighter constraints of $\Omega_{\rm m} = 0.270^{+0.018}_{-0.012}$ and $w = -1.067^{+0.050}_{-0.046}$. Our data are consistent with the accelerating expansion of the Universe driven by a cosmological constant. This is in excellent agreement with recent results from Conley et al. (2011) and Suzuki et al. (2012).

In Figure 4.4, we show two-dimensional probability contours in the $\Omega_{\rm m}$–w plane for SNe Ia in blue, WMAP7 + BAO in green, and the joint constraints from SNe Ia + WMAP7 + BAO in gray. Contours indicate the 68.3%, 95.4%, and 99.7% confidence levels. When combined with the BAO + CMB constraints, the SNe offer significantly tightened constraints on cosmological parameters.

Next, we allow for a universe with curvature and dark energy powered by a cosmological constant. From our SNe fits, we find $\Omega_{\rm m} = 0.161^{+0.079}_{-0.074}$ and $\Omega_\Lambda = 0.641^{+0.117}_{-0.113}$. When combined with constraints from WMAP7 + BAO, we recover concordance cosmology values of $\Omega_{\rm m} = 0.264^{+0.019}_{-0.011}$ and $\Omega_\Lambda = 0.738^{+0.015}_{-0.011}$.

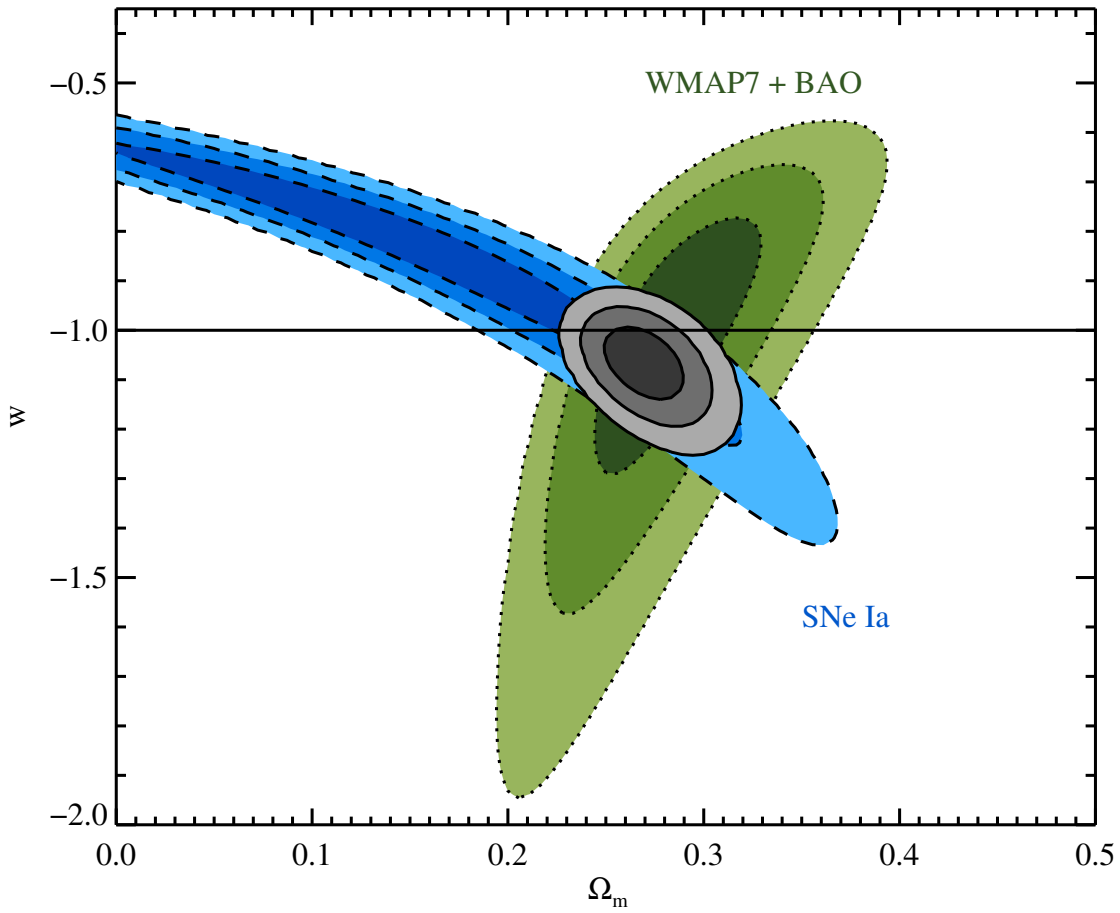

Figure 4.4: Probability contours for Ω_m and w assuming a flat Universe. Contours represent 68.3%, 95.4%, and 99.7% confidence levels. Constraints from SNe Ia are plotted in blue, WMAP7 + BAO in green, and combined in gray. Overplotted as a solid line is the expected equation-of-state parameter for a Universe with a cosmological constant. Our combined SNe Ia + WMAP7 + BAO results are consistent with the concordance ΛCDM cosmology.

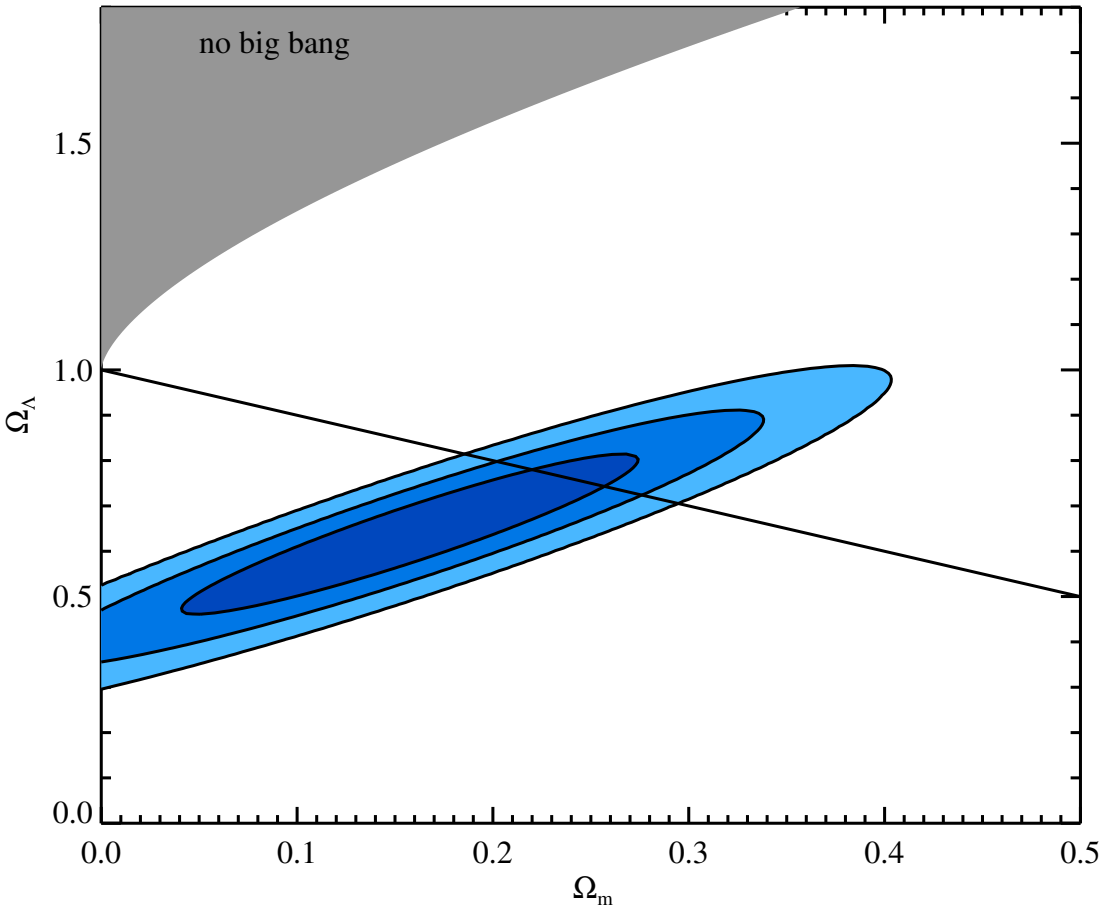

Figure 4.5: Probability contours for Ω_m and Ω_Λ from SNe Ia. Overplotted as a solid line is the expectation for a flat Universe.

In Figure 4.5, we show probability contours in the $\Omega_{\rm m}$–Ω_Λ plane from only SNe Ia. Our results are consistent with a flat, Λ-dominated Universe.

If we restrict our low-z sample to LOSS data with good fits (104 SNe) in addition to SDSS + SNLS + HST, we only lose a small degree of statistical leverage. From our fits with only SNe Ia, we find $\Omega_m = 0.151^{+0.083}_{-0.087}$ and $w = -0.835^{+0.125}_{-0.178}$. The only slight increase in statistical error is a strong indication that we are reaching the statistical limit achievable by current low-z datasets. Future improvements will be gained by eliminating systematic errors.

In Figure 4.6, we compare the probability contours in the $\Omega_{\rm m}$–w plane using our entire low-z sample to only using LOSS. The blue shaded contours represent constraints from using all of our low-z + SDSS + SNLS + HST data. The red outline indicates constraints from LOSS + SDSS + SNLS + HST data. The contours from using just LOSS are slightly larger than with the entire low-z sample. Comparing the area in the innermost contours, the LOSS contour is $\sim$18% larger than the low-z contour.

4.4.2 Tension between Datasets

As a measure of systematic differences between the datasets, we calculate the error-weighted mean residual and its uncertainty in Table 4.6 for the samples used in this study. We fix α and β to their best-fit values. Overall, we do not see any significant residuals between the datasets. The SNLS dataset shows a slightly higher mean residual, but not at a significant level ($\sim 2\sigma$). The slight trend with increasing redshift is not statistically significant.

Within the low-z datasets, the Lit sample shows the largest mean residual of -0.062 ± 0.023 mag at the 2.7σ level. The LOSS, CfA3, and CSP samples, all of which are fit in their natural system, do not show significant mean offsets.

Table 4.6: Tension between SN Samples

Sample	Weighted mean [mag]	Uncertainty [mag]
Low-z	-0.005	0.012
SDSS	-0.011	0.015
SNLS	0.023	0.010
HST	0.035	0.073
Low-z		

Continued on Next Page ...

Table 4.6 –Continued

Sample	Weighted Mean	Uncertainty
LOSS	0.024	0.016
CfA3	0.035	0.022
CSP	-0.007	0.028
Lit	-0.062	0.023

4.4.3 Residuals with SALT2 Parameters

In Figure 4.7, we plot the Hubble residual as a function of x_1 (top panel) and c (the bottom panel). Recall that we define the residual as $\mu_{\rm SN} - \mu(z, \Omega_{\rm m}, \Omega_{\rm DE}, w)$. A negative residual indicates a SN that is too bright (post light-curve correction) for its luminosity distance. Our binned error-weighted mean residual is plotted as red squares and individual measurements are gray points. The bins are constructed such that each bin is of equal width with the point centered on the midpoint of the bin. The error along the abscissa extends across the length of the bin. The error along the ordinate is the standard error in the weighted mean.

We do not see any trend between x_1 and Hubble residual, indicating that our single α value represents the entire range of x_1 values. A slight deviation is seen in our final x_1 bin, but it is not statistically significant ($< 2\sigma$).

In the bottom panel, we do find a linear trend with c and the Hubble residual. SNe with $c < -0.05$ have a negative slope with respect to Hubble residual, implying that our best-fit β value is not applying an appropriate linear correction in this range of SN color. This trend corresponds to a preference for a smaller β for low c values.

Sullivan et al. (2011a) found a similar trend between c and Hubble residual in their analysis of SNLS3 data. The authors attribute the trend in Hubble residual to a dependence of β on the stellar mass of the galaxy. When splitting their sample based on host-galaxy mass, they found strong evidence ($\sim 4.5\sigma$) that low-mass galaxies prefer a higher β value than high-mass galaxies. Since many of our bluest, least reddened SNe are found preferentially in early-type (and presumably massive) galaxies (see Section 4.5.2), this may explain the trend we see in Figure 4.9. A similar result is found by Lampeitl et al. (2010) in a study of the SDSS sample ($\sim 3.5\sigma$). In a future paper (Tucker et al., in prep), we will further explore trends between our sample and host-galaxy properties.

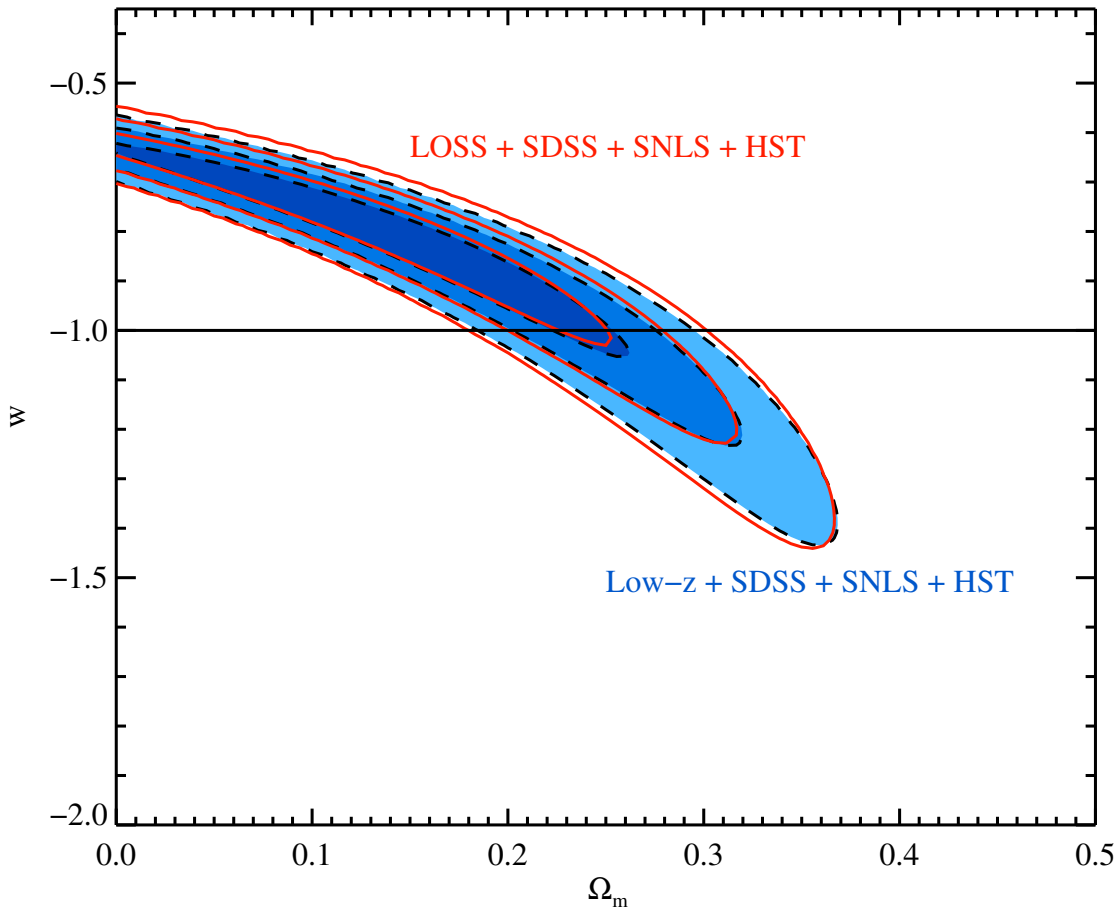

Figure 4.6: Comparison of probability contours for Ω_m and w assuming a flat Universe using the entire low-z sample with other samples versus using LOSS with other samples. Constraints from using the entire low-z sample are plotted in blue while constraints from LOSS are outlined in red.

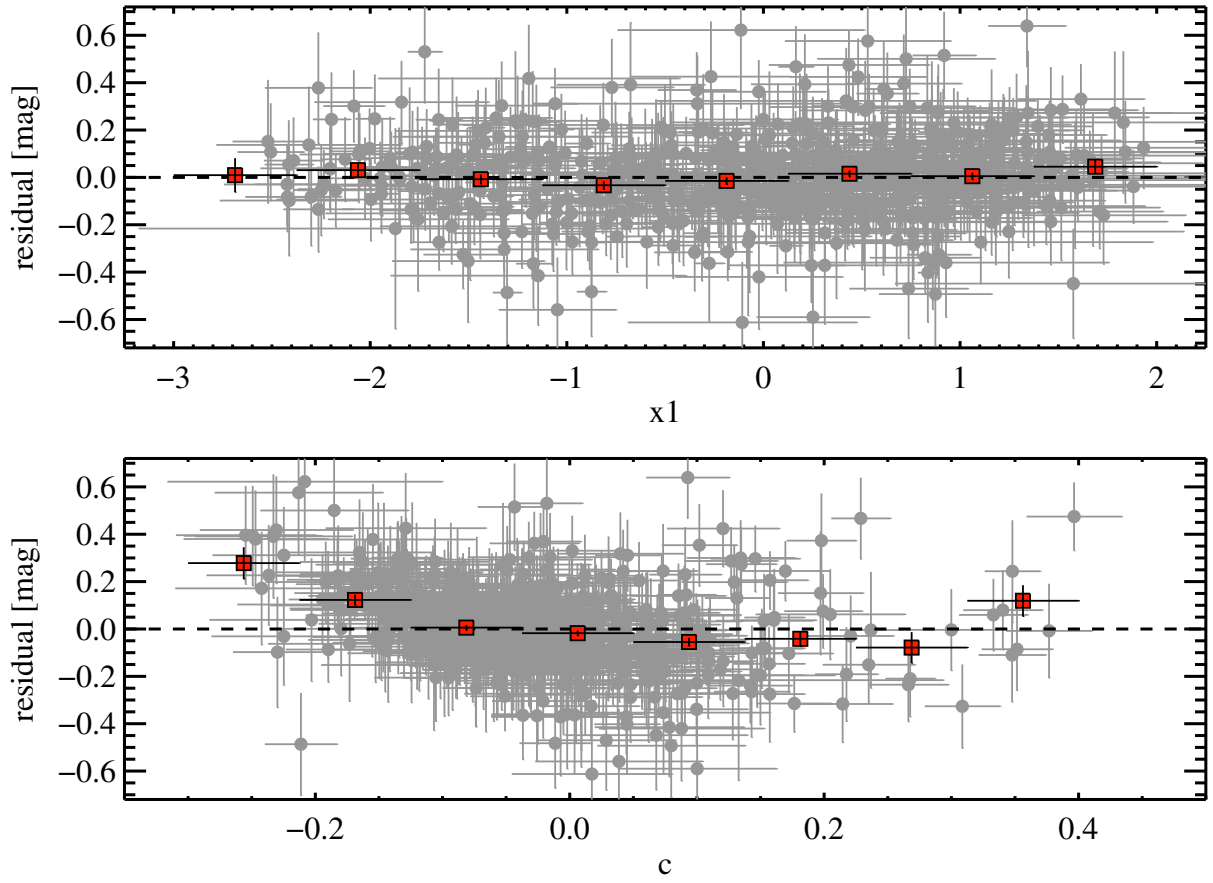

Figure 4.7: Residual as a function of SALT2 parameter. Residuals are measured as $\mu_{\rm SN} - \mu(z, \Omega_{\rm m}, \Omega_{\rm DE}, w)$. We plot the binned error-weighted mean residual as a red square. The bins are of equal width with each point centered at the middle of the bin. In the top panel, we show the Hubble residual against x_1 where we see no trend. In the bottom panel, we show Hubble residual against c. We find a linear trend for $c < -0.05$, indicative that bluer SNe prefer a lower β value.

Alternatively, the different β values may be the results of two different SNe Ia populations that prefer different β values. Wang et al. (2009a) and Silverman et al. (2012a) found that objects with high-velocity (HV) Si II λ6355 features in their spectra near maximum brightness have an observed distribution of $(B-V)_{\rm max}$ colors that is redder compared to spectroscopically normal objects. Wang et al. (2009a) found that when separating SNe into two classes by Si II velocity, the two classes preferred different reddening laws (i.e, different β values). The HV objects with a redder color distribution preferred a smaller beta compared to normal objects. This runs counter to what we observe in our data where the bluest objects appear to prefer a smaller β. We note, however, that making a cut on c is different than making a cut by spectroscopic subclass since the two observed color distributions are offset by only $\sim$0.10 mag and overlap considerably. Future observing programs that include spectroscopic follow-up observations may be able to disentangle these effects. We explore this further in Section 4.5.3 using a subset of the low-z sample that also has spectral measurements.

4.4.4 Systematic Uncertainties

Thus far, we have only treated the statistical error associated with our SN fits. In this section, we will investigate the important role of systematic uncertainties. We consider a systematic error to be an error that affects multiple SNe in our analysis, likely in a correlated manner. In a recent analysis by the SNLS team, Conley et al. (2011) found that the most significant contribution to their systematics was calibration uncertainties. We will focus our attention on understanding how the calibration affects our results.

A major roadblock to improvement in measurements of cosmological parameters is the inability to accurately measure the zero point of a photometric system. In Chapter 2.4.2, we found that the differences between SNe in common between the LOSS and CfA3 samples could be as large as $\sim$0.1 mag (in the Landolt photometry system), although the mean difference over all SNe in common is consistent with 0.0 mag. Similarly in Chapter 3.2.2, in a comparison of the LOSS and CSP photometry for 14 SNe in common, we found differences of 0.03 mag in B and V bands. These comparisons did not include S-corrections to place the SNe on a common photometric system.

As a measure of systematic errors between datasets, we compare SALT2 light-curve parameters for overlapping SNe in Table 4.7. SALT2 measures parameters in SED space using transmission curves for each photometry system which should alleviate any concerns about S-corrections. We find an excellent level of agreement among the 11 overlapping objects in the LOSS and and CSP datasets for measurements of m_B and c. There are indications of a $\sim$0.02 mag offset between LOSS and the other two samples at significant

levels (2.4σ for Lit and 4σ for CfA3).

Comparing the LOSS x_1 values with the CfA3 and CSP samples, we find differences of $\sim$0.1, which translate to differences of $\sim$0.01 mag for typical α values (0.12–0.15). LOSS x_1 values best agree with the Lit sample. All of our samples have the same c values to within 1σ. We do not see a significant trend of the differences between LOSS and another sample with time which would indicate an issue with one of the KAIT filter/CCD combinations (KAIT[1-4]).

A similar comparison between 9 objects in both the CfA3 and CSP samples shows somewhat large offsets in m_B of 0.054 ± 0.012 mag and in x_1 of 0.115 ± 0.032 (error-weighted mean and uncertainty). The c values of the two samples agree to within uncertainties.

Table 4.7: SALT2 Light-Curve Parameter Comparison

	Mean	Std. Dev	WMean ($\sigma_{\rm WM}$)	N
		m_B (mag)		
LOSS − LIT	-0.021	0.039	-0.024 (0.010)	18
LOSS − CFA3	-0.024	0.058	-0.024 (0.006)	47
LOSS − CSP	0.001	0.037	0.002 (0.011)	11
CFA3 − CSP	0.054	0.037	0.054 (0.012)	9
		x_1		
LOSS − LIT	-0.048	0.261	-0.009 (0.026)	18
LOSS − CFA3	-0.082	0.328	-0.083 (0.019)	47
LOSS − CSP	0.048	0.269	0.124 (0.030)	11
CFA3 − CSP	0.074	0.201	0.115 (0.032)	9
		c		
LOSS − LIT	-0.008	0.034	-0.020 (0.026)	18
LOSS − CFA3	-0.016	0.032	-0.019 (0.019)	47
LOSS − CSP	-0.004	0.032	-0.005 (0.030)	11
CFA3 − CSP	0.011	0.025	0.015 (0.032)	9

We have also performed SALT2 fits for the LOSS photometry on the Landolt system (without S-corrections) and find overall that the results agree well. We do note, however,

that we find an error-weighted mean difference of 0.014 ± 0.004 mag in m_B. Differences in c and x_1 are consistent with no difference. Comparing our fits in the standard system to the CfA and Lit improves the offset to ∼0.01 mag, but worsens the comparison to CSP to ∼0.04 mag. The weighted mean residuals for x_1 and c mostly remain the same.

The level of disagreement between the different datasets is somewhat alarming, but also is within the systematic uncertainties attributed to the photometric zero points associated with each sample. However, when combined with the other higher redshift samples, the cumulative effect can alter best-fit cosmological parameters and associated uncertainties.

To model the effect of these uncertainties, we perform a Monte Carlo simulation focusing on the effects of the zero-point uncertainty for the low-z samples. For each filter in each photometry sample, we draw a random systematic uncertainty to add to the SN photometry in that sample's filter. The uncertainty is drawn from a Gaussian distribution centered on 0.0 mag with a σ of 0.02 mag. Our value for σ is based on the mean offsets between different photometric samples which hint at a zero-point uncertainty of ∼0.02–0.03 mag. A realization of a dataset includes perturbed photometry for all of the photometry samples. Each dataset realization is fit by SALT2 for new light-curve parameter estimates and then run through our χ^2 minimization code to find the best-fit cosmological parameters.

When including the zero-point uncertainty assuming a flat Universe, we find that our systematic error translates into an additional systematic error $\Delta w = 0.116$ and $\Delta\Omega_{\rm m} = 0.05$. Relaxing our assumption on flatness, but requiring dark energy described by a cosmological constant, we find $\Delta\Omega_{\rm m} = 0.039$ and $\Delta\Omega_{\rm DE} = 0.098$.

While we have only focused on the calibration zeropoint of the low-z photometry systems, an exhaustive treatment of systematic errors by Conley et al. (2011) find a similar level of systematic uncertainty in their cosmological parameter estimates. However, they only found $\Delta w = 0.065$ from the uncertainty of the low-z zero points. They attributed a zero-point uncertainty of ∼0.01 mag for the various low-z samples which we believe is likely an underestimate. Hicken et al. (2009a) quote an systematic uncertainty of $\Delta w = 0.11$. However, their quoted systematic uncertainty includes combined constraints from a BAO prior from Eisenstein et al. (2005) which will decrease the systematic error from SNe alone.

4.5 Physical Systematics in the Low-z Sample

In this section, we will focus exclusively on looking for physical systematics inferred from the low-z samples. The low-z samples have the advantage of often having complementary spectroscopic coverage and publicly available data on host galaxies. We will fix our cosmological parameters to concordance cosmology values of $(\Omega_{\rm m}, \Omega_{\rm DE}, w) = (0.27, 0.73, -1)$

and our fitting coefficients $(\alpha, \beta) = (0.146, 3.169)$. We note that these values of (α, β) are consistent with the values found if we fix $(\Omega_{\rm m}, \Omega_{\rm DE}, w) = (0.27, 0.73, -1)$ and fit for the coefficients using only the low-z sample. We find $\alpha = 0.154 \pm 0.011$ and $\beta = 3.132^{+0.113}_{-0.111}$.

4.5.1 Is There a Hubble Bubble?

Zehavi et al. (1998) and Jha et al. (2007) presented evidence for a monopole in the peculiar velocity field of galaxies in the local Universe. Their analyses indicated that we live in an underdense region of the Universe relative to the global average energy density, manifesting itself as a larger Hubble constant within $cz < 7500$ km s^{-1}. Both analyses utilized distances from MLCS and found the presence of a "Hubble bubble" at $\sim 2\sigma$ confidence assuming a flat, Λ-dominated Universe with $\Omega_{\rm m} = 0.3$. In a re-analysis of the data from Jha et al. (2007), Conley et al. (2007) found that the presence of the Hubble bubble may actually be an artifact of assuming that dust in other galaxies has the same extinction properties as Milky Way dust with $R_V = 3.1$ ($\beta = 4.1$). Conley et al. (2007) found that the Hubble bubble disappeared using lower values of R_V as preferred by the data when doing a χ^2 minimization of SALT2 parameters similar to the analysis presented here. Our best-fit $\beta = 3.169$ corresponds to $R_V = 2.169$ under the assumption that SALT2 c is an estimate of $E(B-V)$ host-galaxy reddening.

Hicken et al. (2009a) found that the significance and partition redshift of the Hubble bubble was a function of light-curve fitter, assumption of host-galaxy extinction, and even photometry sample. They analyzed departures from a single Hubble law using low-z SN distances estimated from SALT, SALT2, MLCS2k2 with $R_V = 3.1$, and MLCS2k2 with $R_V = 1.7$. Hicken et al. found the most significant detection of a Hubble bubble at the $\sim 5\sigma$ confidence level at $cz = 8400$ km s^{-1} with MLCS2k2 and $R_V = 3.1$. The significance of the void decreased substantially to 1.3σ confidence if SNe with $A_V > 0.5$ mag are excluded. Hicken et al. did not find evidence of a Hubble bubble using distances derived from SALT or SALT2.

Following previous analyses, we work in the more convenient units of km s^{-1} for distances. SN distance moduli, $\mu_{\rm SN}$, are translated by converting to distance (Mpc) and multiplying by H_0. The luminosity distance to $z_{\rm CMB}$ in units of km s^{-1} for a given cosmology is

$$H_0 d_L(z_{\rm CMB}) = c(1 + z_{\rm CMB}) \int_0^{z_{\rm CMB}} \frac{dz'}{[\Omega_{\rm m}(1+z')^3 + \Omega_\Lambda]^{1/2}}. \quad (4.5)$$

The peculiar velocity of a galaxy, u, with respect to the CMB rest frame is given by $u = H_0 d_L(z_{\rm CMB}) - H_0 d_{\rm SN}$. We note that c in the above equation refers to the speed of light. The fractional deviation from a Hubble flow is $\delta H/H = u/H_0 d_{\rm SN}$. We plot $\delta H/H$ for our low-z

sample in the top panel of Figure 4.8. For the most part, deviations from Hubble expansion appear randomly distributed, consistent with a single value of H_0.

We estimate the void amplitude signal by partitioning our low-z sample into two subsamples based on redshift. Starting at $z_{\rm partition} = 0.0106$, we compute H_0 in the inner subsample $z \leq z_{\rm partition}$) and in the outer subsample. We define the void amplitude as $\delta_H = (H_{\rm inner} - H_{\rm outer})/H_{\rm outer}$. We calculate the void amplitude as a function of $z_{\rm partition}$ with the constraint that the minimum number of points in a subsample is ≥ 6. We estimate the void significance by weighting the void amplitude by its uncertainty given by Equation 3 of Zehavi et al. (1998). We plot the void amplitude significance in the middle and lower panels of Figure 4.8, respectively.

We do not see a significant void amplitude in the entire sample of low-z SNe. The largest void amplitude of -0.04 is detected at $cz_{\rm CMB} = 21,000$ km s^{-1}, although the significance of this detection is relatively low and likely due to a small number of objects in our outer subsample. We do not find a significance larger than 1.64σ, indicating that our data are consistent with a single value of H_0. Our maximum void detection occurs at $cz_{\rm partition} = 5300$ km s^{-1}.

We further investigate whether we detect a Hubble bubble in each of our low-z datasets. The LOSS dataset has a peak void amplitude of 1.28σ at $cz \approx 6000$ km s^{-1} which is marginally consistent with what is found for the entire sample. However, the CfA3 and CSP sample show peak void signatures in the opposite direction and in the region $cz \approx 3900 - 4200$ km s^{-1}, although also at a low significance ($< 1.8\sigma$). The most significant void detection is from the Lit sample with a void significance of 2.4σ at $cz = 4200$ km s^{-1}, however, in the opposite direction of the CfA3 and CSP samples. A summary of our results is in Table 4.8.

Table 4.8: Peak Hubble Bubble Significance

Sample	Partition Redshift (km s^{-1})	Void Amplitude	Void Significance
Low-z	5306	0.023	1.638
LOSS	6025	0.022	1.281
CfA3	4406	-0.040	1.757
CSP	4047	-0.038	1.600
Lit	4167	0.058	2.408

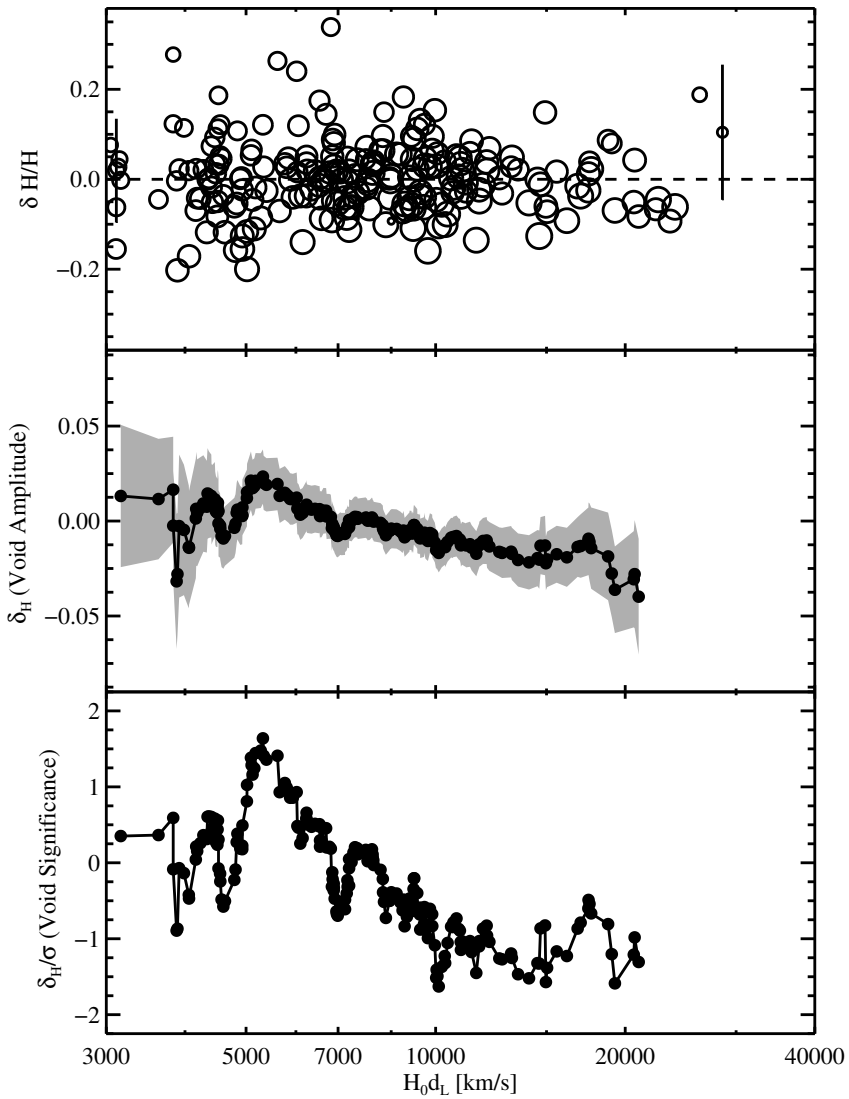

Figure 4.8: Significance of a Hubble bubble in our low-z data. The top panel shows the fractional deviation from the distance luminosity for each object in the low-z sample. The size of each point is inversely proportional to its uncertainty. In the middle panel, we plot the amplitude of a Hubble void signature as a function of redshift. In the bottom panel, we plot the significance of the void amplitude as a function of amplitude. We do not find a significant detection of a Hubble bubble in our data.

To summarize, similar to Hicken et al. (2009a), we find that our analysis is consistent with no Hubble bubble. Our measurement of a void signal depends on the photometry sample, but for each sample the detection is mostly at low significance. Our sample excluded extremely reddened objects which likely have different reddening properties than normal SNe Ia. We find it likely that previous detections of a Hubble bubble were due to the way in which reddening was treated, consistent with the conclusions of Conley et al. (2007) and Hicken et al. (2009a).

4.5.2 Host Galaxies

With our large sample of low-z SNe, we can look for trends as a function of host-galaxy properties. Previous studies comparing Hubble residuals to host-galaxy properties have found that after correcting the SN luminosity for light-curve width and SN color, SNe in more massive galaxies appear brighter than SNe in their less massive counterparts (Kelly et al. 2010; Sullivan et al. 2010; Lampeitl et al. 2010). The physical interpretation of this result remains elusive, but could be due to a dependence on the progenitor metallicity which would be a function of host-galaxy mass (Kasen et al. 2009). In this section, we will study our Hubble residuals and light-curve parameters a function of galaxy morphology (as a proxy for galaxy mass) and projected galactocentric distance (PGCD) to look for trends in our data. Again, we restrict our analysis to low-z objects where discovery information regarding galaxy morphology and offsets from the host-galaxy nucleus are easily available in International Astronomical Union Circulars (IAUCs) and the NASA/IPAC Extragalactic Database[5]. In cases where host-galaxy offsets are not available, we calculate the offset from the difference between the host-galaxy coordinates and the SN coordinates as in the case of objects found by the SNFactory (Aldering et al. 2002).

We caution that the low-z sample suffers from a bias to more massive galaxies due to targeted surveys such as the LOSS (Filippenko et al. 2001; Li et al. 2003a; Leaman et al. 2011), which account for a vast majority of the discoveries in the nearby Universe after 1998. LOSS preferentially monitors more massive galaxies to maximize the number of discovered SNe (Leaman et al. 2011; Li et al. 2011a,c). The low-z sample is not a complete sample and is likely not an accurate representation of the true host-galaxy demographics. We continue with that caveat in mind.

[5]http://nedwww.ipac.caltech.edu/

Morphology

In the top panel of Figure 4.9, we plot Hubble residual as a function of host-galaxy morphology. If more massive galaxies host brighter SNe (after correcting for light-curve width and color), the expectation is that early-type galaxies (E-S0) should have a more negative mean residual in comparison to late-type galaxies (Scd/Sd/Irr). We find a difference in the error-weighted mean residuals (red squares) between Sd/Irr and E of 0.099 ± 0.063 mag in the sense that E host galaxies host brighter SNe post-correction. While this agrees with previous results, our result is only significant at the $\sim 1.6\sigma$ confidence level.

If we bin the data into Early (E–S0), Mid (S0a–Sbc), and Late (Scd/Sd/Irr) galaxy bins, we find that a difference between the Late and Early galaxy bins of 0.050 ± 0.046 mag, consistent with no difference. We find a more significant difference between Mid and Late galaxies of 0.059 ± 0.029 mag. The consistency between our Early and Mid galaxy bins indicates that there may be more to gain by either excluding Late galaxies or treating them separately. We caution that there are only 19 objects in our Late bin, and the rather large weighted mean residual may be a result of small-number statistics. The full set of Hubble residuals as a function of host-galaxy morphology can be found in Table 4.9.

Sullivan et al. (2003) found that the Hubble residual scatter was minimized by using only SNe in early-type hosts, while Hicken et al. (2009b) found that scatter the was reduced by using late-type galaxies. Our analysis finds that both of these galaxy bins produce a scatter that is slightly lower compared to that of Mid galaxies. Early galaxies do slightly better ($\sigma = 0.167$ mag) than Late galaxies ($\sigma = 0.171$ mag), although the difference is statistically insignificant. Mid galaxies have a $\sigma = 0.189$ mag, but also have twice the number of objects in the Early and Late galaxy bins combined.

In the middle panel of Figure 4.9, we plot the SALT2 x_1 distribution as a function of host-galaxy morphology. SNe in early-type galaxies have a smaller weighted x_1 average (narrower light curves, corresponding to underluminous SNe) compared to SNe in mid- and late-type galaxies. This observation has been noted in previous studies (Della Valle & Livio 1994; Hamuy et al. 1996a; Howell 2001; Hicken et al. 2009a).

Table 4.9: Residual as a Function of Galaxy Morphology

Morphology	Mean	Std. Dev	WMean	$\sigma_{\rm WM}$	N
E	-0.017	0.196	-0.034	0.040	21
E/S0	-0.021	0.152	-0.004	0.077	5
S0	0.037	0.140	0.029	0.037	23
S0a	0.113	0.268	0.097	0.081	5

Continued on Next Page ...

Table 4.9 –Continued

Morphology	Mean	Std. Dev	WMean	$\sigma_{\rm WM}$	N
Sa	0.031	0.135	0.033	0.048	13
Sab	-0.020	0.129	-0.004	0.054	12
Sb	-0.032	0.176	-0.027	0.023	57
Sbc	-0.066	0.181	-0.070	0.046	14
Sc	0.022	0.239	0.017	0.035	26
Scd	0.001	0.141	0.023	0.063	8
Sd/Ir	0.063	0.192	0.065	0.049	11
E-S0	0.008	0.167	-0.001	0.025	49
S0a-Sc	-0.011	0.189	-0.010	0.016	127
Scd/Sd/Irr	0.037	0.171	0.049	0.039	19

The presence of SNe Ia in both passive elliptical galaxies with old stellar populations and in spirals with active star formation has led to speculation that SNe Ia may come from at least two progenitor populations (Mannucci et al. 2005; Scannapieco & Bildsten 2005; Sullivan et al. 2006; Neill et al. 2006; Maoz et al. 2011). SNe Ia in late-type galaxies are typically brighter and occur at $\sim$10 times the rate (per unit mass) of SNe Ia in elliptical galaxies leading to the suggestion that these SNe may be linked to young stellar progenitors. SNe Ia in early-type galaxies, on the other hand, more likely track the total mass of the galaxy. This has led rate studies to adopt a two-component model: a "prompt" component proportional to the star-formation rate and a "tardy" component proportional to the total mass. Recently, in an analysis of SNe rates from LOSS, Li et al. (2011c) found intriguing evidence of a rate-size relation across all galaxy classes indicating the SN Ia rate is *not* linearly proportional to galaxy mass. Specifically, the SN rate per unit mass is larger in smaller galaxies compared to larger galaxies. Our analysis hints that different galaxy morphologies host different distributions of SN properties. However, we again caution that our distributions are likely biased and may not reflect the true distribution of SN properties.

In the bottom panel of Figure 4.9, we plot the SALT2 c distribution as a function of galaxy morphology. The reddest SNe occur in Sd/Irr galaxies and the bluest in E-S0. This result is somewhat counterintuitive given the above result that early galaxies host underluminous SNe that are intrinsically redder (Riess et al. 1996; Jha et al. 2007). This may instead reflect the distribution of host-galaxy extinction values. Early-type galaxies are

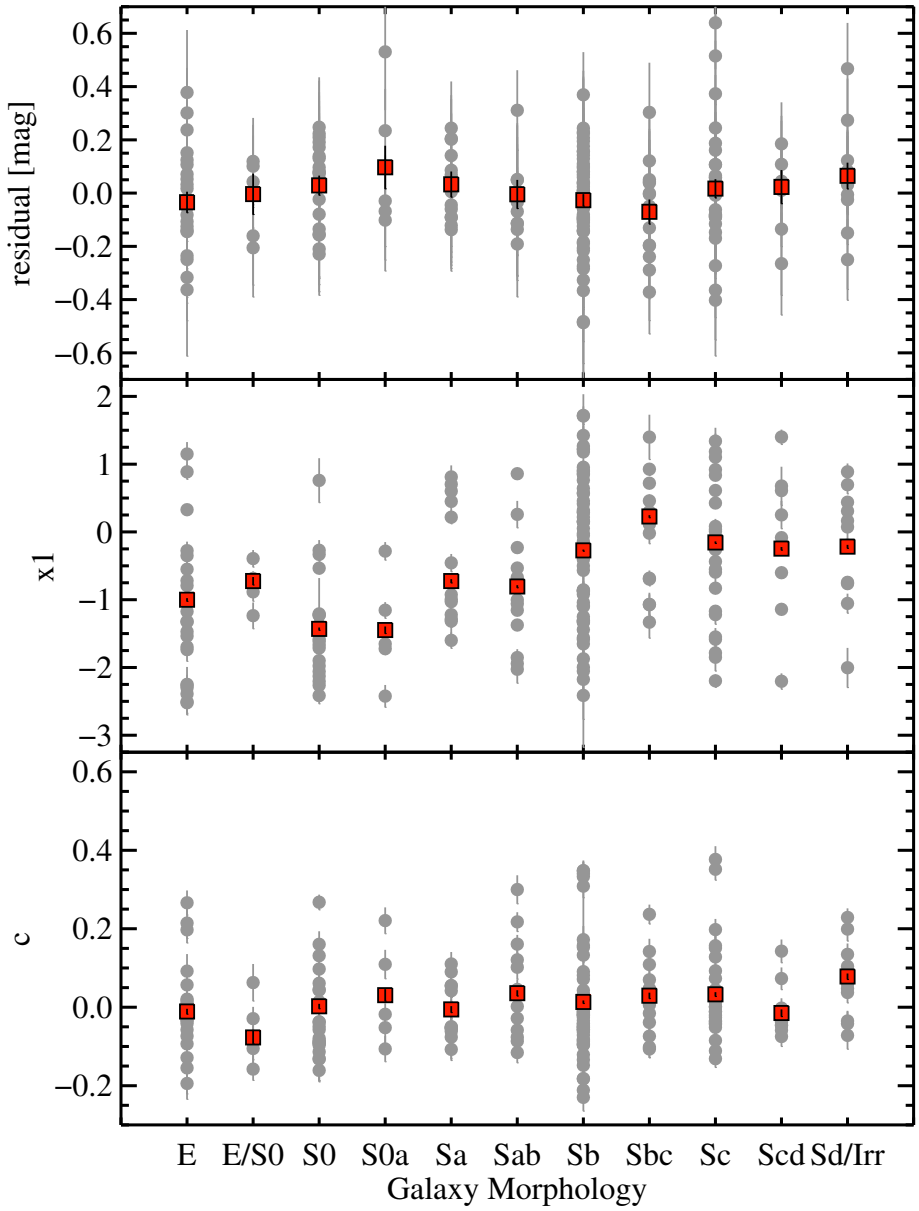

Figure 4.9: Parameters versus galaxy morphology. In the top panel we plot the Hubble residual versus host-galaxy morphology. Residuals are measured in the sense that residual = $m_B - m_{B,\ \mathrm{corr}}$. In the middle panel we plot x_1 versus host-galaxy morphology. In the bottom panel we plot c versus host-galaxy morphology. The red squares are the error-weighted mean value for each morphology bin. We do not find significant evidence of a trend between Hubble residual and host-galaxy morphology.

expected to have a lower dust content and minimal amounts of star formation compared to late-type galaxies which generally exhibit more star formation. The bluer colors in early-type galaxies may reflect the lack of host-galaxy extinction. SNe in our middle galaxy bins show a larger distribution of c values.

Projected Galactocentric Distance

Similar to the above discussion of host-galaxy morphology, we now turn to an analysis with projected galactocentric distance (PGCD). In Figure 4.10, we plot Hubble residual (top panel), x_1 (middle panel), and c (bottom panel) as a function of PGCD. Points are color coded by their host-galaxy morphology as either Early (red squares), Mid (gray circles), or Late (blue triangles) galaxies using the definition of the previous subsection.

We do not see any significant trends of Hubble residual with PGCD or with host-galaxy classification. There is a noticeable lack of SNe in late-type galaxies at a PGCD > 20 kpc which was also noticed by Hicken et al. (2009a). Partitioning our sample into two subsamples using a cut of 10 kpc in PGCD, we find that the inner sample has $\sigma = 0.186$ mag and the outer sample has $\sigma = 0.156$ mag. The larger Hubble residual from SNe within 10 kpc may be the result of systematic uncertainties due to the difficulty in galaxy template subtraction or the increased effects of host-galaxy extinction. Future SN Ia samples may be able to reduce the scatter in Hubble diagrams by only using SNe at a PGCD > 10 kpc.

In the middle panel of Figure 4.10, we plot x_1 against PGCD. As mentioned in the previous subsection, SNe Ia are primarily underluminous (small x_1) in early-type galaxies and overluminous (larger x_1) in late-type galaxies. Mid-type galaxies show a rather uniform distribution within the inner 20 kpc of the host. However, at distances > 20 kpc, the error-weighted x_1 mean increases from -0.473 ± 0.092 to 0.345 ± 0.284 (standard error of the mean), corresponding to a 2.7σ difference.

In the bottom panel of Figure 4.10, we plot c versus PGCD. As one might naively expect, the reddest SNe are primarily located within the inner 10 kpc where host-galaxy reddening will likely affect SN color. Moving out to larger PGCD, SN color becomes increasing bluer for all of our galaxy classes.

4.5.3 Silicon Velocity

Recent attention has been drawn to incorporating velocity information into distance fits. Wang et al. (2009a) found that separating SNe Ia into normal and high-velocity (HV) classifications based on Si II λ6355 velocity near maximum light significantly improved distance estimates. Wang et al. (2009a) found that the two classes have different observed $B_{\max} - V_{\max}$

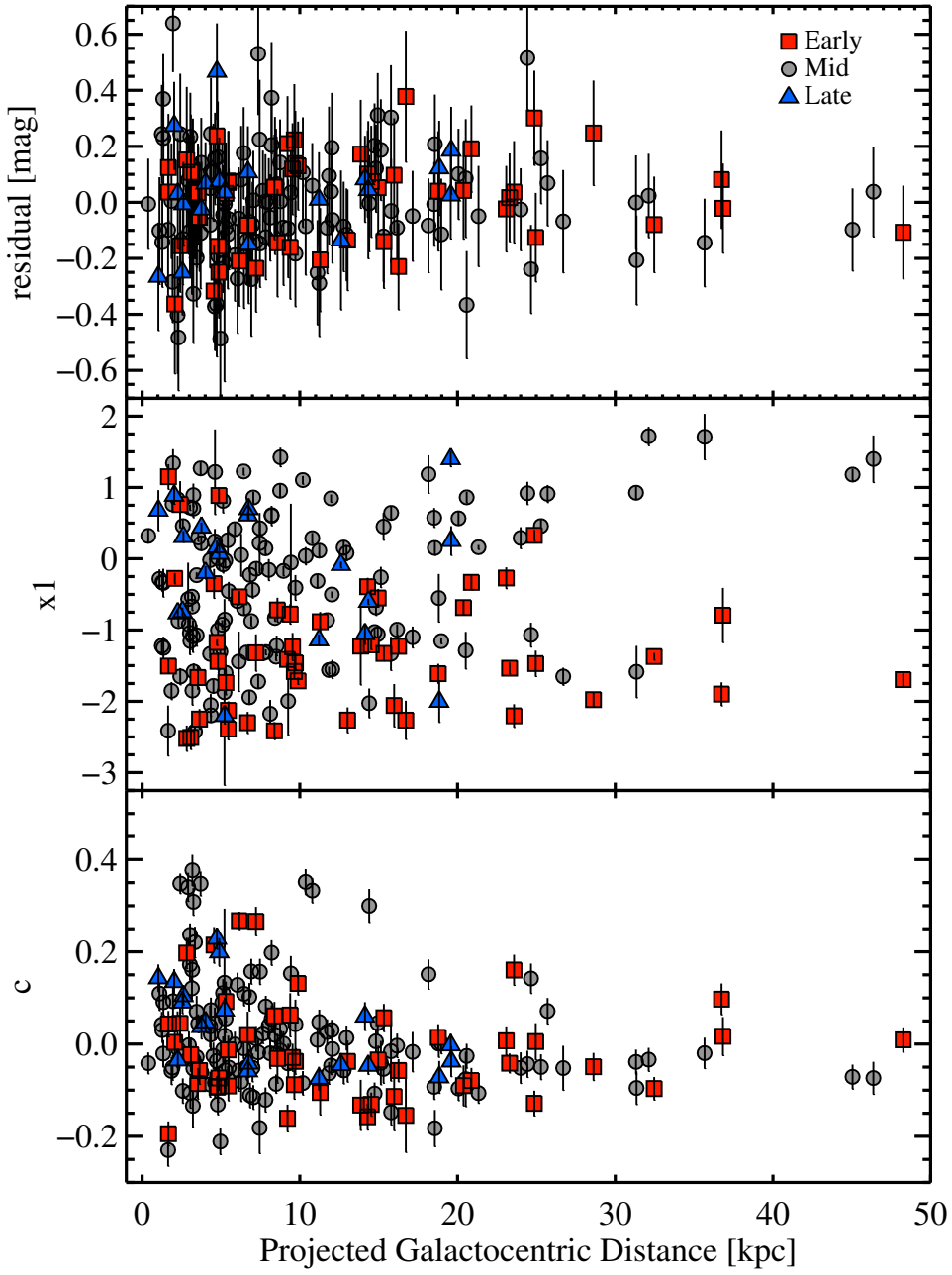

Figure 4.10: Parameters versus projected galactocentric distance. The top panel shows Hubble residual versus PGCD. The middle panel is x_1 versus PGCD, and the bottom panel is c versus PGCD. Points are color coded by galaxy type. We find that the reddest SNe occur within 15 kpc of the host-galaxy nucleus.

distributions while having similar $\Delta m_{15}(B)$ distributions. Performing a χ^2 minimization fit in the same vein as Equation 4.4, the authors found that the HV SNe preferred a lower β than the normal SNe, indicating either a difference in the intrinsic color distribution and/or differences in the reddening law for the two samples.

In this section, we look for trends between our derived light-curve parameters, host-galaxies properties, and Si II velocity as measured by the minimum of the blueshifted feature of the λ6355 line within 5 days of maximum light. Previous studies by Blondin et al. (2011) and Silverman et al. (2012a) found that including velocity information along with light-curve parameters did not substantially improve distance estimates. We match objects in our low-z photometry sample presented here to the BSNIP spectroscopic sample (Silverman et al. 2012c). We also apply the software and algorithmic frarmework laid out by Silverman et al. (2012b) to measure Si II velocities in the near-maximum-light spectra published by Blondin et al. (2011). We have photometric and spectroscopic measurements for 65 objects. We note that LOSS light-curve parameters measured using light curves in the Landolt system were used in a similar study by Silverman et al. (2012a). Here, we use the light-curve parameters derived from the LOSS natural-photometry system.

Building upon this work, Foley & Kasen (2011) use the Wang et al. (2009a) sample and attribute the difference in β to differences in the intrinsic reddening distribution of the two subclasses. Using the CfA spectroscopy sample, Foley et al. (2011) find that splitting objects into these two classes based on Si II at maximum light improves distance measurements.

Rather than separating SNe into two classes, we seek to assess whether incorporating $v_{\rm Si}$ as a continuous parameter along with light-curve parameters improves distance estimates. In Figure 4.11, we plot the Hubble residual versus the measured Si II λ6355 velocity for 65 objects in our low-z sample having spectral measurements from BSNIP. There is no obvious trend between residual and velocity. Performing a Bayesian Monte Carlo linear regression (Kelly 2007), we find a slope consistent with 0, indicating no statistically significant correlation between the two variables (dashed line). We find a Pearson linear-correlation coefficient of -0.044 ± 0.084, consistent with no correlation.

Foley & Kasen (2011) found that distance estimates to SNe Ia may be improved by taking advantage of a relationship between Si II velocity at maximum light and "intrinsic color" (Foley et al. 2011; Foley 2012). Foley et al. (2011) found a 8.8σ relationship between "intrinsic color" and Si II velocity that, when accounted for, decreases the dispersion in distance estimates. However, their definition of intrinsic color assumed a somewhat simplistic offset from the observed $B_{\rm max} - V_{\rm max}$ pseudocolor. Blondin et al. (2012) performed a more sophisticated measurement of intrinsic $B_{\rm max} - V_{\rm max}$ color with rigorous handling of uncertainties and found a significantly reduced correlation at the 2σ level. Their intrinsic

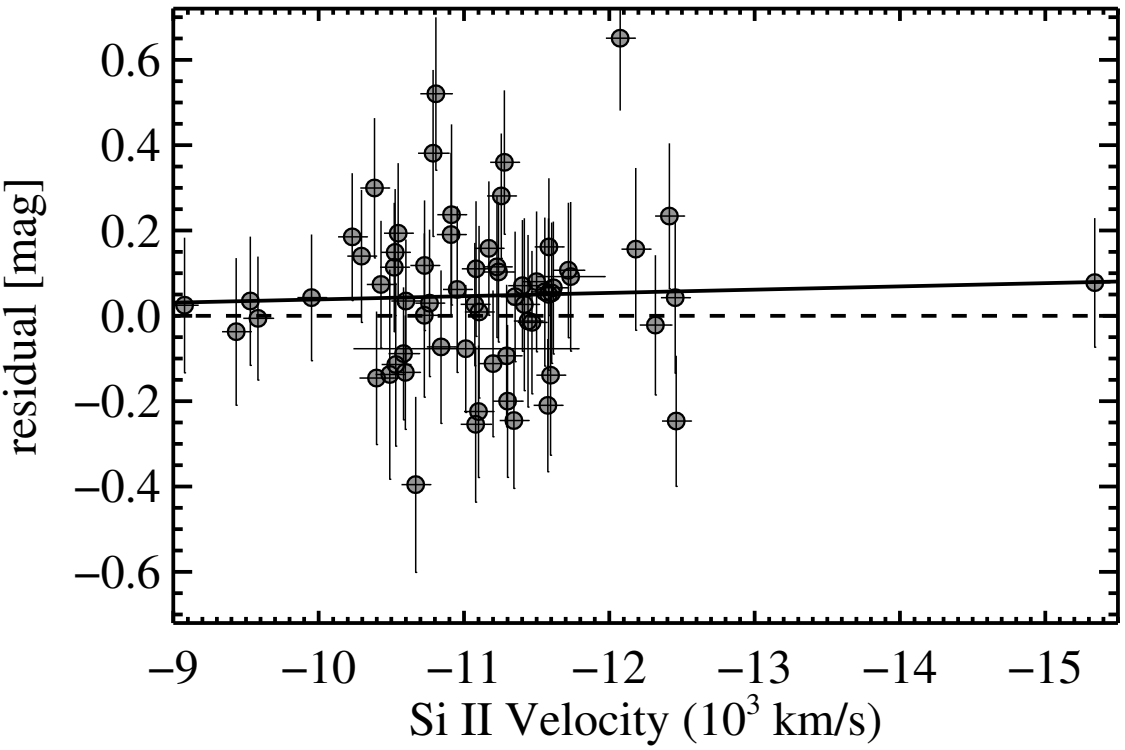

Figure 4.11: Hubble residual versus Si II velocity. Overplotted as a solid line is a linear fit to the data. The slope is consistent with 0, indicating no significant correlation between Hubble residual and Si II velocity.

color estimates were derived from BayeSN (Mandel et al. 2009, 2011) which incorporates population correlations between intrinsic absolute magnitudes, intrinsic colors, light-curve shape, and host-galaxy properties. While our work makes use of the SALT2 c parameter which is more closely related to the $B_{\max} - V_{\max}$ observed color, we do not see evidence that including a linear correction for Si II velocity will improve distance estimates.

In Figure 4.12, we plot the Hubble residual versus c (similar to the bottom panel of 4.7) color coded by Si II velocity. In Section 4.4.3 we noted a trend between Hubble residual and c indicating that the bluest objects preferred a smaller β value. The linear trend is still visible with fewer objects (65 here versus 586 in Section 4.4.3). Wang et al. (2009a) and Foley & Kasen (2011) find that objects classified as high velocity ($v_{\mathrm{Si\ II}} > 11,800$ km s^{-1}) have a redder color distribution compared to normal objects. This is not evident in our plot indicating that the linear trend between c and Hubble residual does correspond to a correlation with $v_{\mathrm{Si\ II}}$.

In Figure 4.13, we plot the Si II velocity for 56 objects having spectroscopic and host-galaxy information. We use the same color code as in the bottom panel of Figure 4.10, with red squares representing Early galaxies (E–S0), gray circles as Mid galaxies (S0a–Sc), and blue triangles for Late galaxies (Scd/Sd/Irr). We do not see an obvious trend regarding the distribution of Si II velocities in any of these galaxy bins. Similarly, Wang et al. (2009b) found that Normal and HV objects reside in similar host-galaxy distributions (see their Figure 3d). Dividing our sample into HV and Normal objects using the criterion of Wang et al. (2009b), we find that both objects have a similar PGCD distribution based on a two-sided Kolmogorov-Smirnoff test (68% probability the two samples are drawn from the same parent distribution).

For the above analysis, we used SNe with velocities taken within 5 d of maximum light in the B band. We have also performed our analysis using the family of velocity evolution curves presented by Foley et al. (2011) derived from the CfA spectral sample (Blondin et al. 2012) to extrapolate our velocities at various phases to velocity at maximum light in the B band. The family of curves is derived for SNe with $1.0 < \Delta m_{15}(B) < 1.5$ mag with velocity measurements made within a week of maximum light under the assumption that a Si II velocity is proportional to its time gradient. Using this relation does not change any of the results presented here.

Previous work by Wang et al. (2009a) and Foley & Kasen (2011) found that separating objects into two classes with different reddening laws improved distance estimates. We do not find any evidence that including Si II velocity as a continuous parameter improves distance estimates or correlates to trends seen in SALT2 c. A more in-depth analysis that can infer the intrinsic color of SNe by disentangling contributions from host-galaxy reddening is required

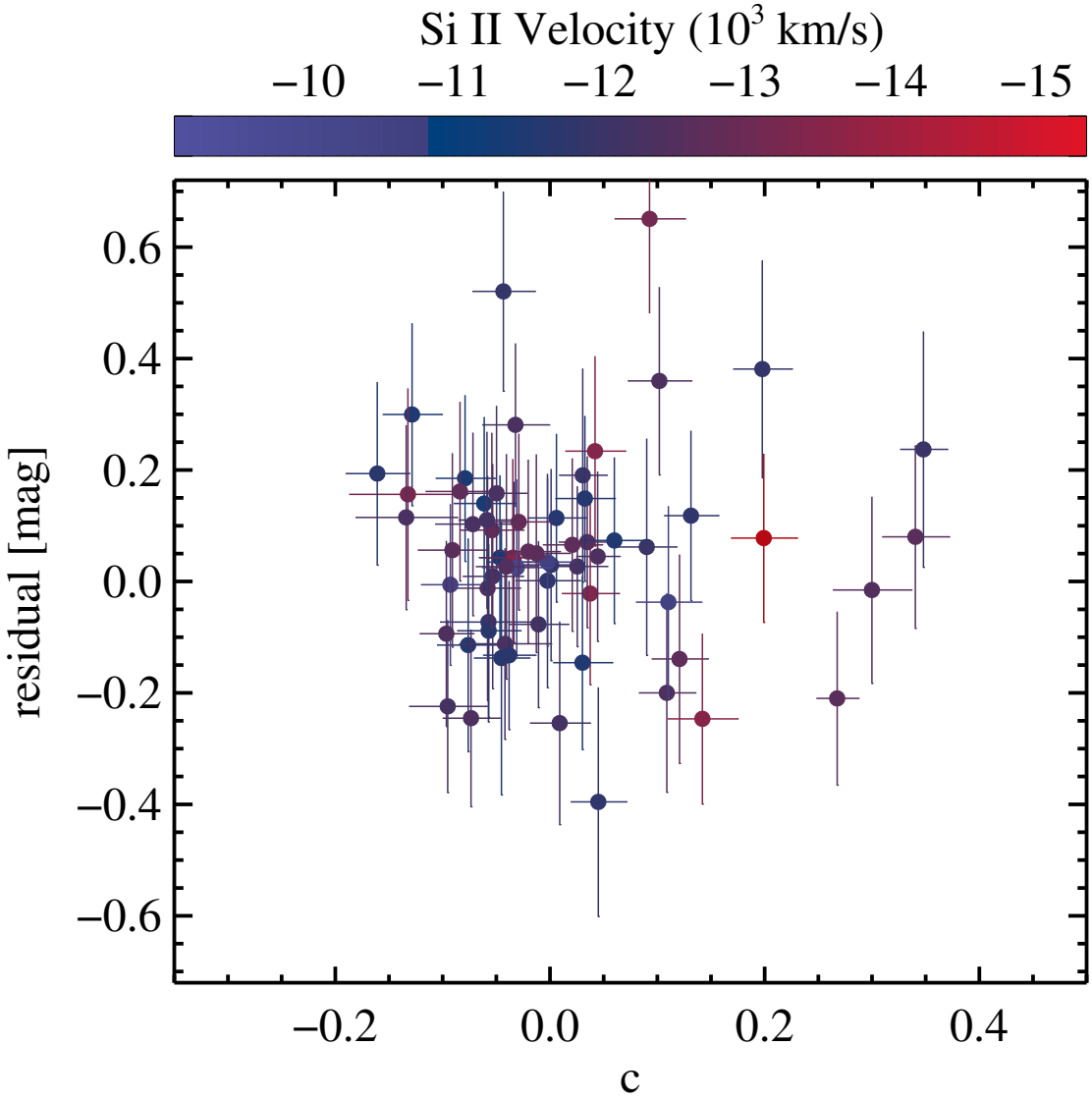

Figure 4.12: Hubble residual versus c color coded by Si II velocity. We do not see an obvious trend with respect to where higher velocity objects are located in this figure.

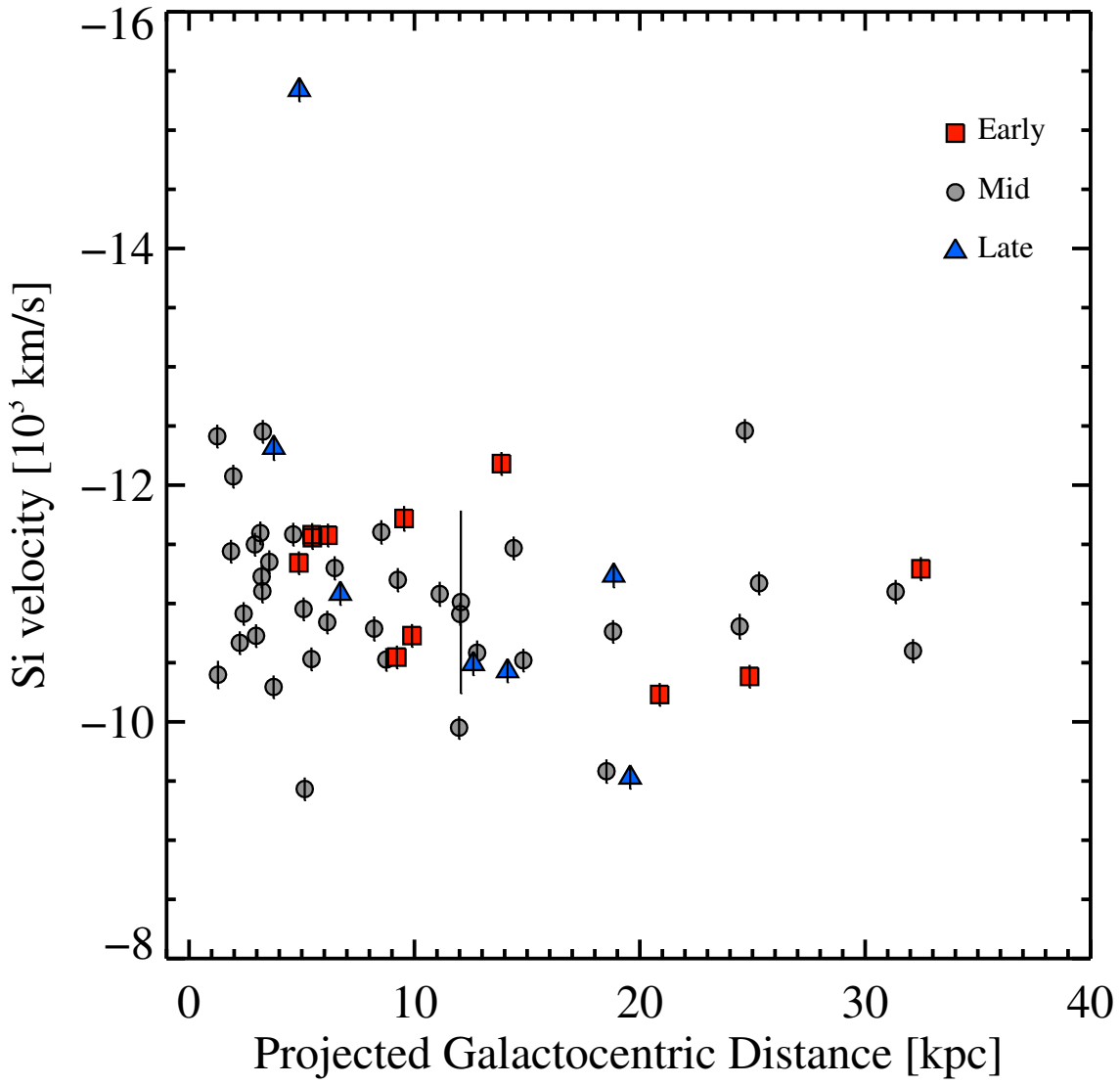

Figure 4.13: Si II velocity versus projected galactocentric distance. Objects are color-coded by galaxy type. Early-type galaxies (E–S0) are red squares, mid-type galaxies (S0a–Sbc) are gray circles, and late-type galaxies (Scd/Sd/Irr) are blue triangles. We do not see a significant difference between velocity and galaxy type, although the average Si II velocity appears to slightly decrease with PGCD.

to better test how velocities may improve distance estimates.

4.6 Conclusions

We have presented a cosmological analysis of the first LOSS data release of the light curves for 165 SNe Ia in addition to other photometry datasets available in the literature. Rather than fitting our photometry from Chapter 2 in the Landolt system, we have re-reduced our data on the natural system of the KAIT and Nickel telescopes and implemented SALT2 with accurate throughput curves for our telescope systems. Both the Landolt and natural system light curves for our SN Ia sample as well as the modifications to the SALT2 package will be made available to the community.

From our SN Ia measurements alone, we measured $w = -0.86^{+0.13}_{-0.16}(\text{stat}) \pm 0.11(\text{sys})$ consistent with a cosmological constant. We reject a Universe devoid of dark energy or a failure of General Relativity at the $> 4\sigma$ level (99.999% confidence). When combined with other probes of cosmology such as BAO (Percival et al. 2010) and measurements of anisotropy in the CMB (Komatsu et al. 2011), we find improved constraints of $w = -1.067^{+0.050}_{-0.046}$. Allowing for curvature in a Universe with a cosmological constant, our results are consistent with a flat, Λ-dominated Universe.

Using a Monte Carlo routine, we investigated the role that zero-point calibration uncertainties play in the error budget for cosmological parameters. Motivated by mean offsets between different low-z datasets for overlapping SNe, we adopt a typical uncertainty of 0.02 mag for the zero point for each filter bandpass of each photometry system. Our uncertainty in the calibration zero point from the low-z datasets propagates into an uncertainty of 0.11 in w. This is smaller than the statistical uncertainty, but still a significant contribution to the total uncertainty. Future low-z SN Ia samples will be best served by adopting a natural photometry system in common with the higher-z samples.

Our data are consistent with no existence of a monopole in the galaxy velocity field produced by a relative under density in the local Universe (i.e., a Hubble bubble). Previous detections were likely due to the treatment of SN color. In this work, we adopt a linear correction term that prefers a coefficient for SN color which implies $R_V \approx 2.2$. Previous detections of the Hubble bubble enforced a prior of $R_V = 3.1$ on host-galaxy dust. Our results agree with the analyses of Conley et al. (2007) and Hicken et al. (2009a).

We found no significant correlations between Hubble residuals and host-galaxy properties. This runs counter to recent studies that find massive galaxies host brighter SNe after correcting for light-curve width and SN color (Kelly et al. 2010; Sullivan et al. 2010; Lampeitl et al. 2010). We caution, however, that our work used galaxy morphology as a proxy for

galaxy mass. We find that early-type (E–S0) and mid-type (S0a–Sc) galaxies have a similar mean residual, while late-type (Scd/Sd/Irr) galaxies have a larger relative residual. The scatter in Hubble residuals is roughly the same in these three galaxy bins. Future studies by our group incorporating more detailed galaxy properties from stellar population synthesis models will better answer whether our dataset agrees with observed trends with host-galaxy mass.

We do not find evidence that including the Si II λ6355 velocity near maximum light as a continuous parameter improves distance estimates. This confirms the results of Blondin et al. (2011) and Silverman et al. (2012a).

Improvements to measurements of cosmological parameters with SNe Ia rest on our ability to limit systematic uncertainties. Our analysis found that zero-point calibration uncertainties between the various low-z samples contribute a sizable fraction to the error budget. Future datasets taken with a single telescope system such as Pan-STARRS and LSST will greatly advance our ability to test cosmological models.

Chapter 5

The Low-Velocity, Rapidly Fading Type Ia Supernova 2002es

A version of this chapter was published in *The Astrophysical Journal* (Ganeshalingam, M., et al. 2011, ApJ, 751,152).

Abstract

SN 2002es is a peculiar subluminous Type Ia supernova (SN Ia) with a combination of observed characteristics never before seen in a SN Ia. At maximum light, SN 2002es shares spectroscopic properties with the underluminous SN 1991bg subclass of SNe Ia, but with substantially lower expansion velocities ($\sim$6000 km s^{-1}) more typical of the peculiar SN 2002cx subclass. Photometrically, SN 2002es differs from both SN 1991bg-like and SN 2002cx-like supernovae. Although at maximum light it is subluminous ($M_B = -17.78$ mag), SN 2002es has a relatively broad light curve ($\Delta m_{15}(B) = 1.28 \pm 0.04$ mag), making it a significant outlier in the light-curve width vs. luminosity relationship. We estimate a ^{56}Ni mass of 0.17 ± 0.05 M$_\odot$ synthesized in the explosion, relatively low for a SN Ia. One month after maximum light, we find an unexpected plummet in the bolometric luminosity. The late-time decay of the light curves is inconsistent with our estimated ^{56}Ni mass, indicating that either the light curve was not completely powered by ^{56}Ni decay or the ejecta became optically thin to γ-rays within a month after maximum light. The host galaxy is classified as an S0 galaxy with little to no star formation, indicating the progenitor of SN 2002es is likely from an old stellar population. We also present a less extensive dataset for SN 1999bh, an object which shares similar photometric and spectroscopic properties. Both objects were found as part of the Lick Observatory Supernova Search, allowing us to estimate that these objects

should account for 2.5% of SNe Ia within a fixed volume. Current theoretical models are unable to explain the observed characteristics of SN 2002es.

5.1 Introduction

Type Ia supernovae (SNe Ia) are the runaway thermonuclear explosions of carbon-oxygen white dwarfs. SNe Ia are characterized spectroscopically by an absence of hydrogen and the presence of intermediate-mass elements (e.g., silicon, sulfur, oxygen) and iron-group elements (iron, cobalt) (e.g., Filippenko 1997, and references therein). A majority of spectroscopically identified SNe Ia form a class of objects with a standardizable luminosity, allowing for their use as accurate distance indicators. Application of SNe Ia on extragalactic scales led to the discovery that the Universe is accelerating in its expansion (Riess et al. 1998; Perlmutter et al. 1999). Subsequent application of large samples of SNe Ia out to high redshifts (Wood-Vasey et al. 2007; Hicken et al. 2009a; Kessler et al. 2009a; Amanullah et al. 2010; Sullivan et al. 2011a; Suzuki et al. 2012) has led to precise estimates of cosmological parameters when combined with measurements of baryon acoustic oscillations (BAO) and anisotropy in the cosmic microwave background (CMB).

The cosmological application of SNe Ia is predicated on the relationship between the peak absolute magnitude of a SN, the width of its light curve, and its color. Phillips (1993) found that SNe with slowly declining light curves had a larger luminosity at maximum light. Applying corrections for light-curve width and SN color (as a measurement of host-galaxy extinction and intrinsic scatter in SN colors) has allowed SNe Ia to be accurate distance indicators to within 10% in distance (Jha et al. 2007; Guy et al. 2007; Conley et al. 2008). There are indications that including spectral information (Foley et al. 2008; Wang et al. 2009a; Bailey et al. 2009; Foley & Kasen 2011; Blondin et al. 2011; Silverman et al. 2012a) and host-galaxy information (Kelly et al. 2010; Sullivan et al. 2010; Lampeitl et al. 2010) further improves distance estimates.

Despite the ability to standardize the luminosity of SNe Ia based on observed light-curve properties, a significant fraction of SN Ia events have peculiar characteristics, including some overluminous and underluminous objects (e.g., Filippenko 1997, and references therein). In particular, Filippenko et al. (1992b) and Leibundgut et al. (1993) found that optical light curves of SN 1991bg evolved rapidly, and its peak luminosity was $\sim$2 mag fainter than that of normal objects. Moreover, the maximum-light spectrum of SN 1991bg showed strong Ti II absorption, indicating a relatively cool photosphere, and the expansion velocity at maximum light as measured from the absorption minimum in the blueshifted Si II λ6355 feature was $\sim$10,000 km s^{-1}, slightly lower than expansion velocities measured for normal SNe Ia ($\sim$

11,000–13,000 km s^{-1}) (Filippenko et al. 1992b). Since the initial identification of SN 1991bg as a subclass of SNe Ia, many members belonging to the subclass have been identified by the SN community. Studies of the host-galaxy morphology indicate that SN 1991bg-like objects are found preferentially in early-type galaxies (Howell 2001; Li et al. 2011a), leading to the suggestion that the progenitors of SN 1991bg-like SNe come from old stellar populations. There is currently debate about the cosmological utility of SN 1991bg-like objects as standardizable candles (Jha et al. 2007; Guy et al. 2007).

More recently, a range of properties for peculiar subluminous SNe Ia have been discovered. Foley et al. (2010b) presented evidence that SN 2006bt spectroscopically resembled SN 1991bg, but photometrically resembled a normal SN Ia. SN 2006bt was discovered at a projected distance of 33.7 kpc from the nucleus of its early-type host galaxy. The Palomar Transient Factory (PTF; Law et al. 2009) has published data on two peculiar subluminous objects, both discovered at large distances from the likely host galaxy. PTF 09dav was an abnormally subluminous SN Ia ($M_B = -15.44$ mag) with a narrow light curve found 41 kpc from its host galaxy (Sullivan et al. 2011b). Maguire et al. (2011) presented data on the subluminous PTF 10ops which shared many similarities with SN 2006bt. PTF 10ops had a broad light curve and was seen at a projected distance of 148 kpc from the nominal host. All objects had spectral features that match those of SN 1991bg, although PTF 09dav had particularly slow expansion velocities of 6100 km s^{-1}.

Objects similar to SN 2002cx (Filippenko 2003; Li et al. 2003b) form another subclass of subluminous peculiar SNe Ia. These objects have maximum-light spectra similar to those of overluminous objects like SN 1991T, characterized by weak Si II λ6355 features and dominated by Fe III lines indicating a hot photosphere. However, the expansion velocities of these objects at maximum light are $\sim$6000 km s^{-1}, indicating an explosion with low kinetic energy per unit mass. There appears to be a great diversity among SN 2002cx-like objects, with a distribution of absolute luminosity and kinetic energy (Narayan et al. 2011; McClelland et al. 2010). SN 2008ha is the faintest member of the subclass, with $M_V = -14.2$ mag and velocities of $\sim$4000–5000 km s^{-1} at maximum light (Foley et al. 2010a).

Here we report our observations of SN 2002es, an object somewhat spectroscopically similar to SN 1991bg, further adding to the puzzle of subluminous SNe Ia. SN 2002es was discovered (Li et al. 2002) on unfiltered CCD images at $\sim$16.3 mag as part of the Lick Observatory Supernova Search (LOSS) with the 0.76-m Katzman Automatic Imaging Telescope (KAIT; Filippenko et al. 2001; Li et al. 2003a) on 2002 Aug. 23.5 (UT dates are used throughout this paper) in UGC 2708. Its J2000 coordinates are $\alpha = 03^{\rm h}23^{\rm m}47^{\rm s}.23$ and $\delta = +40^\circ33'53.5''$, which is 19″ W and 26″ N of the galaxy nucleus (Li et al. 2002). Subsequent optical spectroscopic observations on 2002 Sep. 03 by Chornock et al. (2002)

and Matheson et al. (2002) classified SN 2002es as a SN 1991bg-like object near maximum light based on the presence of strong Ti II, Si II, and O II absorption features, but with an expansion velocity of ∼6000 km s^{-1} as measured from the absorption minimum of the Si II λ6355 feature. This is notably lower than typical expansion velocities of ∼11,000 km s^{-1} found in normal SNe Ia and SN 1991bg-like objects and more typical of SN 2002cx-like objects (Li et al. 2003b).

Noting the peculiarity of SN 2002es, our group started a photometric and spectroscopic campaign to document the evolution of this unique object. Here we present *BVRI* photometry for SN 2002es starting a week before maximum light collected as part of the LOSS SN Ia photometry program (see Chapter 2). Late-time photometry was obtained with the 2.3-m Bok telescope at Steward Observatory on Kitt Peak in Arizona to constrain the late-time decay of the light curve. We also show an extensive optical spectral series covering the evolution of SN 2002es from maximum light to two months after maximum. In addition, we argue that SN 1999bh is a SN 2002es-like event.

The rest of the paper is structured as follows. Our data and reduction techniques are presented in Section 5.2, with a detailed analysis of our photometry and spectroscopy in Section 5.3. In Section 5.4, we discuss possible physical interpretations for the observed properties of SN 2002es and compare SN 2002es to theoretical models. We summarize our results in Section 5.5.

5.2 Observations

5.2.1 Photometry

Broadband photometric follow-up observations of SN 2002es started on 2002 Aug. 24.48 (one week before $B_{\max}$) with KAIT in the *BVRI* bands. SN 2002es was monitored with a 1–2 day cadence for the first month after discovery, resulting in well-sampled light curves. Additional *BVRI* photometry from the 1-m Nickel telescope at Lick Observatory was obtained to complement the KAIT data. Late-time data in *BVR* were taken using the 2.3-m Bok telescope. A *V*-band image of the field from KAIT is shown in Figure 5.1.

Images were bias subtracted and flat fielded using standard procedures in `IRAF`.[1] SN 2002es was sufficiently close to its host galaxy that galaxy subtraction was required to disentangle SN light from galaxy light. Templates for the field were obtained for the KAIT, Nickel, and Bok telescopes after SN 2002es faded beyond the detection limit of each telescope (>2 yr

[1]IRAF: The Image Reduction and Analysis Facility is distributed by the National Optical Astronomy Observatory, which is operated by the Association of Universities for Research in Astronomy (AURA), Inc., under cooperative agreement with the National Science Foundation (NSF).

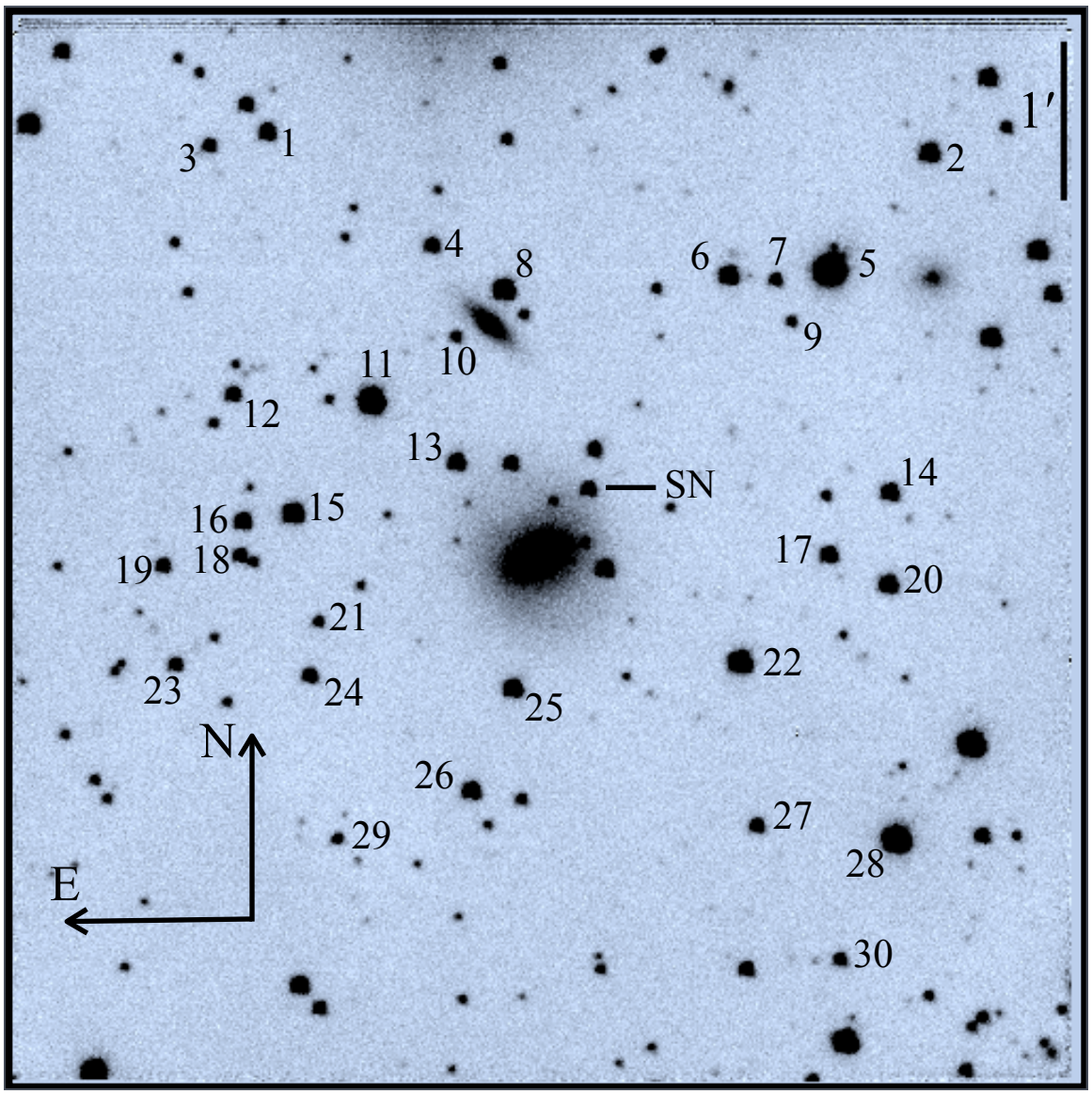

Figure 5.1: KAIT V-band image of SN 2002es. The field is $6.7' \times 6.7'$. The SN and comparison stars are marked. The labels of the comparison stars correspond to the numbers in Table 5.1.

after discovery) and subtracted from the data images. The flux from the SN was measured in comparison to local field stars using point-spread function (PSF) fitting photometry. The uncertainties in our photometric measurements were estimated by randomly injecting artificial stars with the same PSF and magnitude as the SN into the data images. The images with artificial stars were rerun through our galaxy-subtraction and photometry routines, and the scatter in doing this 20 times was adopted as the photometric measurement error.

Instrumental magnitudes were color-corrected to the Landolt system (Landolt 1992, 2009) using the average color terms measured from multiple photometric nights. The magnitudes of local field stars were calibrated against Landolt standards on six photometric nights. The results are reported in Table 5.1. The final photometric error is the photometric measurement error added in quadrature with the error in the calibration of our field stars. The final photometry is presented in Table 5.2.

In addition to the photometry presented here, we supplement our light curves with *UBVRI* data presented for SN 2002es in the CfA3 photometry sample (Hicken et al. 2009b) taken with the 1.2-m telescope at Fred Lawrence Whipple Observatory (FLWO) in Arizona operated by the Harvard Smithsonian Center for Astrophysics (CfA). The agreement between the KAIT and CfA3 data is within ~ 0.05 mag in all bands, with no evidence of a systematic offset. The light curves from all telescopes are presented in Figure 5.2.

5.2.2 Spectroscopy

Low-resolution spectra of SN 2002es were obtained using the Kast dual spectrograph mounted on the 3-m Shane Telescope at Lick Observatory (Miller & Stone 1993), the FAST spectrograph mounted on the 1.5-m Tillinghast telescope at FLWO (Fabricant et al. 1998), and the Low Resolution Imaging Spectrometer on the 10-m Keck I telescope (LRIS; Oke et al. 1995). All of our observations were taken at the optimal parallactic angle to minimize differential light loss (Filippenko 1982).

All spectra of SN 2002es were reduced using standard CCD processing techniques (e.g., Foley et al. 2003; Matheson et al. 2008). Processing and extraction of the one-dimensional spectra were performed in `IRAF` using the optimal extraction algorithm of Horne (1986). The wavelength calibration was obtained by fitting low-order polynomials to calibration-lamp spectra. Our spectra were flux calibrated using our own `IDL` routines. Corrections for telluric absorption features were made using spectrophotometric standards (Wade & Horne 1988) taken at roughly the same airmass as the SN observation. Table 5.3 presents a summary of our spectroscopic observations.

Table 5.1: Photometry of Local Standard Stars

ID	α (J2000)	δ (J2000)	$B(\sigma_B)$ (mag)	$V(\sigma_V)$ (mag)	$R(\sigma_R)$ (mag)	$I(\sigma_I)$ (mag)	$N_{\rm calib}$
1	03:23:57.81	+40:36:08.0	17.403 (011)	16.497 (008)	15.940 (012)	15.462 (007)	4
2	03:23:35.94	+40:36:00.3	16.470 (010)	15.675 (007)	15.206 (007)	14.744 (012)	5
3	03:23:59.75	+40:36:02.8	17.817 (010)	17.174 (011)	16.785 (012)	16.331 (014)	3
4	03:23:52.38	+40:35:25.2	17.440 (010)	16.844 (007)	16.482 (011)	16.104 (011)	4
5	03:23:39.24	+40:35:16.1	14.293 (009)	12.933 (014)	12.191 (002)	11.545 (011)	2
6	03:23:42.58	+40:35:14.0	16.442 (007)	15.702 (003)	15.265 (005)	14.851 (011)	5
7	03:23:41.02	+40:35:12.2	17.978 (011)	17.314 (011)	16.905 (013)	16.482 (010)	5
8	03:23:50.00	+40:35:08.6	15.777 (011)	15.119 (005)	14.727 (007)	14.325 (011)	4
9	03:23:40.51	+40:34:56.4	18.618 (013)	17.970 (004)	17.579 (010)	17.035 (008)	2
10	03:23:51.59	+40:34:50.8	18.657 (013)	17.786 (006)	17.292 (008)	16.865 (006)	3
11	03:23:54.37	+40:34:26.8	14.523 (012)	14.040 (011)	13.736 (013)	13.407 (006)	4
12	03:23:58.96	+40:34:29.2	17.496 (012)	16.721 (011)	16.254 (013)	15.735 (013)	4
13	03:23:51.57	+40:34:03.6	16.938 (010)	16.180 (005)	15.744 (011)	15.296 (015)	4
14	03:23:37.25	+40:33:52.3	17.115 (009)	16.126 (006)	15.542 (007)	15.047 (012)	4
15	03:23:56.96	+40:33:44.5	15.783 (012)	15.258 (012)	14.905 (007)	14.554 (010)	4
16	03:23:58.62	+40:33:41.4	16.993 (010)	16.280 (011)	15.833 (008)	15.395 (015)	4
17	03:23:39.26	+40:33:28.8	16.795 (010)	16.222 (005)	15.863 (008)	15.503 (012)	4
18	03:23:58.71	+40:33:28.4	17.935 (011)	17.021 (003)	16.477 (008)	16.003 (007)	4
19	03:24:01.27	+40:33:24.7	18.038 (013)	16.979 (010)	16.402 (008)	15.814 (017)	3
20	03:23:37.30	+40:33:17.8	16.652 (013)	15.842 (011)	15.360 (009)	14.935 (013)	4
21	03:23:56.13	+40:33:03.5	18.860 (010)	17.906 (005)	17.374 (012)	16.956 (008)	3
22	03:23:42.20	+40:32:48.4	15.821 (011)	14.705 (003)	14.090 (005)	13.512 (009)	5
23	03:24:00.85	+40:32:47.5	17.769 (009)	17.064 (005)	16.658 (006)	16.233 (005)	2
24	03:23:56.43	+40:32:43.2	17.724 (011)	16.895 (004)	16.377 (009)	15.836 (013)	5
25	03:23:49.70	+40:32:38.5	16.919 (009)	15.795 (004)	15.101 (007)	14.540 (003)	4
26	03:23:51.07	+40:31:60.0	16.680 (011)	15.987 (005)	15.583 (007)	15.170 (013)	5
27	03:23:41.64	+40:31:46.7	18.034 (012)	16.877 (011)	16.157 (012)	15.481 (014)	2
28	03:23:37.03	+40:31:41.7	14.570 (007)	13.860 (007)	13.427 (012)	13.003 (016)	3
29	03:23:55.50	+40:31:41.6	18.669 (011)	17.703 (012)	17.062 (011)	16.456 (007)	4
30	03:23:38.90	+40:30:56.3	17.954 (013)	17.261 (010)	16.836 (013)	16.417 (014)	4

1σ uncertainties (in units of 0.001 mag) are listed in parentheses.

Table 5.2: Photometry of SN 2002es

JD − 2,452,000	B (mag)	V (mag)	R (mag)	I (mag)	Telescope
510.98	17.682 (033)	17.245 (028)	17.007 (025)	16.835 (031)	KAIT

Continued on Next Page . . .

Table 5.2 –Continued

JD − 2,452,000	B (mag)	V (mag)	R (mag)	I (mag)	Telescope
511.98	17.625 (029)	17.148 (027)	16.882 (022)	16.711 (029)	KAIT
512.97	17.498 (033)	17.050 (028)	16.786 (027)	16.622 (030)	KAIT
514.00	17.482 (034)	17.009 (029)	16.711 (029)	16.521 (033)	KAIT
515.01	17.453 (035)	16.918 (026)	16.669 (020)	16.470 (030)	KAIT
516.01	···	16.752 (111)	16.552 (097)	16.375 (033)	KAIT
517.02	17.372 (104)	···	16.587 (055)	16.347 (046)	KAIT
518.01	17.307 (044)	16.778 (045)	16.465 (090)	16.374 (022)	KAIT
519.02	17.373 (020)	16.817 (024)	16.503 (020)	16.332 (026)	KAIT
520.01	17.369 (020)	16.762 (020)	16.493 (022)	16.318 (026)	KAIT
520.99	17.414 (026)	16.790 (020)	16.453 (020)	16.303 (026)	KAIT
521.99	···	16.829 (031)	···	16.211 (111)	KAIT
523.02	17.506 (023)	16.829 (021)	16.484 (020)	16.320 (031)	KAIT
524.02	17.550 (026)	16.844 (020)	16.498 (020)	16.339 (037)	KAIT
524.95	17.729 (020)	16.925 (020)	16.514 (020)	16.311 (020)	Nickel
525.95	17.805 (020)	16.985 (020)	16.539 (020)	16.336 (020)	Nickel
528.97	18.094 (020)	17.165 (020)	16.687 (020)	16.400 (020)	Nickel
529.00	18.142 (030)	17.164 (028)	16.640 (023)	16.400 (023)	KAIT
530.01	18.255 (040)	17.193 (025)	16.746 (020)	16.446 (023)	KAIT
531.01	18.323 (039)	17.293 (031)	16.774 (020)	16.492 (022)	KAIT
531.99	18.500 (049)	17.354 (020)	16.814 (020)	16.533 (029)	KAIT
533.00	18.583 (071)	17.525 (080)	16.914 (105)	16.588 (101)	KAIT
535.00	18.779 (037)	17.556 (031)	16.977 (033)	16.621 (025)	KAIT
536.02	18.824 (053)	17.629 (032)	17.042 (033)	16.641 (028)	KAIT
537.99	18.876 (094)	17.717 (050)	17.122 (030)	16.732 (043)	KAIT
540.87	19.041 (155)	17.836 (063)	17.248 (043)	16.792 (058)	KAIT
547.98	19.429 (167)	18.275 (084)	17.715 (036)	17.110 (055)	KAIT
550.97	19.610 (082)	18.464 (061)	17.910 (032)	17.346 (033)	KAIT
551.99	19.744 (032)	18.570 (025)	17.964 (020)	17.417 (042)	Nickel
552.84	19.771 (043)	18.631 (027)	18.010 (021)	17.505 (025)	Nickel
553.96	19.834 (100)	18.602 (070)	18.116 (038)	17.615 (058)	KAIT
561.91	···	···	···	18.481 (334)	KAIT
562.91	···	19.447 (118)	19.167 (109)	18.508 (123)	KAIT

Continued on Next Page . . .

Table 5.2 –Continued

JD − 2,452,000	B (mag)	V (mag)	R (mag)	I (mag)	Telescope
566.87	···	19.579 (161)	19.445 (125)	18.961 (120)	KAIT
573.86	···	20.155 (171)	···	···	KAIT
577.92	···	20.811 (307)	···	···	KAIT
592.89	23.180 (150)	22.711 (110)	22.34 (110)	···	Bok

Note. – 1σ uncertainties (in units of 0.001 mag) are listed in parentheses.

5.2.3 Host Galaxy

The NASA/IPAC Extragalactic Database (NED)[2] lists two discordant values for the heliocentric redshift of UGC 2708 from different sources. The NED webpage for UGC 2708 lists $z_{\rm helio} = 0.028$ as the default redshift determined from marginal measurements of the H I 21-cm line by Monnier Ragaigne et al. (2003). NED warns under the "Essential Note" section that de Vaucouleurs et al. (1991) find $z_{\rm helio} = 0.018$ from optical lines. We obtained a spectrum of UGC 2708 with Kast at Lick Observatory on 2006 July 21.4 to determine the actual redshift of the host galaxy. We find a heliocentric redshift of $z_{\rm hel} = 0.0182 \pm 0.0001$ from measurements of weak, narrow Hα + [N II] emission lines, in good agreement with the value of de Vaucouleurs et al. (1991). The heliocentric redshift of UGC 2708 corresponds to $z_{\rm CMB} = 0.0177$ (in the frame of the cosmic microwave background). We adopt an uncertainty of 300 km s^{-1} to account for any peculiar motions induced by gravitational interactions with neighboring galaxies. For a standard ΛCDM cosmology with $\Omega_{\rm m} = 0.27$, $\Omega_\Lambda = 0.73$, $w = -1$, and $H_0 = 73.8$ km s^{-1} Mpc^{-1} (Riess et al. 2011), we find a luminosity distance $d_L = 73.20 \pm 4.41$ Mpc and a distance modulus $\mu = 34.32 \pm 0.12$ mag. SN 2002es exploded at a projected distance of 11 kpc from the nucleus of UGC 2708.

The original IAUCs that spectroscopically classify SN 2002es (Chornock et al. 2002; Matheson et al. 2002) predate the source for the incorrect redshift listed on NED and likely used the correct redshift supplied by de Vaucouleurs et al. (1991). The correct redshift for SN 2002es was also used in the cosmology analysis of Hicken et al. (2009a).

UGC 2708 was included in a study of SN Ia host-galaxy properties by Neill et al. (2009). The authors estimated galaxy properties by fitting template-galaxy spectral energy

[2]http://ned.ipac.caltech.edu/ .

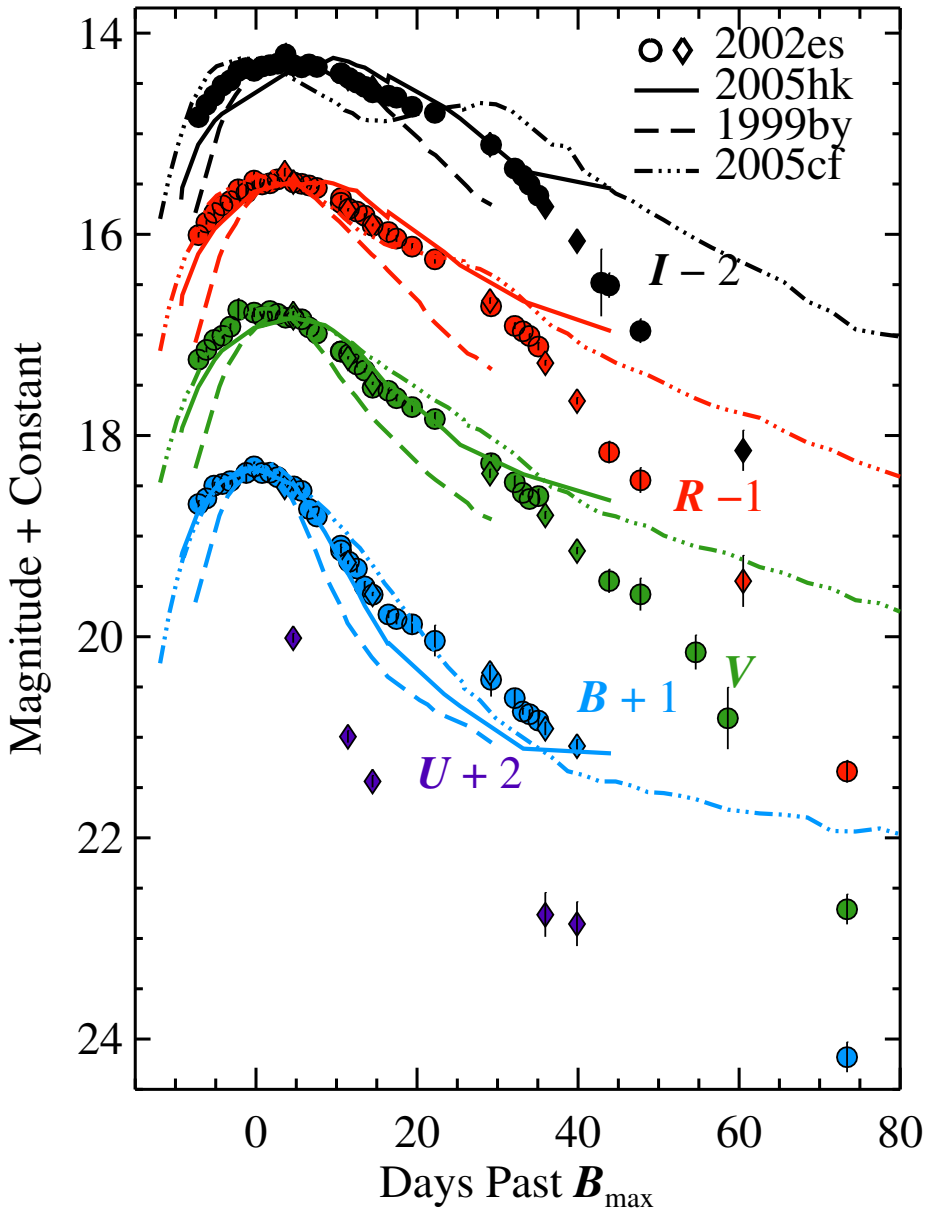

Figure 5.2: *UBVRI* light curves of SN 2002es. Data from the KAIT, Nickel, and Bok telescopes are plotted as circles. Data from Hicken et al. (2009b) are shown as diamonds. For comparison, we include the SN 2002cx-like SN 2005hk (solid line), the SN 1991bg-like SN 1999by (dashed), and the normal SN 2005cf (dot-dashed line). Comparison light curves have been shifted to have the same peak magnitude and phase as SN 2002es. Note the particularly fast decline in all bands at $t > +30$ d compared to the other objects.

distributions (SEDs) to multi-wavelength photometry from the Sloan Digital Sky Survey (SDSS) and the Galaxy Evolution Explorer (GALEX). For UGC 2708, the authors estimated a minimal amount of active star formation and $E(B-V)_{\rm host} = 0.0$ mag. This finding, along with the absence of Na I D absorption at the redshift of the host galaxy in spectra of SN 2002es, indicate that the reddening due to the host galaxy is negligible.

UGC 2708 was also observed spectroscopically as part of SDSS. Using the publicly available line-flux measurements, we find an [N II]/Hα ratio consistent with that of a low-ionization nuclear emission-line region (LINER; Heckman 1980) or a composite galaxy. Coupled with the results from Neill et al. (2009), UGC 2708 is likely a LINER with no active star formation.

Table 5.3: Log of Optical Spectral Observations for SN 2002es

UT Date	Phase[a] (d)	Telescope/Instrument	Exposure Time (s)	Res.[b] (Å)	Observer[c]
2002 Sep. 03.5	+3	Lick/Kast	600	5–12	AF, RC, BS
2002 Sep. 05.5	+5	FLWO/FAST	1200	6–7	MC
2002 Sep. 06.5	+6	FLWO/FAST	1200	6–7	MC
2002 Sep. 10.5	+10	FLWO/FAST	1200	6–7	PB
2002 Sep. 12.5	+12	FLWO/FAST	1200	6–7	MC
2002 Sep. 13.3	+13	Lick/Kast	1200	5–12	RF, SJ, MP
2002 Sep. 28.4	+28	FLWO/FAST	1200	6–7	MC
2002 Oct. 01.3	+30	Lick/Kast	1800	5–12	AF,RF
2002 Oct. 08	+37	Keck I/LRIS	400	6–7	AF,RC
2002 Nov. 08	+67	Keck I/LRIS	1800	6–7	AF, RC,SJ, BB
2002 Nov. 11	+70	Keck I/LRIS	1800	6–7	AF, RC

[a]Rest-frame days relative to the date of $B_{\rm max}$, 2002 Aug. 31.8 (JD 2,452,518.3), rounded to the nearest day.

[b]Approximate spectral resolution.

[c]AF = A. Filippenko, BB = B. Barris, BS = B. Swift, MC = M. Calkins, MP = M. Papenkova, . PB = P. Berlind, RC = R. Chornock, RF = R. Foley, SJ = S. Jha

5.3 Results

5.3.1 Photometry

The light curves of SN 2002es are displayed in Figure 5.2, along with light curves of the normal SN Ia 2005cf (Chapter 2; Wang et al. 2008), the SN 2002cx-like SN Ia 2005hk (Phillips et al. 2007), and the SN 1991bg-like SN Ia 1999by (from Chapter 2).

Basic photometric properties for the light curves of SN 2002es are reported in Table 5.4. All values were measured using a fifth-order polynomial fit directly to the data. Uncertainties were estimated using a Monte Carlo routine to produce 50 realizations of our dataset. Each individual dataset realization was produced by randomly perturbing each photometry data point using its photometric uncertainty assuming a Gaussian distribution. Light-curve properties were measured for each realization, and the final measurements were found by taking the mean and standard deviation of the set of simulated realizations.

The light curves of SN 2002es share some characteristics in common with the subluminous SN 1991bg subtype. SN 2002es lacks a prominent shoulder in the R and I bands (Filippenko et al. 1992b; Leibundgut et al. 1993). The secondary maximum often found in R and I (and more prominently in the near-infrared) is attributed to the cooling of the ejecta to temperatures where the transition from Fe III to Fe II becomes favorable, redistributing flux from shorter wavelengths to longer wavelengths (Kasen 2006). This transition occurs earlier in cooler SNe. From models of the radiative transfer within SNe, Kasen (2006) finds that the timing and strength of the shoulder is dependent on the distribution and amount of ^{56}Ni within the ejecta. Models with a completely homogenized composition and with a small amount of ^{56}Ni result in an I-band light curve with no discernible secondary peak or shoulder. Instead, the two peaks merge to produce a single broad peak. Given the similar absolute magnitudes of SN 2002es and SN 1991bg, the lack of a shoulder or secondary maximum in the R and I bands may be a consequence of low ^{56}Ni production, if the light curve is powered by the decay of ^{56}Ni .

The timing of maximum light in each band is similar to that of SN 1991bg-like SNe. In normal SNe, maximum light in the I band precedes that of B by a few days (as evident in the light curves of SN 2005cf in Figure 5.2). Taubenberger et al. (2008) find that for the SN 1991bg-like SN 2005bl, peak brightness in $UBVRI$ occurred in successive order of bluest to reddest filter with the date of maximum light in each band separated by $\sim$1 d, similar to what is seen in SN 2002es.

The B-band peak magnitude of SN 2002es is 17.33 ± 0.02 mag after correcting for a color excess of $E(B-V) = 0.183$ mag from Milky Way extinction (Schlegel et al. 1998). We assume negligible host-galaxy extinction based on the classification of UGC 2708 as an S0

galaxy and no evidence of Na I D absorption at the host-galaxy redshift. This corresponds to an absolute magnitude of $M_B = -17.78 \pm 0.12$ mag, comparable to other subluminous SNe Ia, but brighter than SN 1991bg-like objects (Taubenberger et al. 2008). The absolute magnitude of SN 2002es is brighter than that of the SN 1991bg-like SN 2005bl by ∼0.5–1 mag in $BVRI$.

Table 5.4: Photometric Properties of SN 2002es

Filter	JD of max − 2,452,000	Mag at max[a]	Peak abs. mag[b]	Δm_{15} (mag)
B	518.30 ± 0.28	17.33 ± 0.02	-17.78 ± 0.12	1.28 ± 0.04
V	519.21 ± 0.28	16.78 ± 0.02	-18.15 ± 0.12	0.74 ± 0.02
R	520.96 ± 0.30	16.47 ± 0.02	-18.35 ± 0.12	0.57 ± 0.02
I	521.39 ± 0.33	16.29 ± 0.02	-18.40 ± 0.12	0.37 ± 0.02

[a]Not corrected for Milky Way or host-galaxy extinction.

[b] Corrected for Milky Way extinction and assuming no host-galaxy extinction.

Despite these similarities with SN 1991bg-like SNe Ia, the light curves of SN 2002es are significantly broader in all bands compared to those of most subluminous objects. Using the decline in magnitudes between maximum light and 15 days after maximum light in the B band as a proxy for light-curve width (Phillips 1993), we measure $\Delta m_{15}(B) = 1.28 \pm 0.04$ mag. Other SN 1991bg-like SNe typically have $\Delta m_{15}(B) \approx 1.9$ mag (Taubenberger et al. 2008).

The light curves of SN 2002es also share similarities to the SN 2002cx-like SN 2005hk. Both objects are subluminous events compared to normal SNe Ia with light curves that are broader than those of SN 1991bg-like objects and lack a shoulder in the R and I bands. SN 2002es has a slower B-band decline than most SN 2002cx-like objects. SN 2005hk had $\Delta m_{15}(B) = 1.56 \pm 0.09$ mag.

As the outer ejecta turn transparent, the light curve is expected to be powered by the thermalization of γ-rays produced by the decay of ^{56}Co (∼50 d after explosion). This is typically observed as a linear fading in all bands. Leibundgut (2000) finds typical decay rates for SNe Ia of 0.014 mag d^{-1} in B, 0.028 mag d^{-1} in V, and 0.042 mag d^{-1} in I. For SN 1991bg, the B-band decline is marginally faster at 0.019 mag d^{-1} and slower in I at 0.040 mag d^{-1}. The V-band decline has been found to be fairly constant among normal and SN 1991bg-like SNe Ia (Leibundgut 2000).

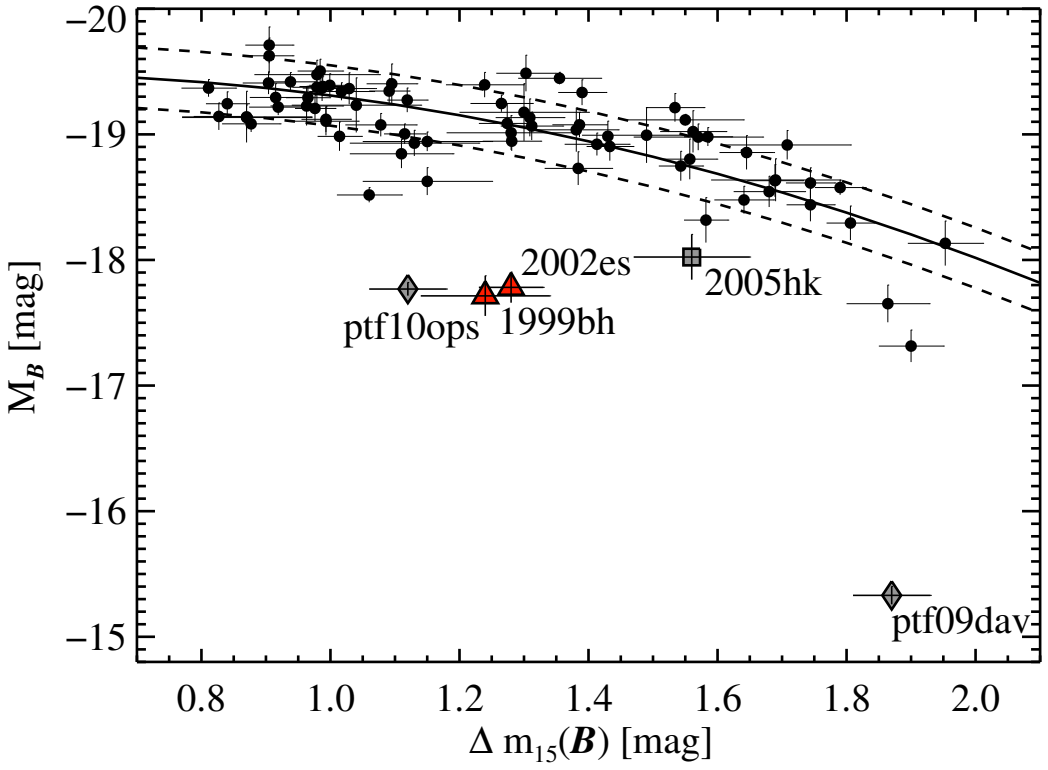

Figure 5.3: M_B as a function of $\Delta m_{15}(B)$ for 76 SNe from Chapter 2 corrected for host-galaxy extinction using values derived from the MLCS distance-fitting software. Overplotted as a solid line is the quadratic Phillips relation from Phillips et al. (1999) shifted along the ordinate to match the data. The dashed lines correspond to the 1σ scatter about the relationship. SN 2002es and SN 1999bh (red triangles) are clear outliers in the relationship. For comparison, we include other subluminous peculiar objects SN 2005hk, PTF 09dav, and PTF 10ops.

Using data at $t > +30$ d (relative to maximum light in the B band), we measure a decline of 0.040 ± 0.004 mag d^{-1} in B, 0.081 ± 0.004 mag d^{-1} in V, 0.101 ± 0.004 mag d^{-1} in R, and 0.099 ± 0.004 mag d^{-1} in I. These rates are substantially faster than expected for an object powered by the decay of ^{56}Co, even after accounting for the declining γ-ray deposition function as the ejecta expand homologously, and cast doubt on whether SN 2002es is necessarily a thermonuclear explosion. In Section 5.4.3, we discuss possible explanations for such a fast decline.

In Figure 5.3, we plot $\Delta m_{15}(B)$ vs. M_B for SN 2002es along with 76 SNe taken from Chapter 2 using host-galaxy extinction values determined with the Multicolor Light-Curve Shape method (MLCS2k2.v006; Jha et al. 2007). The light-curve width vs. luminosity relationship from Phillips et al. (1999), adjusted to $H_0 = 73.8$ km s^{-1} Mpc^{-1}, is overplotted as a solid line with 1σ scatter about the relation indicated by dashed lines. We also include measurements for the peculiar SNe SN 2005hk (Phillips et al. 2007), PTF 09dav (Sullivan et al. 2011b), and PTF 10ops (Maguire et al. 2011). SN 2002es is an obvious outlier (5σ) in the Phillips relation which predicts that SN 2002es should be $\sim$1.3 mag brighter than the observed peak magnitude. The amount of host-galaxy extinction required to explain this discrepancy is unlikely given the absence of Na I D absorption in SN 2002es spectra at the redshift of the host galaxy.

5.3.2 Color Curves

In Figure 5.4, we plot the color evolution of SN 2002es along with SN 2005cf, SN 2005hk, and SN 1999by for comparison. All objects have been corrected for Milky Way extinction using the dust maps of Schlegel et al. (1998). We adopt a host-galaxy color excess of $E(B-V)_{\rm host} = 0.10$ mag for SN 2005cf (Wang et al. 2009b), $E(B-V)_{\rm host} = 0.10$ mag for SN 2005hk (Chornock et al. 2006), and $E(B-V)_{\rm host} = 0.0$ mag for SN 1999by (Garnavich et al. 2004). We assume no host-galaxy extinction for SN 2002es.

The $B-V$ color curve of SN 2002es does not match that of any of our comparison objects. The color evolution is most similar to that of the SN 1991bg-like SN 1999by, but with significant differences in $B-V$ after maximum light in B. Before $t(B_{\rm max})$, SN 2002es and SN 1999by share a similar $B-V$ color evolution that is considerably redder than that of SN 2005cf and SN 2005hk. However, at $\sim$5 d past maximum light in B, SN 1999by quickly becomes redder in $B-V$ while the color evolution of SN 2002es is much more gradual. The $V-R$ and $V-I$ color evolution for SN 2002es and SN 1999by appear much more similar. There is evidence that SN 2002es becomes bluer at $t > +35$ d, although the data are noisy.

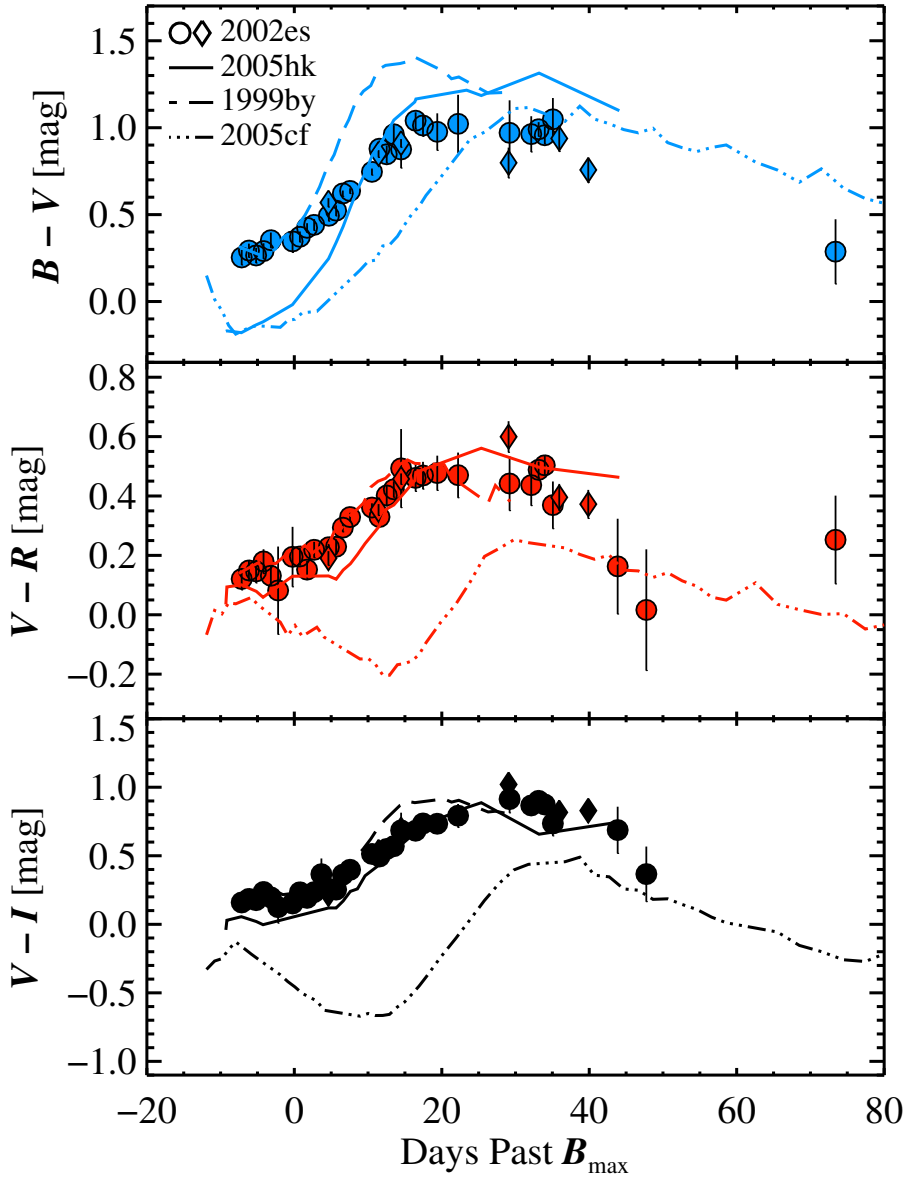

Figure 5.4: Optical color curves of SN 2002es corrected for $E(B-V) = 0.183$ mag from Milky Way extinction. Solid circles are data taken with the KAIT and Nickel telescopes and solid diamonds are from Hicken et al. (2009b). Shown for comparison are SN 2005hk, SN 1999by, and SN 2005cf corrected for extinction using the reddening values provided in their respective reference. SN 2002es is significantly redder in all colors compared to SN 2005cf. None of the comparison color curves provides an adequate match to SN 2002es.

5.3.3 Spectral Properties

In Figure 5.5, we show our time series of spectra covering the evolution of SN 2002es starting 3 d after maximum light in the B band and extending out to two months after maximum light. The absence of Hα and the presence of Si II λ6355 in early-time spectra identify SN 2002es as a SN Ia (e.g., Filippenko 1997). Strong Ti II absorption around 4200 Å is commonly associated with the subluminous SN 1991bg-like subclass of SNe Ia (Filippenko et al. 1992b).

In Figure 5.6, we show our earliest spectrum of SN 2002es compared to spectra of the normal SN 2005cf (Wang et al. 2009b), the subluminous SN 1991bg (Turatto et al. 1996, via the online SUSPECT database[3]), and the SN 2002cx-like SN 2005hk (Phillips et al. 2007). At this phase, SN 2002es shares the most similarities with SN 1991bg. However, the expansion velocity of the photosphere as measured from the minimum in the blueshift of the P-Cyngni profile of Si II λ6355 is 6000 km s^{-1}, significantly lower than typical values of $\sim$11,000 km s^{-1} for normal SNe Ia (Wang et al. 2009a; Foley et al. 2011) and SN 1991bg-like SNe of $\sim$10,000 km s^{-1} (Taubenberger et al. 2008). SN 2002cx-like objects have low ejecta velocities of $\sim$6000 km s^{-1} (Li et al. 2003b; Phillips et al. 2007), comparable to what is found in SN 2002es.

The spectrum of SN 2005hk only covers 3600–7400 Å. Within this spectral range, it shows rather similar features to those of SN 2002es, but with notable differences as well. In particular, it has a weaker Si II λ6355 absorption feature, and no obvious Ti II absorption trough near 4200 Å.

About two weeks after maximum light, SN 2002es begins to show more similarities with SN 2002cx-like objects. In Figure 5.7, we show our spectrum of SN 2002es from 13 d after maximum light compared to those of other objects at a similar phase. At this phase, Si II λ6355 absorption is harder to discern. The Si II/Na I complex around 5700 Å is weaker than what is seen in SN 1991bg. Similar to SN 2002cx-like objects, Fe II $\lambda\lambda$4555, 5129 absorption lines become more apparent and the Ca II H&K lines are similar in strength. However, O I λ7774 and the Ca II near-infrared (NIR) triplet are stronger in SN 2002es compared to SN 2005hk.

In Figure 5.8, we show our +37 d Keck spectrum along with comparison objects. We begin to see emission dominate in the case of the NIR Ca II triplet. The low expansion velocities in SN 2002es and SN 2005hk make it possible to see narrow features which are usually hard to discern due to the smearing of broad high-velocity features in normal SNe Ia. The spectrum is dominated by permitted iron-group elements, but line blending makes it

[3]http://suspect.nhn.ou.edu/$\sim$suspect .

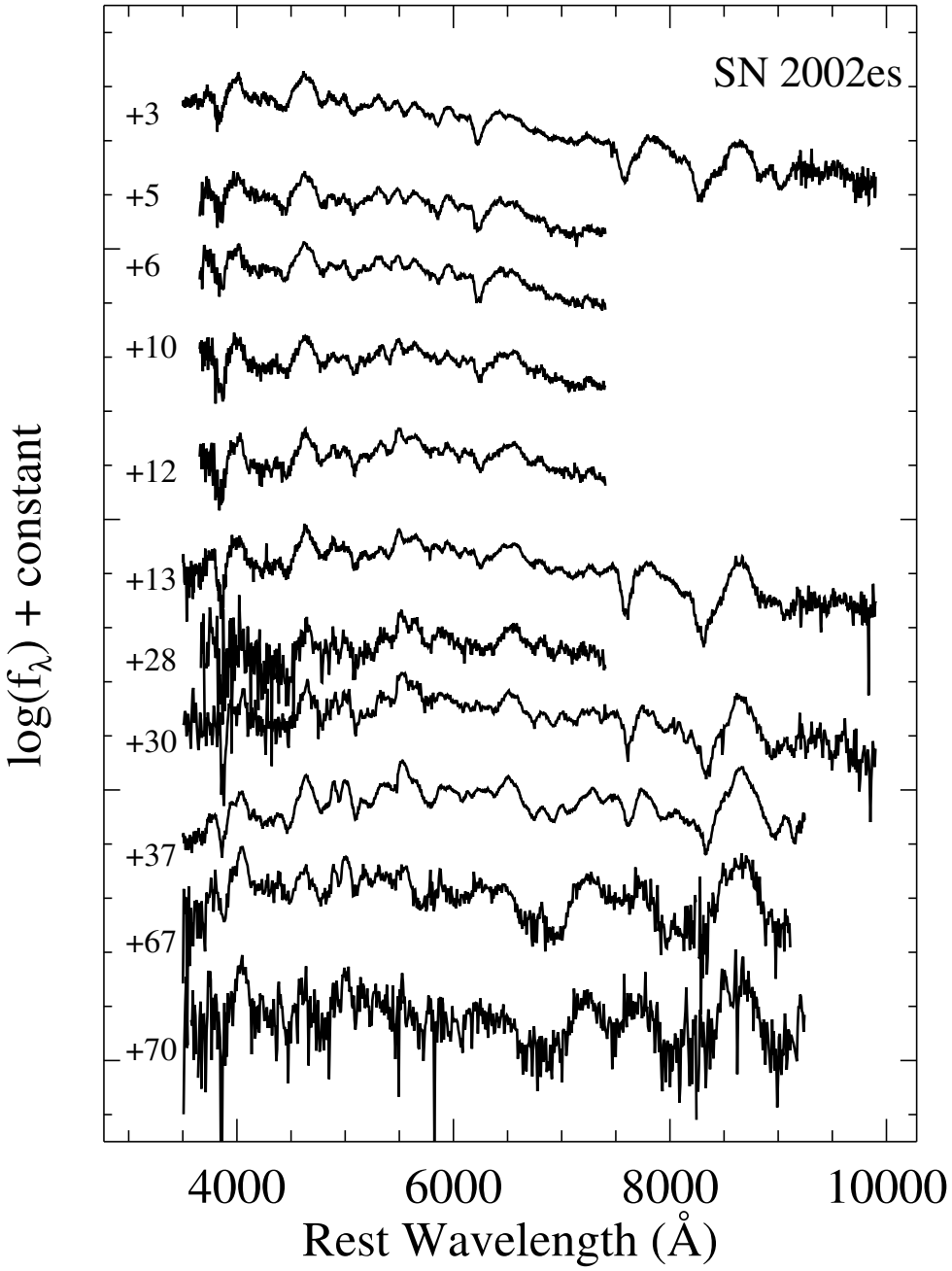

Figure 5.5: Montage of spectra of SN 2002es. All spectra have been shifted to the rest frame by the recession velocity of the host galaxy and corrected for $E(B-V)_{\rm MW} = 0.183$ mag. The phase relative to maximum light in the B band is indicated to the left of each spectrum.

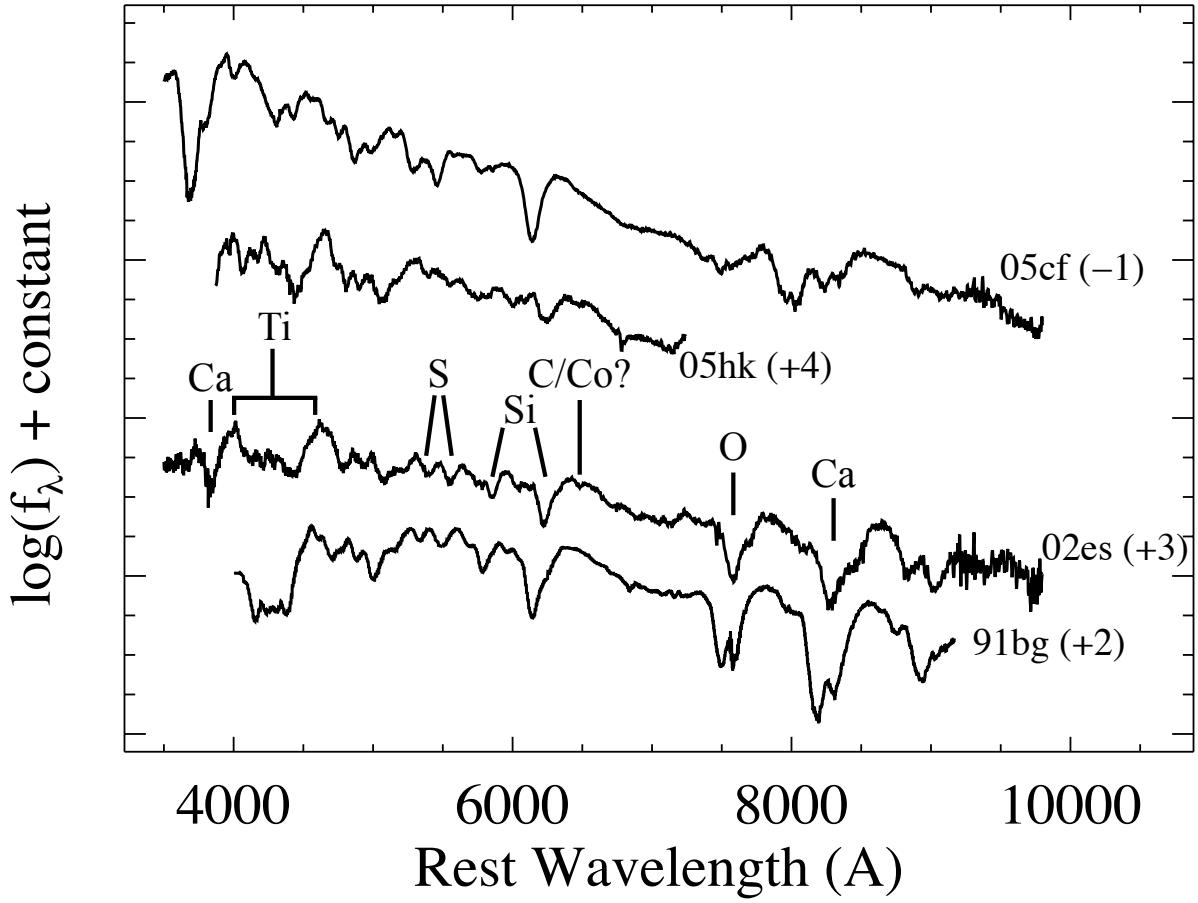

Figure 5.6: Spectrum of SN 2002es taken +3 d after maximum light in B, compared to the spectroscopically normal SN Ia 2005cf (Wang et al. 2009b), the SN 2002cx-like SN 2005hk (Phillips et al. 2007), and the subluminous SN 1991bg (Turatto et al. 1996) at similar phases. All objects have been shifted to the rest frame by their host-galaxy recession velocity and corrected for both Milky Way and host-galaxy extinction using the values in their respective references. Major spectroscopic features are identified. The spectrum of SN 2002es shares many similarities with SN 1991bg, except the former has significantly slower ejecta velocities. In particular, both objects show strong O I and Ti II features. The ejecta velocities of SN 2002es are more similar to those of SN 2005hk.

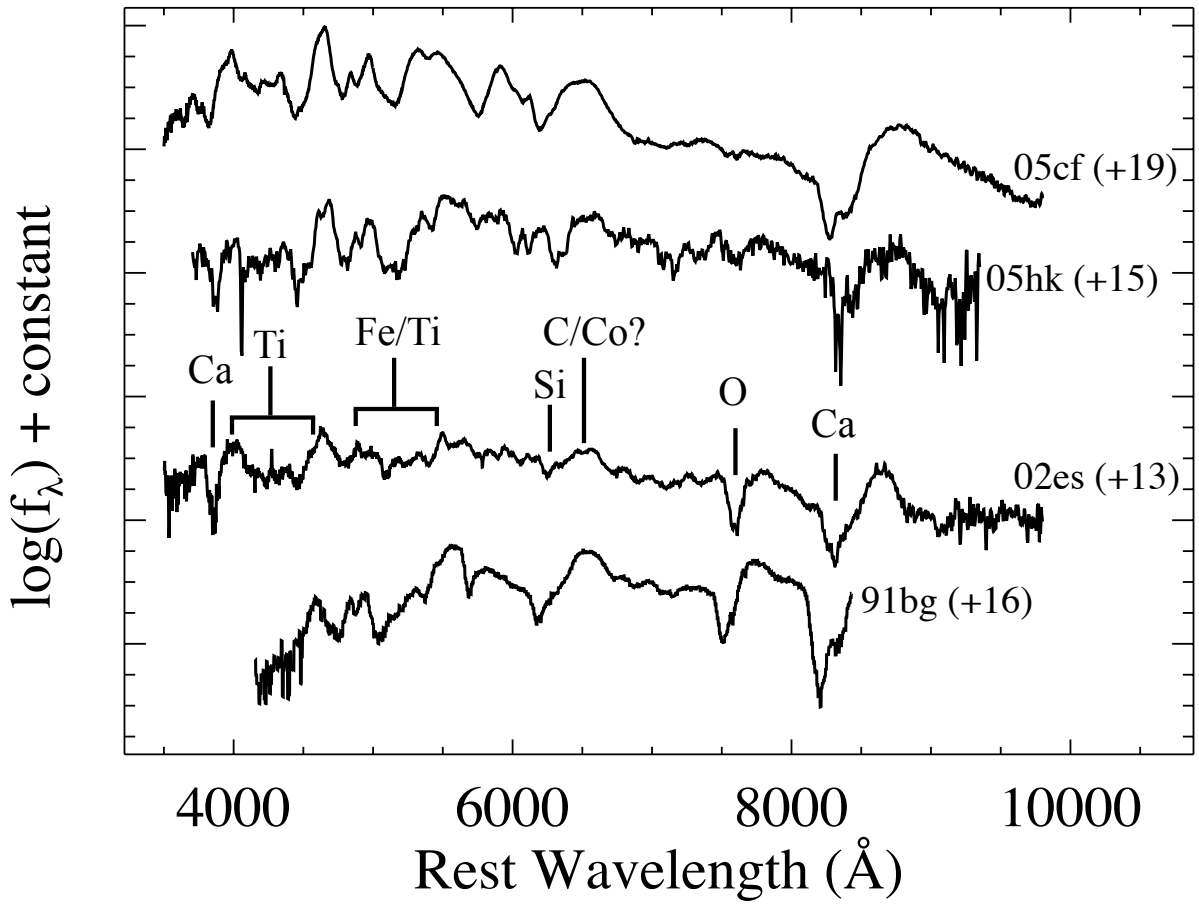

Figure 5.7: Spectrum of SN 2002es taken +13 d after maximum light. For comparison we show SN 2005cf (Wang et al. 2009b), SN 2005hk (Phillips et al. 2007), and SN 1991bg (Turatto et al. 1996) at a similar phase indicated in parentheses to the right of each spectrum. All spectra have been corrected for both Milky Way and host-galaxy extinction using the values in their respective references. Major spectroscopic features are identified.

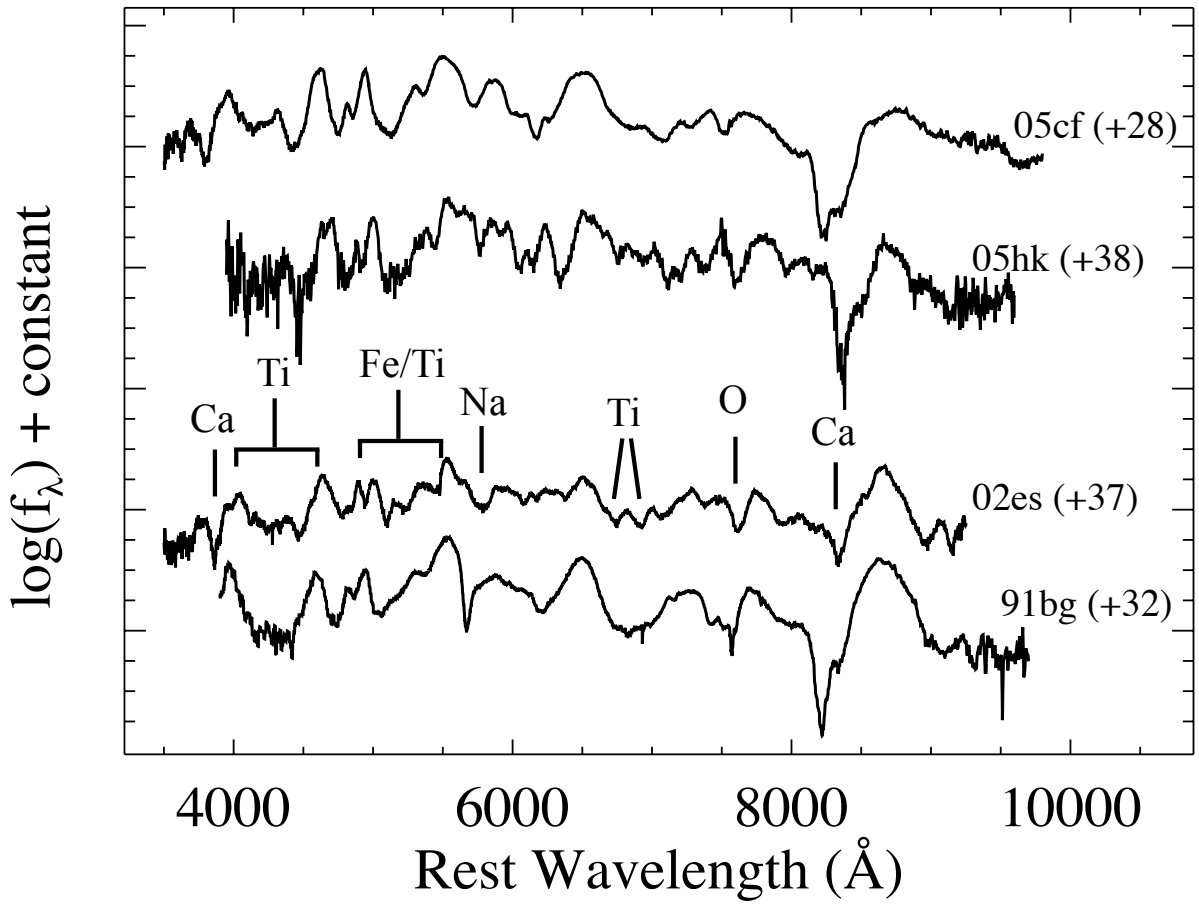

Figure 5.8: Spectrum of SN 2002es taken +37 d after maximum light using LRIS on Keck. For comparison we show SN 2005cf (Wang et al. 2009b), SN 2005hk (Phillips et al. 2007), and SN 1991bg (Turatto et al. 1996) at a similar phase indicated in parentheses. All spectra have been corrected for both Milky Way and host-galaxy extinction using the values in their respective references. Major spectroscopic features are identified.

difficult to uniquely identify features.

We show our combined +67 d and +70 d spectrum of SN 2002es in Figure 5.9, along with spectra of the normal SN 1994D, SN 2005hk, and SN 1991bg at comparable phases. SN 2002es continues to share the most similarities with SN 1991bg. Despite the rapid evolution of the light curves, the spectra do not show signs of being completely nebular. We continue to see continuum emission and absorption in our combined spectrum. There is a hint of forbidden emission lines, possibly [Ca II] or [Fe II] in the region around 7200 Å, but we do not detect other prominent forbidden iron emission features commonly seen in nebular SN Ia spectra (Stanishev et al. 2007; Leloudas et al. 2009). We note that the permitted Ca II emission is not particularly strong, unlike PTF 09dav and the class of Ca-rich objects (Kasliwal et al. 2011).

5.3.4 SYNOW Modeling

The supernova spectral synthesis code SYNOW (Fisher et al. 1997) is useful in identifying the different ion contributions in SN spectra. We use SYNOW as a tool to analyze our +3 d, +13 d, and +37 d spectra to determine the elemental composition of the photosphere. Our synthetic spectra compared to our observed spectra, along with identification of major spectral features, can be found in Figure 5.10.

For our +3 d spectrum, we set the blackbody temperature to 13,000 K with a photospheric velocity of 6200 km s^{-1}. Many of the ions present in our SYNOW spectrum are commonly found in the spectra of SN 1991bg-like objects: Ca II, Ti II, O I, Si II, S II, and Na I. Sullivan et al. (2011b) find evidence of Sc II in spectra of PTF 09dav, a peculiar subluminous SN Ia similar in some characteristics to SN 2002es. We find that including Sc II does not improve the fit to the spectrum of SN 2002es.

Just redward of Si II λ6355 is a notch that looks suspiciously like C II λ6580. The presence of carbon in pre-maximum spectra has recently been found in a substantial fraction ($\sim$20-30%) of SNe Ia (Parrent et al. 2011; Thomas et al. 2011; Folatelli et al. 2012; Silverman & Filippenko 2012) at velocities slightly higher than those of intermediate-mass elements such as Si and Ca. If the notch is due solely to C II, it has a velocity of 4200 km s^{-1}, much lower than the velocities of other ions. With SYNOW, we can fit this feature reasonably well with a blend of C II and Co II with a velocity of 6200 km s^{-1}. We do not see evidence of C II λ7234. The notch is also present in our spectrum at +13 d, but it is not generally visible in normal SNe Ia that exhibit carbon at early times before maximum light. Persistent carbon features lasting two weeks were seen in the exceptionally luminous SN 2009dc (Taubenberger et al. 2011). However, given the subluminous nature of SN 2002es, it shares few characteristics in common with SN 2009dc (Yamanaka et al. 2009; Silverman et al. 2011; Taubenberger et al.

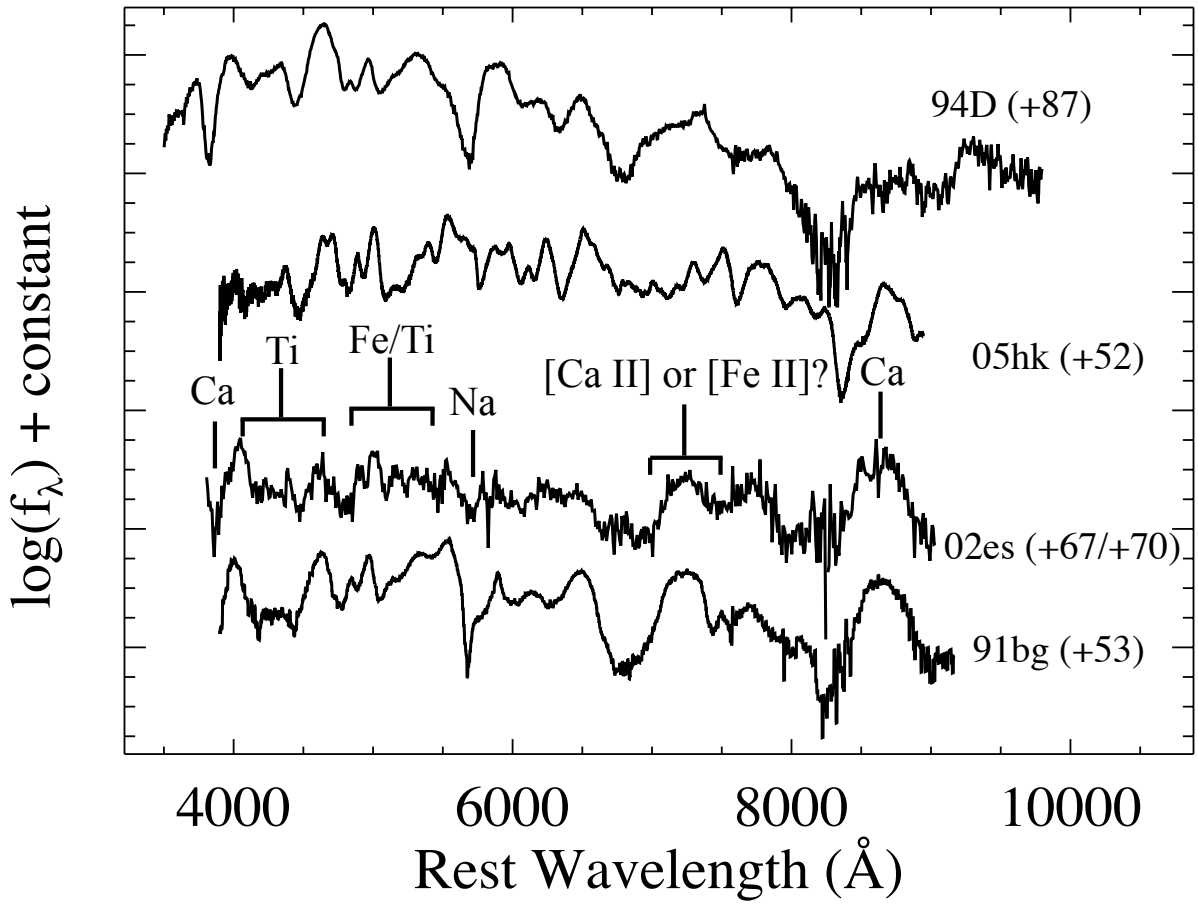

Figure 5.9: Combined spectrum of SN 2002es from +67 d and +70 d after maximum light. For comparison we show the normal SN 1994D (from our database of spectra), SN 2005hk (Phillips et al. 2007), and SN 1991bg (Turatto et al. 1996) at a similar phase indicated in parentheses to the right of each spectrum. All spectra have been corrected for both Milky Way and host-galaxy extinction using the values in their respective references. At this phase, SN 2002es looks similar to SN 1991bg, but with narrower features. Major spectroscopic features are identified.

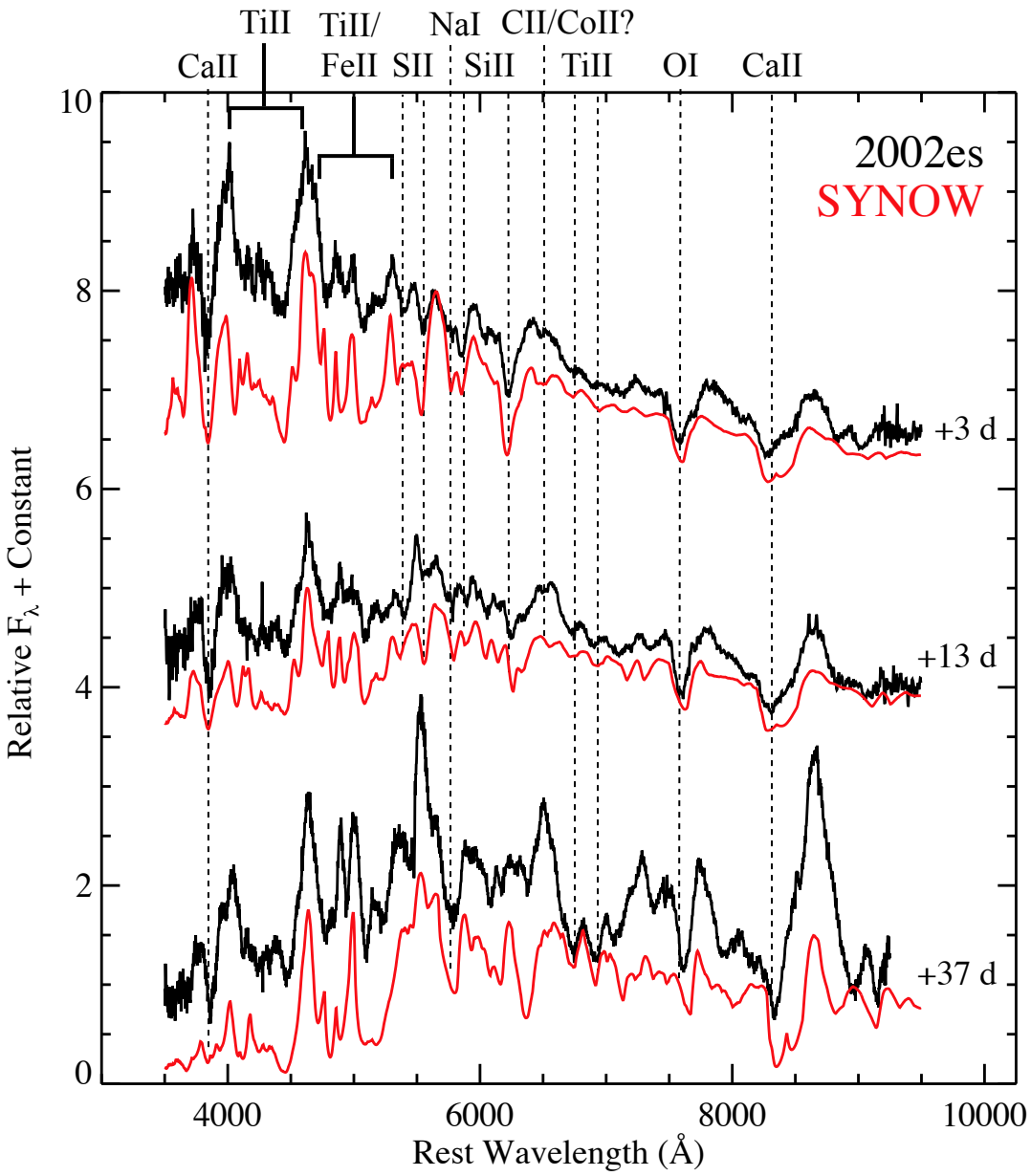

Figure 5.10: Spectra of SN 2002es at +3 d, + 13 d, and +37 d after maximum light compared to our best SYNOW fit for each epoch in red. Ions that contribute to major features are labeled according to the blueshifted absorption minimum of that feature. Our tentative identification of C II is indicated by a question mark.

2011) and similar overly luminous SNe Ia (Howell 2001; Hicken et al. 2007; Scalzo et al. 2010).

In an analysis of the pre-maximum spectrum of SN 2006bt, Foley et al. (2010b) found possible evidence for C II at lower velocities ($\sim$5200 km s^{-1}) than other ions ($\sim$12,500 km s^{-1}). However, unlike the case in SN 2002es, they saw that the feature disappeared after maximum light. This feature, whether attributed to C II or not, hints at a possible connection between the two transients.

In our +13 d spectrum, we set the blackbody temperature to 7500 K with a photospheric velocity of 5500 km s^{-1}. The low velocities of the ions allow for the detection of a forest of absorption lines normally smeared out by higher velocities. We see less evidence for the presence of Si II and S II. Absorption from iron-group elements such as Fe II and Ti II becomes more prominent.

By +37 d, we use a blackbody temperature of 5900 K with a photospheric velocity of 3500 km s^{-1}. At this phase, we begin to see the SN become nebular and there is significant line blending at short wavelengths from iron-group elements. We still detect continuum emission, indicating that the SN is not completely nebular, but we begin to see emission from calcium.

5.3.5 Quantitative Measurements

SNe Ia can be broadly classified by a clustering analysis of spectral and photometric features (Benetti et al. 2005; Branch et al. 2006). Most quantitative measurements make use of Si II features at 5972 Å and Si II λ6355. Nugent et al. (1995) introduced $\mathcal{R}$(Si), the ratio of the depth of Si II λ5972 to λ6355 near maximum light, which is found to correlate with light-curve width. Using $\mathcal{R}$(Si) and the velocity gradient of the Si II λ6355 feature, $\dot{v}$, Benetti et al. (2005) found that SNe Ia could be broken into three distinct subclasses: low velocity gradient (LVG), high velocity gradient (HVG), and FAINT.

We estimate $\mathcal{R}(\mathrm{Si}) = 0.55 \pm 0.05$ from our earliest spectrum of SN 2002es taken +3 d after maximum light. In the top panel of Figure 5.11, we plot $\Delta m_{15}(B)$ against $\mathcal{R}$(Si) for the objects in Benetti et al. (2005) along with SN 2002es and other peculiar subluminous objects. While SN 2002es has a $\mathcal{R}$(Si) value similar to that of FAINT objects, its measured $\Delta m_{15}(B)$ does not match those of FAINT objects. Compared to other peculiar subluminous SNe Ia, SN 2002es is most similar to PTF 10ops (Maguire et al. 2011), both of which are significant outliers in the relationship between $\Delta m_{15}(B)$ and $\mathcal{R}$(Si) found by Benetti et al. (2005).

We measure $\dot{v} = 98 \pm 5$ km s^{-1} d^{-1} (statistical error only) from 6 spectra taken in the range $+3 \leq t \leq +13$ d. In the bottom panel of Figure 5.11, we plot $\Delta m_{15}(B)$ against $\dot{v}$

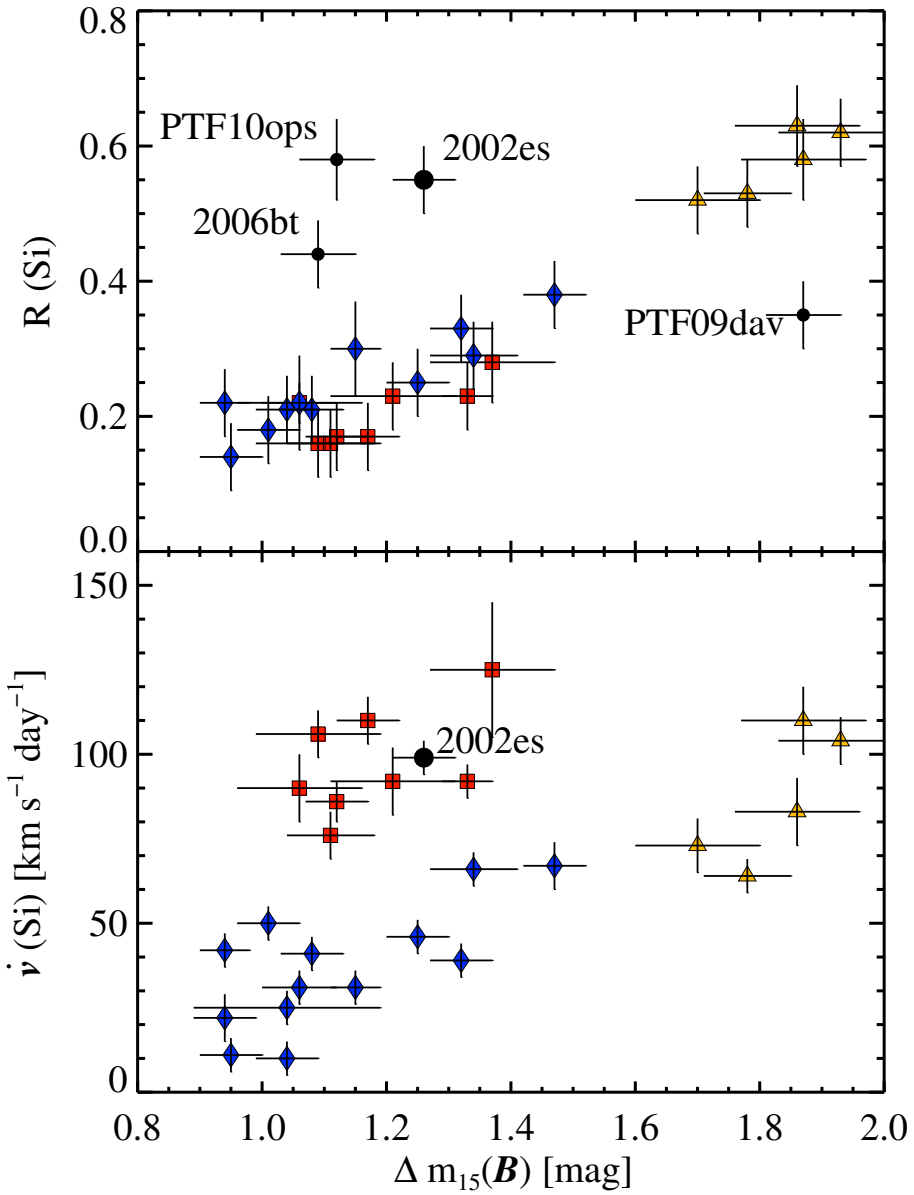

Figure 5.11: *Top panel:* The silicon ratio near maximum light, $\mathcal{R}$(Si II), versus $\Delta m_{15}(B)$. Blue diamonds are low-velocity objects, red squares are high-velocity objects, and yellow triangles are FAINT objects as defined by Benetti et al. (2005). SN 2002es joins PTF 10ops and SN 2006bt as outliers in the relationship between $\mathcal{R}$(Si II) and $\Delta m_{15}(B)$. SN 2002es has a $\mathcal{R}$(Si II) more typical of a FAINT object, despite having a broad light curve. *Bottom panel:* Gradient in the velocity of the Si II feature versus $\Delta m_{15}(B)$. Based on the clustering of this plot, SN 2002es would be classified as a HVG object despite being subluminous.

for SN 2002es and the objects in Benetti et al. (2005), coded by subclass. Based on our measured $\dot{v}$ and $\Delta m_{15}(B)$, SN 2002es falls into the HVG group. FAINT objects also have high velocity gradients, but they have a larger $\Delta m_{15}(B)$ as well (i.e., a narrow light curve). SN 2002es would fall into the FAINT classification if it had a narrower light curve. Both panels indicate that SN 2002es has a unique combination of photometric and spectroscopic properties that lie outside the classification scheme of Benetti et al. (2005).

5.4 Discussion

5.4.1 Bolometric Luminosity

Estimating the bolometric luminosity is particularly difficult without observations in the ultraviolet (UV) and IR, which contribute a sizable fraction of energy for normal SNe Ia. Unfortunately, U-band photometry from Hicken et al. (2009b) starts $\sim$5 days after B-band maximum light. We only make use of $BVRI$ data to construct a "quasi-bolometric" (Nomoto et al. 1990) luminosity light curve for SN 2002es.

We estimate the quasi-bolometric luminosity by warping spectra representing the SED of SN 2002es corrected for Milky Way extinction to match our multi-color photometry using a method similar to that of Howell et al. (2009). We assume there is no host-galaxy extinction (see Section 5.2.3). For each epoch of $BVRI$ photometry, we warp the spectrum using a third-order spline with knots at the effective wavelength of each filter to match the photometric colors. In instances where we are missing photometry from one band, we do a linear interpolation between the nearest photometric epochs. We note that there is a fairly large gap in our B-band photometry at $+40 < t < +70$ d, making our interpolation uncertain. The resulting warped spectrum is integrated over the range 4000–8800 Å (i.e., from the blue limit of the B band to the red limit of the I band) to obtain the optical flux for the photometric epoch. The flux is converted to a luminosity using the distance reported in Section 5.2.3.

Ideally, a spectral series of SN 2002es matched with each photometric epoch (as opposed to a single spectrum) should be used for the most accurate results. The spectra from FAST presented in this paper do not extend to the I band, and thus are not useful for estimating the bolometric luminosity. Given the spectroscopic similarities between SN 1991bg and SN 2002es, we used the above procedure with the SN 1991bg spectral series of Nugent et al. (2002) artificially redshifted by 0.01 to match the slower expansion velocities of SN 2002es.

A bolometric correction is required to turn our quasi-bolometric luminosity based on optical data into a bolometric luminosity that accounts for energy emitted in the UV and

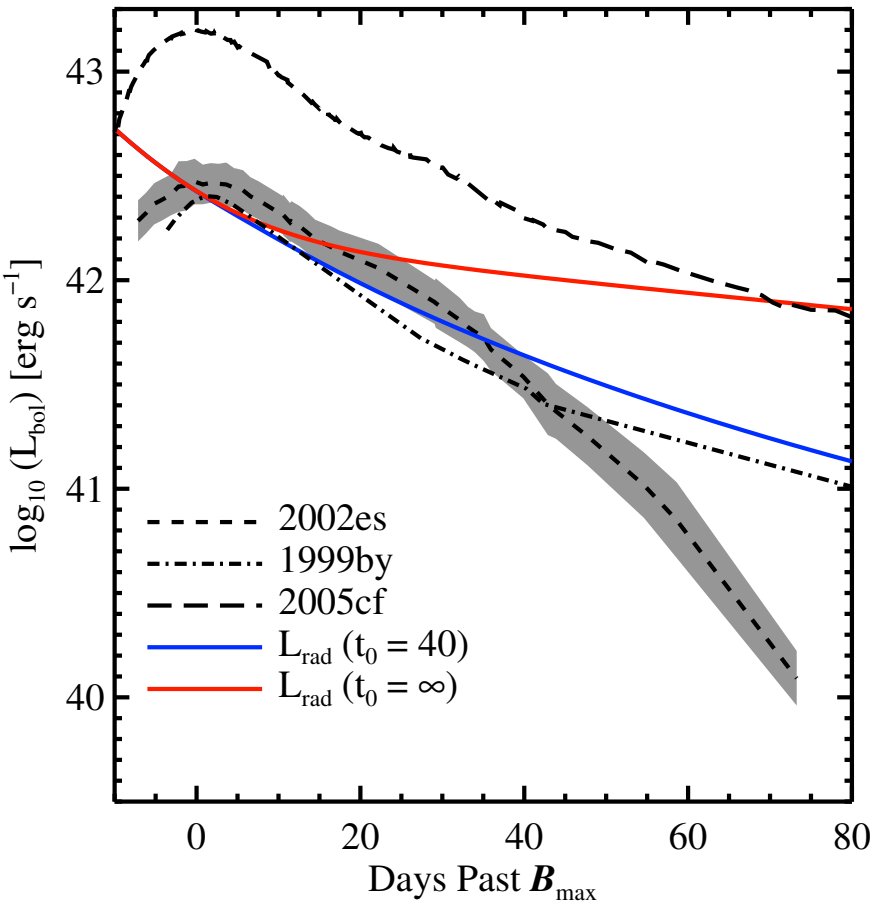

Figure 5.12: Bolometric luminosity of SN 2002es (dashed line) constructed using *BVRI* data and bolometric corrections from SN 1991bg. The shaded region indicates the 1σ errors. Plotted for comparison is the bolometric luminosity of SN 2005cf (longer dashed line; Wang et al. 2009b) and SN 1999by (dot-dash line; Garnavich et al. 2004). The solid blue and dotted red curves are models for the radioactive luminosity using Equation 5.6 assuming different γ-ray trapping efficiencies with an initial $M_{\rm Ni} = 0.17$ M$_\odot$. The red dotted curve assumes full trapping of γ-rays producing a late-time slope that follows the cobalt decay rate. The blue curve is our best fit. Neither curve can reproduce the steep late-time decay in the bolometric light curve of SN 2002es.

IR. Our SN 1991bg spectral series covers 1000–25,000 Å and provides a reasonable first-order approximation of the SED of SN 2002es. We calculate the fraction of flux emitted in the range 4000–8800 Å compared to the total integrated flux for each spectrum in the series. This provides us with an estimate of the flux missed by only using optical data to construct our quasi-bolometric light curve as a function of phase. We apply this correction to arrive at our final bolometric light curve. At maximum light, the *BVRI* data account for ∼70% of the total flux. Given the uncertainties in our estimates, we include a 20% systematic error in our error budget for the bolometric luminosity.

We estimate $L_{\rm bol} = (4.0 \pm 0.9) \times 10^{42}$ erg s^{-1} at ∼1 d after maximum light in the B band. This is slightly larger than the bolometric luminosity of other subluminous SNe Ia (Taubenberger et al. 2008) and ∼25% of the luminosity of SN 2005cf (Wang et al. 2009b).

The luminosity of thermonuclear SNe is powered by the energy deposition of γ-rays and positions produced by the radioactive decay chain ^{56}Ni → ^{56}Co → ^{56}Fe. At maximum light, the rate of energy deposition into the expanding ejecta is roughly equivalent to the luminosity of the SN (i.e., Arnett's law; Arnett 1982). Following Stritzinger & Leibundgut (2005), we can write Arnett's law as

$$L_{\rm bol} = \alpha \times (6.45e^{-t_r/(8.8{\rm d})} + 1.45e^{-t_r/(111.3{\rm d})}) \times \left(\frac{M_{\rm Ni}}{{\rm M}_\odot}\right) \times 10^{43} \text{ erg s}^{-1}, \quad (5.1)$$

where α is a correction factor of order unity to Arnett's law and t_r is the time between explosion and maximum light (i.e., the bolometric rise time).

Assuming the luminosity of SN 2002es is powered by the decay of ^{56}Ni , we can estimate the amount of ^{56}Ni synthesized in the explosion. We set $\alpha = 1$. Unfortunately, we do not have tight constraints on the date of explosion. Prior to the first detection of SN 2002es on 2002 Aug. 23.2 (∼9 d before the time of maximum $L_{\rm bol}$), KAIT obtained an unfiltered image of the field on 2002 Aug. 12.5 with a limiting magnitude of 18.5 (Li et al. 2002). In Chapter 3, we found that the subluminous SN 1999by had a rise time to maximum light in B of 13.33 ± 0.40 d, consistent with other estimates for the rise time of SN 1991bg-like SNe from Taubenberger et al. (2008), while a typical, normal SN Ia has a rise time of ∼18 d. The B-band light curve of SN 2002es has a slower rise to maximum light than SN 1999by and matches the rise of SN 2005hk. Phillips et al. (2007) measure a rise to B-band maximum of 15 ± 1 d for the SN 2002cx-like SN 2005hk. Maguire et al. (2011) constrain the rise time of PTF 10ops, an object that shares similarities to SN 2002es, to ∼19 d. Based on the unique spectroscopic and photometric peculiarities of SN 2002es, it is unclear which object serves as

the best guide to determining the rise time. As a compromise between the different possible rise times, we adopt a rise time to bolometric maximum of $t_r = 16 \pm 3$ d.

From Equation 5.1, we estimate $M_{\rm Ni} = 0.17 \pm 0.05$ M$_\odot$ synthesized in the explosion, which falls at the low end of the range $0.05 < M_{\rm Ni} < 0.87$ M$_\odot$ found by Stritzinger et al. (2006b) for a sample of SNe Ia. SN 1991bg and SN 1999by synthesized ∼0.1 M$_\odot$ of ^{56}Ni .

5.4.2 Energetics

We can estimate the ejected mass, $M_{\rm ej}$, and the kinetic energy, E_0, of the explosion using the rise time. Following the treatments of Arnett (1982) and Pinto & Eastman (2000a,b), we have $t_r^2 \propto \kappa M_{\rm ej}/v_s$, where κ is the mean opacity and v_s is the ejecta velocity. If we compare SN 2002es to a normal SN Ia with $M_{\rm ej} \approx 1.4$ M$_\odot$, $v_s = 10^4$ km s^{-1}, and $t_d = 18$ d, and assume they have similar opacities, we have

$$M_{\rm ej} = 0.66\,{\rm M}_\odot \left(\frac{t_r}{16\ {\rm d}}\right)^2 \left(\frac{v_s}{6000\ {\rm km\ s^{-1}}}\right). \tag{5.2}$$

The largest uncertainty is our calculation is from our estimate of the rise time of $t_r = 16 \pm 3$ d. Including this uncertainty, we find $M_{\rm ej} = 0.66 \pm 0.25$ for our nominal values, significantly lower than the canonical values for a SN Ia.

We can then calculate the kinetic energy

$$E_{\rm k} = 2.4 \times 10^{50}\ {\rm erg} \left(\frac{t_r}{16\ {\rm d}}\right)^2 \left(\frac{v_s}{6000\ {\rm km\ s^{-1}}}\right)^3. \tag{5.3}$$

Including the uncertainty in our rise time gives $E_{\rm k} = (2.4 \pm 0.9) \times 10^{50}$ erg for our nominal values.

The estimated ejected mass and kinetic energy are significantly lower than the canonical values for a SN Ia in part due to the slow expansion velocities measured from the Si feature. We again caution that our estimate for the rise time is not well constrained and can range from 13 d to 19 d.

Following similar arguments made by Howell et al. (2006) and Silverman et al. (2011), we can place constraints on the white dwarf (WD) progenitor mass based on the energetics of the explosion. We construct a series of WD models with central temperature $T = 10^7$ K using the Models for Experiments in Stellar Astrophysics (MESA) code (Paxton et al. 2011) and calculate the binding energy for each model. We find that the nuclear energy released is larger than the combined binding energy and kinetic energy for all of our models. This ensures that there is enough energy to unbind the WD and power the explosion based on the ^{56}Ni mass, but it is unclear what happens to the excess nuclear energy. Realistically, some

of the nuclear energy should go into heating the ejecta. If some fraction of the WD was left unburned, then nuclear energy would decrease. However, our evidence for unburned carbon (see Section 5.3.4) is questionable. Given the uncertainty in our assumptions, we cannot place a strong constraint on the mass of the progenitor.

5.4.3 Late-Time Decay

We build a simple toy model to describe the luminosity due to the deposition of energy from the radioactive decay of ^{56}Ni and ^{56}Co to study the behavior of the bolometric light curve. The energy initially deposited into the ejecta is from the thermalization of γ-rays emitted by radioactive decay of $^{56}\mathrm{Ni} \rightarrow ^{56}$ Co with an e-folding time of 8.8 d. By $\sim$ 20 d, the energy emitted by the decay of $^{56}\mathrm{Co} \rightarrow ^{56}$ Fe exceeds that of ^{56}Ni (e-folding time of 111.3 d). The decay of ^{56}Co can proceed via either electron capture emitting a spectrum of γ-rays (96.5% of emitted energy) or beta decay releasing a positron (3.5% of emitted energy) (Nadyozhin 1994). The luminosity due to the radioactive decay can be written as

$$\begin{aligned} L_{\mathrm{rad}} &= L_{\mathrm{Ni},\gamma}[1 - e^{-\tau}] + \\ &\quad L_{\mathrm{Co,e^+}} + L_{\mathrm{Co},\gamma}[1 - e^{-\tau}], \end{aligned} \tag{5.4}$$

where the factor $(1 - e^{-\tau})$ is the fraction of γ-rays trapped in the expanding ejecta with an optical depth τ. We assume that the positrons are fully trapped within the ejecta and deposit their kinetic energy instantaneously. Note that τ is a function of time, decreasing as the ejecta expand homologously. Following Sollerman et al. (2002, 2004) and Stritzinger et al. (2006a), we write the optical depth to γ-rays in expanding ejecta as

$$\tau = \left(\frac{t_0}{t}\right)^2, \tag{5.5}$$

where t_0 is the fiducial time relative to explosion when the ejecta become optically thin to γ-rays.

Solving the first-order differential equations that describe the parent-daughter relationship between ^{56}Ni and ^{56}Co, we write the radioactive luminosity as

$$\begin{aligned} L_{\mathrm{rad}} &= \lambda_{\mathrm{Ni}} Q_{\mathrm{Ni},\gamma} N_{\mathrm{Ni},0} e^{-\lambda_{\mathrm{Ni}} t}[1 - e^{-\tau}] \\ &\quad + \frac{\lambda_{\mathrm{Ni}} \lambda_{Co}}{\lambda_{\mathrm{Ni}} - \lambda_{\mathrm{Co}}} N_{\mathrm{Ni},0}(e^{-\lambda_{\mathrm{Co}} t} - e^{-\lambda_{\mathrm{Ni}} t}) \\ &\quad \times \left[Q_{\mathrm{Co,e^+}} + Q_{\mathrm{Co},\gamma}(1 - e^{-\tau})\right], \end{aligned} \tag{5.6}$$

where λ_{Ni} and λ_{Co} are the inverse e-folding times for ^{56}Ni and ^{56}Co, respectively; $N_{\mathrm{Ni},0}$ is the initial amount of ^{56}Ni synthesized in the explosion; $Q_{\mathrm{Ni},\gamma}(1.75$ MeV) is the energy

yielded by each ^{56}Ni $\rightarrow^{56}$Co decay; and $Q_{\mathrm{Co},\gamma}$(3.61 MeV) and Q_{Co,e^+}(0.12 MeV) are the energy yielded per ^{56}Co $\rightarrow^{56}$Fe decay via electron capture and beta decay, respectively.

In Figure 5.12, we plot the bolometric light curve of SN 2002es (see Section 5.4.1 for details), as well as the UV-optical-IR (UVOIR) bolometric light curves of SN 2005cf from Wang et al. (2009b) and SN 1999by using data from Garnavich et al. (2004). We also plot models $L_{\mathrm{rad}}(t_0 = 40$ d) and $L_{\mathrm{rad}}(t_0 = \infty$ d) assuming $M_{\mathrm{Ni}} = 0.17$ M$_\odot$ (found using Arnett's law in Section 5.4.1). The model with $t_0 = \infty$ represents the case in which the γ-rays are completely trapped and the luminosity decays according to the ^{56}Co decay rate (0.01 mag d^{-1}).

The bolometric light curve of SN 2002es shows a surprising drop in luminosity at $t >$ +30 d. The decline is significantly faster than the cobalt decay rate and the decline rate for SN 2005cf. Similar results were found for the late-time decline in individual optical bands (see Section 5.3.1). Even when accounting for a γ-ray optical depth that decreases with time due to homologous expansion of the ejecta, we are unable to find a model that reasonably matches the bolometric light-curve decline rate of SN 2002es. Our best match is $t_0 = 40$ d, which adequately describes SN 2002es within the region $0 < t <$ +30 d but fades too slowly at $t >$ +30 d.

The decay of the bolometric light curve in the range $+30 < t < +70$ d appears incompatible with the gradual escape of γ-rays through homologously expanding ejecta and implies that the ejecta become optically thin to γ-rays very rapidly. If the ejecta are optically thin to γ-rays, then the luminosity should be powered by the thermalized kinetic energy of positrons, assuming some fraction of the positrons are trapped in the ejecta. We estimate the nickel mass required to power the light curve by positrons at our last photometry epoch ($t = 89.3 \pm 3$ d after explosion) using Equation 5.6 and setting $\tau = 0$ (i.e., the ejecta are optically thin to γ-rays). For complete positron trapping, we estimate $M_{\mathrm{Ni}} = 0.05 \pm 0.02$ M$_\odot$ is required to power the luminosity at this phase; this is a factor of 3 less than our previous estimate using Arnett's law at maximum light. A corollary to the assumption of complete positron trapping is that the light-curve decay should follow the cobalt decay rate, which is clearly not seen. If we allow for only partial trapping, we need a positron trapping fraction of $\sim$0.3 to match our M_{Ni} from Arnett's law.

The unexpectedly fast decline calls into question whether SN 2002es was powered by ^{56}Ni decay. Here we discuss possible ways to reconcile a thermonuclear SN with the measured decline rate.

Dust formation around the SN would lead to a drop in optical flux as high-energy photons are reprocessed to longer IR wavelengths. In models of dust formation in the ejecta of SNe Ia, Nozawa et al. (2011) find that the conditions required to produce dust occur

100–300 d after maximum light. However, due to the low densities in SN Ia ejecta, the dust grains are small (< 0.01 μm), and the expected IR emission associated with dust has not yet been detected in late-time observations of SNe Ia (Gerardy et al. 2007). We also do not find evidence of an increase in the red continuum in our spectra or asymmetries in line features in our late-time spectra as have been seen in other SNe that formed dust (e.g., Smith et al. 2008). Our last epoch of photometry taken +73 d after maximum light gives $B - R \approx 0.5$ mag, while photometry of SN 2005cf taken from Wang et al. (2009b) gives $B - R \approx 0.7$ mag. SN 2002es is bluer than SN 2005cf, which is opposite the effect we would expect if dust were facilitating the rapid fading.

Axelrod (1980) predicts that SNe Ia should undergo an "infrared catastrophe" (IRC) at late times, once the temperature drops below a critical threshold ($\sim$1000 K). Models of the IRC predict that a thermal instability shifts the bulk of emission from the optical to fine-structure transitions of iron in the IR about 500–700 d after maximum light. Without IR data, we are unable to determine whether the IR flux increases as the optical flux decreases, although the onset of the IRC at such an early phase is certainly unexpected. Our last spectrum of SN 2002es taken 70 d after maximum light shows permitted lines in absorption, indicating that the ejecta have not yet become nebular and the temperature has probably not dropped sufficiently low to facilitate the onset of the IRC. The IRC has never been detected in late-time observations of other SNe Ia, although Leloudas et al. (2009) evoke the possibility of the IRC occurring locally in clumpy ejecta to explain the missing flux in the late-time light curve of SN 2003hv.

5.4.4 A Pure Explosion Model

Another possible model for the evolution of the light curve of SN 2002es is that the energy deposited into the ejecta is derived from the explosion of the progenitor, and there is no subsequent heating. Such a model was explored by Kasliwal et al. (2010) to explain the rapidly evolving SN 2010X. The explosion energy (E_0) is deposited instantaneously into the ejecta. At maximum light, $L_{\rm max} \approx E_0/t_d(0)$, where $t_d(0)$ is the initial diffusion time for photons through the ejecta. The diffusion time is $t_d(0) \propto M_{\rm ej}\kappa/R_0$, where R_0 is the initial radius of the SN. Assuming $\kappa = 0.1$ cm^2 g^{-1} for Fe-rich ejecta (Pinto & Eastman 2000b), $L_{\rm max} = 4.0 \times 10^{42}$ erg s^{-1}, and $M_{\rm ej} = 0.66$ M$_\odot$, we estimate an initial progenitor radius of $R_0 \approx 10^{12}$ cm.

This value is similar to the estimate presented by Kasliwal et al. (2010), in which they argue that such a radius would require a progenitor with an extended hydrogen envelope. Based on the absence of hydrogen in spectra of SN 2010X they reject this hypothesis. Similarly, given the lack of hydrogen in our spectra of SN 2002es, we also find a pure explosion

an unlikely mechanism to power the luminosity of SN 2002es.

5.4.5 A Core-Collapse SN?

If SN 2002es was not powered by ^{56}Ni decay, it is reasonable to investigate core-collapse mechanisms that could explain the properties of SN 2002es. However, the lack of hydrogen emission in optical spectra of SN 2002es rules out a massive star with a large hydrogen envelope as a progenitor, leaving the possibility that SN 2002es could be a SN Ic. The star-formation history of the host galaxy strongly favors an older stellar population, making the progenitors of SNe Ibc unlikely as well (Leaman et al. 2011). If SN 2002es is a core-collapse event, it would have to be the result of a low-mass star following an atypical evolutionary path to a SN Ic.

Perets et al. (2010) discussed data on SN 2005E, a low-luminosity SN Ib (based on the absence of hydrogen and the presence of helium) with calcium-rich ejecta that exploded in the outskirts of its early-type host galaxy. Although the observed properties of SN 2005E and SN 2002es are different (e.g., SN 2002es is much brighter, has slower expansion velocities, and no detectable helium), SN 2005E and other objects like it may be core-collapse SNe connected to old stellar populations. Kasliwal et al. (2011) studied the observed properties of the emerging class of Ca-rich objects and found that they could not be explained by conventional core-collapse or thermonuclear explosions.

Another possible atypical core-collapse object was SN 2008ha, a low-luminosity Type I SN (based on the absence of hydrogen) that peaked at -14.2 mag with extremely low ejecta velocities ($\sim$4000–5000 km s^{-1}; Valenti et al. 2009; Foley et al. 2009, 2010a). Valenti et al. (2009) argued that SN 2008ha and the family of SN 2002cx-like objects may be the result of the core collapse of hydrogen-poor, low-mass stars. Their analysis of SN 2008ha spectra showed little evidence for the IMEs commonly associated with the byproducts of a thermonuclear explosion and an absence of forbidden iron lines at late times. Coupled with the low luminosity and low ejecta velocities, the authors interpret SN 2008ha as a core-collapse event that produced little ^{56}Ni . However, Foley et al. (2010a) presented an early-time spectrum of SN 2008ha that clearly exhibits IMEs such as silicon, sulfur, and carbon, arguing in favor of the thermonuclear explosion of a C/O WD.

5.4.6 SN 1999bh: A SN 2002es-Like Object

Combing through our photometric (see Chapter 2) and spectral (Silverman et al. 2012c) databases, we recognized that SN 1999bh shares many of the same properties as SN 2002es.

Although our photometric and spectroscopic coverage of SN 1999bh is not as extensive as our SN 2002es dataset, the available data provide a compelling case to link the two objects.

Table 5.5: Log of Optical Spectral Observations for SN 1999bh

UT Date	Phase[a] (d)	Telescope/Instrument	Exposure Time (s)	Res.[b] (Å)	Observer[c]
1999 Apr. 09.3	+6	FLWO/FAST	1200	6–7	MC
1999 Apr. 24.4	+21	Lick/Kast	1800	6–11	AF, WL

[a]Rest-frame days relative to the date of $B_{\max}$, 2002 Aug. 31.8 (JD 2,452,518.3), rounded to the nearest day.
[b]Approximate spectral resolution.
[c]AF = A. Filippenko, MC = M. Calkins, WL = W. Li.

BVRI photometry of SN 1999bh are taken from Chapter 2. Spectra of the object were obtained using the Kast dual spectrograph on the Shane 3-m telescope at Lick Observatory and the FAST spectrograph mounted on FLWO at Mount Hopkins. A journal of our observations is available in Table 5.5. The spectra were reduced using the techniques described in Section 5.2.2.

SN 1999bh was discovered in NGC 3435 by Li (1999) as part of LOSS on 1999 March 29.2. Subsequent spectroscopic follow-up observations by Aldering et al. (1999) classified the object as a SN Ia near maximum light on 1999 Apr. 02. The authors estimate a redshift of 0.028, likely based on SN features. The redshift of NGC 3435 listed in NED is $z_{\rm helio} = 0.0172$. We measure a redshift of $z_{\rm helio} = 0.0168$ from narrow Hα + [N II] lines from the host galaxy in a spectrum of SN 1999bh taken on 1999 Apr. 24 using the Kast dual spectrograph mounted on the Shane 3-m telescope. We adopt this redshift for the remainder of our analysis. The luminosity distance to NGC 3435 calculated using $z_{\rm CMB} = 0.0172$ is $d_L = 70.8 \pm 5.3$ Mpc. At this redshift, SN 1999bh exploded at a projected distance of 3.5 kpc from the nucleus of NGC 3435.

Figure 5.13 shows the *BVRI* light curves of SN 1999bh; we see that those of SN 2002es provide an excellent match in all bands. Both objects exhibit broad light curves despite being subluminous, and lack a prominent shoulder in the R or I bands.

Using SN 2002es as a template, we measure the date of maximum light to be JD $2,451,271.8 \pm 1$ d (1999 Apr. 3.3). After correcting for $E(B-V) = 0.015$ mag from Milky Way extinction using the dust maps of Schlegel et al. (1998), we measure $B_{\max} = 18.63 \pm 0.06$

mag. Due to the faintness of the object, we were unable to follow SN 1999bh sufficiently long to measure the light-curve decay rates at $t > +30$ d.

Based on the presence of Na I D absorption at the redshift of NGC 3435 in spectra of SN 1999bh, we can be certain there is some amount of extinction due to the host galaxy. We estimate an equivalent width of 0.8 ± 0.2 Å of Na I D absorption at the redshift of the host galaxy from our spectrum taken on 1999 Apr. 09. Translating Na I D EW measurements to an inferred $E(B-V)$ reddening gives $0.1 < E(B-V) < 0.2$ mag depending on whether we use the relationship given by Barbon et al. (1990) or Turatto et al. (2003). Blondin et al. (2009) and Poznanski et al. (2011), however, have shown that while there is a positive correlation between the presence of Na I D absorption and host-galaxy extinction, Na I D absorption is not a strong predictor for the amount of extinction.

Instead, we estimate the amount of host-galaxy extinction by matching the $B-V$ color of SN 1999bh to that of SN 2002es. This assumes that any difference in colors is purely associated with host-galaxy extinction and not intrinsic differences between the colors of the two objects. We find that $E(B-V)_{\rm host} = 0.48 \pm 0.07$ mag.

We also estimate the host-galaxy reddening by matching our SN 1999bh spectra to corresponding SN 2002es spectra. We perform a fit to match the SED of the two objects applying a CCM reddening law (Cardelli et al. 1989) with $R_V = 3.1$ to deredden our SN 1999bh spectra. We obtain a best fit of $E(B-V)_{\rm host} = 0.59 \pm 0.01$ mag (statistical error only) matching our +5 d spectrum of SN 1999bh to our +3 d spectrum of SN 2002es, and $E(B-V)_{\rm host} = 0.49 \pm 0.01$ mag matching our +20 d spectrum of SN 1999bh to our +13 d spectrum of SN 2002es. These values are consistent with what we derived above using the $B-V$ color at maximum light. We adopt $E(B-V)_{\rm host} = 0.48 \pm 0.07$ mag as the host-galaxy extinction.

In Figure 5.14 we show the color curves of SN 1999bh corrected for Milky Way and host-galaxy reddening. The curves of SN 2002es provide an excellent match for the color evolution of SN 1999bh. The $B-V$ and $V-R$ colors agree almost perfectly. The $V-I$ color of SN 1999bh is bluer than expected, compared to that of SN 2002es.

After correcting for Milky Way and host-galaxy extinction, the absolute magnitude at peak of SN 1999bh was $M_B = -17.71 \pm 0.27$ mag, almost the same luminosity as SN 2002es. We estimate $\Delta m_{15}(B) = 1.24 \pm 0.10$ mag. Having a light-curve width that is comparable to that of SN 2002es, SN 1999bh is another example of a 5σ outlier in the Phillips relation as shown in Figure 5.3.

In Figure 5.15 we illustrate our two epochs of spectroscopy compared to SN 2002es at a comparable phase. In the top panel, we show our spectra around maximum light; SN 1999bh lacks hydrogen and exhibits Si II λ6355, confirming its classification as a SN Ia. In addition,

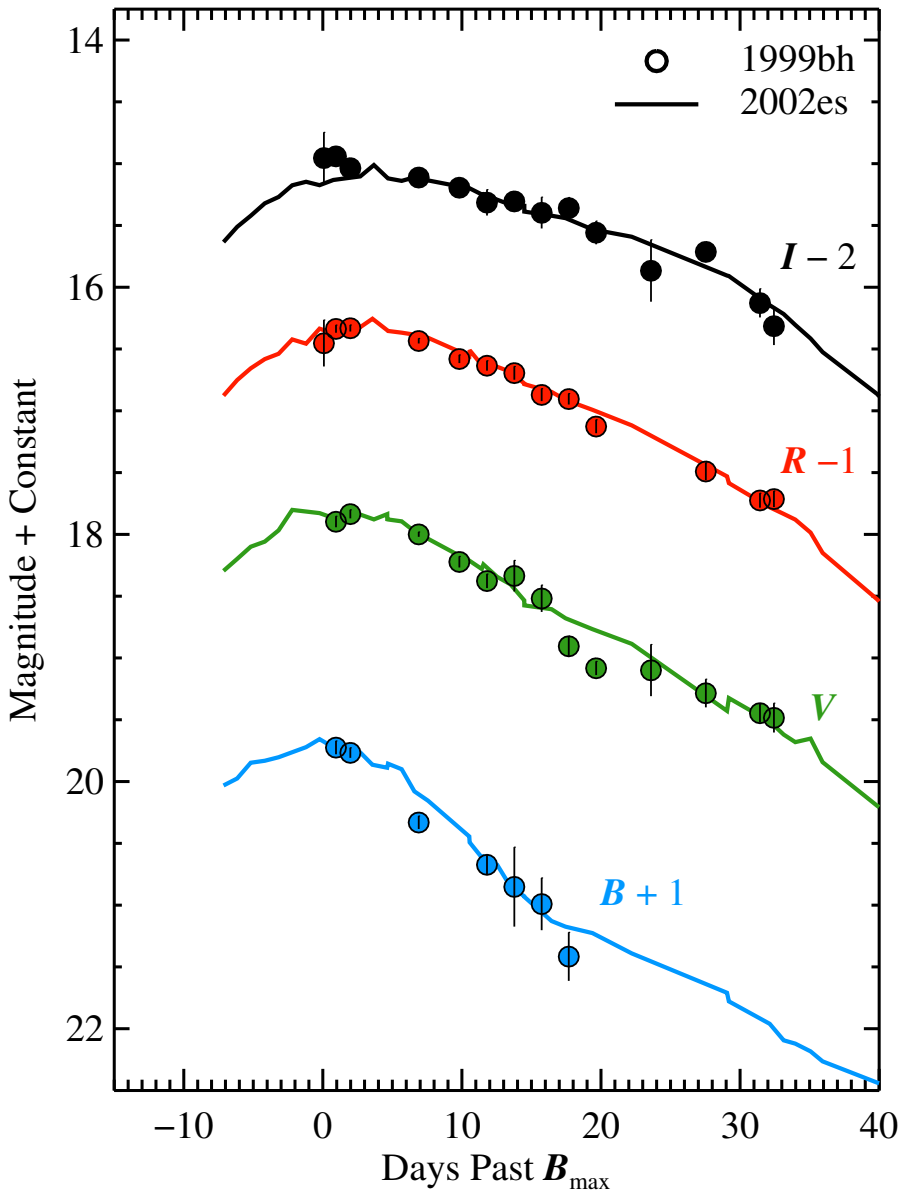

Figure 5.13: *BVRI* light curves of SN 1999bh (filled circles) in comparison to SN 2002es (solid lines). The light curves of both objects have been shifted relative to the time of $B_{\max}$ and peak magnitude. The light curves of SN 1999bh display a striking similarity to those of SN 2002es. Both sets of light curves are particularly broad, despite being subluminous and spectroscopically similar to those of SN 1991bg.

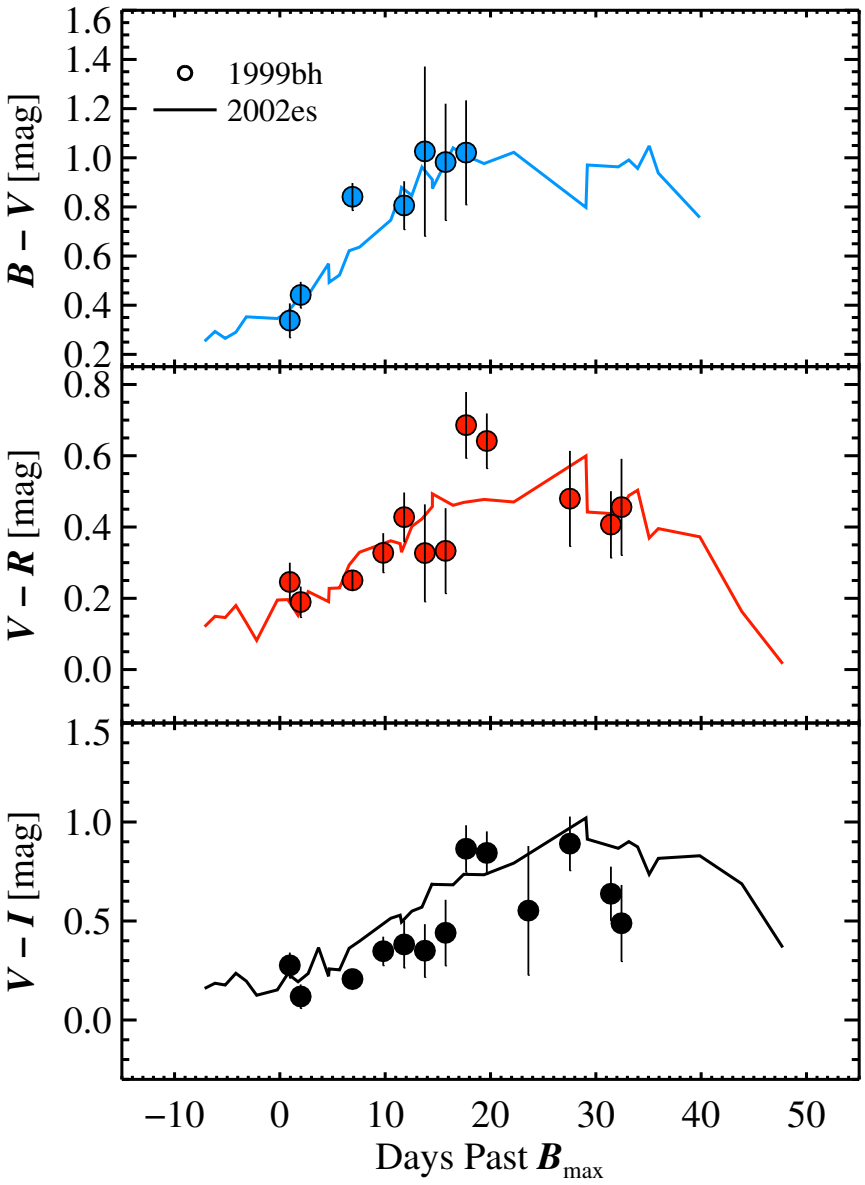

Figure 5.14: Color curves of SN 1999bh (solid circles) compared to SN 2002es (solid lines). SN 1999bh has been corrected for $E(B-V)_{\rm MW} = 0.015$ mag and $E(B-V)_{\rm host} = 0.48$ mag. The color curves of SN 2002es, corrected for $E(B-V)_{\rm MW} = 0.183$ mag, provide an excellent match for SN 1999bh.

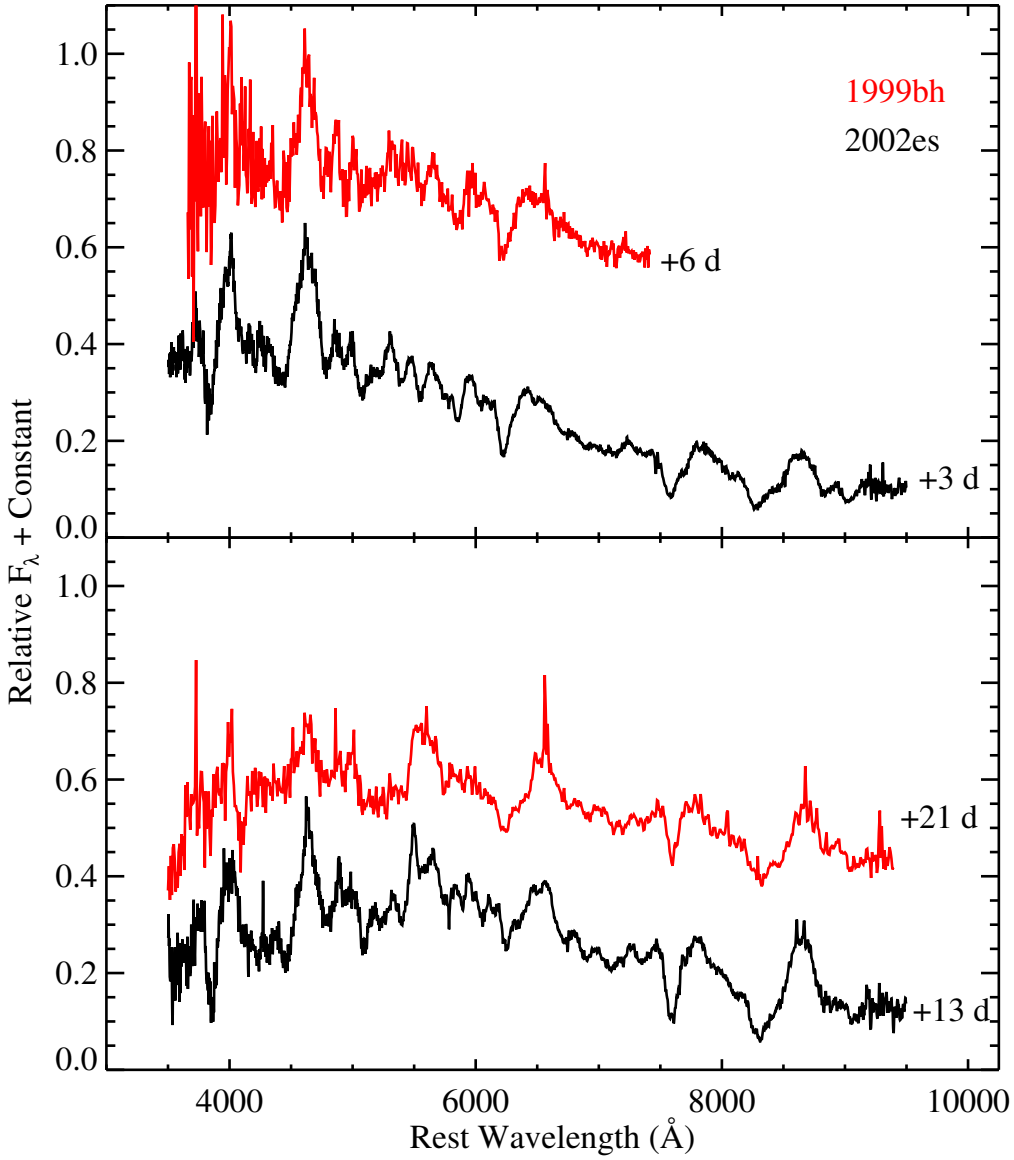

Figure 5.15: Spectra of SN 1999bh (red) in comparison to SN 2002es (black). The spectra have been corrected for the effects of host-galaxy recession. Spectra of SN 1999bh have been corrected for $E(B-V) = 0.01$ mag due to Milky Way extinction and $E(B-V) = 0.48$ mag from host-galaxy extinction using a CCM reddening law with $R_V = 3.1$. Spectra of SN 2002es have been corrected for $E(B-V) = 0.183$ mag due to Milky Way extinction.

there is strong Ti II absorption, linking it to the SN 1991bg subclass. The ejecta velocity measured from the minimum blueshift of Si II λ6355 is $\sim$6000 km s^{-1}, similar to that of SN 2002es. In the bottom panel, we show our spectra from roughly 3 weeks after maximum light. Again, we see striking similarities between the two objects. We note that the narrow feature at the wavelength of Hα in both spectra is from the host galaxy.

The host of SN 1999bh is classified by van den Bergh et al. (2002) as an Sb galaxy. Given the narrow Hα, [N II], and Na I D features superimposed on our spectra of SN 1999bh, it is likely that SN 1999bh lies along the line-of-sight of a star-forming region in NGC 3435. However, it is not possible to determine whether SN 1999bh is actually associated with the star-forming region or is behind it. Unlike the case for SN 2002es, the host galaxy of SN 1999bh does not help constrain the stellar population associated with SN 1999bh.

Table 5.6: Comparison of Properties of Subluminous SN 1991bg-Like Objects

SN	M_B (mag)	$\Delta m_{15}(B)$ (mag)	$v^{\rm a}_{\rm phot}$ (km s^{-1})	$\mathcal{R}$(Si)	Source
SN 1991bg	-16.60 ± 0.03	1.93 ± 0.10	10,100	0.62 ± 0.05	Taubenberger et al. (2008)
SN 2006bt	-18.83 ± 0.06	1.09 ± 0.06	10,500	0.44 ± 0.05	Foley et al. (2010b)
PTF 09dav	-15.33 ± 0.08	1.87 ± 0.06	6100	0.35 ± 0.05	Sullivan et al. (2011b)
PTF 10ops	-17.66 ± 0.06	1.12 ± 0.06	10,000	0.58 ± 0.06	Maguire et al. (2011)
SN 2002es	-17.78 ± 0.12	1.28 ± 0.04	6000	0.55 ± 0.05	This work

[a] As measured by the minimum in the absorption feature attributed to Si II λ6355.

5.4.7 Rate

Both SN 2002es and SN 1999bh were included in the LOSS SN rate study (Leaman et al. 2011; Li et al. 2011a,c) in the luminosity function (LF) subsample used to calculate the volumetric rate for different SN Ia subtypes. The LF subsample is considered to represent a complete sample of 74 SNe Ia within 80 Mpc. In Li et al. (2011c), both objects are classified as SN 2002cx-like SNe. Within a fixed volume, SN 2002es-like objects should account for $\sim$2.5% of SNe Ia. It is worth noting that the reclassification of SN 2002es and SN 1999bh decreases the reported volumetric fraction of SN 2002cx-like objects from 5.0% to 2.5% as well. We caution that our rate calculation is limited by the small number of SN 2002es-like objects in the LF sample.

5.4.8 Comparison to Other Peculiar SN 1991bg-Like SNe

The spectroscopic subclass of SN 1991bg-like SNe has been shown to have their own form of Phillips relation (i.e., correlation between light-curve decline and luminosity), similar to what is found among normal SNe Ia (Phillips et al. 1999; Garnavich et al. 2004; Taubenberger et al. 2008). However, there are notable exceptions in the literature of SNe that share superficial similarities to SN 1991bg, but have unique properties not seen in the broader SN 1991bg subclass. Here we will compare and contrast SN 2002es with known peculiar SN 1991bg-like SNe.

Foley et al. (2010b) found that SN 2006bt had broad, slowly evolving light optical curves ($\Delta m_{15}(B) = 1.09 \pm 0.06$ mag) typical of a luminous event, but spectra more similar to those of a cooler, subluminous event. A spectrum of the host galaxy from the SDSS (Abazajian et al. 2009) shows no signs of emission lines, indicating no recent star formation. Coupled with the position of SN 2006bt in the halo of the galaxy, the authors concluded that the progenitor of SN 2006bt was likely a low-mass star. Assuming no host-galaxy extinction, the peak absolute magnitude of SN 2006bt was $M_B = -18.94 \pm 0.06$ mag, slightly less luminous than normal SNe Ia, but not a significant outlier in the Phillips relation. SN 2006bt had a light-curve width similar to that of SN 2002es, but is significantly brighter. Unlike SN 2002es, the late-time decay in the light curves of SN 2006bt are consistent with ^{56}Ni decay. SN 2006bt had faster expansion velocities at maximum light compared to SN 2002es.

PTF has been a prolific discovery engine for unique transient events. Two subluminous SNe, in particular, may be related to SN 2002es: PTF 09dav (Sullivan et al. 2011b) and PTF 10ops (Maguire et al. 2011). Both events have maximum-light spectra that resemble those of SN 1991bg. PTF 09dav had slow expansion velocities of ~ 6100 km s^{-1} (similar to those of SN 2002es), while PTF 10ops had more typical velocities of $\sim 10,000$ km s^{-1}. Photometrically, both PTF 10ops and SN 2002es have broad light curves despite being subluminous. Both objects occupy a similar position off of the Phillips relation in Figure 5.3. PTF 09dav has a more typical SN 1991bg-like light-curve shape ($\Delta m_{15}(B) = 1.87 \pm 0.06$ mag), but was ~ 1.5 mag fainter than typical subluminous SNe Ia ($M_B = -15.5$ mag). However, SN 2002es is the only object where the optical light curves plummet after $t > +30$ d.

In Table 5.6, we summarize the photometric and spectroscopic properties of other peculiar SN 1991bg-like SNe in comparison to SN 2002es. While SN 2002es shares some characteristics with each of these SNe, no single previously published object is exactly like SN 2002es.

5.4.9 Models

Explaining the properties of SN 2002es within the confines of current models is challenging. Based on the star-formation history of the host galaxy of SN 2002es (Neill et al. 2009), we expect the progenitor to be from a relatively old stellar population, indicating that it was an explosion of either a low-mass single star or a WD. In Section 5.4.5 we examined the possibility that SN 2002es is the result of core collapse of a low-mass single star. In this section, we explore possible models to explain the observed properties of SN 2002es assuming a WD progenitor.

The ".Ia" model has been proposed to explain rapidly evolving, subluminous thermonuclear events. They are the result of helium accretion onto a WD from a double-degenerate white dwarf AM Canum Venaticorum (AM CVn) binary system (Bildsten et al. 2007; Shen & Bildsten 2009; Shen et al. 2010) leading to a thermonuclear explosion of the accreted He envelope. These events are expected to have both a luminosity and a timescale that is one tenth that of SNe Ia. Calculations of observable properties by Shen et al. (2010) find that the rise time of these objects is < 10 d, with a fast decline after maximum. SN 2002es, on the other hand, has a rather broad light curve, with a rise that is likely longer than 10 d based on a first detection by LOSS of 9 days before the time of bolometric maximum light. The ejecta velocities are also expected to be $\sim 10^4$ km s^{-1}, almost a factor of two larger than what is observed in SN 2002es.

Woosley & Kasen (2011) studied a broader set of one-dimensional simulations with models involving a sub-Chandrasekhar-mass carbon-oxygen (CO) WD undergoing helium accretion, including models that explode just the helium envelope and models that explode the entire star. The authors survey the parameter space of WD masses, accretion rates, and initial WD luminosities to produce model spectra and light curves for the resulting transient.

Models in which just the helium shell explodes (either through detonation or deflagration) have rise times < 10 d and $\Delta m_{15}(B) > 2.0$ mag. The fast evolution of the B band is caused by the small ejecta mass (depending on the size of the envelope) and the redistribution of flux from the optical to the NIR by IGEs in the ejecta (Kasen 2006). Detonations of "cold" WDs ($L = 0.01$ L$_\odot$) produce spectra lacking IMEs, which are clearly seen in our spectra of SN 2002es. One of the more promising models from the set of helium-envelope explosions involved "hot" WDs ($L = 1$ L$_\odot$). These explosions produce a significant amount of IMEs, resulting in spectra resembling SN 1991bg with ejecta velocities $\sim$9000 km s^{-1}. These models produce a very small amount of ^{56}Ni ($\sim 10^{-4}$ M$_\odot$) and are instead powered by ^{48}Cr, producing a light curve with a 3 d rise time and peak absolute magnitude of -13. A light curve powered by ^{48}Cr and subsequent decay to ^{48}V (half life $\tau = 16$ d) is an appealing explanation for the rapid fading of SN 2002es at $t > +30$ d; however, these models evolve

too fast and have ejecta velocities that are inconsistent with what we observe.

Deflagrations within the helium envelope led to incomplete burning, producing lower ejecta velocities ($\sim$4000 km s^{-1}) and broader light curves caused by the increased diffusion time in comparison to the detonation model of comparable brightness. The light curves of these models are also powered by the decay of ^{48}Cr, producing faint transients ($M_B \approx -14$ mag). However, the evolution of these light curves is still much too fast compared to SN 2002es.

Outcomes from exploding the entire star generally depended on the initial luminosity of the WD. "Cold" WDs required a larger accreted mass to ignite the helium envelope and drive an explosion of the entire star. As a result, the "cold" models contained an outer envelope of IGEs (synthesized from helium) which acted as a heating source to ionize IMEs and reduce their opacity. Model spectra of these events lack Si II, S II, and Ca II, all of which are present in SN 2002es. The "hot" models, on the other hand, explode with a smaller accreted envelope, allowing IMEs to appear in the spectra. In fact, the synthetic spectra for these objects look remarkably like those of normal SNe Ia and even produce a width-luminosity relation, similar to the Phillips relation, but with a different slope. However, the minimum expansion velocities seen in these models are $\sim$11,000 km s^{-1}, much higher than what is observed for SN 2002es.

Pakmor et al. (2010, 2011) find in simulations that the merger of nearly equal-mass WDs leads to underluminous explosions similar to SN 1991bg. Their model follows the evolution and subsequent explosion of two WDs of equal mass (0.89 M$_\odot$). They find explosions that have roughly the same kinetic energy as a normal SN Ia ($\sim 10^{51}$ erg s^{-1}), but lower velocities due to the larger ejecta mass. Less ^{56}Ni (0.1 M$_\odot$) is synthesized due to lower densities in the final merged object, resulting in a subluminous event. Synthetic light curves of their models are similar to those of SN 1991bg, but broader, with $\Delta m_{15}(B) = 1.4$–1.7 mag. Synthetic spectra show strong titanium, as well as the presence of IMEs such as Si II and O I at velocities lower than typically seen in SN 1991bg-like objects. All of these match characteristics seen in SN 2002es. However, their models do not predict the fast drop in flux at $t > +30$ d, which is a key characteristic that makes SN 2002es a unique object.

5.5 Conclusions

SN 2002es is a peculiar, subluminous SN Ia with a unique combination of observables. At maximum light, spectra of SN 2002es are similar to the subluminous SN 1991bg, indicating a cool photosphere, but with ejecta velocity of $\sim$6000 km s^{-1}. Such slow velocities are more characteristic of SN 2002cx-like objects. While also subluminous, SN 2002cx had

a maximum-light spectrum resembling that of SN 1991T, which is characteristic of a hot photosphere.

Photometrically, SN 2002es has a broad light curve ($\Delta m_{15}(B) = 1.28$ mag), despite being subluminous with a peak absolute magnitude of $M_B = -17.78$ mag. SN 2002es is a 5σ outlier in the Phillips relation (Phillips 1993; Phillips et al. 1999) used to calibrate the light-curve width vs. luminosity relationship for SNe Ia. The R- and I-band light curves are broad and lack the shoulder typically seen in SNe Ia.

Quantitative measurements of spectral features such as the silicon ratio ($\mathcal{R}$(Si); Nugent et al. 1995) and the Si II λ6355 velocity gradient are similar to those of SN 1991bg-like objects. However, SN 2002es is an outlier in the usual relationships, which show strong correlations between these spectral measurements and light-curve parameters (Benetti et al. 2005; Branch et al. 2006).

From Arnett's law, we estimate a synthesized radioactive nickel mass of 0.17 $M_\odot$ required to power the light curve. However, the bolometric light curve shows an unexpected drop in luminosity at $t > +30$ d. We are unable to fit the bolometric light curve with a toy model of the radiated luminosity that accounts for a decrease in the γ-ray trapping function as the ejecta expand homologously. If SN 2002es is a thermonuclear event, then the ejecta became optically thin to γ-rays in an unexpectedly dramatic fashion. Similarly, we are unable to explain the rapid decay by invoking dust formation or the infrared catastrophe (Axelrod 1980). Alternatively, SN 2002es could be powered by some other mechanism not yet understood.

SN 2002es exploded in the outskirts of the early-type S0 galaxy UGC 2708. SED fitting from Neill et al. (2009) and emission-line diagnostics indicate that UGC 2708 is likely a LINER galaxy with no current star formation. This points to a old star, likely a WD, as the progenitor to SN 2002es.

Finding a published model that matches the peculiar collection of observables found in SN 2002es is particularly challenging. We have not found a convincing match by comparing SN 2002es to Woosley & Kasen (2011) models of WDs undergoing helium accretion from a companion star. Models of the merging and subsequent detonation of two equal-mass WDs from Pakmor et al. (2010, 2011) are promising, but do not reproduce the drop in luminosity one month after maximum light.

Looking through the existing LOSS photometry presented in Chapter 2 and the Berkeley Supernova Ia Program spectral database (BSNIP; Silverman et al. 2012c), we identify SN 1999bh as a probable SN 2002es-like event. Spectra and photometry of the object, while limited, match many of the observed characteristics of SN 2002es. Both objects are included in the LOSS SN rate studies (Leaman et al. 2011; Li et al. 2011a,c), allowing us to estimate

that roughly 3% of SNe Ia should be SN 2002es-like SNe within a fixed volume.

Ongoing surveys for transient objects, such as PTF and Pan-STARRS, are likely to find more objects resembling SN 2002es. PTF has already published results for two peculiar subluminous objects which share some similarities to SN 2002es, but also have distinct differences. We expect that future datasets will shed light on understanding the bizarre nature of these subluminous objects.

Chapter 6

Conclusions

6.1 Summary of Thesis

LOSS began in 1997 with the goal of systemically discovering and observing optical transients. The telescope at the heart of LOSS, KAIT, has been a pioneering discovery engine providing the astronomical community with an impressive number of SNe. This thesis has been the presentation and analysis of the LOSS SNe Ia data taken from 1998–2008. Chapter 1 provided an introduction to SNe and the motivation to study these objects. Here, I give a brief summary of the results presented in this thesis.

In Chapter 2, I presented *BVRI* light curves of 165 SNe Ia from LOSS. The light curves are well sampled (cadence of 3–4 days) with an average of 21 photometry epochs. I described the LOSS monitoring campaign and photometry reduction pipeline. A majority of the LOSS light curves begin before maximum light in the B band. Comparing the LOSS dataset to that of Hicken et al. (2009b) (with 69 overlapping SNe), I found that as an ensemble the photometry is consistent. Differences between the datasets are typically small, although individual SNe may differ by as much as 0.1 mag, and occasionally even more. Such disagreement in specific cases can have significant implications for combining future large datasets. Understanding the differences between different photometric campaigns will be an important next step in eliminating systematic uncertainties in SN Ia cosmological analyses.

In Chapter 3, I presented an analysis of the B-band and V-band rise-time distributions of nearby SNe Ia to explore the explosion physics of SNe Ia. Of the 165 objects presented in Chapter 2, 70 objects have light curves that start a week before maximum light. The longer the time between explosion and maximum light (i.e., the rise time), the slower the decline of the light curve after maximum. However, SNe with slower post-maximum decline rates have a faster rise than would be expected from a single-parameter family of light curves,

indicating that SN Ia light curves are not a single-parameter family of varying widths.

Comparison of the B-band rise-time distribution for spectroscopically normal SNe Ia to those exhibiting high-velocity spectral features indicates that high-velocity (HV) SNe Ia have shorter B-band rise times compared to their spectroscopically normal counterparts. After normalizing the B-band light curves to $\Delta m_{15}(B) = 1.1$ mag, spectroscopically normal SNe Ia have a rise time of 18.03 ± 0.24 d, while HV SNe have a faster B-band rise time of 16.63 ± 0.29 d. Despite differences in the B band, HV and normal SNe Ia have similar rise times in the V band. The physical origin of the difference is possibly rooted in the different opacity mechanisms at work in the B and V bands. Line blanketing from Fe-group elements is the dominant source of opacity for wavelengths shorter than ~ 4300 Å, the peak of the B band. At longer wavelengths, such as the V band, electron scattering is the dominant source of opacity. Rapidly moving ejecta, as is the case with HV objects, will broaden absorption features, diminishing the B-band flux without affecting the V-band flux.

The expanding fireball model often used to describe the early luminosity of a SN Ia (Riess et al. 1999b; Conley et al. 2006; Hayden et al. 2010b; Nugent et al. 2011), predicts $L \propto t^2$. The measured initial rise of nearby SN Ia B-band light curves gives a power law with index $2.20^{+0.27}_{-0.19}$, consistent with a parabolic rise predicted by an expanding fireball toy model. In addition, Chapter 3 presented a comparison of early-time B-band data to models for the predicted signature of companion interaction arising from the single-degenerate progenitor scenario (Kasen 2010). There is a substantial degree of degeneracy between the adopted power-law index of the SN light-curve template, the rise time, and the amount of shock emission required to match the data. However, a model involving a red giant undergoing Roche-lobe overflow is inconsistent with the data regardless of the adopted power law.

The LOSS SNe provide an effective anchor point to estimate cosmological parameters when combined with datasets at higher redshift. As described in Chapter 4, the light-curve fitting software SALT2 (Guy et al. 2007) was run on our natural-system light curves to measure light-curve parameters for LOSS light curves and available SN Ia datasets in the literature. Of the 226 low-z objects, 91 objects are from LOSS, including 45 SNe without previously published distances. The SN data are consistent with a flat, Λ-dominated Universe when combined with constraints from the anisotropies in the cosmic microwave background (Komatsu et al. 2011) and measurements of baryon acoustic oscillations (Percival et al. 2010).

The holy grail of SN Ia cosmology remains the discovery of another parameter that correlates with luminosity to improve SN distance estimates. When looking at Hubble residuals as a function of host-galaxy morphology, there is no evidence for a significant trend in the low-redshift data, although the scatter in Hubble residuals is reduced by only using SNe residing within a projected distance < 10 kpc of the host-galaxy nucleus. Hubble residuals

do not correlate with the expansion velocity of Si II λ6355 measured in optical spectra near maximum light. Improvements in cosmological analyses within low-redshift samples can be achieved by better constraining calibration uncertainties in the zero points of photometric systems.

Chapters 2–4 focused on a statistical analysis of SN Ia properties. Chapter 5, instead, focused entirely on a new class of SNe Ia based on the observed properties of SN 2002es. At maximum light, SN 2002es shares spectroscopic properties with the underluminous SN 1991bg subclass of SNe Ia, but with substantially lower expansion velocities ($\sim$6000 km s^{-1}) more typical of the peculiar SN 2002cx subclass. Photometrically, SN 2002es differs from both SN 1991bg-like and SN 2002cx-like supernovae. Although at maximum light it is subluminous ($M_B = -17.78$ mag), SN 2002es has a relatively broad light curve ($\Delta m_{15}(B) = 1.28 \pm 0.04$ mag), making it a significant outlier in the light-curve width versus luminosity relationship. One month after maximum light, SN 2002es undergoes an unexpected plummet in the bolometric luminosity. The late-time decay of the light curves is inconsistent with the estimated ^{56}Ni mass of 0.17 M$_\odot$, indicating that either the light curve was not completely powered by ^{56}Ni decay or the ejecta became optically thin to gamma rays within a month after maximum light. The host galaxy is classified as an S0 galaxy with little to no star formation, indicating the progenitor of SN 2002es is likely from an old stellar population. Based on rates from LOSS, SN 2002es-like objects should account for roughly 2.5% of SNe Ia within a fixed volume. Current theoretical models are unable to explain the observed characteristics of SN 2002es.

6.2 The Future

In the 15 years since the inception of LOSS, a number of surveys have come online to systematically discover and monitor optical transients over a wide range of redshifts. Many have built off the lessons learned from the LOSS search strategy. Improvements to the understanding of SNe Ia will require both well-observed individual SNe and large datasets found via these surveys. Here, I will discuss the future prospects for SN Ia science.

PTF and PanSTARRS are two ongoing surveys in the process of collecting light curves for hundreds of SNe Ia over a wide range of redshifts. These homogenous datasets have the potential to eliminate issues relating to systematic errors due to combining datasets in cosmological analyses. Follow-up programs that take advantage of a wide-wavelength range, including the UV and IR, will provide deep insights into SN Ia physics. In particular, collecting a larger dataset of space-based UV observations of low-z SNe may help shed understanding on the U-band anomaly discussed in Chapter 4.3.

A number of studies have shown a correlation between SN Ia luminosity (post light-curve correction) and host-galaxy mass (Kelly et al. 2010; Sullivan et al. 2010; Lampeitl et al. 2010). However, the nature of this relationship is poorly understood. What connects the luminosity of a SN to the global properties of its host galaxy? These studies use SED fits to broadband photometry of the host galaxy to derive global host-galaxy properties such as stellar mass, star-formation rate, and metallicity. However, these global properties may not necessarily reflect the local environment of the SN. Future studies utilizing spectroscopy of host galaxies at the SN position may provide a measure of a more localized quantity (e.g., metallicity, star-formation rate) that correlates with SN luminosity, and perhaps hints at the physical understanding behind the connection to the host galaxy.

Although most of this thesis focused on the statistical properties of a large sample of SNe Ia, individual SNe Ia found within days of explosion offer a unique probe of the physics governing the explosion and the progenitor system. SN 2011fe was discovered by PTF within 11 hr of explosion (Nugent et al. 2011) and was used to derive constraints on the primary star that exploded (Nugent et al. 2011; Bloom et al. 2012) and the secondary companion (Li et al. 2011b). LOSS discovered SN 2009ig (Foley et al. 2012b) and SN 2012cg (Silverman et al. 2012d) within days of explosion. In 2011, the LOSS search strategy was modified in the hopes of finding more SNe shortly after explosion to further push the limits of our understanding of the early-time behavior of SNe.

In Chapter 3, I presented a relationship between the B-band rise time and the Si II velocity near maximum light. Finding this relationship required having companion spectra for objects in the LOSS photometric sample. Work by Wang et al. (2009a) and Foley & Kasen (2011) has shown that distance estimates to SNe can be improved by separating SNe based on Si II velocity. Verifying and understanding these relationships will require both photometric and spectroscopic data. Future surveys will benefit from including a spectroscopic component to follow-up photometric monitoring to search for other relationships between photometric and spectroscopic data.

The LOSS SN Ia photometry sample is a valuable dataset that will hopefully provide the SN Ia field new grounds to explore SN Ia physics, especially when combined with the BSNIP spectroscopic sample (Silverman et al. 2012c). Future datasets will build off the LOSS data and analysis to further push the limits of our understanding of SN Ia physics and cosmology.

Bibliography

Abazajian, K. N., et al. 2009, ApJS, 182, 543
Alard, C., & Lupton, R. H. 1998, ApJ, 503, 325
Aldering, G., Knop, R., & Nugent, P. 2000, AJ, 119, 2110
Aldering, G., Nugent, P., Ellis, R., Perlmutter, S., & Folha, D. 1999, IAU Circ., 7138, 3
Aldering, G., et al. 2002, in Society of Photo-Optical Instrumentation Engineers (SPIE) Conference Series, Vol. 4836, Society of Photo-Optical Instrumentation Engineers (SPIE) Conference Series, ed. J. A. Tyson & S. Wolff, 61–72
Altavilla, G., et al. 2004, MNRAS, 349, 1344
—. 2007, A&A, 475, 585
Amanullah, R., et al. 2010, ApJ, 716, 712
Anupama, G. C., Sahu, D. K., & Jose, J. 2005, A&A, 429, 667
Arnett, W. D. 1982, ApJ, 253, 785
Astier, P., et al. 2006, A&A, 447, 31
Axelrod, T. S. 1980, PhD thesis, California Univ., Santa Cruz.
Baade, W., & Zwicky, F. 1934, Proceedings of the National Academy of Science, 20, 254
Bailey, S., et al. 2009, A&A, 500, L17
Barbon, R., Benetti, S., Rosino, L., Cappellaro, E., & Turatto, M. 1990, A&A, 237, 79
Benetti, S., et al. 2005, ApJ, 623, 1011
Bessell, M. S. 1990, PASP, 102, 1181
Bildsten, L., Shen, K. J., Weinberg, N. N., & Nelemans, G. 2007, ApJ, 662, L95
Blondin, S., Mandel, K. S., & Kirshner, R. P. 2011, A&A, 526, A81+
Blondin, S., Prieto, J. L., Patat, F., Challis, P., Hicken, M., Kirshner, R. P., Matheson, T., & Modjaz, M. 2009, ApJ, 693, 207
Blondin, S., & Tonry, J. L. 2007, ApJ, 666, 1024
Blondin, S., et al. 2012, AJ, 143, 126
Bloom, J. S., et al. 2012, ApJ, 744, L17
Bohlin, R. C., & Gilliland, R. L. 2004, AJ, 128, 3053
Boisseau, J. R., & Wheeler, J. C. 1991, AJ, 101, 1281

Branch, D., & Tammann, G. A. 1992, ARA&A, 30, 359
Branch, D., et al. 2006, PASP, 118, 560
Candia, P., et al. 2003, PASP, 115, 277
Cardelli, J. A., Clayton, G. C., & Mathis, J. S. 1989, ApJ, 345, 245
Chevalier, C., & Ilovaisky, S. A. 1991, A&AS, 90, 225
Chornock, R., Filippenko, A. V., Branch, D., Foley, R. J., Jha, S., & Li, W. 2006, PASP, 118, 722
Chornock, R., Swift, B., Filippenko, A. V., & Li, W. D. 2002, IAU Circ., 7965, 2
Conley, A., Carlberg, R. G., Guy, J., Howell, D. A., Jha, S., Riess, A. G., & Sullivan, M. 2007, ApJ, 664, L13
Conley, A., et al. 2006, AJ, 132, 1707
—. 2008, ApJ, 681, 482
—. 2011, ApJS, 192, 1
Contreras, C., et al. 2010, AJ, 139, 519
Cooke, J., et al. 2011, ApJ, 727, L35
de Vaucouleurs, G., de Vaucouleurs, A., Corwin, Jr., H. G., Buta, R. J., Paturel, G., & Fouque, P. 1991, Third Reference Catalogue of Bright Galaxies (New York: Springer-Verlag)
Della Valle, M., & Livio, M. 1994, ApJ, 423, L31
Di Stefano, R., Voss, R., & Claeys, J. S. W. 2011, ApJ, 738, L1
Eisenstein, D. J., et al. 2005, ApJ, 633, 560
Ellis, R. S., et al. 2008, ApJ, 674, 51
Fabricant, D., Cheimets, P., Caldwell, N., & Geary, J. 1998, PASP, 110, 79
Filippenko, A. V. 1982, PASP, 94, 715
—. 1997, ARA&A, 35, 309
Filippenko, A. V. 2003, in From Twilight to Highlight: The Physics of Supernovae, ed. W. Hillebrandt & B. Leibundgut, 171
Filippenko, A. V. 2005a, in Astronomical Society of the Pacific Conference Series, Vol. 342, 1604-2004: Supernovae as Cosmological Lighthouses, ed. M. Turatto, S. Benetti, L. Zampieri, & W. Shea, 87
Filippenko, A. V. 2005b, in Astrophysics and Space Science Library, Vol. 332, White dwarfs: cosmological and galactic probes, ed. E. M. Sion, S. Vennes, & H. L. Shipman, 97–133
Filippenko, A. V., Li, W. D., Treffers, R. R., & Modjaz, M. 2001, in Astronomical Society of the Pacific Conference Series, Vol. 246, IAU Colloq. 183: Small Telescope Astronomy on Global Scales, ed. B. Paczynski, W.-P. Chen, & C. Lemme, 121–+
Filippenko, A. V., et al. 1992a, ApJ, 384, L15

—. 1992b, AJ, 104, 1543
Fisher, A., Branch, D., Nugent, P., & Baron, E. 1997, ApJ, 481, L89+
Folatelli, G., et al. 2010, AJ, 139, 120
—. 2012, ApJ, 745, 74
Foley, R. J. 2012, ApJ, 748, 127
Foley, R. J., Brown, P. J., Rest, A., Challis, P. J., Kirshner, R. P., & Wood-Vasey, W. M. 2010a, ApJ, 708, L61
Foley, R. J., Filippenko, A. V., & Jha, S. W. 2008, ApJ, 686, 117
Foley, R. J., & Kasen, D. 2011, ApJ, 729, 55
Foley, R. J., Narayan, G., Challis, P. J., Filippenko, A. V., Kirshner, R. P., Silverman, J. M., & Steele, T. N. 2010b, ApJ, 708, 1748
Foley, R. J., Sanders, N. E., & Kirshner, R. P. 2011, ApJ, 742, 89
Foley, R. J., et al. 2003, PASP, 115, 1220
—. 2009, AJ, 138, 376
—. 2012a, AJ, 143, 113
—. 2012b, ApJ, 744, 38
Frieman, J. A., et al. 2008, AJ, 135, 338
Garavini, G., et al. 2004, AJ, 128, 387
Garnavich, P. M., et al. 2004, ApJ, 613, 1120
Gerardy, C. L., et al. 2007, ApJ, 661, 995
Goldhaber, G., et al. 2001, ApJ, 558, 359
Guy, J., Astier, P., Nobili, S., Regnault, N., & Pain, R. 2005, A&A, 443, 781
Guy, J., et al. 2007, A&A, 466, 11
—. 2010, A&A, 523, A7
Hamuy, M., Phillips, M. M., Suntzeff, N. B., Schommer, R. A., Maza, J., & Aviles, R. 1996a, AJ, 112, 2398
Hamuy, M., et al. 1996b, AJ, 112, 2408
Hatano, K., Branch, D., & Deaton, J. 1998, ApJ, 502, 177
Hayden, B. T., et al. 2010a, ApJ, 722, 1691
—. 2010b, ApJ, 712, 350
Heckman, T. M. 1980, A&A, 87, 152
Hicken, M., Garnavich, P. M., Prieto, J. L., Blondin, S., DePoy, D. L., Kirshner, R. P., & Parrent, J. 2007, ApJ, 669, L17
Hicken, M., Wood-Vasey, W. M., Blondin, S., Challis, P., Jha, S., Kelly, P. L., Rest, A., & Kirshner, R. P. 2009a, ApJ, 700, 1097
Hicken, M., et al. 2009b, ApJ, 700, 331

—. 2012, ApJS, 200, 12
Hillebrandt, W., & Niemeyer, J. C. 2000, ARA&A, 38, 191
Holtzman, J. A., et al. 2008, AJ, 136, 2306
Horne, K. 1986, PASP, 98, 609
Howell, D. A. 2001, ApJ, 554, L193
Howell, D. A., et al. 2006, Nature, 443, 308
—. 2009, ApJ, 691, 661
Hsiao, E. Y., Conley, A., Howell, D. A., Sullivan, M., Pritchet, C. J., Carlberg, R. G., Nugent, P. E., & Phillips, M. M. 2007, ApJ, 663, 1187
Hubble, E. 1929, Proceedings of the National Academy of Science, 15, 168
Iben, Jr., I., & Tutukov, A. V. 1994, ApJ, 431, 264
James, F., & Roos, M. 1975, Computer Physics Communications, 10, 343
Jha, S., Branch, D., Chornock, R., Foley, R. J., Li, W., Swift, B. J., Casebeer, D., & Filippenko, A. V. 2006a, AJ, 132, 189
Jha, S., Riess, A. G., & Kirshner, R. P. 2007, ApJ, 659, 122
Jha, S., et al. 2006b, AJ, 131, 527
Justham, S. 2011, ApJ, 730, L34
Kasen, D. 2006, ApJ, 649, 939
—. 2010, ApJ, 708, 1025
Kasen, D., & Plewa, T. 2007, ApJ, 662, 459
Kasen, D., Röpke, F. K., & Woosley, S. E. 2009, Nature, 460, 869
Kasliwal, M. M., et al. 2010, ApJ, 723, L98
—. 2011, submitted (arXiv:1111.6109)
Kelly, B. C. 2007, ApJ, 665, 1489
Kelly, P. L., Hicken, M., Burke, D. L., Mandel, K. S., & Kirshner, R. P. 2010, ApJ, 715, 743
Kessler, R., et al. 2009a, ApJS, 185, 32
—. 2009b, PASP, 121, 1028
Kirshner, R. P. 2004, Proceedings of the National Academy of Science, 101, 8
Klein, R. I., & Chevalier, R. A. 1978, ApJ, 223, L109
Komatsu, E., et al. 2011, ApJS, 192, 18
Kowalski, M., et al. 2008, ApJ, 686, 749
Krajnović, D., Cappellari, M., de Zeeuw, P. T., & Copin, Y. 2006, MNRAS, 366, 787
Krisciunas, K., Hastings, N. C., Loomis, K., McMillan, R., Rest, A., Riess, A. G., & Stubbs, C. 2000, ApJ, 539, 658
Krisciunas, K., et al. 2001, AJ, 122, 1616
—. 2004a, AJ, 127, 1664

—. 2004b, AJ, 128, 3034
—. 2011, AJ, 142, 74
Lampeitl, H., et al. 2010, ApJ, 722, 566
Landolt, A. U. 1983, AJ, 88, 439
—. 1992, AJ, 104, 340
—. 2009, AJ, 137, 4186
Landolt, A. U., & Uomoto, A. K. 2007, AJ, 133, 768
Law, N. M., et al. 2009, PASP, 121, 1395
Leaman, J., Li, W., Chornock, R., & Filippenko, A. V. 2011, MNRAS, 412, 1419
Leibundgut, B. 2000, A&A Rev., 10, 179
Leibundgut, B., et al. 1993, AJ, 105, 301
Leloudas, G., et al. 2009, A&A, 505, 265
Leonard, D. C. 2007, ApJ, 670, 1275
Leonard, D. C., Li, W., Filippenko, A. V., Foley, R. J., & Chornock, R. 2005, ApJ, 632, 450
Li, W. 1999, IAU Circ., 7135, 2
Li, W., Chornock, R., Leaman, J., Filippenko, A. V., Poznanski, D., Wang, X., Ganeshalingam, M., & Mannucci, F. 2011a, MNRAS, 412, 1473
Li, W., Filippenko, A. V., Chornock, R., & Jha, S. 2003a, PASP, 115, 844
Li, W., Filippenko, A. V., & Riess, A. G. 2001a, ApJ, 546, 719
Li, W., Filippenko, A. V., Treffers, R. R., Riess, A. G., Hu, J., & Qiu, Y. 2001b, ApJ, 546, 734
Li, W., Swift, B., & Ganeshalingam, M. 2002, IAU Circ., 7959, 1
Li, W., et al. 2001c, PASP, 113, 1178
—. 2003b, PASP, 115, 453
—. 2011b, Nature, 480, 348
—. 2011c, MNRAS, 412, 1441
Li, W. D., et al. 2000, in American Institute of Physics Conference Series, Vol. 522, American Institute of Physics Conference Series, ed. S. S. Holt & W. W. Zhang, 103–106
Lira, P. 1996, Master's thesis, MS thesis. Univ. Chile (1996)
Lira, P., et al. 1998, AJ, 115, 234
Livio, M. 2000, in Type Ia Supernovae, Theory and Cosmology, ed. J. C. Niemeyer & J. W. Truran, 33
Maeda, K., et al. 2010, Nature, 466, 82
—. 2011, MNRAS, 413, 3075
Maguire, K., et al. 2011, MNRAS, 418, 747
Mandel, K. S., Narayan, G., & Kirshner, R. P. 2011, ApJ, 731, 120

Mandel, K. S., Wood-Vasey, W. M., Friedman, A. S., & Kirshner, R. P. 2009, ApJ, 704, 629
Mannucci, F., Della Valle, M., Panagia, N., Cappellaro, E., Cresci, G., Maiolino, R., Petrosian, A., & Turatto, M. 2005, A&A, 433, 807
Maoz, D., Mannucci, F., Li, W., Filippenko, A. V., Della Valle, M., & Panagia, N. 2011, MNRAS, 412, 1508
Martin, D. C., et al. 2005, ApJ, 619, L1
Matheson, T., Challis, P., Kirshner, R., Berlind, P., & Filippenko, A. V. 2002, IAU Circ., 7965, 3
Matheson, T., et al. 2008, AJ, 135, 1598
Matzner, C. D., & McKee, C. F. 1999, ApJ, 510, 379
Mazzali, P. A., Benetti, S., Stehle, M., Branch, D., Deng, J., Maeda, K., Nomoto, K., & Hamuy, M. 2005, MNRAS, 357, 200
McClelland, C. M., et al. 2010, ApJ, 720, 704
Miknaitis, G., et al. 2007, ApJ, 666, 674
Miller, J. S., & Stone, R. P. S. 1993, Lick Obs. Tech. Rep. 66 (Santa Cruz: Lick Obs.)
Modjaz, M., Li, W., Filippenko, A. V., King, J. Y., Leonard, D. C., Matheson, T., Treffers, R. R., & Riess, A. G. 2001, PASP, 113, 308
Modjaz, M., et al. 2009, ApJ, 702, 226
Monnier Ragaigne, D., van Driel, W., Schneider, S. E., Balkowski, C., & Jarrett, T. H. 2003, A&A, 408, 465
Nadyozhin, D. K. 1994, ApJS, 92, 527
Narayan, G., et al. 2011, ApJ, 731, L11
Neill, J. D., et al. 2006, AJ, 132, 1126
—. 2009, ApJ, 707, 1449
Nomoto, K., Filippenko, A. V., & Shigeyama, T. 1990, A&A, 240, L1
Nozawa, T., Maeda, K., Kozasa, T., Tanaka, M., Nomoto, K., & Umeda, H. 2011, ApJ, 736, 45
Nugent, P., Kim, A., & Perlmutter, S. 2002, PASP, 114, 803
Nugent, P., Phillips, M., Baron, E., Branch, D., & Hauschildt, P. 1995, ApJ, 455, L147+
Nugent, P. E., et al. 2011, Nature, 480, 344
Oke, J. B. 1974, ApJS, 27, 21
Oke, J. B., et al. 1995, PASP, 107, 375
Pakmor, R., Hachinger, S., Röpke, F. K., & Hillebrandt, W. 2011, A&A, 528, A117
Pakmor, R., Kromer, M., Röpke, F. K., Sim, S. A., Ruiter, A. J., & Hillebrandt, W. 2010, Nature, 463, 61
Parrent, J. T., et al. 2011, ApJ, 732, 30

Pastorello, A., et al. 2007a, MNRAS, 377, 1531
—. 2007b, MNRAS, 376, 1301
Patat, F., Benetti, S., Cappellaro, E., Danziger, I. J., della Valle, M., Mazzali, P. A., & Turatto, M. 1996, MNRAS, 278, 111
Paxton, B., Bildsten, L., Dotter, A., Herwig, F., Lesaffre, P., & Timmes, F. 2011, ApJS, 192, 3
Percival, W. J., et al. 2010, MNRAS, 401, 2148
Perets, H. B., et al. 2010, Nature, 465, 322
Perlmutter, S., et al. 1997, ApJ, 483, 565
—. 1999, ApJ, 517, 565
Phillips, A. C., & Davis, L. E. 1995, in Astronomical Society of the Pacific Conference Series, Vol. 77, Astronomical Data Analysis Software and Systems IV, ed. R. A. Shaw, H. E. Payne, & J. J. E. Hayes, 297
Phillips, M. M. 1993, ApJ, 413, L105
Phillips, M. M., Lira, P., Suntzeff, N. B., Schommer, R. A., Hamuy, M., & Maza, J. 1999, AJ, 118, 1766
Phillips, M. M., Wells, L. A., Suntzeff, N. B., Hamuy, M., Leibundgut, B., Kirshner, R. P., & Foltz, C. B. 1992, AJ, 103, 1632
Phillips, M. M., et al. 2006, AJ, 131, 2615
—. 2007, PASP, 119, 360
Pignata, G., et al. 2008, MNRAS, 388, 971
Pinto, P. A., & Eastman, R. G. 2000a, ApJ, 530, 744
—. 2000b, ApJ, 530, 757
Poznanski, D., Ganeshalingam, M., Silverman, J. M., & Filippenko, A. V. 2011, MNRAS, 415, L81
Poznanski, D., et al. 2009, ApJ, 694, 1067
Prieto, J. L., Rest, A., & Suntzeff, N. B. 2006, ApJ, 647, 501
Pskovskii, Y. P. 1984, Soviet Ast., 28, 658
Richmond, M., Treffers, R. R., & Filippenko, A. V. 1993, PASP, 105, 1164
Riess, A. G., Press, W. H., & Kirshner, R. P. 1995, ApJ, 438, L17
—. 1996, ApJ, 473, 88
Riess, A. G., et al. 1998, AJ, 116, 1009
—. 1999a, AJ, 117, 707
—. 1999b, AJ, 118, 2675
—. 2004, ApJ, 607, 665
—. 2005, ApJ, 627, 579

—. 2007, ApJ, 659, 98
—. 2009, ApJS, 183, 109
—. 2011, ApJ, 732, 129
Scalzo, R. A., et al. 2010, ApJ, 713, 1073
Scannapieco, E., & Bildsten, L. 2005, ApJ, 629, L85
Schlegel, D. J., Finkbeiner, D. P., & Davis, M. 1998, ApJ, 500, 525
Schmidt, B. P., et al. 1998, ApJ, 507, 46
Shen, K. J., & Bildsten, L. 2009, ApJ, 699, 1365
Shen, K. J., Kasen, D., Weinberg, N. N., Bildsten, L., & Scannapieco, E. 2010, ApJ, 715, 767
Silverman, J. M., & Filippenko, A. V. 2012, MNRAS accepted (arXiv:1202.3788)
Silverman, J. M., Ganeshalingam, M., Li, W., & Filippenko, A. V. 2012a, MNRAS accepted (arXiv:1202.2130)
Silverman, J. M., Ganeshalingam, M., Li, W., Filippenko, A. V., Miller, A. A., & Poznanski, D. 2011, MNRAS, 410, 585
Silverman, J. M., Kong, J. J., & Filippenko, A. V. 2012b, MNRAS accepted (arXiv:1202.2129)
Silverman, J. M., et al. 2012c, MNRAS accepted (arXiv:1202.2128)
—. 2012d, ApJL accepted (arXiv:1206.1328)
Smith, N., Foley, R. J., & Filippenko, A. V. 2008, ApJ, 680, 568
Soderberg, A. M., et al. 2008, Nature, 453, 469
Sollerman, J., et al. 2002, A&A, 386, 944
—. 2004, A&A, 428, 555
Stanishev, V., et al. 2007, A&A, 469, 645
Stetson, P. B. 1987, PASP, 99, 191
Stritzinger, M., & Leibundgut, B. 2005, A&A, 431, 423
Stritzinger, M., Leibundgut, B., Walch, S., & Contardo, G. 2006a, A&A, 450, 241
Stritzinger, M., Mazzali, P. A., Sollerman, J., & Benetti, S. 2006b, A&A, 460, 793
Stritzinger, M., Suntzeff, N. B., Hamuy, M., Challis, P., Demarco, R., Germany, L., & Soderberg, A. M. 2005, PASP, 117, 810
Stritzinger, M., et al. 2002, AJ, 124, 2100
Stritzinger, M. D., et al. 2011, AJ, 142, 156
Strolger, L., et al. 2002, AJ, 124, 2905
Strovink, M. 2007, ApJ, 671, 1084
Sullivan, M., et al. 2003, MNRAS, 340, 1057
—. 2006, ApJ, 648, 868

—. 2010, MNRAS, 406, 782
—. 2011a, ApJ, 737, 102
—. 2011b, ApJ, 732, 118
Suzuki, N., et al. 2012, ApJ, 746, 85
Taubenberger, S., et al. 2008, MNRAS, 385, 75
—. 2011, MNRAS, 412, 2735
Thomas, R. C., et al. 2011, ApJ, 743, 27
Tripp, R. 1998, A&A, 331, 815
Tripp, R., & Branch, D. 1999, ApJ, 525, 209
Turatto, M., Benetti, S., & Cappellaro, E. 2003, in From Twilight to Highlight: The Physics of Supernovae, ed. W. Hillebrandt & B. Leibundgut, 200
Turatto, M., Benetti, S., Cappellaro, E., Danziger, I. J., Della Valle, M., Gouiffes, C., Mazzali, P. A., & Patat, F. 1996, MNRAS, 283, 1
Upadhye, A., Ishak, M., & Steinhardt, P. J. 2005, Phys. Rev. D, 72, 063501
Valenti, S., et al. 2009, Nature, 459, 674
van den Bergh, S., Li, W., & Filippenko, A. V. 2002, PASP, 114, 820
Wade, R. A., & Horne, K. 1988, ApJ, 324, 411
Wang, L., Baade, D., Höflich, P., Wheeler, J. C., Kawabata, K., Khokhlov, A., Nomoto, K., & Patat, F. 2006, ApJ, 653, 490
Wang, X., et al. 2008, ApJ, 675, 626
—. 2009a, ApJ, 699, L139
—. 2009b, ApJ, 697, 380
Webbink, R. F. 1984, ApJ, 277, 355
Whelan, J., & Iben, Jr., I. 1973, ApJ, 186, 1007
Wood-Vasey, W. M., et al. 2007, ApJ, 666, 694
—. 2008, ApJ, 689, 377
Woosley, S. E., & Kasen, D. 2011, ApJ, 734, 38
Yamanaka, M., et al. 2009, ApJ, 707, L118
Zehavi, I., Riess, A. G., Kirshner, R. P., & Dekel, A. 1998, ApJ, 503, 483
Zhang, T., et al. 2010, PASP, 122, 1

Appendix A

LOSS Natural-System Photometry

Deriving SN photometry in the natural system of the telescope requires determining the natural-system magnitudes of local field standards. In Chapter 2, we described the process of deriving Landolt magnitudes of local standard stars on photometric nights during our observing campaign. We transform the Landolt magnitudes to natural-system magnitudes using the set of equations

$$b = B + C_B(B - V), \quad \text{(A.1)}$$

$$v = V + C_V(B - V), \quad \text{(A.2)}$$

$$r = R + C_R(V - R), \text{ and} \quad \text{(A.3)}$$

$$i = I + C_I(R - I), \quad \text{(A.4)}$$

where lowercase letters present natural system magnitudes, uppercase letters represent Landolt-system magnitudes, and C_X are the observed color terms from Table 2.4 in Chapter 2 derived from observations of Landolt (1992, 2009) standards on photometric nights. Catalogs for local-field stars for our 165 SNe fields can be downloaded from our website[1].

There is a concern that we are introducing a systematic error by transforming our Landolt magnitudes for local field stars to the natural-system by simply using the averaged color terms derived from transforming natural-system magnitudes to Landolt magnitudes. In a sense, we are taking natural-system photometry transforming it to the Landolt system and then transforming it back to the natural system.

A more straightforward approach would create a catalog of Landolt (1992, 2009) standards on the natural system of each telescope system by applying a linear color correction (e.g., A.1 – A.4). Then for each photometric night, solve for the photometric solution using only a zero point and an airmass term and apply that solution to the SN fields to get the

[1] http://hercules.berkeley.edu/database

natural magnitudes of each local field star. The downside of this approach is that if a field is calibrated using observations with the Nickel telescope, the local field star magnitudes will be on the Nickel photometry system and cannot be used to calibrate KAIT observations.

To ensure that our approach did not introduce a significant systematic error, we tested the two approaches on a few SN fields and found that differences were within < 0.01 mag.

Next, we calculate the zero points of our bandpasses. The zero point of a photometric system is defined as

$$ZP_X = 2.5 \times \log_{10} \int_0^\infty F_\lambda S_X(\lambda) \frac{\lambda}{hc} d\lambda + m_0, \tag{A.5}$$

where S_X is the transmission function for the X band, F_λ is the SED of the standard, and m_0 is the magnitude of the standard in the Landolt system. Vega has been a historical favorite choice for the photometry zero point, but it has many shortcomings such as a poorly constrained Landolt magnitude, and it is too bright to be imaged on modern telescopes (Conley et al. 2011). The Supernova Legacy Survey (SNLS) adopted BD $+17^\circ$ 4806 which has a known Landolt magnitude (Landolt & Uomoto 2007) and a high-quality *Hubble Space Telescope* spectral observation (Bohlin & Gilliland 2004).

Instead of determining the zero point using a single star, we derive the zero point using the catalog of spectrophotometric standard stars presented by Stritzinger et al. (2005). Using the transmission curves given in Chapter 2.2.2, we synthesize instrumental magnitudes using spectra of 100 spectrophotometric standards[2]. We then fit for the zero point of each band with the equations

$$b = B + C_B(B - V) + ZP_B, \tag{A.6}$$
$$v = V + C_V(B - V) + ZP_V, \tag{A.7}$$
$$r = R + C_R(V - R) + ZP_R, \text{ and} \tag{A.8}$$
$$i = I + C_I(R - I) + ZP_I \tag{A.9}$$

where lowercase letters are the synthesized instrumental magnitudes, uppercase letters represent Landolt system magnitudes, C_X are color terms from Table 2.4 in Chapter 2, and ZP_X are the desired zero points of the natural photometric system. The zero points of the KAIT[1-4] and Nickel bandpasses can be found in Table A.1.

[2]Download from http://www.das.uchile.cl/∼mhamuy/SPECSTDS/.

Table A.1: Zero points for LOSS Passbands[a]

Telescope System	ZP_B	ZP_V	ZP_R	ZP_I
KAIT1	15.304	14.913	15.357	14.686
KAIT2	15.361	14.914	14.975	14.452
KAIT3	15.332	14.921	15.008	14.457
KAIT4	15.249	14.922	14.973	14.439
NICKEL	15.224	14.828	14.930	14.703

[a]Zero points are give in magnitudes.